**UNIVERSITY OF SOUTHAMPTON**

FACULTY OF ENGINEERING, SCIENCE & MATHEMATICS

OPTOELECTRONICS RESEARCH CENTRE

# FABRICATION AND APPLICATIONS OF ZINC INDIFFUSED CHANNEL WAVEGUIDES IN PERIODICALLY POLED LITHIUM NIOBATE

by

Lu Ming

A thesis submitted for the degree of
Doctor of Philosophy

May 2005

UNIVERSITY OF SOUTHAMPTON

## ABSTRACT

FACULTY OF ENGINEERING, SCIENCE & MATHEMATICS
OPTOELECTRONICS RESEARCH CENTRE

Doctor of Philosophy

# FABRICATION AND APPLICATIONS OF ZINC INDIFFUSED WAVEGUIDES IN PERIODICALLY POLED LITHIUM NIOBATE

by

Lu Ming

A comprehensive investigation of high conversion efficiency second harmonic generation (SHG) devices based on zinc indiffused channel waveguides in periodically poled lithium niobate (PPLN) is reported in this thesis.

The thesis covers all stages from the production of PPLN by domain inversion on a micron scale through to optical testing. The factors affecting poling quality, such as crystal discrepancies from different suppliers, electrode materials, patterning quality, and mask design, are investigated and analysed systematically. In addition, back-switch poling methods (involving poling a sample completely and then re-poling) are demonstrated. By using optimized processes combining high electric-field poling with the use of conductive liquid gel as an electrode, we have successfully fabricated high quality PPLN samples with short periods (less than 6.5μm), magnesium doped PPLN (PPMgLN), periodically poled lithium tantalate (PPLT), and hexagonally poled lithium niobate (HexLN).

Quasi-phase-matched (QPM) wavelength conversion devices based on lithium niobate channel waveguides were realized. Fabrication methods for Zn-diffused channel waveguides in z-cut PPLN by thermal diffusion of metallic Zn film have been investigated. A new approach using atmospheric pressure diffusion to make single mode waveguides for different fundamental wavelengths was successful. Optimised devices gave second harmonic generation conversion efficiency of $59\%W^{-1}cm^{-2}$ for 1552.4nm with 81% conversion for a pulsed source being achieved. Studies of green and blue generation exposed limitations with the technique for shorter wavelength operation, and these are discussed and modelled.

# Acknowledgements

I would like to extend my gratitude and to deeply thank my supervisor, Professor **Peter G. R. Smith**, for his excellent supervision and being patient on teaching. I have benefited a lot from his extensive knowledge in physics, nonlinear optics and many brilliant ideas and his can-do attitude. Without his constant encouragement, guidance on my PhD program and support and warm help with my family during the past years of my stay in UK, I could never completed my research and would never have been able to gain these experiences in my research field.

I am especially grateful to Dr. **Corin Gawith** for sharing his knowledge of fabrication of periodically poled lithium niobate and his support of my daily research work. I have gained much knowledge in experimental techniques from him. Many thanks also for much valuable advice on writing papers and his strict corrections to them.

I like to express my sincere appreciation to the members of my research group, Dr. R. B. Williams, Dr. Gregory D. Emmerson, Dr. Sam P. Watts and Dr. Dennis A. Guilhot, for their kind help and collaborations on the experimental work and on the co-authored papers.

I wish to say many thanks to Prof. James Wilkinson, Prof. Rob Eason, Dr. Katia Gallo, Dr. David Shepherd, Dr. Martin V. O'Connor, Dr. Xian Feng, Dr. Collin Sones, for their support and providing the opportunities to use the Prism Coupling equipment, Ti:sapphire laser, OPO and the optical spectrum analyzer that are indispensable for my experiments.

My thanks to David Sager, Ping Hua, the workshop crew and the many people I have worked with in ORC for their support and help during my PhD research.

To my wife, Hong Ye Jing, for giving me the most careful and loving support and encouragement and always being there through both the good and the bad in my life. To my parents for their supports and understanding. To my sister and brother in law, for their many good suggestions to my PhD research program and care in my life. And finally to my daughter for endless happiness brought to me.

# CONTENTS

# DECLARATION OF AUTHORSHIP

I, ……**Lu Ming**……., [please print name]

declare that the thesis entitled [enter title]

**"FABRICATION AND APPLICATIONS OF ZINC INDIFFUSED CHANNEL WAVEGUIDES IN PERIODICALLY POLED LITHIUM NIOBATE"**

……

and the work presented in it are my own. I confirm that:

- this work was done wholly or mainly while in candidature for a research degree at this University;
- where any part of this thesis has previously been submitted for a degree or any other qualification at this University or any other institution, this has been clearly stated;
- where I have consulted the published work of others, this is always clearly attributed;
- where I have quoted from the work of others, the source is always given. With the exception of such quotations, this thesis is entirely my own work;
- I have acknowledged all main sources of help;
- where the thesis is based on work done by myself jointly with others, I have made clear exactly what was done by others and what I have contributed myself;
- none of this work has been published before submission; or [delete as appropriate] parts of this work have been published as: [please list references]

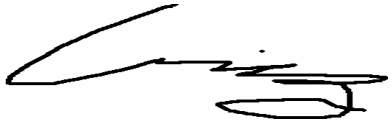

Signed: .....

Date: 26/06/2005.....

**“I hear and I forget.**
**I see and I remember.**
**I do and I understand”**

*Confucius (551 BC - 479 BC)*
*Chinese philosopher & reformer*

# Chapter 1

## Introduction

This chapter presents the motivation for this research and an overview of periodically poled lithium niobate and its applications, with an emphasis on its uses in nonlinear optics.

### 1.1 Motivation

Periodically poled lithium niobate (PPLN) is a nonlinear optical conversion material whose nonlinear properties can, to some extent, be engineered [1,2]. Periodic reversal of the domains within lithium niobate can be used to select the operating wavelength, with wavelengths throughout most of the visible, near-infrared, and mid-infrared regions being obtainable [3,4,5]. Thus, in addition to temperature and angle tuning, which are the conventional ways of tuning a frequency conversion device, PPLN can also be tuned by varying the period of the poling [6]. The output wavelengths are thus essentially determined during the fabrication of the PPLN material, and not by the thermal or mechanical forces to which the material is exposed. However, temperature and angle tuning can still be used to fine-tune the output wavelengths [7]. Figure 1.01 illustrates a PPLN structure in which the lithium niobate crystal domain has been periodically inverted to form a PPLN grating.

**Figure 1.01.** PPLN structure

PPLN is suitable for many applications in different fields. Based upon the quasi-phase-matching (QPM) technique in lithium niobate [8], frequency conversion of a laser beam in a spectral range from 400nm to 4,500nm can be achieved [9,10,11]. PPLN's remarkable properties make it particularly suitable for applications in optical frequency conversion such as Optical Parametric Oscillation (OPO) [12,13] and Optical Parametric Amplification (OPA) [14,15,16]; for electro-optic Bragg-deflectors for switching and modulating light [17,18]; and for sensors for aerospace and environmental monitoring [19,20].

For application in frequency conversion, PPLN exhibits a significant increase in the effective nonlinear coefficient when compared to birefringently phase-matched lithium niobate. Therefore, highly efficient frequency conversion can be obtained, and since the conversion efficiency of a nonlinear crystal is proportional to the square of the effective nonlinear coefficient [ 21 ], much more efficiently than using birefringent phase matching. Frequency doubled Nd:YAG lasers have also been used to generate high power visible light [22] and tuneable IR output as far as 6.3μm [23]. In addition PPLN material can be used as the nonlinear material for parametric oscillators and amplifiers based on high-power fibre sources [ 24 ], where the compatibility of fibre and PPLN provides an attractive route for compact devices for tuneable IR generation and amplification [25,26].

Through the use of modern semiconductor and micro-engineering technology multiple gratings have been formed on a single crystal chip to generate multiple signal wavelengths simultaneously from a single pump source [ 27 ]. Further applications of PPLN in optics involve the electro-optic effect, which has allowed the construction of modulators with switching speeds approaching 1ns [28]. Using the piezoelectric effect, PPLN can also be used as an acousto-optic transducer [29].

By combining PPLN and waveguide structures, high optical intensities of the interacting beams can be maintained over the whole length of the waveguide to improve efficiency by two to three orders of magnitude as compared to bulk devices [30]. PPLN waveguide can be used for the development of optical frequency mixers which are well suited for optical fibre communication and other all optical signal processing applications. Such optical frequency mixers can be considered as an enabling technology to realize high capacity and transparency in Wavelength Division Multiplexing (WDM) [31,32] and in high-speed Time Division Multiplexing (TDM) systems [33], as shown in Figure 1.02.

PPLN waveguides provide a route for a number of different optical signal processing functions desirable in next generation telecoms. In WDM systems, which take advantage of erbium-doped-fibre amplifiers (EDFA) to allow amplification of more than one hundred wavelengths simultaneously, multiple signal channels carried by

different wavelengths are independently transmitted through the same fibre. Such systems, multiplexing over one hundred channels in a single fibre, have been demonstrated in a Dense WDM (DWDM) system [34]. In a TDM system, multiple channels at low bit rate are allocated to different time slots and multiplexed into a high bit rate stream. Currently the capacity of a single fibre is approaching one terabit-per-second in TDM systems [35]. By combining WDM and TDM systems, over three terabits-per-second transmission capacity for a single fibre has been achieved [36].

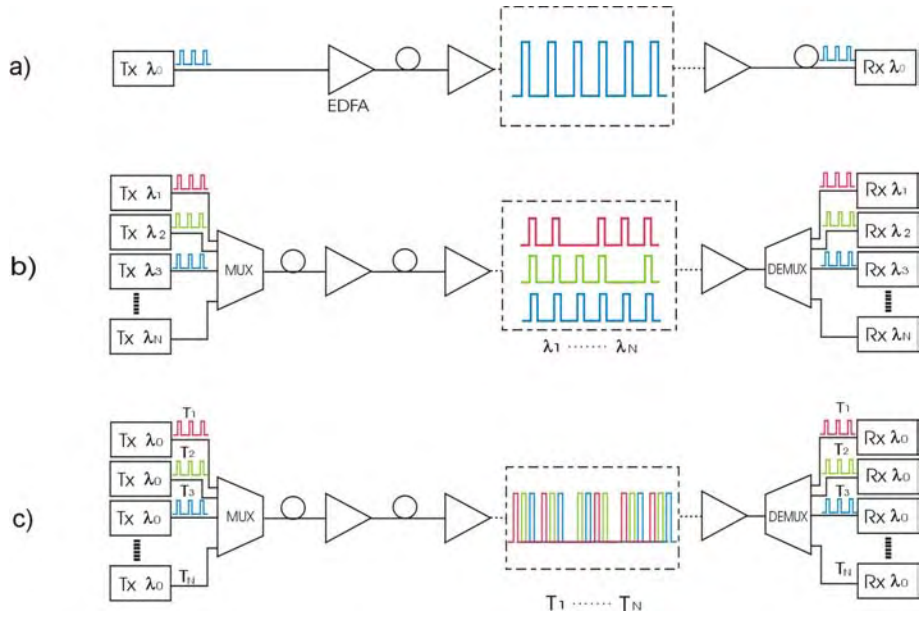


**Figure 1.02.** Schematic diagrams of optical fibre telecom systems. (a) Single channel system; (b) Wavelength Division Multiplexing (WDM) system; (c) Time Division Multiplexing (TDM) system. (EDFA: Erbium Doped Fibre Amplifier; TX: Transmitter; RX: Receiver.)

Several potential optical frequency mixer devices which are based upon the quasi-phase-matching (QPM) technique in PPLN waveguides have been practically and successfully demonstrated, including efficient WDM wavelength converters within the 1.5μm band or between the 1.3μm band and the 1.5μm band, spectral inverters for dispersion compensation in fibre link and multiple-channel wavelength converters for dynamic reconfiguration and broadcasting. The multiple-channel QPM structure formed by superimposition of a phase-reversal grating upon a uniform QPM grating can be tailored for multiplexed wavelength conversion based on 1.3μm to 1.5μm bands of telecom window [37]. All the above applications require high quality PPLN and PPLN waveguide structures in order to achieve high conversion efficiency

A number of methods are currently employed for fabricating waveguides in PPLN, the most popular of which are annealed proton exchange (APE) [38] and titanium diffusion [39]. However, each of these techniques has some limits of applicability. A recently developed alternative to these techniques is zinc-indiffusion. This approach offers potential to combine PPLN with the relative simplicity and low processing temperature of zinc indiffusion. Unlike APE, zinc indiffused waveguides support both TM and TE modes and show enhanced resistance to photorefractive damage in lithium niobate [40] which allows us to develop room temperature devices. Room temperature operation is important for fiber pigtailing.

In this research, the factors which influence the poling quality of PPLN and different poling methods have been investigated and a novel channel waveguide fabrication method using zinc indiffusion has been demonstrated, PPLN channel waveguide devices based on this technology have been characterized.

## 1.2 Outline of Thesis Structure

This thesis consists of nine chapters including this first introductory chapter which includes the motivation for the research, an overview of the thesis content and a brief introduction to PPLN and PPLN waveguides and their application

Chapter 2 introduces the basic theories of nonlinear optics, second harmonic generation (SHG) and quasi-phase-matching (QPM). Three wave interactions are also introduced.

Chapter 3 describes the main properties and applications of lithium niobate, this chapter highlights the main physical and nonlinear optical properties of lithium niobate which influence the fabrication and performance of PPLN based devices. Crystal growth techniques are outlined, and the crystallographic properties are described.

Chapter 4 begins by introducing electrical poling of lithium niobate, the fabrication procedures for periodically poled lithium niobate (PPLN) using an electric field poling technique with liquid gel electrodes are reviewed, Alternative methods of

domain inversion in lithium niobate are also discussed and the methods of grating quality assessment are presented. The factors affecting poling quality are reported in the middle section of this chapter. Various novel poling techniques, such as backswitch poling, are presented. The chapter finishes by presenting novel hexagonally poled lithium niobate (HexLN), periodically poled lithium tantalate (PPLT) and Mgo-doped PPLN (PPMgLN) devices researched as part of this thesis and in collaboration with other research groups inside and outside of the Optoelectronics Research Centre (ORC).

Chapter 5 introduces the waveguide theory used to design a channel waveguide device based on a PPLN substrate. Optical waveguide are known to maintain high energy density over a long distance and can thus be used to realize an SHG device having substantially higher conversion efficiency than bulk. The effective index method is described and used to carry out simple waveguide modeling.

Chapter 6 briefly introduces the existing channel waveguide fabrication technologies used with PPLN and describes our work carried out to integrate zinc indiffused waveguides and PPLN for use in harmonic generation. Different types of PPLN waveguides are reviewed with the zinc indiffusion technique shown to exhibit several advantages over other methods such as proton exchange or titanium indiffusion. The mechanisms of zinc diffusion in lithium niobate are discussed. The refractive index profile of Zn:$LiNbO_3$ is described by a theoretical model based on an empirical equation. The final section in this chapter presents results achieved in successfully fabricating zinc indiffused waveguide device for first order and third order SHG which are then described in chapter 7 and chapter 8.

Chapter 7 describes the optical characterization of the PPLN channel waveguide devices described in chapter 6. The mode profile and NA of the waveguides formed under different indiffusion conditions are investigated, the propagation loss and the polarization dependence of the waveguide are also measured. The optimum waveguide fabrication parameters are then discussed. The final part of this chapter presents quasi-phase-matched second-harmonic generation (SHG) experiments in PPLN waveguide devices. The SHG conversion efficiency for a fundamental beam of

1552.4nm wavelength was measured by using a DFB single-mode laser diode at low input power and an OPO at a high input power source.

Chapter 8 describes visible light generation experiments using the PPLN waveguide devices fabricated based on the procedures described in chapter 6. Green light (532nm) was obtained by frequency doubling incident beams from a Nd:YAG laser through the PPLN waveguide device. The photorefractive effect induced by the green light is discussed in the middle section of this chapter. Blue light (417.5nm) achieved through third order SHG by frequency doubling a tuneable Ti: Sapphire laser is presented in the final part of this chapter. Overall conclusions and a discussion of potential future work and improvement that can be carried out at the University of Southampton are discussed in chapter 9.

## References

[1] N. Bloembergen, "Nonlinear Optics", Benjamin, New York, (1965)

[2] D. C. Hanna, "Periodically-poled lithium niobate - a 'designer' material for nonlinear optics", *PR '99*, Elsinore Denmark, SA01 (Invited) (1999)

[3] G. D. Miller, R. G. Batchko, W. M. Tulloch, D. R. Weise, M. M. Fejer, R. L. Byer, "42%-efficient single-pass CW second-harmonic generation in periodically poled lithium niobate", *Opt. Lett.*, Vol.**22**, p.1834-1836 (1997)

[4] M. Yamada, N. Nada, T. Yamaguchi, M. Saitoh, and K. Watanabe, "A quasi-phase-matched waveguide for the blue second-harmonic generation", *Electronics and Communications in Japan*, Part 2, Vol.**77**, p.52-61 (1994)

[5] E. J. Lim, M. M. Fejer, and R. L. Byer, "Second-harmonic generation of green light in periodically poled planar lithium niobate waveguide", *Electron. Lett.*, Vol.**25**, p.174-176 (1989)

[6] S. A. Akhmanov and R. V. Khokhlov., "Problems in Nonlinear Optics", Akad. Nauk. USSR, Moscow (1964). English edition, Gordon and Breach, New York, (1973)

[7] M. M. Fejer, G. A. Magel, D. H. Jundt, and R. L. Byer, "Quasi-phase-matched second harmonic generation: tuning and tolerances", *IEEE J. Quantum Electron*., Vol.**28**, p.2631-2654 (1992)

[8] J. A. Armstrong, N. Bloembergen, J. Ducuing, and P. S. Pershan, "Interactions between light waves in a nonlinear dielectric", *Phys. Rev*., Vol.**127**, p.1918-1939 (1962)

[9] M. M. Fejer, "Nonlinear Optical Frequency Conversion", *Physics Today*, Vol.**47**, p.25-32 (1994)

[10] R. L. Byer, "Quasi-phase matched nonlinear materials and application to devices", *Nonlinear Optics, Principles, Materials, Phenomena and Devices*, Vol.**7**, p.235-245 (1994)

[11] R. L. Byer, "Quasi-phase matched nonlinear interactions and devices", *Journal of Nonlinear Optical Physics & Materials*, Vol.**6**, p.549-591 (1997)

[12] L. E. Myers, G. D. Miller, R. C. Eckardt, M. M. Fejer, and R. L. Byer, "Quasi-phase-matched 1.064µm-pumped optical parametric oscillator in bulk periodically poled $LiNbO_3$", *Opt. Lett.*, Vol.**20**, p.52-54 (1995)

[13] P. E. Britton, H. L. Offerhaus, D. J. Richardson, P. G. R. Smith, G. W. Ross and D. C. Hanna, "A parametric oscillator directly pumped by a 1.55µm erbium fibre laser", *Opt. Lett.*, Vol.**24**, p.975-977 (1999)

[14] R. A. Baumgartner and R. L. Byer, "Optical parametric amplification", *IEEE J. Quantum Electron.*, Vol.**15**, p.432-444 (1979)

[15] P. E. Britton, N. G. R. Broderick, D. J. Richardson, P. G. R. Smith, G. W. Ross, D. C. Hanna, "Wavelength-tuneable high-power pico-second pulses from a fibre pumped diode-seeded high-gain parametric amplifier", *Opt. Lett*., Vol.**23**, p.1588-1590 (1998)

[16] A. C. Chiang, T. D. Wang, Y. Y. Lin, C. W. Lau, Y. H. Chen, B. C. Wong, Y. C. Huang, J. T. Shy, Y. P. Lan, Y. F. Chen, and P. H. T. Tsao, "Pulsed Optical Parametric Generation, Amplification, and Oscillation in Monolithic Periodically Poled Lithium Niobate Crystals", *IEEE J. Quantum Electron.*, Vol.**40**, p.791-801 (2004)

[17] M. Yamada, "Electrically induced Bragg-diffraction grating composed of periodically inverted domains in lithium niobate crystals and its application devices", *Review of Scientific Instruments*, Vol.**71**, p.4010-4016 (2000)

[18] J. A. Abernethy, R. W. Eason, P. G. R. Smith, "Bulk optical Bragg deflectors at 1.064µm based on an electro-optically induced grating in periodically poled lithium niobate", *CLEO/Pacific Rim Chiba*, ME2-3, p.102-103 (2001)

[19] D. Richter, D. G. Lancaster, and F. K. Tittel, "Development of an automated diode-laser-based multi component gas sensor", *Appl. Opt.*, Vol.**39**, p.4444-4450 (2000)

[20] D. Richter, D. G. Lancaster, R. F. Curl, W. Neu, F. K. Tittel, "Compact mid-infrared trace gas sensor based on difference-frequency generation of two diode lasers in periodically poled $LiNbO_3$", *Appl. Phys*., B Vol.**67**, p.347–350 (1998)

[21] R. L. Byer, "Quasi-phase matched nonlinear interactions and devices", *Journal of Nonlinear Optical Physics & Materials*, Vol.**6**, p.549-591 (1997)

[22] V. Pruneri, J. Webjörn, P. St. J. Russell, J. R. M. Barr, D. C. Hanna, "Intracavity second harmonic generation of 0.532µm in bulk periodically poled lithium niobate", *J. Opt. Commun.*, Vol.**116**, p.159-162 (1995)

[23] L. Lefort, K. Puech, Y. P. Svirko, G. W. Ross, P. G. R. Smith, D. C. Hanna, "Optical parametric oscillation beyond 6.3µm in periodically-poled lithium niobate", *Proc. CLEO/Europe '98*, Glasgow Scotland, CFF1 (1998)

[24] M. V. O'Connor, M. A. Watson, D. C. Hanna, D. P. Shepherd, L. Lefort, J. H. V. Price, A. Malinowski, J. Nilsson, N. G. R. Broderick, D. J. Richardson, "Fibre-laser-pumped femtosecond PPLN OPO", *QEP 15* Glasgow, p.139-140 (2001)

[25] P. G. R. Smith, P. E. Britton, D. Taverner, N. G. Broderick, D. J. Richardson, G. W. Ross, C. B. E. Gawith, J. A. Abernethy, H. L. Offerhaus, D. C. Hanna, "Review of erbium fibre laser based nonlinear optics in periodically poled lithium niobate (PPLN)", *International Workshop on Periodically Microstructured Nonlinear Optical Materials* Madrid, (2001)

[26] D. J. Richardson, A. B. Grudinin, D. C. Hanna, "Fiber laser pumped parametric devices based on periodically poled lithium niobate", *OSA Annual Meeting/ILS-XIV* Baltimore USA, FL1 (Invited) (1998)

[27] N. G. R. Broderick, G. W. Ross, D. J. Richardson, D. C. Hanna, "HeXLN: A 2-dimensional nonlinear photonic crystal", *Nonlinear Guided Waves & Their Applications '99 Dijon*, (Postdeadline), PD1 (1999)

[28] D. Taverner, P. Britton, P. G. R. Smith, D. J. Richardson, G. W. Ross and D. C. Hanna, "High Efficient second harmonic and sum frequency generation of nanosecond pulses in a cascaded erbium doped fibre: PPLN source", *Opt. Lett.*, Vol.**23**, p.162-164 (1998)

[29] H. Gnewuch, N. Zayer, C. N. Pannell, G. W. Ross, P. G. R. Smith, "Some initial results with acoustic superlattice transducers made by domain inversion of $LiNbO_3$", *IoP meeting: Acousto-optic interactions components and techniques*, London, (1999)

[30] M. Yamada, N. Nada, M. Saitoh, K. Watanabe, "First-order quasi-phased matched $LiNbO_3$ waveguide periodically poled by applying an external field for efficient blue second-harmonic generation", *Appl. Phys. Lett.*, Vol.**62**, p.435-437 (1993)

[31] I. P. Kaminow, C. R. Doerr, C. Dragone, T. Koch, U. Koren, A. A. M. Saleh, A. J. Kirby, C. M. Ozveren, C. M. B. Schofield, R. E. Thomas, R. A. Barry, D. M. Castagnozzi, V. W. S. Chan, B. R. Jr. Hemenway, D. Marquis, S. A. Parikh, M. L. Stevens, E. A. Swanson, S. G. Finn, R. G. Gallager, "A wideband all-optical WDM network", *IEEE J. Lightwave Technol.*, Vol.**14**, p.780-799 (1996)

[32] C. A. Brackett, A. S. Acampora, J. Sweitzer, G. Tangonan, M. T. Smith, W. Lennon, K. C. Wang, R. H. A. Hobbs, "Scalable multi-wavelength multi-hop optical network: a proposal for research on all-optical networks", *IEEE J. Lightwave Technol.*, Vol.**11**, p.736-753 (1993)

[33] A. E. Willner, "Mining the optical bandwidth for a terabit per second", *IEEE Spectrum*, Vol.**34**, p.32-41 (1997)

[34] A. K. Srivastava, Y. Sun, J. Sulhoff, C. Wolf, M. Zirngibl, R. Monnard, A. R. Chraplyvy, A. A. Abramov, R. P. Espindola, T. A. Strasser, J. R. Pedrazzani, A. M. Vengsarkar, J. L. Zyskind, J. Zhou, D. A. Ferrand, P. F. Wysocki, J. B. Judkins, and Y. P. Li, "1 Tb/s transmission of 100 WDM 10 Gb/s channels over 400 km of TrueWave fiber", *OFC'98*, PD10 (1998)

[35] M. Nakazawa, E. Yoshida, T. Yamamoto, E. Yamada, A. Sahara, "TDM single channel 640 Gbit/s transmission experiment over 60 km using a 400 fs pulse train and a walk-off free, dispersion flattened nonlinear optical loop mirror", *OFC'98*, PD14 (1994)

[36] S. Kawanishi, H. Takara, K. Uchiyama, I. Shake, and K. Mori, "3 Tbit/s (160 Gbit/s × 19 channel) OTDM-WDM transmission experiment", *OFC'99*, PD1 (1999)

[37] K. Mizzuchi, K. Yamamoto, "Waveguide second harmonic generation device with broadened flat quasi-phase-matching response by use of a grating structure with located phase shifts", *Opt. Lett.*, Vol.**23**, p.1880-1882 (1998)

[39] Y. N. Korkishko, V. A. Fedorov, T. M. Morozova, F. Caccavale, F. Gonella, and F. Segato, "Reverse proton exchange for buried waveguides in $LiNbO_3$", *JOSA A*. **15**, p.1838-1842 (1998)

[40] J. Amin , V.Pruneri, J. Webjörn, P. St. J. Russell, D.C. Hanna, J. S. Wilkinson, "Blue light generation in a periodically poled Ti: Lithium Niobate channel waveguide", *Opt. Commun.*, Vol.**135**, p.41-44 (1997)

[41] W. M. Young, M. M. Fejer, M. J. F. Digonnet, A. F. Marshall, and R. S. Feigelson, J. "Fabrication, Characterization and Index Profile Modeling of High-Damage Resistance Zn-Diffused Waveguide in Congruent and MgO: Lithium Niobate", *Lightwave Technol.*, Vol.**10**, p.1238-1246 (1992)

# Chapter 2

## Introduction to Nonlinear Optics

Chapter one described the motivation of this research and some applications of periodically poled lithium niobate devices and nonlinear processes. In this chapter, the basic concepts of nonlinear optics and relevant fundamental concepts and mathematics required for this thesis are explained.

### 2.1 Historical Background

The first $\chi^{(2)}$ nonlinear process (optical second harmonic generation) was observed by Franken *et al*. [1] in 1961 by using a ruby laser focused in a crystal of quartz. The success of this experiment can be attributed to the enormous increase of power provided by a laser source compared to the existing incoherent sources. Although the conversion efficiency was only ~$10^{-6}$, as there was no proper phase matching, the principle of second harmonic generation was shown.

Shortly after Franken's result showing non-phase-matched second harmonic generation, Kleinman [2], Giordmaine [3], and Maker *et al*. [4] demonstrated that phase matching could be achieved in birefringent crystals by using the property of birefringence to compensate the index dispersion of the crystal. Three years later in 1965, Wang & Racette observed significant gain in a three frequency mixing experiment [5]. In 1968 Geusic *et al*. [6] showed efficient doubling of a continuous wave Nd:YAG laser using the crystal $Ba_2NaNb_5O_{15}$. One year later, 70% conversion efficiency was achieved in KDP and a frequency doubled CW Nd:glass laser was also demonstrated by Hagen [7].

In the last three decades, research in nonlinear optics was concentrated on discovering and developing new nonlinear optical materials with suitable birefringence properties. The slow progress in finding new nonlinear crystals led researchers to revisit the idea of quasi-phase-matching (QPM), first suggested by Armstrong and Bloembergen *et al*.,[8] this technique involved the use of periodically altering the sign of the nonlinear coefficient to achieve the quasi-phase-matching in

the crystal. A detailed theoretical treatment of quasi-phase-matched interactions was provided by Fejer *et al*. [9]. Throughout this period different techniques were attempted to produce periodically poled nonlinear samples for QPM [10,11].

In the early nineties, the technique of periodic poling by applying a patterned strong electric field across a ferroelectric crystal was developed. Lithium niobate was first periodically poled by applying an external electric field at room temperature by Yamada *et al*. [12] in 1993, while here in University of Southampton it was first achieved by Webjörn in 1994 [13]. Since this first demonstration this method has established itself as an important way to obtain highly nonlinear material that will phase-match any desired interaction [14,15,16].

## 2.2 Basic Theory

The basic theory of nonlinear optics is introduced in this section. The following section is based closely on the treatments presented by R. L. Byer [17,18] and R. W. Boyd [19], and we start from the electromagnetic theory, and then define some basic concepts.

### 2.2.1 Nonlinear Optics

A light wave consists of electromagnetic fields which change sinusoidally at optical frequencies. When a light wave is incident on a dielectric medium, charged particles in the medium will be displaced from their equilibrium positions and start to oscillate in the applied electric field, forming oscillating electric dipoles [17]. On a macroscopic scale, these oscillating electric dipoles build up in the medium resulting in a charge redistribution at optical wavelengths which is described by the polarization *P*. The polarization can be written as an expansion in powers of the electric field *E* [20,21].

$$P(t) = \varepsilon_0(\chi^{(1)}E(t) + \chi^{(2)}E(t)^2 + \chi^{(3)}E(t)^3 + \ldots) \qquad 2.01$$

where $\chi^{(1)}$ is the linear optical susceptibility of the medium and is related to the medium's refractive index *n* by $\chi^{(1)} = n^2\text{-}1$, $\varepsilon_0$ is the permittivity of free space, $\chi^{(2)}$ is the second-order nonlinear susceptibility, $\chi^{(3)}$ is the third-order nonlinear

susceptibility and so on, $\chi^{(2)}, \chi^{(3)}$.... describe the most important nonlinear optical properties of the medium.

For a weak applied electric field *E*, the charge can follow the field almost exactly and the polarization *P* is linearly proportional to the applied electric field *E*. For larger amplitudes of the applied electric field, the relationship between *P* and *E* becomes nonlinear, and the $\chi^{(2)}$ and $\chi^{(3)}$ terms will be important.

In order to demonstrate the theory of nonlinear effects, consider an applied electric field:

$$E(t) = E_0 \cos(\omega t) \qquad 2.02$$

Inserting Eq.(2.02) into Eq.(2.01) , we can get [22]:

$$P(t) = \varepsilon_0(\chi^{(1)}E_0\cos\omega t + \frac{1}{2}\chi^{(2)}E_0^2(1+\cos 2\omega t) + \frac{1}{4}\chi^{(3)}E_0^3(3\sin(\omega t+\frac{\pi}{2}) - \sin(3\omega t+\frac{3\pi}{2})) + \ldots) \qquad 2.03$$

From above equation, it reveals that the polarization contains not only the linear component, but also a d.c. term and nonlinear components at frequencies of $2\omega, 3\omega, \ldots$. Thus light waves at new frequencies can be generated through the nonlinear effect.

The term $\chi^{(2)}$ gives rise to a number of interesting optical phenomena such as second harmonic generation (SHG), d.c. rectification [17, 23], see Figure 2.01, optical parametric oscillation (OPO), and three-wave mixing processes [24, 25]. The term $\chi^{(3)}$ results in third harmonic generation, two photon absorption [26,27], and four-wave mixing, etc [28,29]. As second harmonic generation is the focus of this thesis, the effects that arise from $\chi^{(2)}$ will be further derived, although a similar methodology can be applied to third harmonic effects.

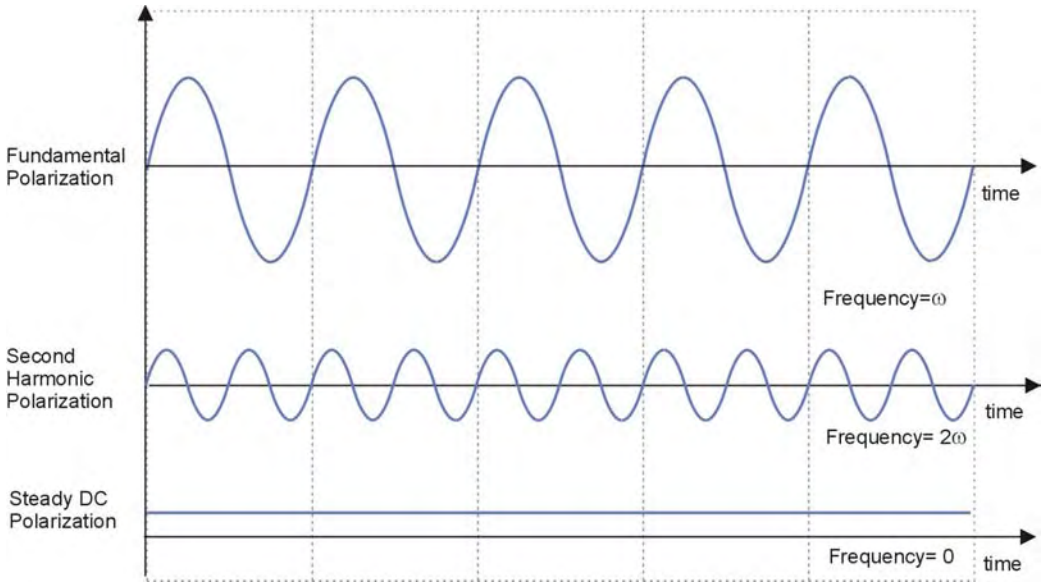


**Figure 2.01.** Fourier analysis of the nonlinear polarisation shows that it contains components oscillating at the fundamental frequency, twice the fundamental frequency (second-harmonic), and a steady dc component, as illustrated in Reference [30].

### 2.2.2 Nonlinear Optical Susceptibilities

When two waves $\omega_1$ and $\omega_2$ interact and combine in a medium to form a new wave $\omega_3$ through $\chi^{(2)}$, the polarization of the wave $\omega_3$ depends on the polarizations and the propagation directions of the two interacting waves $\omega_1$ and $\omega_2$, therefore a tensor $\chi^{(2)}_{ijk}$ in the frequency domain is used to describe the susceptibilities $\chi^{(2)}$ in the time domain in Eq.(2.01). The nonlinear polarization can be written in the form of a second order nonlinear susceptibility tensor $\chi^{(2)}_{ijk}$.

$$P_i\ (\omega_3) = \varepsilon_0 \sum_{jk} \chi^{(2)}_{ijk} E_j(\omega_1) E_k(\omega_2) \qquad 2.04$$

The field component at frequency $\omega$ can be defined by the Fourier relation

$$U(t) = \frac{1}{2}\left[U(\omega) \exp\, i(\vec{k}\cdot\vec{r} - \omega t) + cc\right] \qquad 2.05$$

Substitute Eq.(2.05) into Eq.(2.04):

$$P_i(\omega_3) = \varepsilon_0 \sum_{jk} \frac{\chi^{(2)}_{ijk}}{2}(\omega_3, \omega_2, \omega_1) E_j(\omega_2) E_k(\omega_1) \exp i\left(\Delta k \cdot \vec{r}\right) \qquad 2.06$$

Where $\omega_3 = \omega_1 + \omega_2$ , $\Delta k = k_1 + k_2 - k_3$ , $k = 2\pi n / \lambda$, $\lambda$ is the wavelength of interacting wave. It is convenient to write the driving polarization for $\chi_{ijk}^{(2)}$ in terms of a nonlinear tensor $d_{ijk}^{(2)}$ defined by:

$$P_i(\omega_3) = \varepsilon_0 \sum_{jk} d_{ijk}^{(2)}(\omega_3, \omega_2, \omega_1) E_j(\omega_2) E_k(\omega_1) \exp i(\Delta k \cdot \vec{r}) \qquad 2.07$$

From Eq.(2.06) and Eq.(2.07), we can find that : $\chi_{ijk}^{(2)} = 2d_{ijk}^{(2)}$

The second order susceptibility $d_{ijk}^{(2)}$ has 27 components and third order $d_{ijnm}^{(3)}$ has 81 components, however, in the research project presented in this thesis, only particular $d_{ijk}^{(2)}$ components are important.

We are generally interested in a particular process with a given frequency combination and well-defined polarization directions. Due to some symmetry properties of crystal, $d_{ijk}{}^{(2)}$ can be reduced from 27 components to 18 components, $d_{ijk} = d_{im}$, where *m* is 1-6 [17].

| | | | | 32 | 31 | 21 |
|---|---|---|---|---|---|---|
| (jk) | 11 | 22 | 33 | 23 | 13 | 12 |
| m | 1 | 2 | 3 | 4 | 5 | 6 |

The 3×6 matrix of $d_{im}$ becomes: $d_{im} = \begin{pmatrix} d_{11} & d_{12} & d_{13} & d_{14} & d_{15} & d_{16} \\ d_{21} & d_{22} & d_{23} & d_{24} & d_{25} & d_{26} \\ d_{31} & d_{32} & d_{33} & d_{34} & d_{35} & d_{36} \end{pmatrix}$

In central symmetric crystal $d_{ijk}^{(2)}$ is zero, which explains why second harmonic generation and frequency mixing only occur in non-centrosymmetric crystals.

### 2.2.3 Nonlinear Wave Propagation

To understand how to achieve effective nonlinear conversion, we must look at the spatial solution of the nonlinear response.

We start our study from the Maxwell's equation, as we know:

$$\nabla \times E = -\mu_0 \frac{\partial H}{\partial t} \tag{2.08a}$$

$$\nabla \times H = \frac{\partial D}{\partial t} + J \tag{2.08b}$$

Where $D = \varepsilon_0 E + P$, $J = \sigma E$ and $P = \varepsilon_0 \chi^{(1)} E + P_{NL}$. Therefore substitution gives:

$$\nabla \times H = \sigma E + \varepsilon_0 \frac{\partial E}{\partial t} + \varepsilon_0 \chi^{(1)} \frac{\partial E}{\partial t} + \frac{\partial P_{NL}}{\partial t} = \sigma E + \varepsilon \frac{\partial E}{\partial t} + \frac{\partial P_{NL}}{\partial t} \tag{2.09}$$

Where $\varepsilon = \varepsilon_0 (1 + \chi^{(1)})$. Now using the fact that:

$$\nabla \cdot D = 0, \nabla \times E = -\mu_0 \frac{\partial H}{\partial t}, \text{ thus } \nabla \times \nabla \times E = -\frac{\partial}{\partial t}(\mu_0 \nabla \times H) = \nabla(\nabla \cdot E) - \nabla^2 E.$$

The Maxwell equations may be combined to give:

$$\nabla^2 E = \mu_0 \sigma \frac{\partial E}{\partial t} + \mu_0 \varepsilon \frac{\partial^2 E}{\partial t^2} + \mu_0 \frac{\partial^2 P_{NL}}{\partial t^2} \tag{2.10}$$

Now assuming the electric fields of plane wave travel with frequencies $\omega_1, \omega_2, \omega_3$, and the direction of propagation is in one direction along *z*, the three waves can be described by equations:

$$E_i^{\omega_1}(z,t) = \frac{1}{2}(E_{1i}(z) e^{i(k_1 z - \omega_1 t)} + c.c) \tag{2.11}$$

$$E_j^{\omega_2}(z,t) = \frac{1}{2}(E_{2j}(z) e^{i(k_2 z - \omega_2 t)} + c.c) \tag{2.12}$$

$$E_k^{\omega_3}(z,t) = \frac{1}{2}(E_{3k}(z) e^{i(k_3 z - \omega_3 t)} + c.c) \tag{2.13}$$

Where $i, j, k$ are $x, y, z$; wave vector, $k = \frac{2\pi n}{\lambda}$, and $\omega_3 = \omega_1 + \omega_2$.

When $\omega_1 = \omega_3 - \omega_2$, we substitute Eq.(2.11) into Eq.(2.10), Eq.(2.10) is expanded as:

$$\nabla^2 E_i^{\omega_1}(z,t) = \frac{\partial^2}{\partial z^2} E_i^{\omega_1}(z,t) = \frac{1}{2}\frac{\partial^2}{\partial z^2}(E_{1i}(z) \exp\left(i(k_1 z - \omega_1 t)\right) + c.c) \tag{2.14}$$

$$= (-\frac{k_1^2}{2} E_{1i}(z) + i k_1 \frac{dE_{1i}(z)}{dz} + \frac{d^2 E_{1i}(z)}{dz^2}) \exp\left(i(k_1 z - \omega_1 t)\right) + c.c$$

$$= (-i\omega_1 \mu_0 \sigma - \omega_1^2 \mu_0 \varepsilon)\left(\frac{E_{1i}(z)}{2} \exp i(k_1 z - \omega_1 t) + c.c\right) - \mu_0 \frac{\partial^2}{\partial t^2}(P_{NL}(z,t))$$

Now considering the nonlinear polarization:

$$P_{NL}^{\omega_1} = d_{ijk} E_j^{\omega_2 *} E_k^{\omega_3} \tag{2.15}$$

$$\begin{aligned} P_{NL} &= \frac{d_{ijk}}{2}(E_{2j}^{*} E_{3k} e^{i[(k_3-k_2)z-(\omega_3-\omega_2)t]} + c.c) \\ &= \frac{d_{ijk}}{2}(E_{2j}^{*} E_{3k} e^{i[(k_3-k_2)z-\omega_1 t]} + c.c) \end{aligned} \tag{2.16}$$

Assuming the slow varying amplitude approximation: $\frac{dE_{1i}}{dz} k_1 >> \frac{d^2 E_{1i}}{dz^2}$, and ignoring higher orders, we then substitute Eq.(2.16) into Eq.(2.14) and remembering that :

$\omega^2 P >> \omega \frac{\partial P}{\partial t} >> \frac{\partial^2 P}{\partial t^2}$; $\omega E >> \frac{\partial E}{\partial t}$; $k = n\omega / c$; $\mu_0 \varepsilon_0 = 1/c^2$, the following equations are obtained [17]:

$$\frac{dE_{1i}}{dz} = -\frac{\sigma_1}{2}\sqrt{\frac{\mu_0}{\varepsilon_1}} E_{1i} - \frac{1}{2} i\omega_1 \sqrt{\frac{\mu_0}{\varepsilon_1}} d_{ijk} E_{3k} E_{2j}^{*} \exp(i\Delta k z) + c.c \tag{2.17}$$

$$\frac{dE_{2j}^{*}}{dz} = -\frac{\sigma_2}{2}\sqrt{\frac{\mu_0}{\varepsilon_2}} E_{2j}^{*} - \frac{1}{2} i\omega_2 \sqrt{\frac{\mu_0}{\varepsilon_2}} d_{ijk} E_{1i} E_{3k}^{*} \exp(i\Delta k z) + c.c \tag{2.18}$$

$$\frac{dE_{3k}}{dz} = -\frac{\sigma_3}{2}\sqrt{\frac{\mu_0}{\varepsilon_3}} E_{3k} - \frac{1}{2} i\omega_3 \sqrt{\frac{\mu_0}{\varepsilon_3}} d_{ijk} E_{1i} E_{2j} \exp -(i\Delta k z) + c.c \tag{2.19}$$

Where the $\Delta k = k_3 - k_2 - k_1$,

## 2.3 Second Harmonic Generation (SHG)

### 2.3.1 Three Wave Processes

The $\chi^{(2)}$ interaction involves three waves which may either be input or generated within the nonlinear material. There are three kind of interactions, they are sum frequency generation (SFG) or up-conversion; difference frequency generation (DFG) or mixing, and optical parametric generation (OPG) [24,25].

SFG describes the situation where two longer wavelengths (lower frequencies $\omega_1$ and $\omega_2$) are mixed with each other to generate a shorter wavelength (higher sum-frequency $\omega_3$) via the second order nonlinear susceptibility $\chi^{(2)}$. A schematic description of SFG is shown in Figure 2.02(a). The interaction can be expressed as:

$$\omega_1 + \omega_2 = \omega_3$$

Second harmonic generation (SHG) is a special case of SFG in which $\omega_1 = \omega_2$.

DFG describes the situation where a higher frequency $\omega_3$ and a lower frequency $\omega_2$ are mixed with each other to generate a difference frequency $\omega_1$ via the second order nonlinear susceptibility $\chi^{(2)}$. This process generates a longer wavelength. A schematic description of DFG is shown in Figure 2.02(b).

$$\omega_3 - \omega_2 = \omega_1$$

OPG uses a highest frequency (shorter wavelength) $\omega_3$ to generate two lower frequencies (longer wavelength) $\omega_2$, $\omega_1$ via the second order nonlinear susceptibility $\chi^{(2)}$. The generated pairs at frequencies $\omega_1$ and $\omega_2$ are determined by the phase-matching condition: $\Delta k = k_3 - k_2 - k_1 = 0$. This process can be thought of as the reverse process of SFG. For historical reasons we refer to $\omega_3$ as the pump, $\omega_1$ as the signal and $\omega_2$ as the idler (normally $\omega_2 < \omega_1$).

$$\omega_3 = \omega_2 + \omega_1$$

When $\omega_2 = \omega_1$, the process is said to be degenerate. An Optical Parametric Oscillator (OPO) makes use of this interaction. A schematic description of this process is shown in Figure 2.02(c).

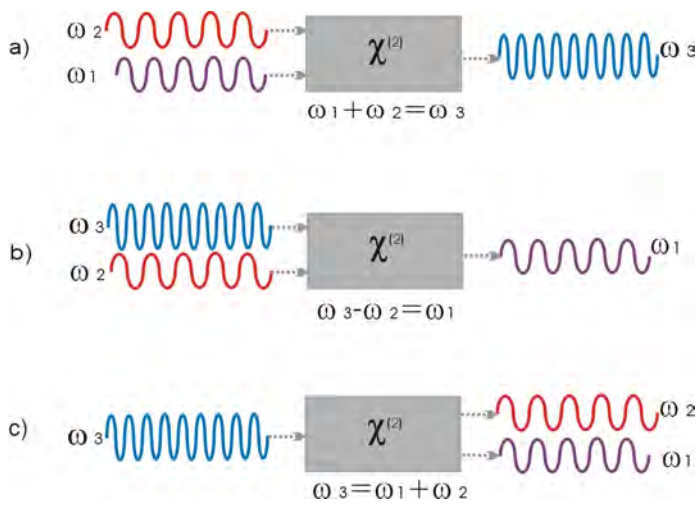


**Figure 2.02.** The three wave processes. (a) Sum frequency generation; (b) Difference frequency generation; (c) Optical parametric generation.

### 2.3.2 Second Harmonic Generation with Plane Waves

The simplest $\chi^{(2)}$ nonlinear interaction is second harmonic generation (SHG), and it is also one of the most important.

A driving field at frequency $\omega$ produces a nonlinear polarisation at frequency $2\omega$, based on Eq.(2.04), when the $\omega_2 = \omega_1 = \omega,$ and $\omega_3 = 2\omega.$ The polarisation at frequency $2\omega$ is given by:

$$P_i(2\omega\ ) = \varepsilon_0 \sum_{ijk} d_{ijk} E_j(\omega) E_k(\omega) \exp i\left((2k_\omega - k_{2\omega}) \cdot \vec{r}\right) \qquad 2.20$$

$$P(2\omega) = \varepsilon_0 d_{eff} E(\omega) E(\omega) \exp i(2k_\omega - k_{2\omega}) \cdot \vec{r} \qquad 2.21$$

$$P(\omega) = \varepsilon_0 d_{eff} E(2\omega) E(\omega)^* \exp - i(2k_\omega - k_{2\omega}) \cdot \vec{r} \qquad 2.22$$

Where $d_{eff}$ is an effective nonlinear coefficient that depends on the direction of propagation and the polarisation of the fields with respect to the crystal relative orientation etc. We use the effective nonlinear coefficient $d_{eff}$ to replace the term $d_{ijk}$. For the case of no absorption (neglecting the conductivity term in Eqs.(2.17-2.19)), the coupled equations reduce to:

$$\frac{dE(\omega)}{dz} = -i\omega \sqrt{\frac{\mu_0}{n_\omega^2 \varepsilon_0}} d_{eff} E(\omega) E(2\omega)^* \exp\left(i\Delta k z\right) \qquad 2.23$$

$$\frac{dE(2\omega)}{dz} = -i\omega \sqrt{\frac{\mu_0}{n_{2\omega}^2 \varepsilon_0}} d_{eff} E(\omega) E(\omega) \exp - \left(i\Delta k z\right) \qquad 2.24$$

where the $\Delta k = k_3 - k_2 - k_1 = k(2\omega) - 2k(\omega)$.

### 2.3.3 Low Conversion Efficiency Limit

To simplify things, we assume that the transfer of power has a negligible effect on the amplitude of the input wave, we can therefore neglect the z dependence of $E(\omega)$ in Eqs.(2.23-2.24). Further we assume that all the input is at frequency $\omega$, we can obtain the solution from Eq.(2.24) by integration of both sides:

$$E(2\omega)_{z=l} = -i\omega\sqrt{\frac{\mu_0}{n_{2\omega}^2\varepsilon_0}}d_{eff}E(\omega)^2 l\,\mathrm{sinc}(\Delta kl/2) \tag{2.25}$$

Where $\mathrm{sinc}(f) = \sin(f)/f$, $l$ is the interaction length, the generated wave intensity is proportional to:

$$E(2\omega)\cdot E(2\omega)^* = \frac{\mu_0\omega^2 d_{eff}^2 l^2}{\varepsilon_0\ n_{2\omega}^2}E(\omega)^4\,\mathrm{sinc}^2(\Delta kl/2) \tag{2.26}$$

### 2.3.4 Second Harmonic Conversion Efficiency for a Collimated Gaussian Beam

Using the relationship between electric field $E$ and intensity $I$, the intensity of the second harmonic wave $I_{2\omega}$ is given by:

$$I_{2\omega} = \frac{P_{2\omega}}{A} = \frac{1}{2}n_{2\omega}\sqrt{\frac{\varepsilon_0}{\mu_0}}E(2\omega)\cdot E(2\omega)^* \tag{2.27}$$

$$I_{\omega} = \frac{P_{\omega}}{A} = \frac{1}{2}n_{\omega}\sqrt{\frac{\varepsilon_0}{\mu_0}}E(\omega)\cdot E(\omega)^* \tag{2.28}$$

$$P_{2\omega} = \frac{1}{2}n_{2\omega}\sqrt{\frac{\varepsilon_0}{\mu_0}}\frac{\mu_0\omega^2 d_{eff}^2 l^2}{\varepsilon_0\ n_{2\omega}^{\ 2}}E(\omega)^4 A\,\mathrm{sinc}^2(\Delta kl/2) \tag{2.29}$$

$$P_{\omega} = \frac{1}{2}n_{\omega}\sqrt{\frac{\varepsilon_0}{\mu_0}}E(\omega)\cdot E(\omega)^*\cdot A \tag{2.30}$$

$$\eta_{SHG} = \frac{I_{2\omega}}{I_{\omega}} = \frac{P_{2\omega}}{P_{\omega}} = \frac{2\omega^2 d_{eff}^2 l^2}{n_{\omega}^2 n_{2\omega}c^3\varepsilon_0}\frac{P_{\omega}}{A}\mathrm{sinc}^2(\Delta kl/2) \tag{2.31}$$

Where $P_{2\omega}$ is the power of the second harmonic wave, the term $A$ is the effective area which is given by: $A = \pi w_0^{\ 2}/2$, $w_0$ is the the Gaussian beam electric field radius, $l$ is the effective interaction length, $\eta_{SHG}$ is the conversion efficiency.

The second harmonic intensity after an interaction distance $l$ is given by:

$$I_{2\omega} = \frac{2\omega^2}{n_{2\omega}n_{\omega}^2c^3\varepsilon_0}d_{eff}^2 l^2 I_{\omega}^2\,\mathrm{sinc}^2(\Delta kl/2) \tag{2.32}$$

Where:

$$\Delta k = k_{2\omega} - 2k_{\omega} = \frac{4\pi}{\lambda_{\omega}}(n_{2\omega} - n_{\omega}) \tag{2.33}$$

As all useful nonlinear materials have normal dispersion, the refractive indices will differ for the different wavelengths ($n_{2\omega} \neq n_{\omega}$). The second harmonic power $P_{2\omega}$ will change periodically along the interaction distance $l$ in an un-poled lithium niobate crystal, see Figure 2.03. It should be noted that this analysis does not hold for focused Gaussian beams, where the theory due to Boyd [19] shows a linear length dependence, rather than the quadratic length dependence shown above.

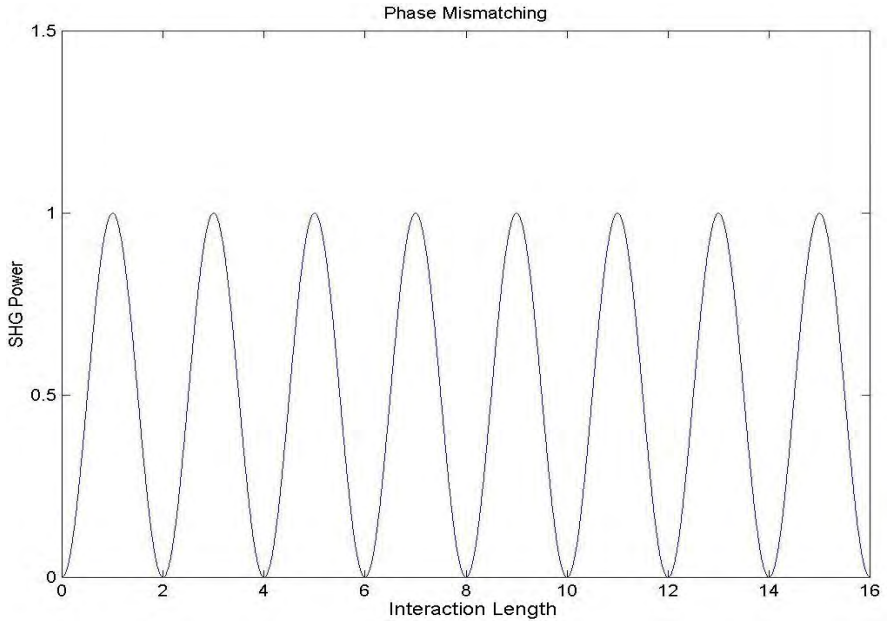


**Figure 2.03.** The second harmonic power with phase mismatch, $P_{2\omega}$ shows a periodic change along the interaction distance $l$ in an un-poled lithium niobate crystal.

From the above plot, it can be seen that the $P_{2\omega}$ oscillates along the interaction length governed by $\sin^2(\Delta kl/2)$. When $\Delta kl = \pi$ the interaction has occurred over one coherence length, from Eq.(2.32), the coherence length is :

$$l_c = \frac{\lambda_{\omega}}{4(n_{2\omega} - n_{\omega})} \qquad 2.34$$

The coherence length provides the critical dimension for quasi-phase matching.

## 2.4 Quasi-Phase-Matching (QPM)

### 2.4.1 Phase-Matching

From Eq.(2.29), we can find that the power at $2\omega$ oscillates along the length of interaction governed by the phase synchronism factor $\mathrm{sinc}(\Delta kl/2)$. As the $k$-vector of the interacting waves is wavelength dependent, the difference in phase velocities of

fields at different frequencies can produce a cumulative phase mismatch which can seriously limit the power conversion efficiency and effective interaction length of nonlinear devices.

Phase-matching is a method to compensate for the phase difference between the interacting waves and thus optimise the conversion efficiency in the nonlinear processes. Consider second harmonic generation, from Eq.(2.31), if we want to increase the conversion efficiency $\eta_{SHG}$, we need to maximise all the terms on the right hand side of Eq.(2.31). First consider the term $d_{eff}^2$ and $I_\omega$ when in the low conversion limit condition. They are length independent, because the term $l^2$ is fixed for a particular nonlinear device and the available fundamental intensity is set by the laser available. So we should focus on the last term, which has a maximum value of 1 unit when $\Delta k = k_{2\omega} - 2k_\omega = 0$, therefore $k_{2\omega} = 2k_\omega$, which is known as "phase-matching". But generally $n_{2\omega} \neq n_\omega$ with normal dispersion, so term $\Delta k \neq 0$. The vector $k_{2\omega}, k_\omega$ relationship is shown in Figure 2.04.

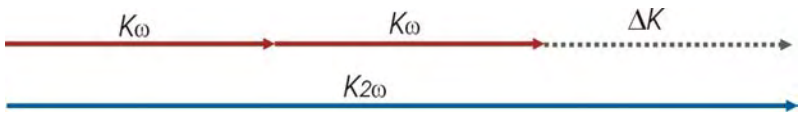


**Figure 2.04.** Phase-mismatching

There are several methods to overcome the phase-mismatch problem. The main types of phase-matching are birefringent phase-matching (BPM) and quasi-phase-matching (QPM) [17] which will be discussed in the following sections.

### 2.4.2 Birefringent Phase-Matching

The basic idea of birefringent phase-matching is to use the birefringence properties of a material; which means that light with orthogonal polarisations propagating through such a material will experience different values of the refractive index. Generally birefringent crystals have three different optical axes (triaxial crystals). But for $LiNbO_3$, two optical axes are equal, thus only two optic axes exist in the crystal (biaxial crystal), they are the ordinary axis (o-axis) and extraordinary axis (e-axis), with corresponding refractive indices $n_o$, $n_e$. A light wave propagating with its polarisation parallel to an o-axis is known as an ordinary wave, or o-wave and light

propagating with its polarization parallel to the e-axis is known as an extraordinary wave, or e-wave. $n_e$ may be either greater than or less than $n_0$, known as positive or negative birefringence respectively ($LiNbO_3$ is negative birefringent crystal).

There are two type of birefringent phase-matching, Type I birefringent phase-matching implies that both waves at $\omega$ have the same polarization whereas the generated wave at $2\omega$ has the orthogonal polarization with respect to $\omega$, see Figure 2.05(a). Type II birefringent phase-matching implies that one wave at $\omega$ is an o-wave and the other is an e-wave whereas the wave at $2\omega$ is either an o-wave or an e-wave, see Figure 2.05(b).

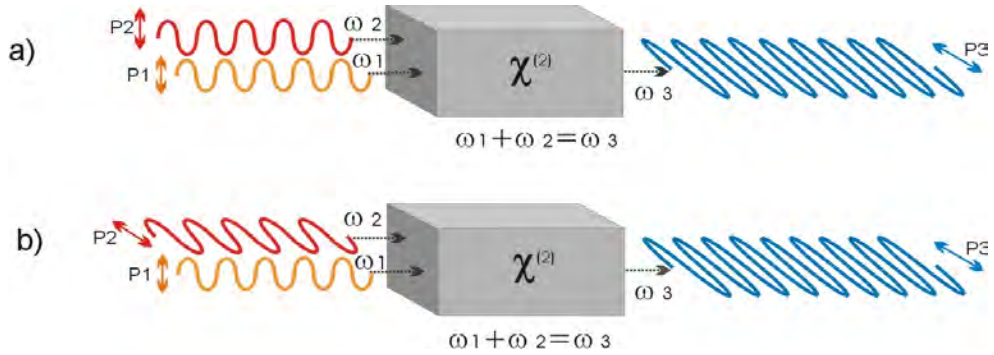


**Figure 2.05.** Two type of birefringent phase-matchings. (a) Type I birefringent phase-matching; (b) Type II birefringent phase-matching.

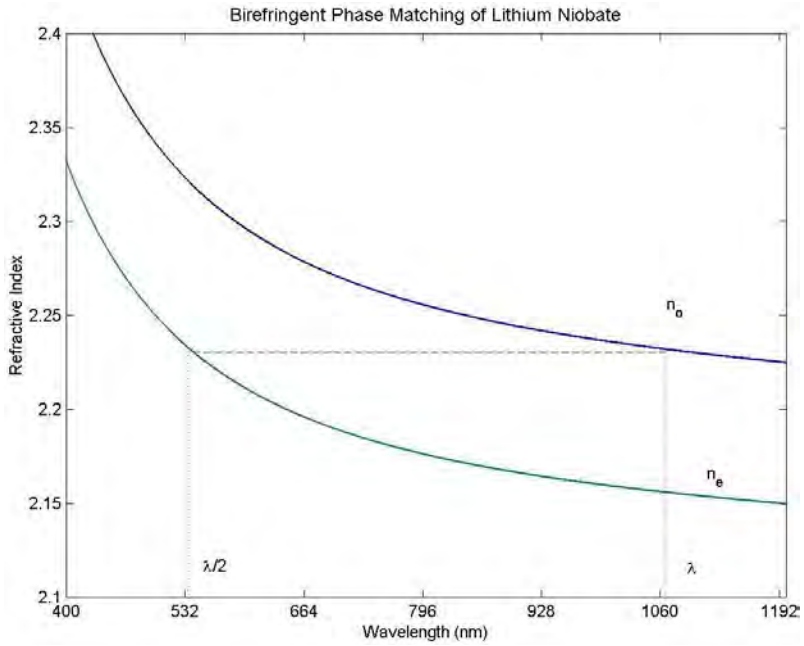


**Figure 2.06.** Ordinary refractive index at the fundamental wavelength (1064nm) matches the extraordinary refractive index at second harmonic wavelength (532nm) at 140ºC [31,32].

Phase matching in bulk $LiNbO_3$ can be achieved by Type I birefringent phase-matching for certain incident wavelengths, for example 1064nm, where the $n_0$ of the fundamental beam ($\lambda$ = 1064nm) matches with the $n_e$ of the SHG beam ($\lambda$=532nm) at 140ºC, see Figure 2.06.

### 2.4.3 Quasi-Phase-Matching (QPM)

Birefringent phase-matching in many materials leads to useful nonlinear devices, but it does have its limitations, particularly for the generation of wavelengths in mid-infrared region; as very few nonlinear materials are both transparent and birefringently phase-matchable beyond 4µm [ 33 ]. However, efficient nonlinear interaction is possible if an additional vector is introduced into the interacting wave vector mismatch equation Eq.(2.33) to keep $\Delta k = k_g$ for nonlinear interactions of any three waves.

Consider a situation for SHG where a wave with frequency $\omega$ propagates through the crystal, but the nonlinear interaction of the fundamental wave and second harmonic wave are phase mismatched. After one coherence length, any generated second harmonic wave is out of phase with the waves generated in the previous coherence length, and so destructively interfere. So the second harmonic wave is converted back to the fundamental wave periodically throughout the interaction length, resulting in a negligible conversion efficiency, see Figure 2.03.

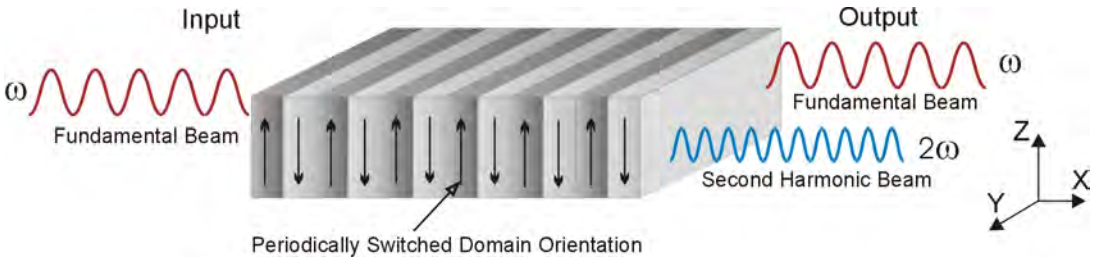


**Figure 2.07.** Periodic modulation of the nonlinear coefficient within a crystal, such as PPLN.

The phase mismatch can be overcome by introducing an additional *k*-vector through periodically reversing the polarization of the nonlinear crystal. The SHG conversion will continue to build through the whole interaction length. This process is referred to as quasi-phase-matching (QPM), the periodically reversed nonlinear coefficient within the crystal is referred to as a grating with a period of $\Lambda = 2l_c$, where $l_c$ is the

coherence length defined in Eq.(2.34). It is the grating phase vector $k_g$ that brings the nonlinear interaction back into phase, see Figure 2.07.

$$\Delta k = k_{2\omega} - 2k_{\omega} - k_g \qquad 2.35$$

Where, $k_g$ is the grating wave vector, given as:

$$k_g = \frac{2\pi m}{\Lambda} \qquad 2.36$$

$$\Lambda = \frac{\lambda_{\omega} m}{2\left(n_{2\omega} - n_{\omega}\right)} = 2ml_c \qquad 2.37$$

Where, $\Lambda$ is the grating period, and $m$ is referred to as the order of the quasi-phase-matched process. Therefore, the appropriate grating period can be chosen to compensate phase mismatch. Figure 2.08 illustrates the different orders of QPM. Curve (a) represents the first order of the QPM; Curve (b) represents the second order of QPM with a duty cycle of 25% (duty cycle means the ratio of the width of the reversed domain to the grating period); Curve (c) represents third order QPM; Curve (d) represents phase-mismatch; Curve (e) represents birefringent phase-matching.

There are several advantages to quasi-phase-matching (QPM) over more traditional birefringent phase-matching (BPM). Firstly it is possible to achieve the phase matching condition within crystals which have limited birefringence properties but have large nonlinear coefficients. Secondly the highest nonlinear coefficient of a nonlinear crystal can be used by a combination of wave propagation direction and polarization. For example in lithium niobate, the largest nonlinear coefficient is the $d_{33}$ term, but this requires the polarization of all interacting waves to be parallel to the e-axis, which can only be done via QPM. Lastly a nonlinear crystal can be tailored to phase-match any combination of interacting wavelengths within the transparency range of the crystal [17,18,34].

This chapter has reviewed the historical background of nonlinear optics. The basic theory of the nonlinear process and fundamental concepts are introduced, the methods of phase-matching, in particular quasi-phase-matching (QPM), are explained. The nonlinear properties of lithium niobate will be discussed in the following chapter.

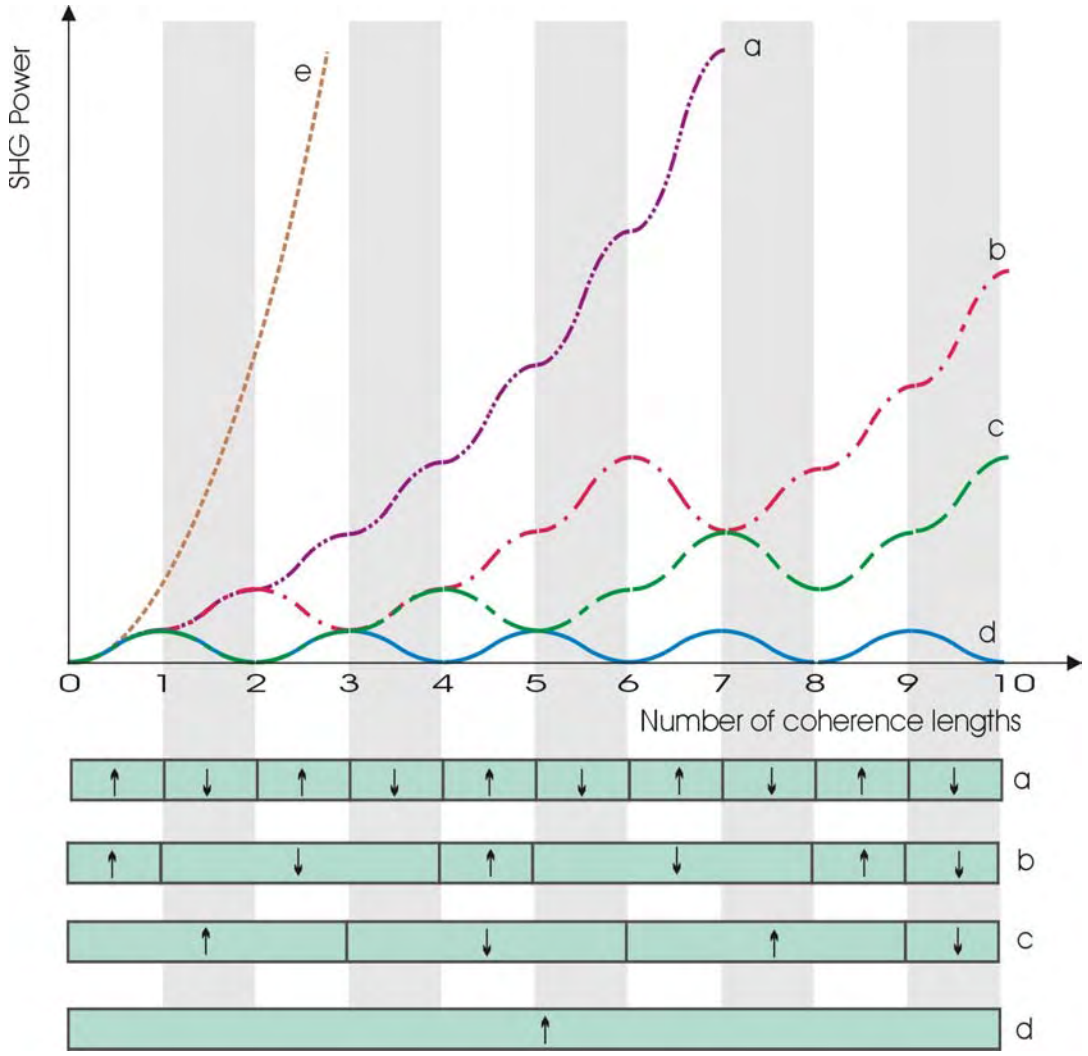


**Figure 2.08.** Different order of QPM. (a) First order QPM; (b) Second order QPM with a duty cycle of 25%; (c) Third order QPM; (d) Phase-mismatch; (e) Birefringent phase-matching.

## References

[1] P. A. Franken, A. E. Hill, C. W. Peters, and G. Weinreich, "Generation of Optical Harmonics", *Phys. Rev. Lett.*, Vol.**7**, p.118-119 (1961)

[2] D. A. Kleinman, "Nonlinear Dielectric Polarization in Optical Media", *Phys. Rev.*, Vol.**126**, p.1977-1979 (1962)

[3] J. A. Giordmaine, "Mixing of Light Beam in Crystals", *Phys. Rev. Lett.*, Vol.**8**, p19-21 (1962)

[4] P. D. Maker, R. W. Terhune, M. Nisenoff, and C. M. Savage, "Effects of Dispersive and Focussing on the Production of Optical Harmonics", *Phys. Rev. Lett.*, Vol.**8**, p.21-24 (1962)

[5] C. C. Wang and G. W. Racette, "Measurement of Parametric Gain Accompanying Optical Difference Frequency Generation", *Phys. Lett.*, Vol.**6**, p.169-171 (1965)

[6] J. E. Geusic, H. J. Levinstein, J. J. Rubin, S. Singh and L. G. Van Uitert, "The Nonlinear Optical Properties of $Ba_2NaNb_5O_{15}$", *Appl. Phys. Lett.*, Vol.**11**, p.269-271 (1968)

[7] W. F. Hagen and P. C. Magnante, "Efficient Second-Harmonic Generation with Diffraction-Limited and High-Spectral-Radiance Nd-Glass Lasers", *J. Appl. Phys.*, Vol.**40**, p.219-224 (1969)

[8] J. A. Armstrong, N. Bloembergen, J. Ducuing and P. S. Persan, "Interactions between Light Waves in a Nonlinear Dielectric", *Phys. Rev.*, Vol.**127**, p.1918-1920 (1962)

[9] M. M. Fejer. G. A. Magel, D. H. Jundt, and R. L. Byer, "Quasi-phase-matched second harmonic generation: tuning and tolerances", *IEEE J. Quantum Electron.*, Vol.**28**, p.2631-2654 (1992)

[10] S. Miyazawa, "Ferroelectric Domain Inversion in Ti-Indiffused $LiNbO_3$ Optical Waveguide", *J. Appl. Phys.*, Vol.**50**, p.4599-4603 (1979)

[11] J. Webjörn, F. Laurell and G. Arvidsson, "Fabrication of Periodically Domain-Inverted Channel Waveguides in Lithium Niobate for Second Harmonic Generation", *J. Lightwave Technol.*, Vol.**7**, p.1597-1601 (1989)

[12] M. Yamada, N. Nada, M. Saitoh and K. Watanabe, "First-order quasi-phased matched $LiNbO_3$ waveguide periodically poled by applying an external field for efficient blue second-harmonic generation", *Appl. Phys. Lett.*, Vol.**62**, p.435-437 (1993)

[13] J. Webjorn, V. Pruneri, P. St. J. Russell, J. R. M. Barr and D. C. Hanna, "Quasi-phase-matched blue light generation in bulk lithium niobate, electrically poled via periodic liquid electrodes", *Electron. Lett.*, Vol.**30**, p.894-896 (1994)

[14] V. Pruneri, J. Webjörn, P. St. J. Russell, J. R. M. Barr, D. C. Hanna, "Intracavity second harmonic generation of 0.532μm in bulk periodically poled lithium niobate", *J. Opt. Commun.*, Vol.**116**, p.159-162 (1995)

[15] L. E. Myers, W. R. Bosenberg, "Periodically Poled Lithium Niobate and Quasi-Phase-Matched Optical Parametric Oscillators", *IEEE J. Quantum Electron.*, Vol.**33**, p.1663-1672 (1997)

[16] R. L. Byer, "Quasi-phase matched nonlinear interactions and devices", *Journal of Nonlinear Optical Physics & Materials*, Vol.**6**, p.549-592 (1997)

[17] R. L. Byer, " Parametric Oscillators and Nonlinear Optics", Department of Applied Physics, Stanford University, California, U.S.A, P. G. Harper & B. S. Wherrett, "Nonlinear Optics", Academic Press, (1977)

[18] R. L. Byer, "Quasi-Phase-matched Nonlinear Interactions and Devices", *Journal of Nonlinear Optical Physics & Materials*, Vol.**6**, No.4, p.549-592 (1997)

[19] R. W. Boyd , "Nonlinear Optics", Rochester, New York, Academic Press, (1992)

[20] P. G. Harper and B. S. Wherret, "Nonlinear optics", Scottish Universities Summer School in Physics $16^{th}$, Heriot-Watt University, (1975)

[21] E. Hecht, "Optics", $2^{nd}$ Edition, Addison-Wesley, (1987)

[22] J. Wilson and J. F. B. Hawkes, "Optoelectronics an introduction", Prentice Hall, (1989)

[23] M. Bass, P. A. Franken, J. F. Ward, and G. Weinreich, "Optical rectification", *Phys. Rev. Lett.*, Vol.**9**, p.446-448 (1962)

[24] P. A. Franken, and J. F. Ward, "Optical harmonics and nonlinear phenomena", *Rev. Mod. Phys.*, Vol.**35**, p.23-39 (1963)

[25] J. A. Giordmaine and R. C. Miller, "Tunable coherent parametric oscillation in $LiNbO_3$ at optical frequencies", *Phys. Rev. Lett.*, Vol.**14**, p.973-976 (1965)

[26] R. W. Terhune, P. D. Maker, and C. M. Savage, "Optical harmonic generation in calcite", *Phys. Rev. Lett.*, Vol.**8**, p.404-406 (1962)

[27] W. Kaiser and C. G. B. Garrett, "Two-photon excitation in $CaF_2:Eu^{2+}$", *Phys. Rev. Lett.*, Vol.**7**, p.229-231 (1961)

[28] G. Eckhardt, R. W. Hellwarth, F. J. McClung, S. E. Schwartz, and D. Weiner, "Stimulated Raman scattering from organic liquids", *Phys. Rev. Lett.*, Vol.**9**, p.455-457 (1962)

[29] R. Y. Chiao, C. H. Townes, and B. P. Stoicheff, "Stimulated brillouin scattering and coherent generation of intense hypersonic waves", *Phys. Rev. Lett.*, Vol.**12**, p.592-595 (1964)

[30] A. Yariv, "Quantum electronics", 3rd Edition, John Wiley and Sons, (1989)

[31] D. H. Jundt, "Temperature-dependent Sellmeier equation for the index of refraction, $n_e$, in congruent lithium niobate", *Opt. Lett.*, Vol.**22**, p.1553-1555 (1997)

[32] K. S. Abedin and H. Ito, "Temperature-dependent dispersion relation of ferroelectric lithium tantalate", *J. Appl. Phys.*, Vol.**80**, p.6561-6563 (1996)

[33] V. Pruneri, "Electric field periodically inverted $LiNbO_3$ for optical frequency conversion", University of Southampton, PhD Thesis, (1996)

[34] M. Yamada, N. Nada, T. Yamaguchi, M. Saitoh, and K. Watanabe, "A quasi-phase-matched waveguide for the blue second-harmonic generation", *Electronics and Communications in Japan*, Part 2, Vol.**77**, p.52-61 (1994)

# Chapter 3

## Properties and Applications of Lithium Niobate

Lithium niobate is a widely used material in optoelectronics. In this chapter we provide a brief review of the structure and growth of lithium niobate, its linear and nonlinear optical properties [1] and define the appropriate terms and material coefficients for single crystals. The primary applications of lithium niobate are shown schematically in Figure 3.01 [2,3,4,5]. This chapter concentrates on the main physical and non-linear optical properties of lithium niobate which influence the fabrication and performance of PPLN based devices.

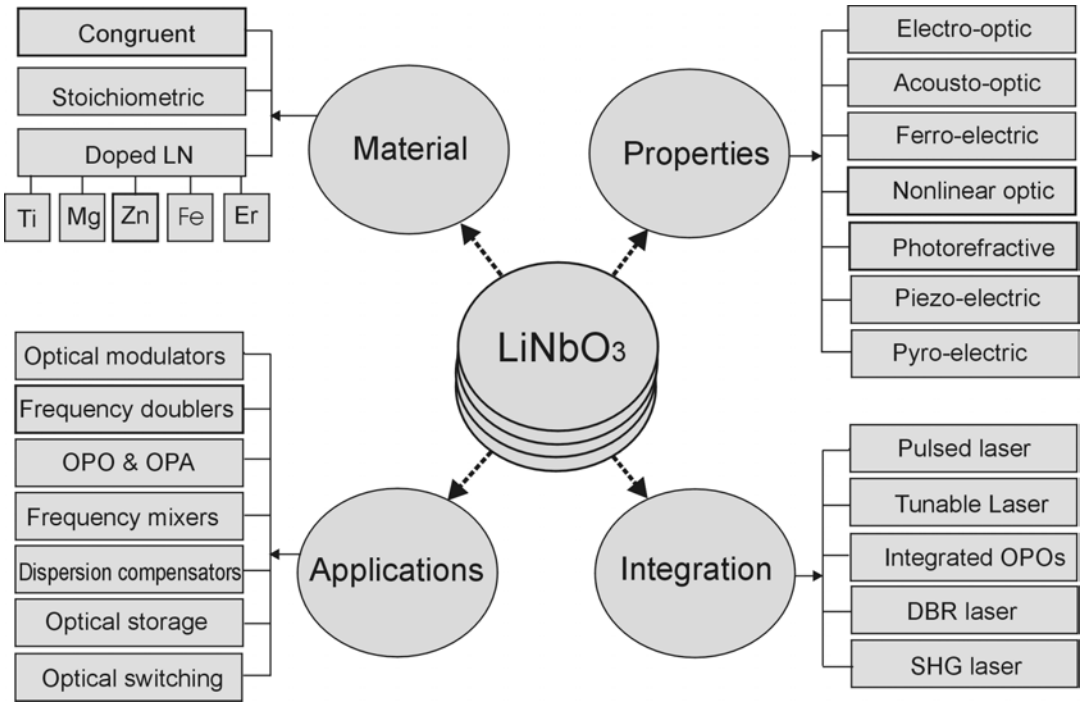


**Figure 3.01.** Layout diagram of lithium niobate's properties and its applications.

### 3.1 Properties of Lithium Niobate

Lithium niobate has many important properties. It is a birefringent and ferroelectric material with large pyroelectric, piezoelectric, nonlinear optical and electro-optical coefficients. It also exhibits very strong photorefractive sensitivity when doped with transition-metal dopants, such as Fe, Cu, Mn [2,3,4]. These properties make lithium niobate an important material for applications in a wide range of fields, such as acoustic and optical devices in microwave communications, optical telecoms,

frequency conversion and holographic data storage. In this chapter we briefly describe the main characteristics and properties that play an important role during PPLN and channel waveguide fabrication.

### 3.1.1 The Structure of Lithium Niobate

Lithium niobate is a man-made, ferroelectric material whose Curie temperature is approximately 40ºC below its melting point of 1253ºC. In addition, strong bulk photovoltaic and photorefractive effects are also exhibited in this material. With a worldwide production of five tonnes per year, it ranks as the second largest quantity man-made crystal after silicon [6].

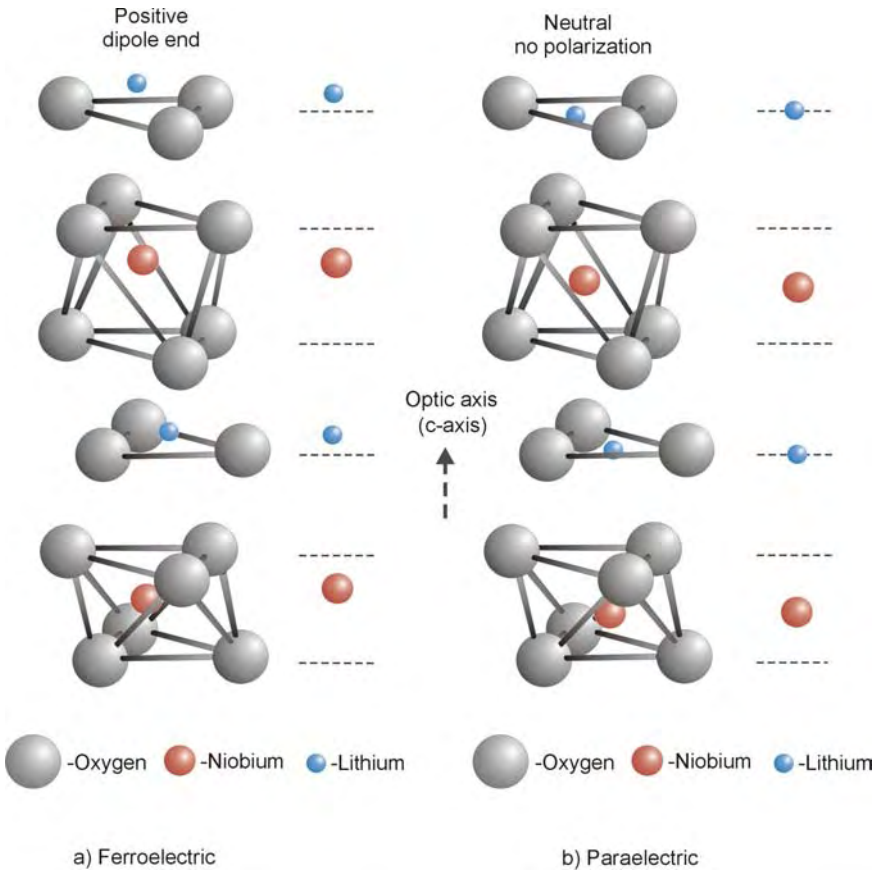


**Figure 3.02.** The structure of lithium niobate [3, 4]. Lithium niobate exhibits (a) ferroelectric properties below the Curie temperature, and (b) paraelectric properties above the Curie temperature.

The crystal structure of lithium niobate is a succession of distorted octahedrons along the polar *c*-axis (optic axis). There are six flat oxygen layers in a hexagonal unit cell. The Oxygen atoms do not lie above one another but are arranged in a screw-like fashion, see Figure 3.02 [3]. Lithium niobate exhibits ferroelectric properties below its Curie temperature of 1210ºC [3], in this phase, lithium and niobium ions are not

situated at equal distances between the planes of oxygen atoms, the lithium and niobium ions are displaced along the optical axis of crystal, resulting in a spontaneous polarization $P_s$, see Figure 3.02(a). Conversely above its Curie temperature, lithium niobate shows the properties of a paraelectric [3,4], in this phase, the lithium ions are situated at the centre of a plane of oxygen ions and the niobium ions are located at the centre of oxygen octahedra, leading to a symmetrical configuration with no spontaneous polarization, see Figure 3.02(b).

It is the position of the metallic ions in the ferroelectric phase that gave rise to the dipole moment. In order to invert this moment and hence change the direction of polarization, the ions of lithium and niobium must be forced to pass through the oxygen layers. The required force is very large and can only been created using high electric fields across the optical axis. Increasing the temperature to close to the Curie point reduces the required electric field, but as this temperature is so close to its melting point, this approach is not used for fabricating periodically poled lithium niobate (PPLN).

### 3.1.2 Crystal Growth

Lithium niobate crystals were first be made by Matthias and Remeika [7]. The crystal is relatively easy to grow, exhibits low optical loss, and attractively high acoustic and nonlinear optical coefficients. In addition lithium niobate crystal is relatively robust and simple to polish. This combination of factors has led to it being widely researched and it being adopted for large scale commercial growth.

The main method for crystal growth of lithium niobate is the Czochralski technique [3]. Single crystals are grown from molten lithium niobate materials [3], the growth is initiated by a small crystal seed, and then the crystal and melt are rotated in opposite directions in order to guarantee the homogeneity and to prevent thermal gradients at the crystal surface. The result of the crystal growth process is a cylindrical crystal rod with a diameter of a few inches. The solid crystal boule is then cut to form thin lithium niobate wafers.

Conditions necessary for the producing perfect crystals are suggested by Prokhorov and Kuz’minov [5]. By finely tuning the fabrication conditions, such as the bias

current, during Czochralski growth, more complex reversed ferroelectric domain structures can be grown. This was first been demonstrated by Feisst and Koidl [8] in 1985, where the Czochralski growth technique was used to pull a periodically poled lithium niobate crystal from a congruent melt, the periodic domain pattern was stacked along the *y* axis with domain thicknesses of 8μm [8].

Some physical properties of lithium niobate are determined by the composition of the melt or solution and the metallic ions ratio (Li to Nb) during the growth process. Most of commercially available lithium niobate material is congruently grown, ie. Lithium ions concentration ratio (Li/(Li+Nb)) in the melt is 48.4% resulting in considerable deficiency of lithium ions. This defect structure of congruently melting lithium niobate allows the addition of dopants, such as, Ti, Mg, Zn, In, Fe through thermal indiffusion or doping during the crystal growth processes. In contrast to congruent lithium niobate, stoichiometric lithium niobate has an almost ideal 50:50 lithium to niobium ratio resulting in much improved performance characteristics. The samples involved in the experimental research in this thesis are *z*-cut congruent lithium niobate wafers with a thickness of 500μm, the samples are from different suppliers with a slight variation of parameters, but basically the materials are all congruent in composition, where LiO accounts for around 48.4% by molar ratio, the samples are all classified as optical grade with mechanical and chemically polished surfaces [9].

### 3.1.3 Linear Optical Properties

Lithium niobate is a birefringent material with an ordinary refractive index, $n_o$ (electric field polarization is normal to the *c*-axis), and an extraordinary refractive index, $n_e$ (electric field is parallel with the *c*-axis), these refractive indices are dependent on the wavelength of incident beam and crystal temperature. The relations within the transparency range of lithium niobate (0.34μm to 4.6μm) are expressed by the Sellmeier equations [10] given as the following.

$$n_o^2(\lambda,T) = A_{1o} + \frac{A_{2o} + B_{1o}F^2}{\lambda^2 - (A_{3o} + B_{2o} \times F^2)^2} + B_{3o}F - A_{4o}\lambda^2 \qquad 3.01$$

$$n_e^2(\lambda,T) = A_{1e} + \frac{A_{2e} + B_{1e}F^2}{\lambda^2 - (A_{3e} + B_{2e} \times F^2)^2} + B_{3e}F - A_{4e}\lambda^2 \qquad 3.02$$

Where $\lambda$ is the wavelength in μm, $F = (T - T_0)/(T + T_0 + 546)$ is a function of the crystal temperature $T$ in ºC, $T_0$ is a reference temperature. The other coefficients can be found in reference 10. Figure 3.03 shows refractive index of $n_o$ and $n_e$ at a temperature $T$ = 25ºC [10]. More accurate extraordinary refractive index of lithium niobate beyond 5μm are described by a revised Sellmeier equation [11].

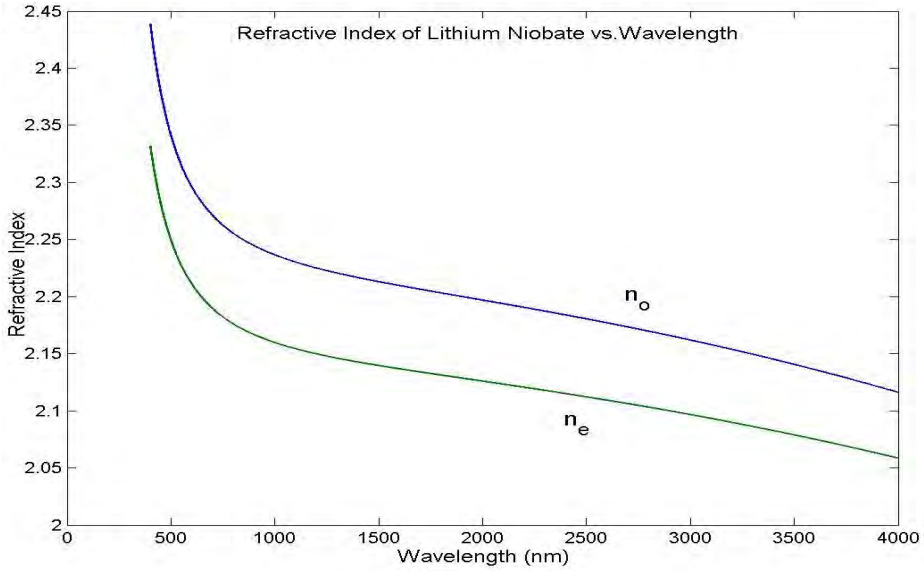


**Figure 3.03.** Refractive index of lithium niobate vs. wavelength, the temperature is 25ºC.

### 3.1.4 Nonlinear optical properties

As a ferroelectric birefringent material $LiNbO_3$ exhibits second order and higher order optical nonlinearities, a feature of major interest for the work in this thesis since all useful three wave interactions rely on this property. The relation between electric field $E$ and polarization $P$, including the linear, second-order and higher-order nonlinear terms, and other relevant nonlinear optic concepts have been reviewed in chapter 2. Often in the literature the second nonlinear part is written using the equation: $P_i^{(2)} = 2\varepsilon_0 d_{ijk}^{(2)} E_j E_k$, Where $d_{ijk} = \chi_{ijk}/2$ is called the nonlinear coefficient [12]. In the case of $LiNbO_3$, there are only three independent nonlinear coefficients $d_{22}$, $d_{31}$, $d_{33}$. Table 3.01 lists the values taken from previous reports [13,14,15].

**Table 3.01** Nonlinear coefficients for $LiNbO_3$ at 1.06μm

| | $d_{22}$ (pm/V) | $d_{31}$ (pm/V) | $d_{33}$ (pm/V) |
|---|---|---|---|
| ref.13, 15 | 2.5 | 5.95 | 34.4 |
| ref.14 | 2.1 | 4.3 | 27 |

### 3.1.5 Ferroelectric Properties

By their crystal structure, crystalline materials can be divided into centro-symmetric and noncentro-symmetric materials. From the 21 noncentro-symmetric point groups, 20 classes are piezoelectric, i.e. they show an electrical polarisation under mechanical stress. From these, 10 of them are pyroelectric classes. These are materials showing a spontaneous polarisation which is dependent on temperature. From these, a subgroup is the ferroelectric materials that have a spontaneous electrical polarisation, where the direction of polarization can be altered by an external electrical field [16], see Figure 3.04.

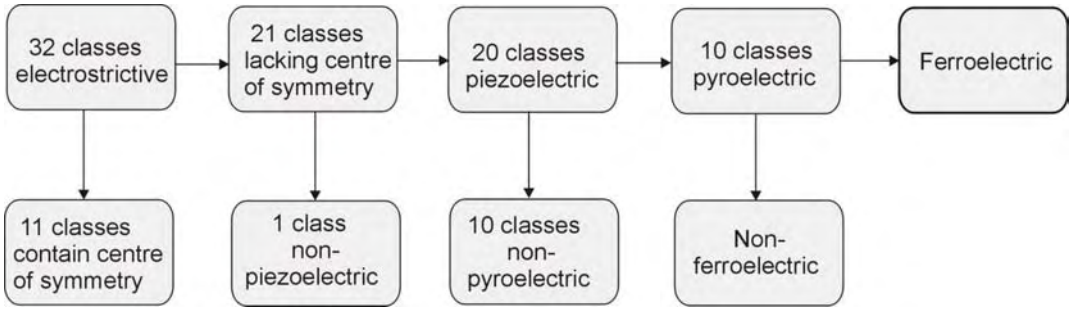


**Figure 3.04.** The family of crystalline materials.

The name ferroelectricity was coined because the $P-E$ relation of these materials is very similar to the $B-H$ relation of ferromagnetic materials, where the spontaneous electric polarization $P_s$ is defined as the dipole moment per unit volume, or surface charge per unit area. Most ferroelectrics also possess a Curie temperature $T_c$ (above which they become paraelectric), and the material has an internal domain structure. The polarisation $P$ versus electric field $E$ dependency shows hysteresis behaviour, the detail of this behaviour is discussed in section 4.2 of chapter 4.

### 3.1.6 Photorefractive Effect

The photorefractive effect is an optical phenomenon where the refractive index of a material is changed by a spatially modulated light pattern. Since it was first discovered in 1966 at Bell Laboratories [17], the photorefractive effect has led to some limited applications [18,19]. But in the nonlinear optical devices presented in this thesis, it is an unwelcome effect, resulting in a deterioration in optical

performance, such as distortion of the mode profile, fluctuation of the output power and low conversion efficiency for the interacting waves, etc [20,21].

The origin of the photorefractive effect in congruent lithium niobate is accepted to be due to the presence of iron impurities during the growth process. Iron exists in two different oxidation states and provides a means to store charge distributions in the crystal. When an incident beam propagates through the crystal, see Figure 3.05(a), an optically induced space charge field is generated, and the beam will cause charge to migrate along the optical axis, where the $Fe^{2+}$ and $Fe^{3+}$ ion can be excited by absorption of photons to produce electrons and holes respectively;

$$Fe^{2+} + h\upsilon \Rightarrow Fe^{3+} + e^{-} \qquad Fe^{3+} + h\upsilon \Rightarrow Fe^{2+} + e^{+}$$

Where, $h$ is Planck's constant, $\upsilon$ is the frequency of the incident beam and e is the electron charge.

Eventually, charges are trapped, preferentially at donator or acceptor sites in the crystal, resulting in a local charge carrier distribution as in Figure 3.05(b). This local charge distribution causes an electric space charge field which is $\pi/2$ out of phase with respect to the local charge distribution due to Gauss's law, as shown in Figure 3.05(c). Due to the electro-optic effect in the crystal, the refractive index is changed in proportion to the local electric field, as sketched in Figure 3.05(d) [22]. Since both electrons and holes play a role in photorefractive phenomenon, the photorefractive susceptibility of the material is therefore determined by the oxidation state ratio of $Fe^{2+}$ to $Fe^{3+}$.

Several methods can be adopted to control and reduce the photo-refraction problem. In lithium niobate, the photorefractive effect is self-annealing when the temperature is above 180ºC for visible wavelength radiation, and 100ºC for wavelength in the near infrared. In this way the photorefractive effect can be minimized or eliminated by controlling the temperature. In addition, increasing the dark conductivity (natural thermal migration of charges) of the material by using dopants, such as zinc ions (Zn:$LiNbO_3$) [23] or magnesium ions (Mgo:$LiNbO_3$) [24,25], can effectively suppress the photorefractive effect. Other methods include optimising the ratio of $Fe^{2+}$/ $Fe^{3+}$ by oxidisation or reduction [26] and only using wavelengths above 1μm.

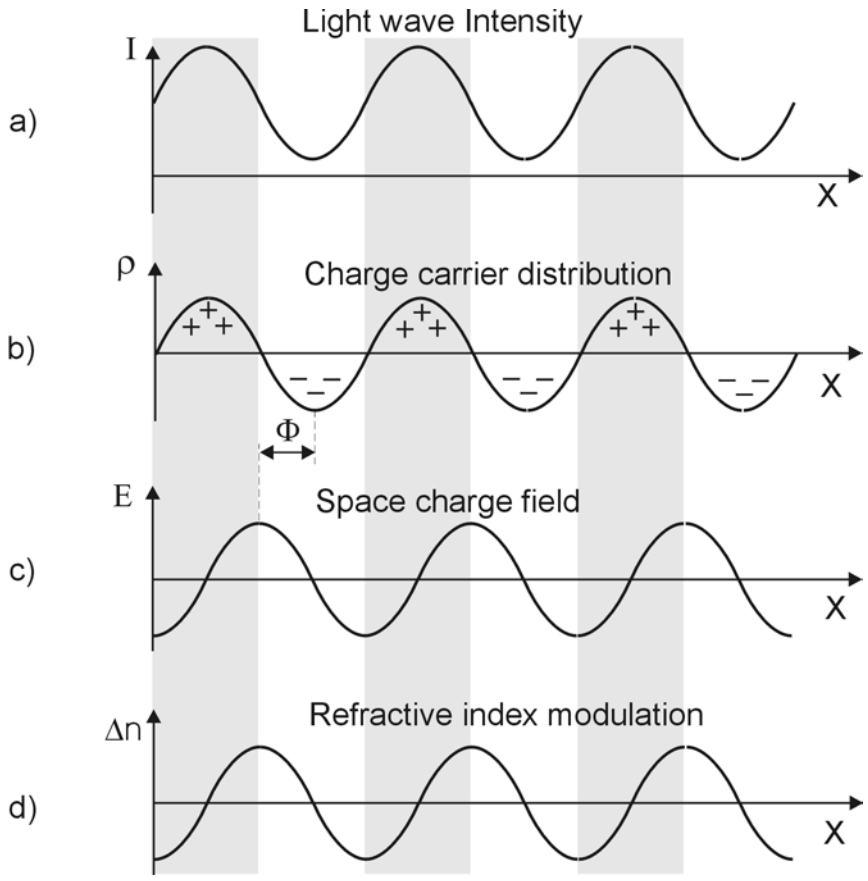


**Figure 3.05.** The photorefractive effect. (a) Interference creates a light pattern; (b) Charge carrier distribution; (c) The local charge distribution produces an electric space charge field; (d) The refractive index distribution proportional to the electric field which is phase shifted by 90° relative to the incident light [27].

## 3.2 Applications of Lithium Niobate

Due to its excellent piezoelectric and ferroelectric properties and large electro-optic and nonlinear coefficients, lithium niobate has been used for a variety of applications [3,4]. It is one of the most thoroughly researched man-made crystal.

Applications that utilize the large electro-optic coefficients of lithium niobate are the optical modulator [28] and microwave phase shifters [29]. The photorefractive effect in lithium niobate can be enhanced by adding metallic dopants, such as Fe, Ce to the crystal, and iron-doped photorefractive lithium niobate can be used as an optical switch, as a holographic storage medium for optical data [30,31] and for optical limiting, where a photorefractive material can be used to create a one way window that allows the transmission of coherent light from one side while blocking it from the other [32].

With a broad spectral transmission region, which ranges from 0.4μm to 5.0μm, and a large nonlinear coefficient, combined with quasi-phase matching (QPM) [33], lithium niobate can be used to generate tuneable wavelengths over a broad wavelength range [34, 35], applications include optical parametric oscillators (OPO) [36], optical parametric amplifiers (OPA) [37], difference frequency mixing [38] and second harmonic generation of laser diodes in the 1.3μm to 1.55μm range [39,40].

QPM conversion devices based on channel waveguides in periodically-poled lithium niobate (PPLN) represent a means of achieving efficient compact visible coherent laser sources. The waveguides can be fabricated in the lithium niobate by annealed proton exchange (APE) [41], titanium diffusion [42], and zinc indiffusion [43]. Potential applications of PPLN waveguide lead towards specialised sources, such as cw blue light generation for biomedical fluorescence microscopy and low-cost devices for telecommunications wavelength conversion. In recent years, particular interest has been applied to the development of room temperature devices to eliminate the problems associated with photorefractive damage in this material [44].

This chapter has introduced the structure and growth of lithium niobate, reviewed its linear and nonlinear properties and its applications, in particular those which influence the fabrication and performance of periodically poled lithium niobate (PPLN) waveguide devices. The fabrication of PPLN will be described in following chapter.

## References

[1] P. G. Harper and B. S. Wherret, "Nonlinear optics", Scottish Universities Summer School in Physics 16th, Heriot-Watt University, (1975)

[2] M. E. Lines, A. M. Glass, "Principles and applications of ferroelectrics and relates materials", Claredon Press Oxford, (1977)

[3] A. Rauber, "Chemistry and physics of lithium niobate", *Current topics in material science* 1 E Kaldis, North-Holland, (1978)

[4] R. S. Weis, T. K. Gaylord, "Lithium Niobate : Summary of physical properties and crystal structure", *Appl. Phys.*, A Vol.**37**, p.191-203 (1985)

[5] A. M. Prokhorov, Y. S. Kuz'minov, "Physics and chemistry of crystalline lithium niobate", *Adam Hilger* Bristol, (1990)

[6] D. Jundt, Crystal Technology Inc

[7] B. T. Matthias, J. P. Remeika, "Ferroelectricity in the Ilmenite Structure", *Phys Rev.*, Vol.**76**, p.1886-1887 (1949)

[8] A. Feisst and P. Koidl, "Current induced periodic ferroelectric domain structures in $LiNbO_3$ applied for efficient nonlinear optical frequency mixing", *Appl. Phys. Lett.*, Vol.**47**, p.1125-1127 (1985)

[9] D. P. Morgan, "Properties of lithium niobate", EMIS Datareview Series No.5, (*INSPEC London*), p.26 (1989)

[10] G. J. Edwards, M. Lawrence, "A temperature-dependent dispersion equation for congruently grown lithium niobate", *Opt. Quantum Electron.*, Vol.**16**, p.373-374 (1984)

[11] D. H. Jundt, "Temperature-dependent Sellmeier equation for the index of refraction, $n_e$, in congruent lithium niobate", *Opt. Lett*., Vol.**22**, p.1553-1555 (1997)

[12] V. G. Dmitriev, G. G. Gurzadyan and D. N. Nikogosyan, "Handbook of nonlinear optical crystals", *Springer verlag*, Berlin Heidelberg, (1991)

[13] M. M. Choy and R. L. Byer, "Accurate second order susceptibility of visible and infrared nonlinear crystal", *Phys. Rev*., B Vol.**14**, p.1693-1706 (1976)

[14] D. A. Roberts, "Simplified characterization of uniaxial and biaxial nonlinear optical crystals: a plea for standardization of nomenclature and conventions", *IEEE J. Quantum Electron*., Vol.**28**, p.2057-2074 (1992)

[15] V. Pruneri, "Electric field periodically inverted $LiNbO_3$ for optical frequency conversion", ORC, University of Southampton, PhD Thesis, (1996)

[16] Ferroelectric Standards Sub-Committee of Ferroelectrics Committee, "IEEE Standard Definitions of Terms Associated with Ferroelectric and Related Materials", *Draft*, (2001)

[17] A. Ashkin, G. D. Boyd, J. M. Dziedzic, R. G. Smith, A. A. Ballman, J. J. Levinstein, K. Nassau, "Optically-induced refractive index inhomogeneities in $LiNbO_3$ and $LiTaO_3$", *Appl. Phys. Lett*., Vol.**9**, p.72-74 (1966)

[18] A. M. Glass, "The photorefractive effect", *Opt. Eng.*, Vol.**17**, p.470-479 (1978)

[19] N. V. Kukhtarev, V. B. Markov, S. G. Odulov, M. S. Soskin, and V. L. Vinetskii, "Holographic storage in electro-optic crystals. I. Steady state", *Ferroelectrics*, Vol.**22**, p.949-960 (1979)

[20] D. L. Staebler and W. Phillips, "Fe-doped $LiNbO_3$ for read-write applications", *Appl. Opt.*, Vol.**13**, p.788-794 (1974)

[21] K. Chah, M. Aillerie, M. D. Fontana, and G. Malovichko, "Electro-optic properties in Fe:doped $LiNbO_3$ crystals as a function of composition", *Opt. Commun.*, Vol.**176**, p.261-265 (2000)

[22] J. Wilson and J. F. B. Hawkes, "Optoelectronics an introduction", 2nd Edition, Prentice Hall, (1989)

[23] B. Herreros and G.Lifante, "$LiNbO_3$ Optical Waveguides by Zn diffusion from Vapor Phase", *Appl. Phys. Lett*., Vol.**66**, p.1449-1451 (1995)

[24] D. A. Bryan, R. Gerson, and H. E. Tomaschke, "Increased optical damage resistance in lithium niobate", *Appl. Phys. Lett*., Vol.**44**, p.847-849 (1994)

[25] A. Harada and Y. Nihei, "Bulk periodically poled MgO-$LiNbO_3$ by corona discharge method", *Appl. Phys. Lett*., Vol.**69**, p.2629-2631 (1996)

[26] G. Cook, D. C. Jones, C. J. Finnan, L. L. Taylor, and T. W. Vere, "Optical limiting with lithium niobate", *SPIE*, Vol.**3798**, p.2-16 (1999)

[27]G. Cook, D. C. Jones, C. J. Finnan, L. L. Taylor, and T. W. Vere, "Optical limiting with lithium niobate", *SPIE*, Vol.**3798**, p.2-16 (1999)

# Chapter 4

# Fabrication of PPLN and Investigation of Poling Quality

## 4.1 Introduction

The origin of research on ferroelectric domain switching for nonlinear optics may be dated back to 1962, when Armstrong *et al*. [1] proposed the idea that nonlinear optical phenomena could be enhanced enormously by periodic inversion of the sign of the nonlinear optical susceptibility in the dielectric material, while the linear optical properties remain the same. These ideas were developed by Miller in 1964, who described the effects on second harmonic generation due to anti-parallel ferroelectric domains in $BaTiO_3$ [2,3].

There are many different methods to fabricate PPLN including:

1. Crystal growth (for example, the off-centered Czochralski growth technique) which was first studied by D. Feng *et al*. [4] in lithium niobate and developed by other groups since then [5,6,7].
2. Chemical diffusion of titanium into the surface of a heated crystal of lithium niobate which was first suggested by Fejer following the earlier observations in 1979 by Miyazawa [8,9].
3. Electron beam processing by P. W. Haycock *et al*.[10]
4. The applied electric field poling method which was first successfully used by Yamada *et al*. in 1993 [11], which investigated the possibility of direct application of an electric field to metal electrodes deposited by lithographic processing on the surface of the crystal.

The first steps towards domain inversion by electric fields had been taken in early work by Camlibel [12] in 1969. However, dielectric breakdown and the lack of domain control during the poling prevented progress toward QPM. Following a series of studies undertaken in Russia in 1970's, Yamada *et al*. successfully controlled domain inversion by using the applied electric field poling process.

Although domain modulation during crystal growth or through electric beam methods produced samples adequate for initial device demonstration, the technique was not

suitable for volume production of QPM material. Similarly the chemical diffusion method can potentially be used to mass produce inverted domain chips, but controlling the quality proves difficult.

Therefore, a goal of domain switching research was to develop a lithography-based patterning process for creating inverted domains with controlled period and duty cycle, such a process is necessary for mass production at low cost of QPM chips that are engineered to optimize device performance. With these requirements, applied electric field poling technique appears to be the best candidate technique. Taking advantage of modern microelectronic fabrication techniques, the applied electric field poling methods have developed rapidly [13,14,15,16,17].

In this chapter, the technology of applied electrical field poling method has been reviewed and discussed, and the procedure used at Southampton University is presented [18]. The experiments carried out during this research are based on optimising this technique for production of high quality samples with short period PPLN gratings for SHG applications. The promising results of this research are presented and different poling methods are discussed.

## 4.2 Review of Applied Electric Field Poling

Poling of a ferroelectric material is the process by which a net remnant polarization $P_r$ is produced under the application of an electric field exceeding the coercive field $E_c$ to a multi-domain or single-domain ferroelectric [19]. Switching is the process by which the domain polarizations are reversed (or reoriented) to give a new value of $P_r$ [20] under the application of an electric field exceeding the coercive field. Ferroelectric crystals can be multiple domain or single domain, so to pole crystal, an electric field is usually applied along one of the possible polar axes of crystal, see Figure 4.01. Since $E_c$ is generally smallest near $T_c$ (the Curie temperature), cooling the crystal through $T_c$ with an applied electric field is the common poling method to obtain a single domain crystal.

As the applied electric field is increased, favorably oriented domains with respect to the electric field direction grow at the expense of other domains. When the electric

field continues to increase in magnitude, the least favorably oriented domains begin to switch to the direction most nearly coinciding with the applied electric field direction until no further domain reorientation can occur, resulting in a hysteresis loop [21] between the saturation arm of the *P* and *E*, see Figure 4.01. The polarization achieved at the highest applied fields ($E_c$) is the maximum polarization $P_{max}$, when the electric field is removed, the resulting polarization states (at $E = 0$) are defined as the remnant polarization $P_r$. Figure 4.01(a) illustrates the transition of a multi-domain ferroelectric from a depoled state ($P = 0$) to the saturated state $P_{max}$, then switched back to the depoled state when a reversed electric field is applied (state from A to stage D in Figure 4.01(a)). In a ferroelectric single-domain crystal initially poled to $P_r$ (or with the spontaneous polarization $P_s$), it is possible to switch the polarization to the opposite sign by applying an electric field. Figure 4.01(b) illustrating the transition of single-domain ferroelectric from an initial poled state ($P = + P_r$) to the saturated state ($P = P_{max}$), then switched to the opposite state ($P = - P_r$), (state from A to stage D in Figure 4.01(b)).

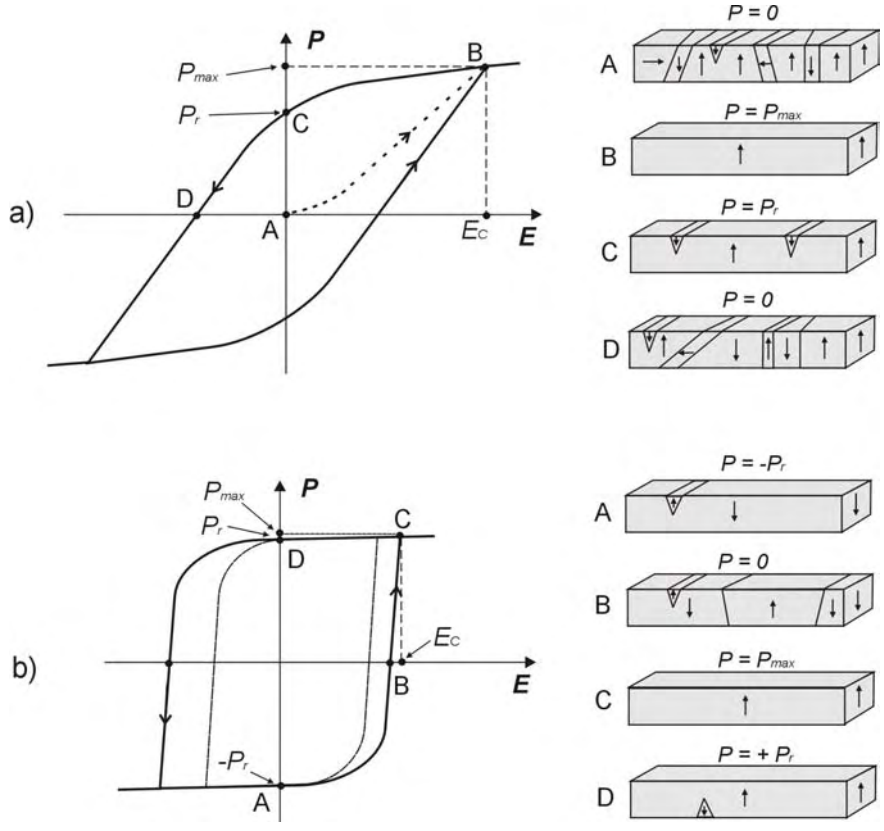


**Figure. 4.01.** Polarization versus electric field hysteresis loop during the poling process. (a) *P-E* hysteresis loop during poling a multiple domain ferroelectric crystals; (b) *P-E* hysteresis loop during poling a single domain ferroelectric crystals. The right side diagrams show the domain structures corresponding to changes in an applied electric field along z-axes [21].

Polarization switching (from $\pm P_r$ to $\mp P_r$) occurs through nucleation and growth of domains that are favorably oriented with respect to the applied electric field [21]. Due to the existence of domains, $P_r$ is always $\leq P_s$, the spontaneous polarization of the crystal [21]. Commercial $LiNbO_3$ wafer are normally supplied as a single-domain ferroelectric crystal, in which case, $P_r \approx P_s$.

## 4.3 Fabrication of PPLN

The following section details the fabrication process for PPLN that has been developed at the Optoelectronics Research Centre (ORC) of University of Southampton over the last ten years [22,23,24,25]

### 4.3.1 Cleaning

Cleaning the sample is the first step in the fabrication of periodically poled lithium niobate (PPLN), the surface of the sample must be completely washed and cleaned in order to remove any kind of particles of dirt or wax etc. This step is quite important, because any contamination on the surface of sample would lead to a poor quality photo-resist layer or can even make the sample break down during the poling process, by tracking of current across the sample surface.

All the cleaning processing is carried out in the class 1000 clean room. The sample is first put in different cleaning agents at the class 100 bench in an ultrasonic bath at a temperature of 50°C, the detailed procedure for cleaning is listed in Table 4.01.

**Table 4.01** The procedure of sample cleaning

| Cleaning Agent | Time (min) | Function |
|---|---|---|
| Ecoclear | 20 | Remove wax and other organic contaminants |
| Acetone | 20 | Remove Ecoclear and organic residue |
| IPA | 20 | Remove Acetone and organic residue |
| Microclean | 20 | Detergent, remove inorganic and IPA residue |
| Distilled water | 10 | Remove Microclean |
| Distilled water | 10 | A second rinse to remove any residue |

The samples are then blow dried by a dry air gun and stored in a desiccator until the next processing step, generally samples of lithium niobate are not put in an oven after

chemical cleaning (a technique often used with other materials to ensure all moisture is removed from a sample) in order to avoid pyroelectric charge building up on the surface resulting in spontaneous poling of the samples.

### 4.3.2 Patterning

The next step is patterning, in which the -*z* surface of samples is covered by photo-resist (S1813) with a thickness from 1.0μm to 1.8μm. When the photo-resist is spin coated onto the samples, the thickness can be controlled by adjustment of the spin speed and the spin time, the details are given in the following Table 4.02

**Table 4.02** Thickness vs. spin speed and spin time (thickness was measured by Alpha Step)

| Photo-resist | Spin speed (r/min) | Spin time (min) | Thickness (μm) |
|---|---|---|---|
| S1813 | 6000 | 1.0 | 1.0 |
| S1813 | 4000 | 1.0 | 1.3 |
| S1813 | 2000 | 1.0 | 1.8 |

In the experiments described above, three different thicknesses of photo-resist have been characterised, an investigation regarding the thickness of the resist is discussed in following section. The ORC have concentrated on the fabrication of PPLN for several years and found that higher quality and better-defined gratings are obtained if the samples are patterned on the –*z* face, using a gel electrode method developed at the ORC. After spinning of the photo-resist, the samples are then put into an oven at 90°C for 60 minutes. As a precaution, the oven door should be opened for around 2 minutes to let the temperature cool down to around 55°C. The samples are covered by two glass Petri-dishes in order to avoid a rapid temperature increase, and thus limit pyroelectric charge building up on the surface.

A mask aligner is used to create the PPLN grating pattern. The target mask is installed on the Karl Suss MA4 mask aligner, with the metal face of the mask downwards. Before transferring the required PPLN grating from the mask to a lithium niobate sample, some glass samples should be first exposed to UV light ($\lambda$ = 436nm), for different times in order to check the optimum exposure time. The photo-resist thickness and pattern profile of each glass sample is measured using an Alpha Step instrument. Figure 4.02 shows a typical trace for a patterned PPLN grating. A suitable mark-space ratio (the open area to the covered area) is around 40:60 (with the open

area slightly narrow than the covered area) for gratings with period over than 10μm, and 30:70 for gratings with a period less than 10μm. The profile of the grating and the exposure time are highly critical for the mark-space ratio of the grating, and therefore it is important for the quality of the poling. A detailed investigation regarding exposure time is listed in following section.

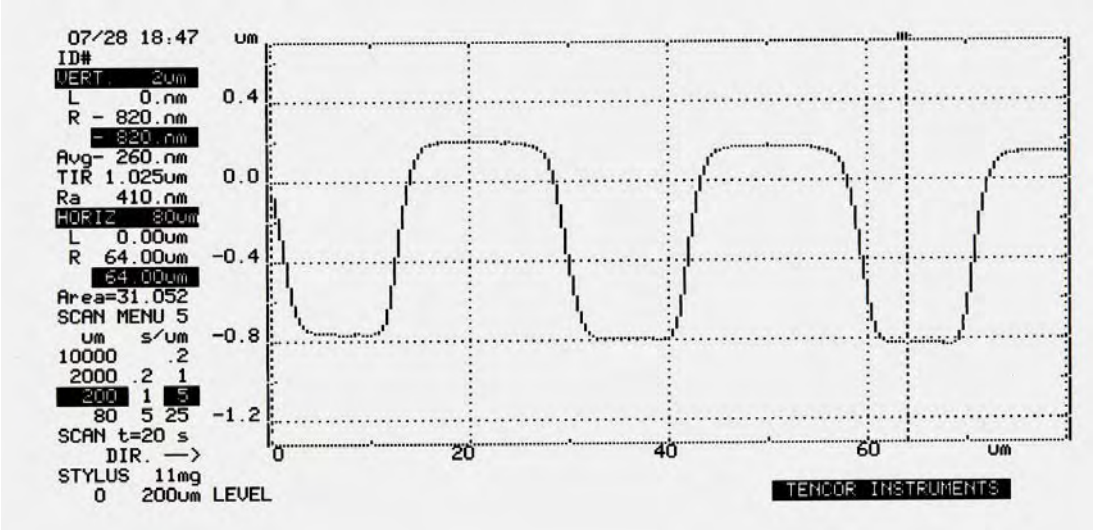


**Figure 4.02.** Typical profile of patterned photo-resist gratings on lithium niobate by photolithography

### 4.3.3 Poling

The area surrounding the poling region must be covered by a PVC insulation tape on the negative *z* face, the width of the tape should be more than 4mm, which means the shortest distance from the edges of the sample to the uncovered area is more than 4mm. This prevents charge leaking around the edges of the sample resulting in breakdown of the sample during the poling. Next the sample is covered by electronically conductive liquid ECG gel on the both sides. The gel will fill all the gaps between the photo-resist (this can be proved by checking the uniformity of the PPLN after poling), this method is simple, versatile and very effective in controlling the region of poling, this is shown schematically in Figure 4.03.

In most PPLN fabrication systems high voltage poling is controlled by applying a series of high voltage pulses to the crystal through a large load resistor. The load resistor limits the available voltage and thus limits the poling current. The area of the crystal inverted during a pulse is related to the amount of charge which has flowed. The current during a pulse is integrated to give an appropriate overall amount of

charge. This approach is somewhat unsatisfactory for number of reasons, in particular the main problem is that the rate of poling, which is proportional to the current flowing, is controlled by trying to guess in advance how much voltage should be applied across the sample [26]. This is rather like trying to control the amount of current flowing through a forward biased diode by guessing a voltage.

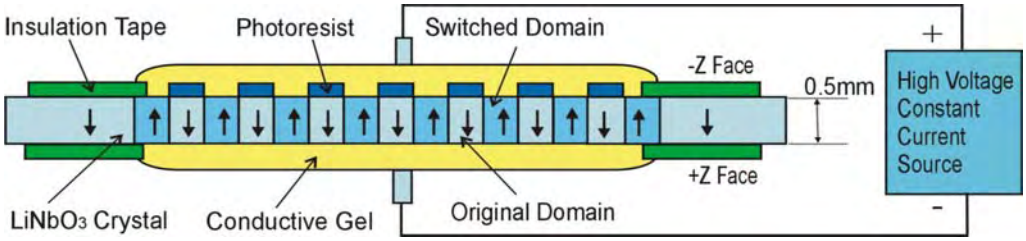


**Figure 4.03.** Schematic diagram of PPLN poled under electronic field.

In the poling systems developed at the Optoelectronics Research Centre (ORC) in University of Southampton, a current programmed approach is used. In this system a pre-determined current profile is applied and feedback is used to give the correct voltage, which in turn, gives the correct current. This approach allows direct control of poling rate, and has been found to give better PPLN quality and higher process yield. The system works by having a high voltage trans-conductance amplifier to provide rapid control of current through feedback, and a low speed power supply to provide a bias signal to give the majority of field needed. The schematic operation is shown in the Figure 4.04

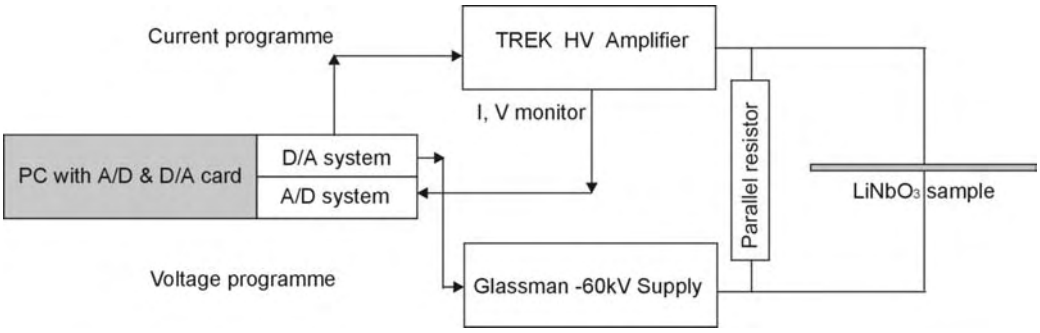


**Figure 4.04.** Electronic circuit of the poling device.

The patterned sample is held in a holder which connects positive and negative electrodes. The poling is controlled by the Trek HV amplifier used in trans-conductance mode to provide a ±10kV swing in voltage. A negative bias voltage is provided by the -60kV Glassman supply. In trans-conductance mode the Trek amplifier supply can be voltage programmed to give a particular current, a

programmed waveform is supplied by computer via the D/A buffer during the poling process, this waveform controls, via the trans-conductance circuit, the current flowing through the sample. By choosing a suitable current waveform the poling can be controlled for both poling rate and total switched charge. During the poling process, the sample is subject to an electric field (≈ 22kVmm$^{-1}$) between the two electrodes [27], the voltage required across sample is increased automatically until domain switching occurs. When a desired charge $Q$ is delivered to sample, an area $A$ will be poled, as the charge is the integral of the current over time, the process of poling can be monitored by checking the current. Different current levels will determine the time taken to pole the sample, and the total charge needed to switch the domain can be calculated based on Eq.(4.01):

$$Q = \int Idt = Ps \cdot A = Ps \cdot W \cdot L \cdot N \qquad 4.01$$

Where, $Q$ is the total charge needed to switch the domain, $I$ is the current flow, $A$ is the poling area in mm$^2$, $L$ is the length of grating in mm, $Ps$ is the spontaneous polarisation, for $LiNbO_3$, $Ps$ = 0.72μC·mm$^{-2}$, $N$ is the number of gratings being poled, $W$ is the width of gratings in mm. Figure 4.05 shows typical current and voltage trace.

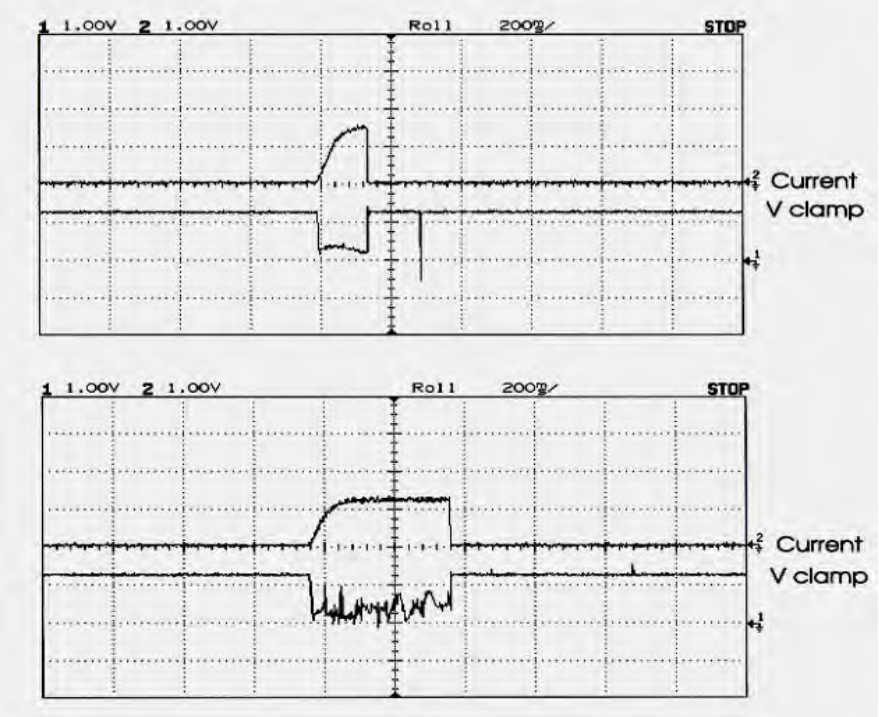


**Figure 4.05.** The current and voltage trace of poling processes, the upper plot shows the recorded trace for $Q$ = 20μC, The bottom one shows trace for $Q$ = 110μC.

### 4.3.4 Assessment of PPLN Grating

In order to compare the different poling methods and assess the poling quality of PPLN samples, we require a method of evaluating the quality of the PPLN gratings. There are several ways to assess PPLN gratings, the first way is a visual inspection of the domain gratings under a microscope using crossed polarizers, see Figure 4.06. Due to the residual stress and associated birefringence, the domain boundaries can be seen quite clearly after poling. From this we can obtain a rough idea of domain boundary straightness, under or over poling, grating uniformity, etc.

The second way of permanently revealing the PPLN gratings is etching the samples in a HF:$HNO_3$ mixture with volume ratio of 1:2 for around 2-4minutes [25]. The HF:$HNO_3$ mixture only attacks the –z face, removing around 0.7μm per hour, and leaving the +z face untouched, this can be clearly seen in photograph taken with an optical microscope, see Figure 4.07.

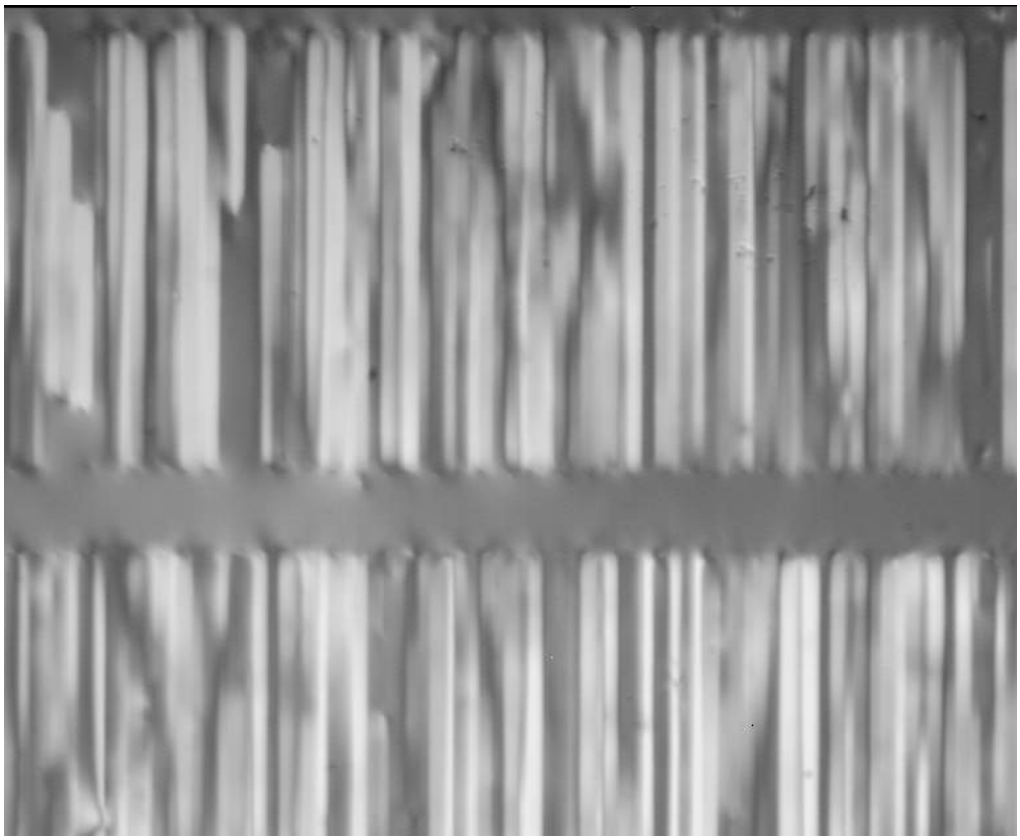

**Figure 4.06.** PPLN structure showing grating domain under a microscope using crossed polarizers.

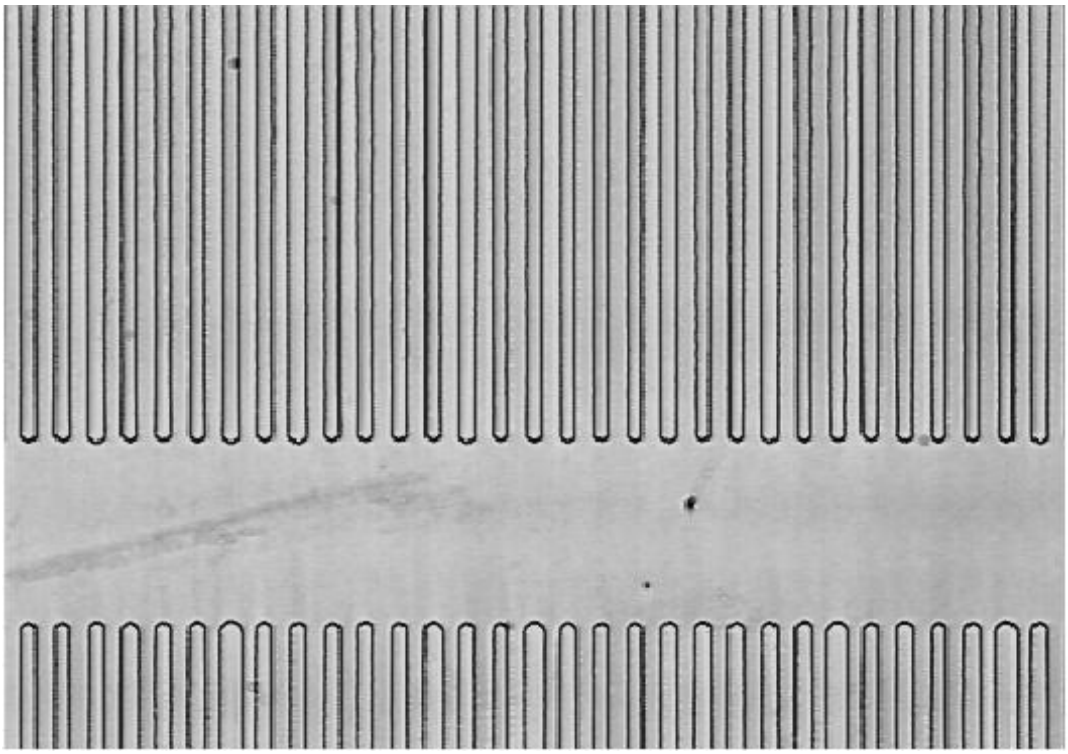

**Figure 4.07.** PPLN photograph taken under optical microscope after wet etching in $HF:HNO_3$.

The poling quality of the PPLN can be assessed and compared after the wet etching under the microscope. The assessments used in this report are listed as following:

a) Broken-down during poling. The sample has broken-down due to a surface defect or excessive voltage across the sample, the breakdown point usually can be seen on the surface of sample, see figure 4.08(a).
b) Complete over-poling. The domains under the grating area patterned by the photo-resist have been completely switched due to the excess charge forced through the sample, a large switched domain area was formed instead of a PPLN grating, see figure 4.08(b).
c) Under-poling. Only part of domains under the grating area patterned by the photo-resist have been switched due to insufficient charge injected in that area, the switched domain was formed only along the boundary of the grating area. The rest of the area is not poled, see figure 4.08(c).
d) Over-poling. The domains have merged together forming a big switched domain due to too much charge injected locally, usually another area is under-poled to compensate to the over-poled area if the overall correct amount of charge is injected, see figure 4.08(d).

e) Good poling. The switched domain grating follows the pattern of the photo-resist, the uniformity of the grating is good and the mark-space ratio is around 50:50, see figure 4.08(e).

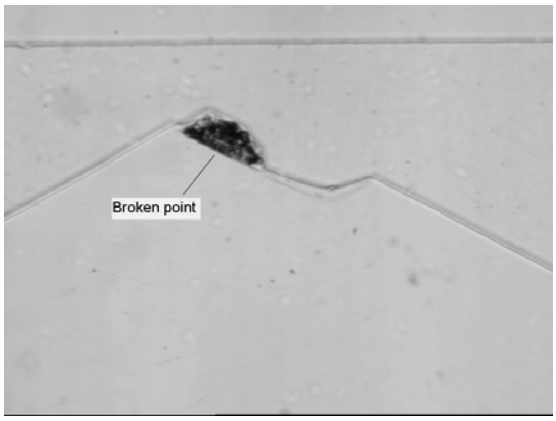


(a) Broken-down and sample cracking during poling

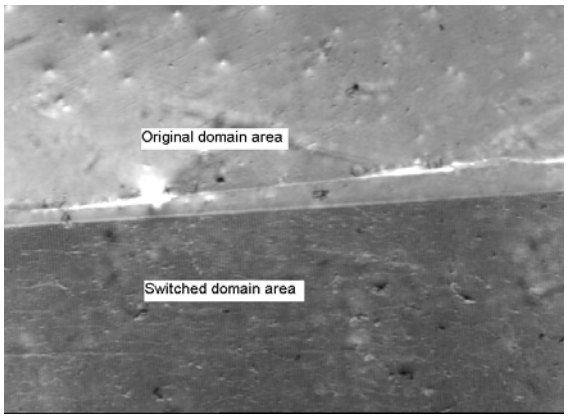


(b) Complete over-poling.

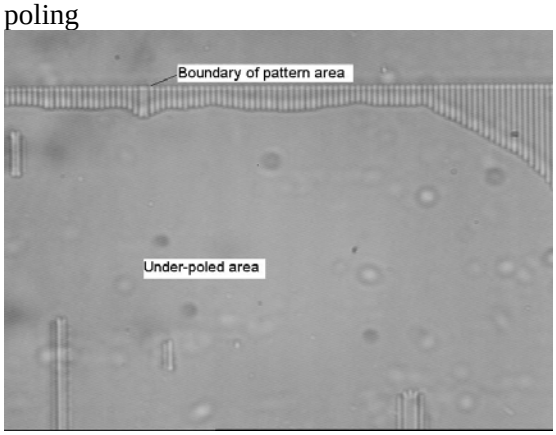


(c) Under-poled.

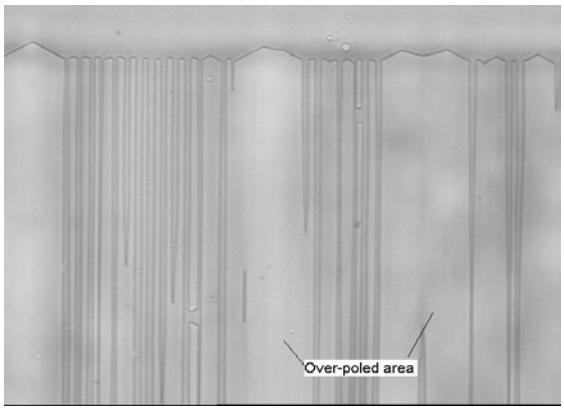


(d) Over-poling.

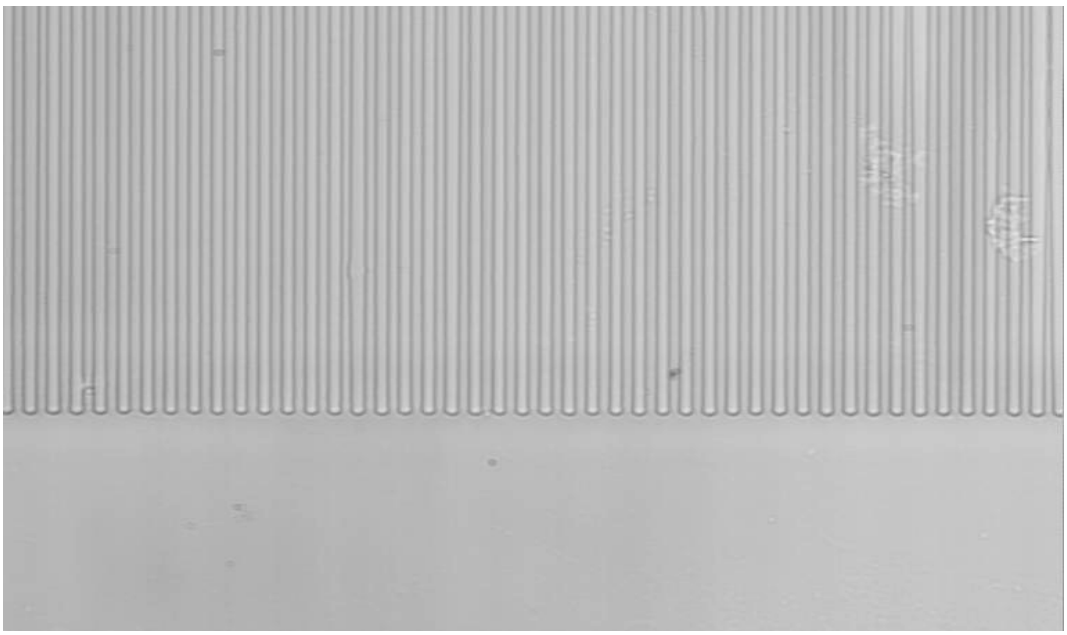

(e) Good poling.

**Figure 4.08(a)-(e).** Assessment of the poling quality of the PPLN grating.

## 4.4 Investigations and Analysis of Poling Quality

This section reviews factors affecting poling quality. The presented analysis and results were performed during this project and have led to significant improvements in poling quality of PPLN crystals at University of Southampton.

The quality of PPLN gratings is determined by a large number of factors during the whole patterning and poling process. Those factors include the poling techniques, the quality of the mask, the fidelity of the photo-resist pattern, material used for the electrode etc. Figure 4.09 lists the critical factors which determine the quality of the PPLN.

In experiments carried out in this research, a large number of samples from different suppliers have been poled with different photo-resist thickness, exposure times, different electrode materials and different patterning methods. Also the backswitching technique has been investigated. The following sections will go through some of these factors in detail.

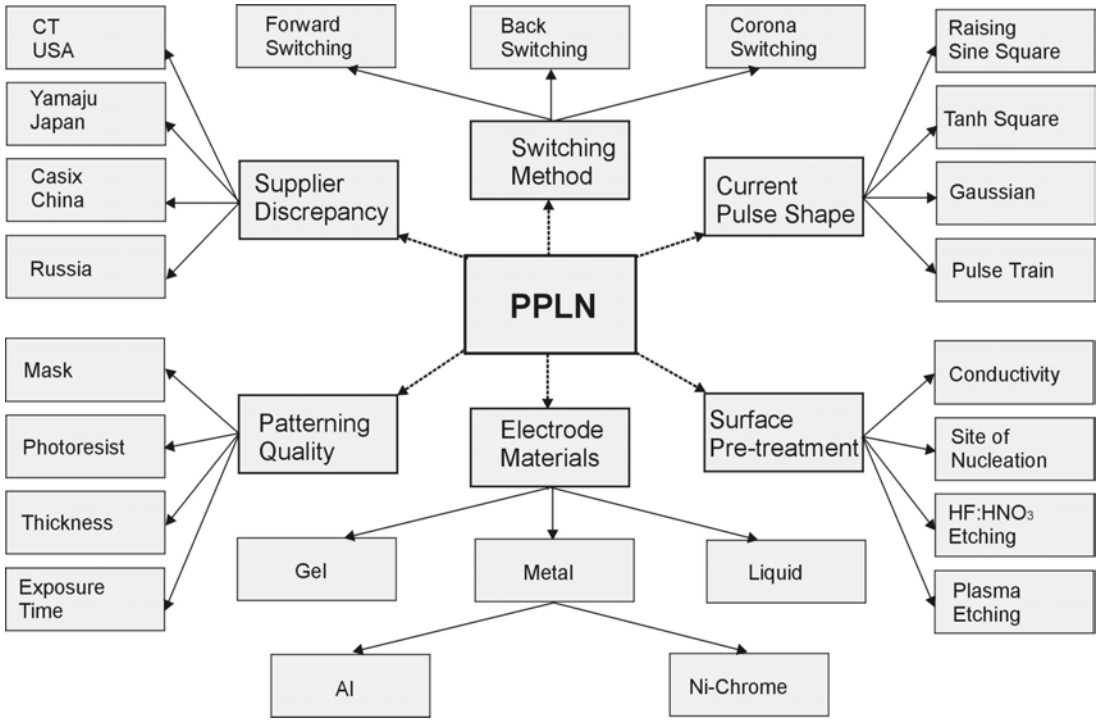


**Figure 4.09.** Breakdown of the PPLN grating quality influential factors.

### 4.4.1 Supplier Discrepancies

At the moment the main sources of lithium niobate for the ORC are listed in Table 4.03. All the wafers have been ordered based on the same specification, but the result of poling is different for samples from different suppliers.

**Table 4.03** The main source of lithium niobate

| No. | Name of supplier | Country | Assessment |
|---|---|---|---|
| 1 | Crystal Technology (CT) | USA | Good poling |
| 2 | Mitsui | Japan | Over-poling |
| 3 | Yamaju (YA) | Japan | Over-poling |
| 4 | Via Crystran | China | Under-poling |
| 5 | Via Crystran | Russia | Under-poling |

In the work in this thesis, samples from CT, Russia, YA and China have been poled using identical fabrication procedures, but it was found that differently sourced material gave very different quality gratings, see Figure 4.10.

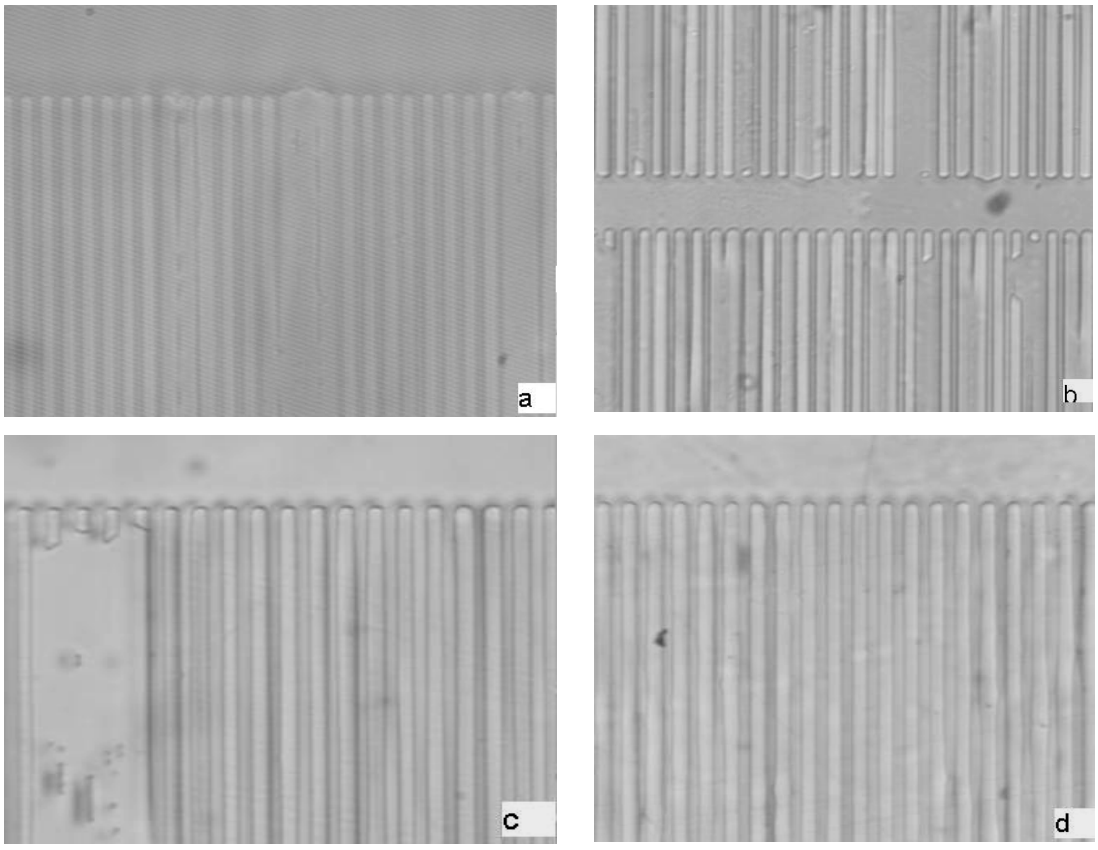


**Figure 4.10.** Supplier discrepancies of PPLN grating. All the poling parameters of the samples are same, the period of the gratings is 18.5μm. (a) Sample No.402 from YA; (b) Sample No.806 from China; (c) Sample No.830 from Russia; (d) Sample No.803 from CT.

From the above figures, it was found that even though all the parameters of the poling processes are the same, the samples from Russia and China were under-poled, the sample from Japan was a little bit over-poled, the samples from CT have a better poled grating. Experiments also demonstrated that even when the wafer comes from the same supplier, the results of poling can be different. This may be due to the different polishing methods adopted by different suppliers and the processing variation during the lithium niobate crystal growth.

The underlying mechanisms for the poling processes are still being investigated by several groups worldwide, and have not been finally confirmed, but it is thought that poling processes are governed by two mechanisms, nucleation of new domains and domain wall motion [28,29,30,31]. It is known that the surface quality of a sample directly affects the nucleation points on the surface of samples, and thus affects poling quality. Two factors should be considered, they are conductivity and surface defects. Low conductivity is good for poling quality, because low conductivity can reduce charge motion beneath the insulating patterned electrodes [32], however surface defect are good for nucleation on the surface of sample. Previous work has suggested that acid treatment before the cleaning process greatly increases the density of nucleation points on the surface of sample [25], but during this work acid pre-treatment was tried, and no advantage was measurable. In addition, during the cooling stage in the baking process of the photo-resist patterning, unwanted surface charge is accumulated pyroelectrically on the surface of crystal. When the electric field associated with this isolated surface charge exceeds the coercive field, spontaneous poling dot start to forms on the surface of crystal. These spontaneous poling dots directly reduce poling quality.

Several practical methods were adopted to improve the poling quality. Firstly, the spontaneous poling dots can be effectively reduced by putting the sample on a conductive metal mesh during the baking of the photo-resist, the surface charge is thus neutralized through discharge between the sample and the metal mesh. The poling results show that the resulting PPLN was dramatically improved.

Secondly, increasing the number of nucleation points in the areas to be poled can improve the uniformity of the domain gratings. It was found that the nucleation stage

always starts at the corner and edge of the defined grating strips, this is because the electric field in that area is larger at these points than that in other areas. This leads to the idea that the number of corners and edges of the pattern can be artificially increased through superstructure designs. The details of this are discussed in the following sections.

Finally, it was found that the quality of PPLN samples poled after a time delay of greater than twelve hours after the patterning of the photo-resist is better than that of PPLN samples poled immediately after the patterning process. The underlying reason is not fully understood at the moment, but it is believed that the surface charge distribution on the sample induced by the UV exposure follows the pattern of the mask to form a surface charge pattern, which can directly affect the poling quality. This surface charge pattern is time dependent and will vanish over time due to the finite conductivity of the surface of the sample.

### 4.4.2 Grating Mask Design

The grating mask design has a significant influence on the poling quality of the PPLN. It was found that the optimal grating structures for large period PPLN are not optimum for fine period PPLN, thus different mask design are required for each PPLN period.

The poling process under high electric field is illustrated in Figure 4.11. During this process, it is thought that poling starts at nucleation points on the surface of the crystal which are found at the edges and corners of the photo-resist defined grating where the electric field is strongest [33], see Figure 4.11(a). The second stage is domain tip propagation, see Figure 4.11(b), the tip of the nucleated domain propagates parallel to the *z* axis to the opposite face of the crystal. The third stage is domain tip termination, see Figure 4.11(c), when the tip of the nucleated domain reaches the opposite face of the crystal, a pair of domain tips begin to merge together resulting in a larger domain. The final stage is switched domain wall propagation, when the tip of an isolated domain terminates at the opposite face of a sample, the diameter of the domain at both faces increased rapidly and its facets propagate in the direction of the crystal *x* and *y* axes, see the Figure 4.11(d).

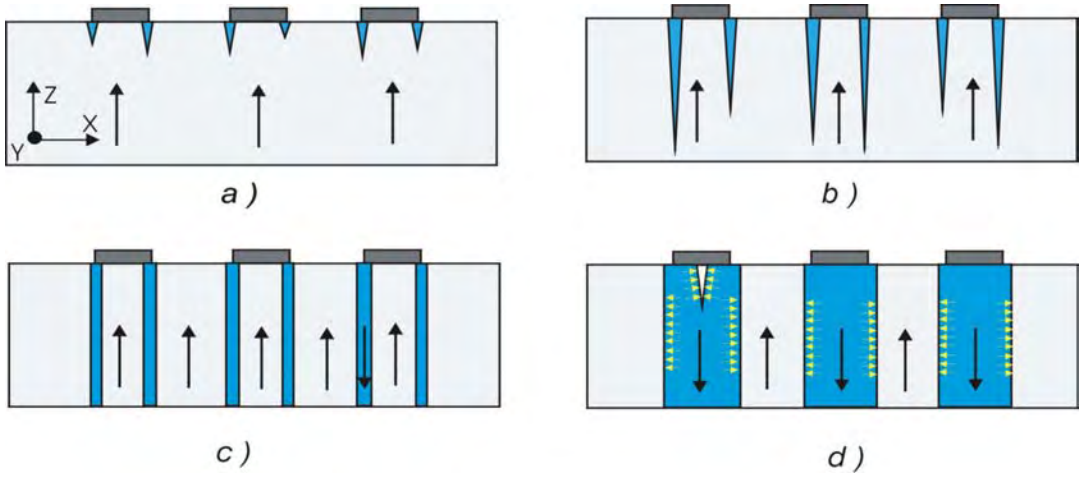


**Figure 4.11.** The four stages of domain switching during electric field periodic poling. (a) Domain nucleation at the electrode edges or corners; (b) Domain tip propagation toward the opposite face of the crystal; (c) Termination of the domain tip at the opposite side of the crystal; (d) Propagation of the domain walls out from under the electrodes.

During the poling process (using the samples from CT), it was found that the some parts of the domain beneath the electrodes was not poled when the period of the grating was large, for example with a 30μm period, see Figure 4.12. It was also found the domain between the electrodes was often merged to form a big switched domain when the period of the grating was small, for example for a 6.5μm period, see Figure 4.13.

It is believed that during the stage of wall propagation, the side wall of the domain propagates inside the area under the electrodes as well as outwards outside of that area, this is indicated by the small yellow arrows in Figure 4.11(d). When poling the large period gratings, the electrodes stripes are too wide for the two tip penetration domains under the edges to merge together before the poling process stops. Figure 4.12 shows such a revealed domain after wet etching. When poling fine period gratings, the opening gap between the electrode stripes is too narrow so that domain walls propagating outside the resist merge together before the poling process stops, see Figure 4.13. In addition it was found that the quality and uniformity of gratings is better along the edge of the patterned area where the electric field is higher than in the middle of each grating area, see Figure 4.14.

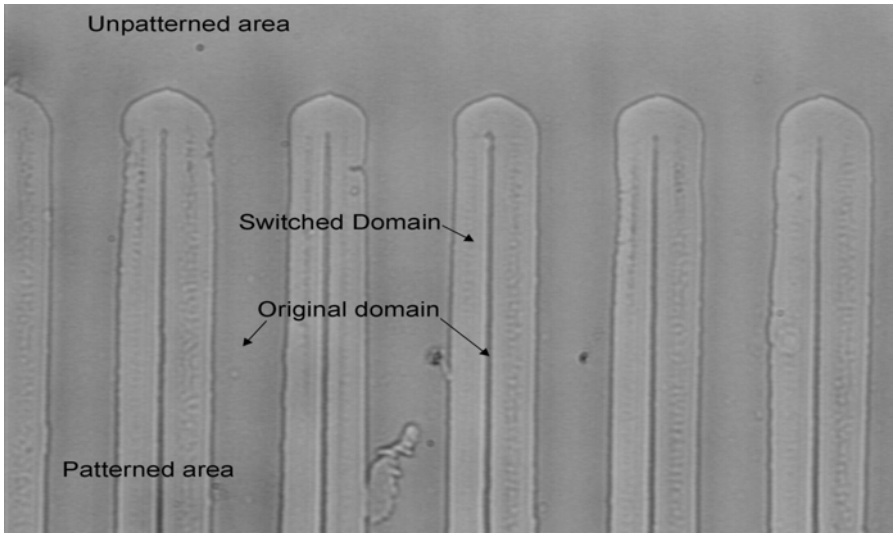


**Figure 4.12.** A small part of the domain beneath the electrodes is not poled when the period of the grating is large. The period of this grating is 30μm.

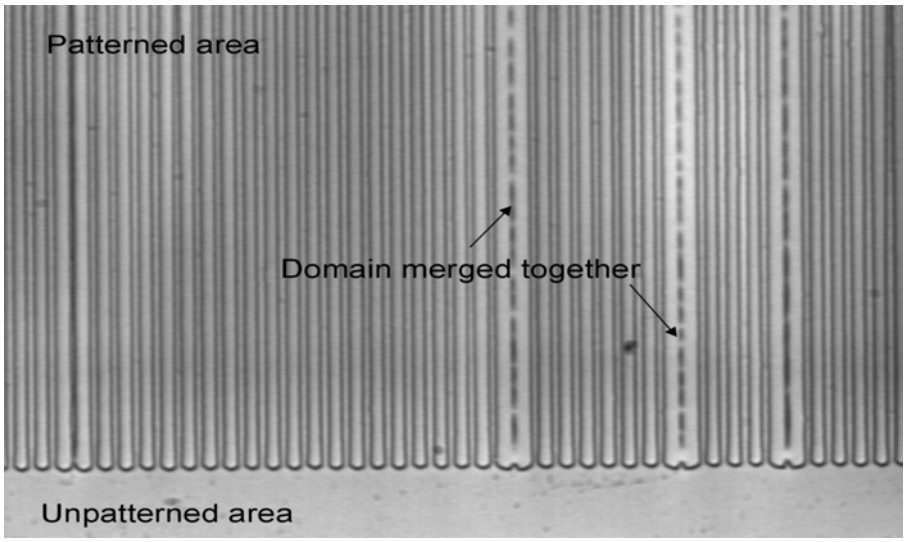


**Figure 4.13.** The opening gap between the electrode stripes is too narrow so that tip domains spread under the resist strips and merge together before the poling process stops.

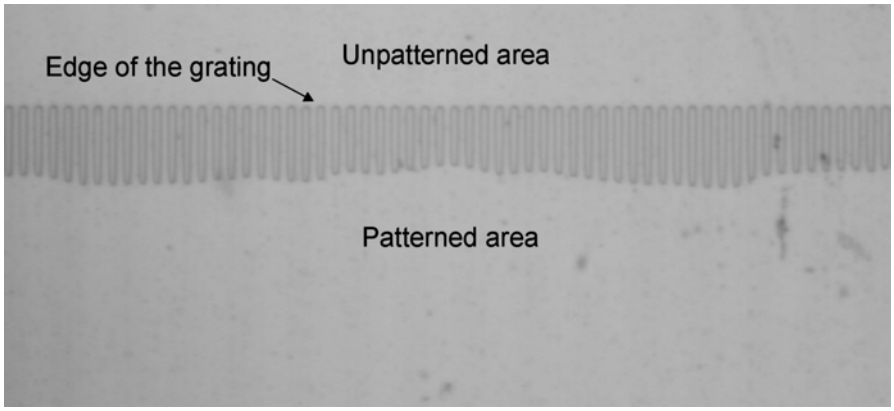


**Figure 4.14.** The quality and uniformity of grating is better along the edge of patterned area showing the higher electric field found at these points.

### 4.4.3 Superstructure Designs

To help overcome the problems (associated with poor uniformity) a new mask was designed for different period gratings, see Figure 4.15. During the scope of this project, it was found that for large periods, see Figure 4.15(a), better poling quality was achieved by using multiple small openings within each grating plane, see Figure 4.15(b) and (c), allowing more photo-resist defined edges and corners. For fine period gratings, see Figure 4.15(d), narrow width gratings or a set of narrow sub-sections in the grating structure results in better poling quality, see Figure 4.15(e) and (f).

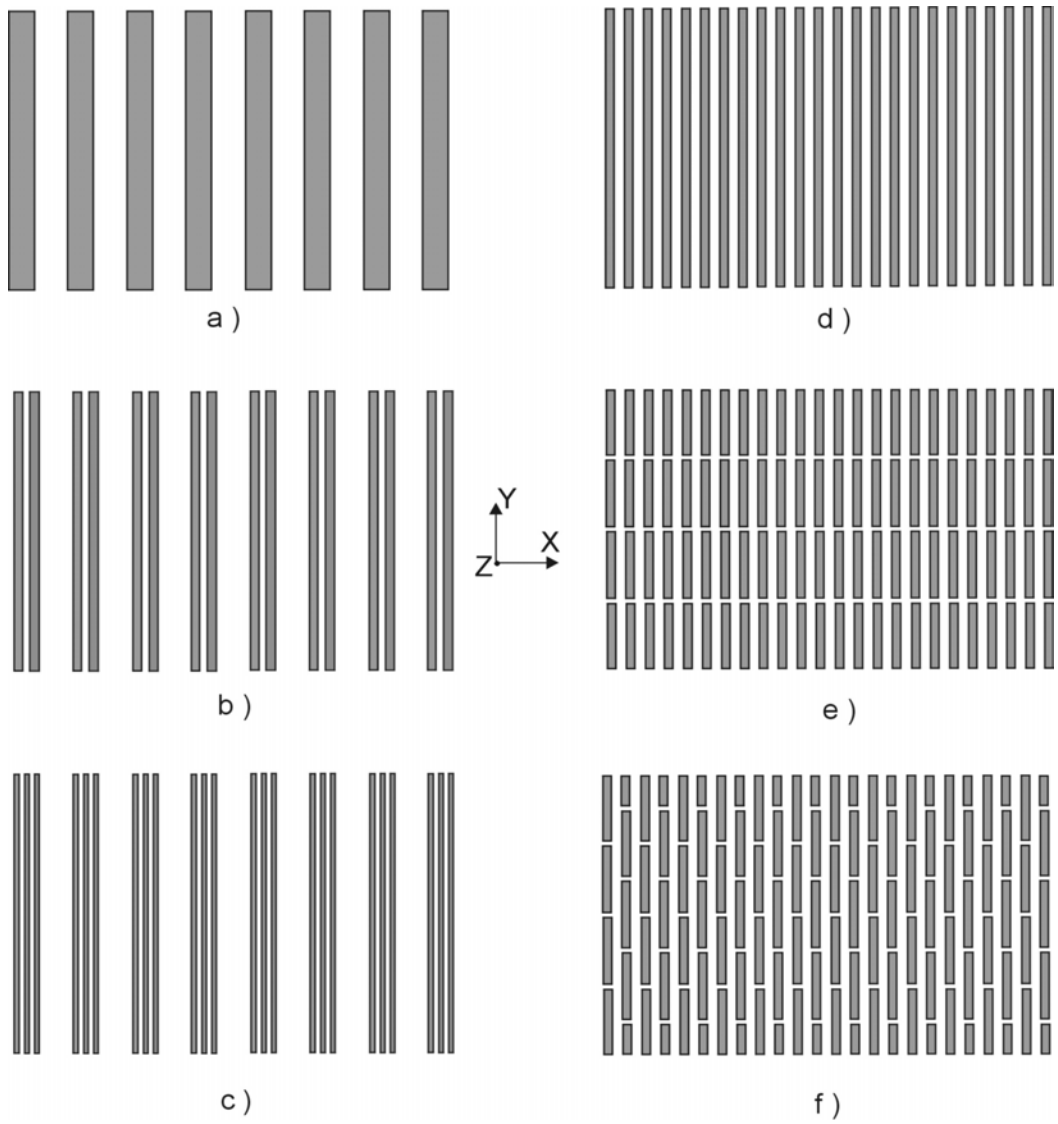


**Figure 4.15.** Different grating mask designs. (a) Normal grating mask design for large periods of PPLN; (b) One small opening within domains of the grating; (c) Two small openings within domains of the grating; (d) Normal grating design for fine period PPLN; (e) Narrow width grating or a set of narrow sub-sections of the grating; (f) The brick wall structure grating.

By using the same charge as required to invert a regular grating, the domain walls spread and merge in these superstructure gratings to yield high quality PPLN, see Figure 4.16.

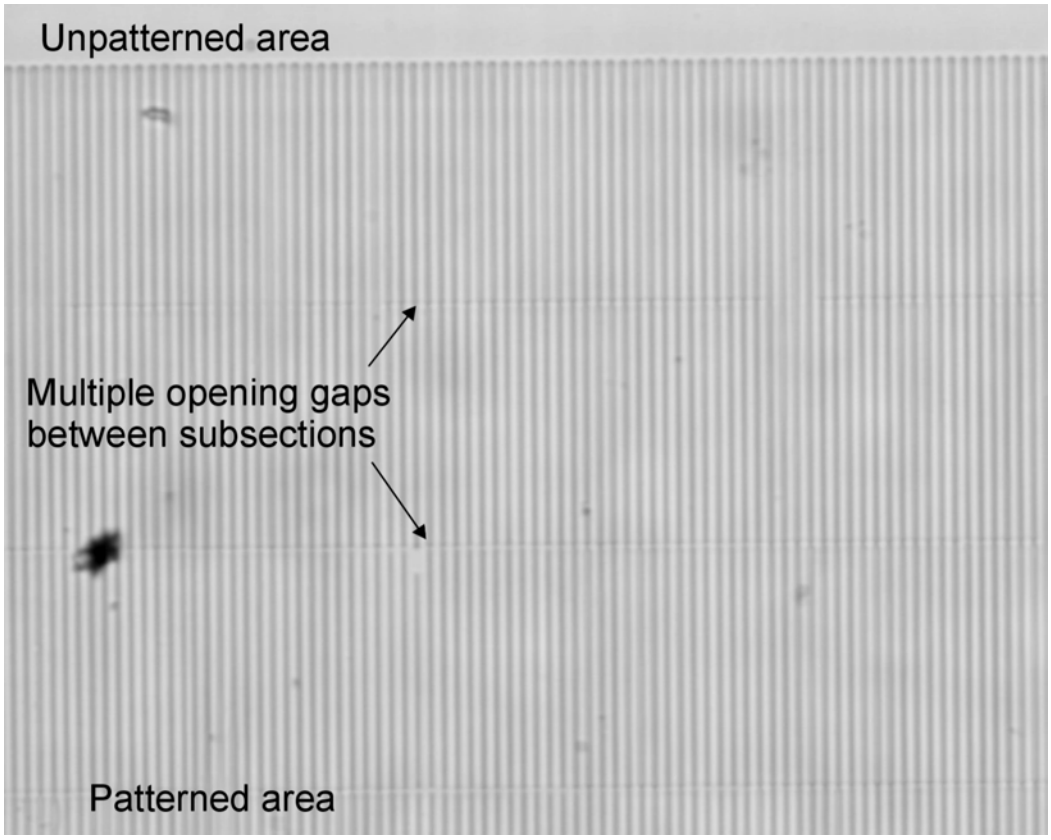


**Figure 4.16.** By using the newly designed mask shown in Figure 4.15(e), much better quality gratings were obtained, the period of the grating is 6.5μm

### 4.4.4 UV Exposure Time

Before patterning the lithium niobate, different exposure times on glass samples are always tried and measured under the microscope. This step is the necessary before each patterning run because the intensity of the UV light is time dependent, and will decay slowly over several weeks. The UV light intensity used in this thesis is $\approx 8.2 mW/cm^2$ (This figure was measured by using a Karl Suss UV Intensity Monitor No.1000). Table 4.04 shows different thicknesses of photo-resist gratings on $LiNbO_3$ for varying exposure times. A correct mark-space ratio (opened area to closed area ratio) of the photo-resist is needed to give good PPLN gratings. The high quality poling achieved in this work proved that this method of checking the exposure time is effective and acceptable.

**Table 4.04** Photographs of sample grating under the microscope

| Thickness PR (μm) | Exposure time (s) | Grating Λ (μm) | Pattern photo | Comment |
|---|---|---|---|---|
| 1.0 | 3 | 6.5 | 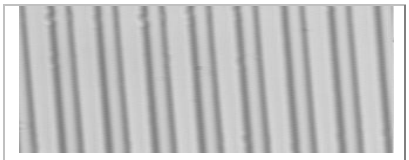 | Under-exposed |
| 1.0 | 4 | 6.5 | 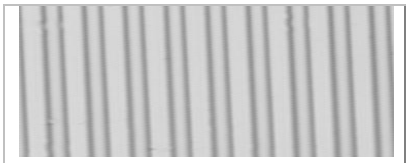 | Under-exposed |
| 1.0 | 4.5 | 6.5 | 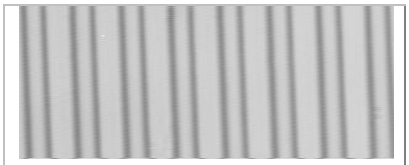 | Correctly exposed |
| 1.0 | 5 | 6.5 | 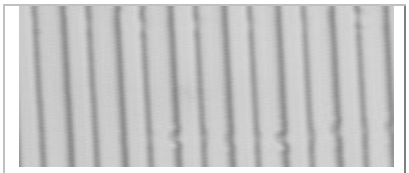 | Slightly over-exposed |
| 1.0 | 5.5 | 6.5 | 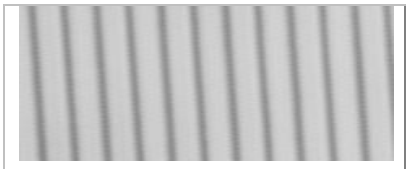 | Over-exposed |
| 1.3 | 5.5 | 6.5 |  | Under-exposed |
| 1.3 | 6 | 6.5 | 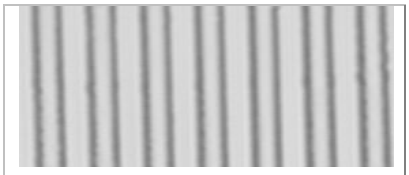 | Correctly exposed |
| 1.8 | 5.5 | 6.5 |  | Correctly exposed |
| 1.8 | 6 | 6.5 | 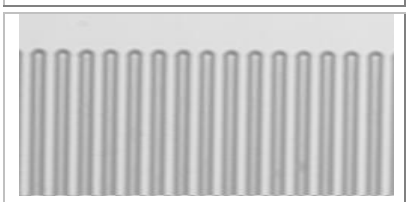 | Over-exposed |

### 4.4.5 Thickness of Photo-resist

Different thicknesses of photo-resist have also been investigated, photo-resist Shipley S1813 was used for which the thickness vs. the spin speed is listed in the Table 4.02. Samples with different periods of gratings were patterned with varying thicknesses of photo-resist and different UV exposure times were poled using the same poling process, the poling results are listed in Table 4.05.

Through comparison and investigation, the following conclusion was drawn:

1) The mark-space ratio of the patterned grating is important for poling quality, for large periods of PPLN (normally over 10μm), a suitable mark-space ratio is 40:60. For fine periods of PPLN (less than 10μm), a 30:70 mark-space ratio is suggested.
2) The thickness of the photo-resist layer is more critical for the finer periods of grating than for the longer ones. Increasing the thickness of the photo-resist can effectively suppress the domain wall propagation beneath the patterned area, thereby greatly improving the poling quality, see Figure 4.17 to 4.20.
3) The correct UV exposure times are grating period dependent, longer grating periods need longer exposure times compared with the shorter ones.

**Table 4.05** Comparison of the thickness of photo-resist and exposure time.

| No. | Thickness (μm) | Exposure time (s) | grating Λ (μm) | Comments |
|---|---|---|---|---|
| 800 | 1.0 | 7 | 30 | Some sections of over-poling |
| 803 | 1.0 | 9 | 30 | Large areas over-poling |
| 801 | 1.0 | 4.5 | 6.5 | Large areas over-poling |
| 802 | 1.0 | 4.75 | 6.5 | Complete over-poling |
| 900 | 1.3 | 5.5 | 6.5 | Over-poling |
| 901 | 1.3 | 6 | 6.5 | Large areas of over-poling |
| 902 | 1.3 | 8 | 30 | Small areas over-poling |
| 903 | 1.3 | 8.5 | 30 | Some areas of over-poling |
| 904 | 1.8 | 6 | 6.5 | Little over-poling |
| 905 | 1.8 | 5.5 | 6.5 | Good poling |
| 906 | 1.8 | 8.5 | 30 | Good poling , small areas of over-poling |
| 907 | 1.8 | 9 | 30 | Good poling , small areas of over-poling |
| 910 | 1.8 | 7 | 10 | Good poling |

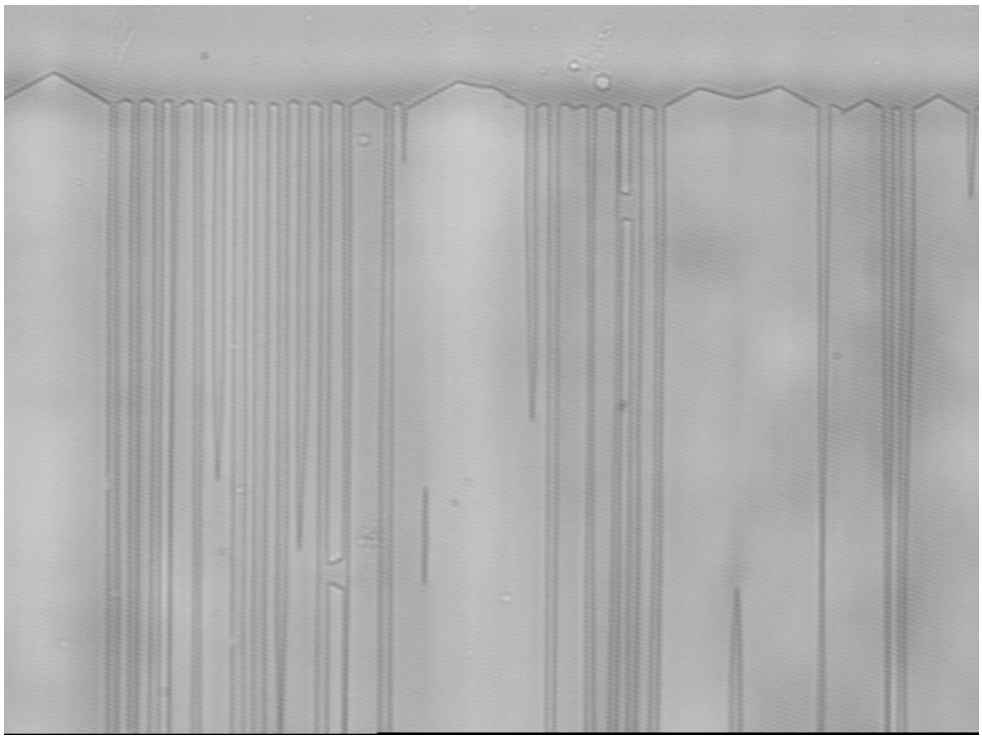

**Figure 4.17.** PPLN sample (code No.801) with 6.5μm period grating poled by gel electrode, the thickness of the photo-resist S1813 was 1.0μm. The PPLN quality is poor. Large areas were under-poled while some areas were over-poled (overlapped).

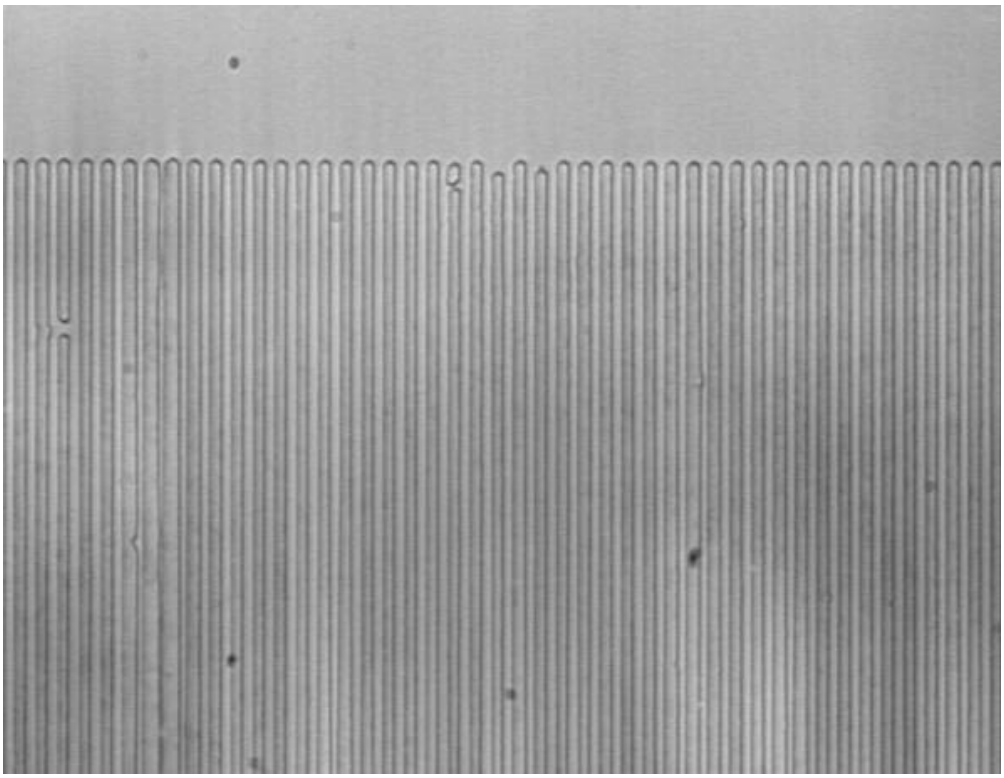

**Figure 4.18.** PPLN sample (code No.900) with 6.5μm period grating poled by gel electrode, the thickness of the photo-resist S1813 was 1.3μm. The PPLN quality is obviously better.

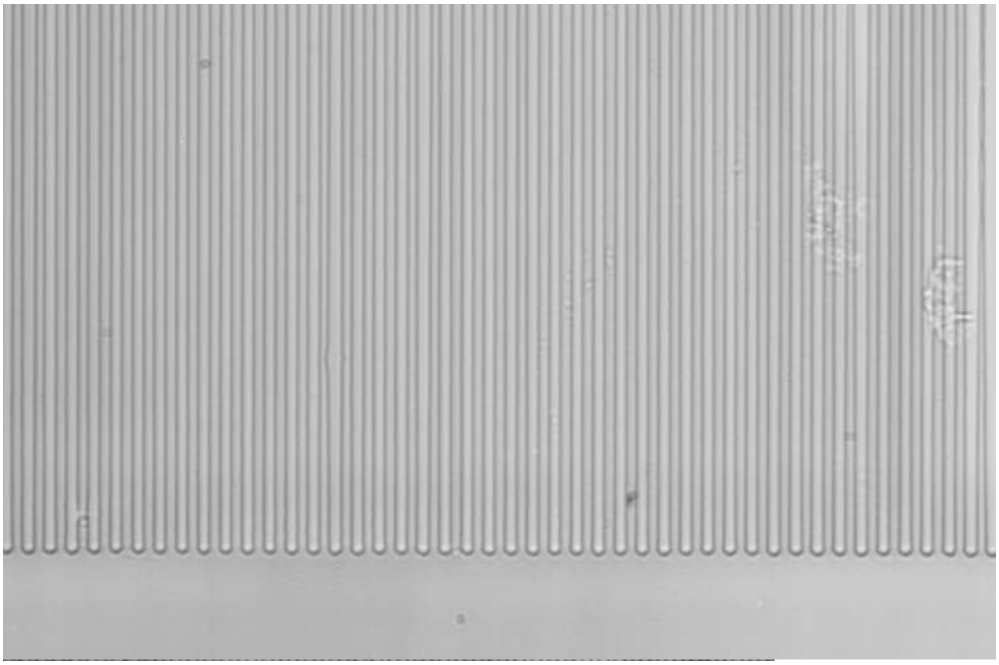

**Figure 4.19.** PPLN sample (code No.905) with 6.5μm period grating poled by gel electrode, the thickness of the photo-resist S1813 was 1.8μm. With very thick photo-resist, the PPLN quality is dramatically improved.

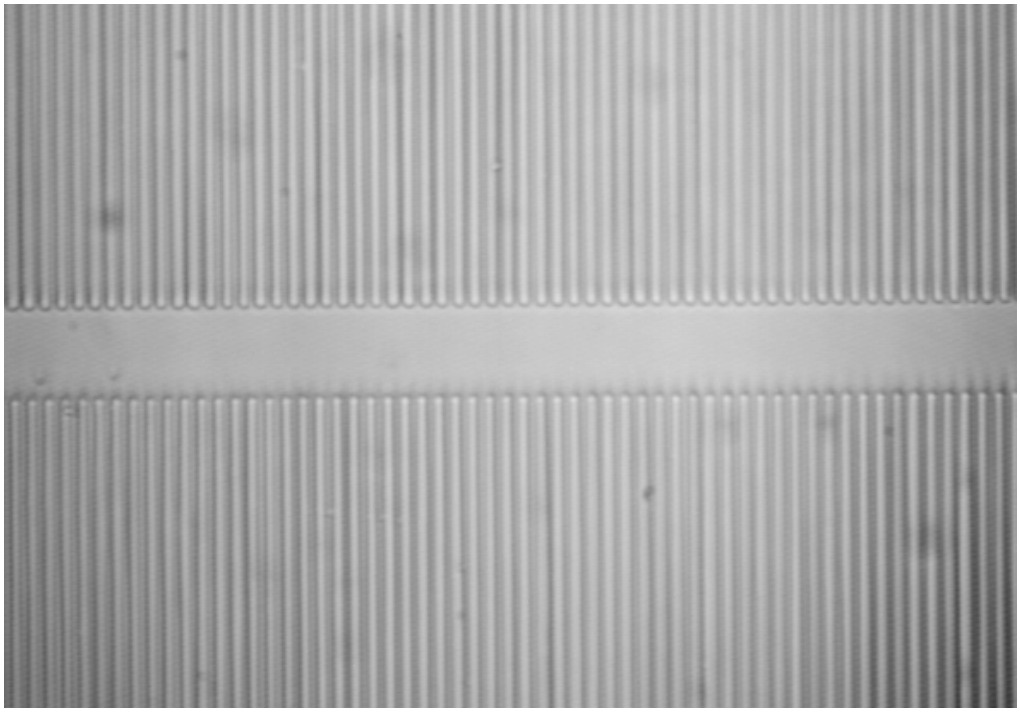

**Figure 4.20.** PPLN sample (code No.910) with 10μm period grating poled by gel electrode, the thickness of the photo-resist S1813 was 1.8μm. The uniformity of the grating is very good.

To summarise these results, it can be suggested that for fine grating periods, say around 6μm, a suitable thickness for the photo-resist S1813 is around 1.8μm, the

exposure time is around 5.5 seconds with a UV intensity of 8.2mW/cm$^2$; while for the longer period gratings, say around 30μm, the thickness of the photo-resist S1813 can be either 1.3μm or 1.8μm, the exposure time should be around 8.5 seconds or 9 seconds with UV intensity of 8.2mW/cm$^2$.

A possible explanation for why thicker photo-resist is better for poling fine period PPLN gratings can be based on Figure 4.21.

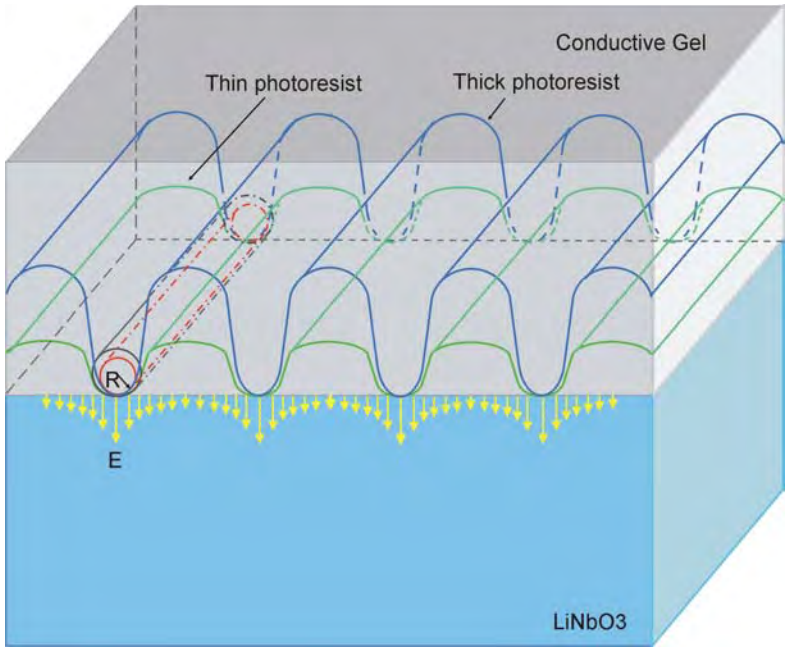


**Figure 4.21.** Schematic diagram of the dependence of the curvature radius *R* to the thickness of the patterned photo-resist for fine period PPLN gratings.

From Figure 4.21, it can be seen that when thicker photo-resist is used with the same mask, the curvature of the patterned electrode tips will become smaller. For a cylindrical insulator with a radius of *R* and uniform charge $Q_l$ per unit length, the relationship between the field strength and the radius can be expressed in Eq.(4.02).

$$E = \frac{Q_l}{4\pi\varepsilon_0 R} \qquad 4.02$$

Where *E* is the field strength; $Q_l$ is the charge per unit length on the surface of sample; $\varepsilon_0$ is the permittivity of free space; *R* is the radius of the cylindrical insulator. The field strength *E* on the surface of a cylindrical insulator is inversely proportional to the radius of curvature *R*. A small radius of curvature leads to a high fielder strength on the surface of the sample for a fixed potential. This may be reason that the 1.8μm thick photo-resist was better for poling fine period gratings.

### 4.4.6 Metal Electrodes

In the literature, two kinds of metal electrode poling methods are reported. One is direct metal electrode poling without an insulator covering layer [34], see Figure 4.22(a), another is insulator covering metal electrode poling which was adopted by the research group in Stanford University [31], see Figure 4.22(b). The metals used as the electrode for poling are various, while aluminium (Al) and nichrome (Ni-Cr, 80:20 weight percent) are the metals that have been used in the experiments in this thesis.

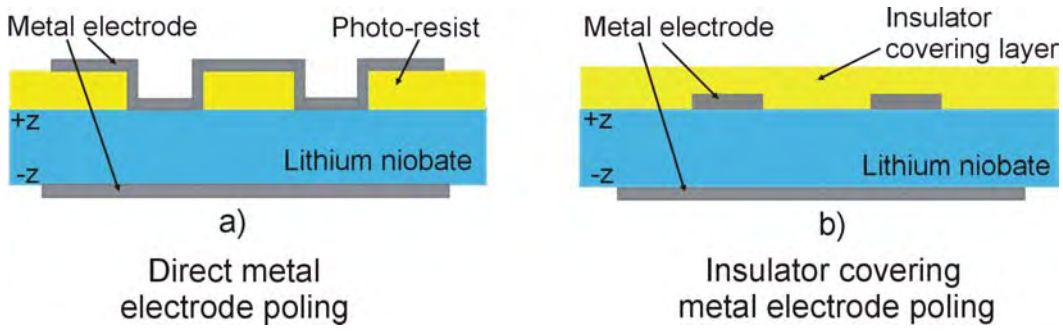


**Figure 4.22.** Schematic diagram of the two kinds of metal electrode poling methods. (a) Direct metal electrode poling method; (b) Insulator covering metal electrode poling method.

Metal evaporation on the surface of substrate is a standard process in the semiconductor industry, the target metal, Al or Ni-Cr, is put into a chamber and then the air is evacuated to around $5 \times 10^{-6}$ bar. Electrical current is used to heat the metal until it begins to evaporate. The evaporation rate and the thickness of the metal can be controlled by adjusting the current, in this experiment an Edwards Coater E306 was used to evaporate the Al and Ni-Cr, the relevant parameters are listed in Table 4.06.

**Table 4.06** The relevant parameters of Al evaporation

| Metal | Density | Acoustic impedance | Rate | Thickness |
|---|---|---|---|---|
| Al | 2.7 g·cm$^{-3}$ | $8.17 \times 10^5$ g·cm$^{-2}$s$^{-1}$ | 2-5 nm·s$^{-1}$ | 2μm |
| Ni-Cr (80:20) | 8.6 g·cm$^{-3}$ | $26.8 \times 10^5$ g·cm$^{-2}$s$^{-1}$ | 2-5 nm·s$^{-1}$ | 2μm |

The thickness of metal layer evaporated on the +z face of sample is 2μm. The final thickness of metal layer was measured by the Alpha Step, previous calibration shows that the final thickness is 200nm less than the thickness shown by Edwards Coater E306, so the final thickness of the metal electrode was around 1.8μm. During poling processes, the conductive gel is used to make sure that the metal layer on +z face fully contacts with the electrode circuit, conductive gel is still used as electrode on the –z face, see Figure 4.23.

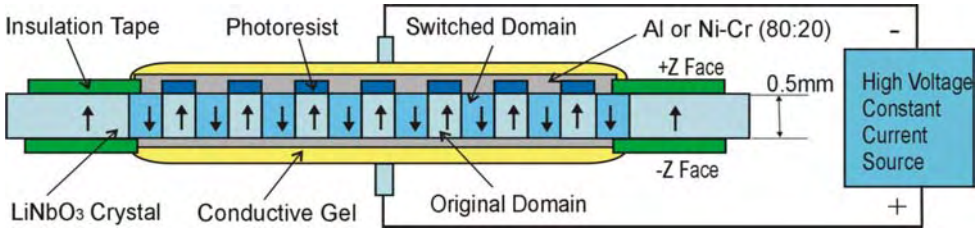


**Figure 4.23.** PPLN poled by using a metal electrode on the +*z* face and gel electrode on the –*z* face.

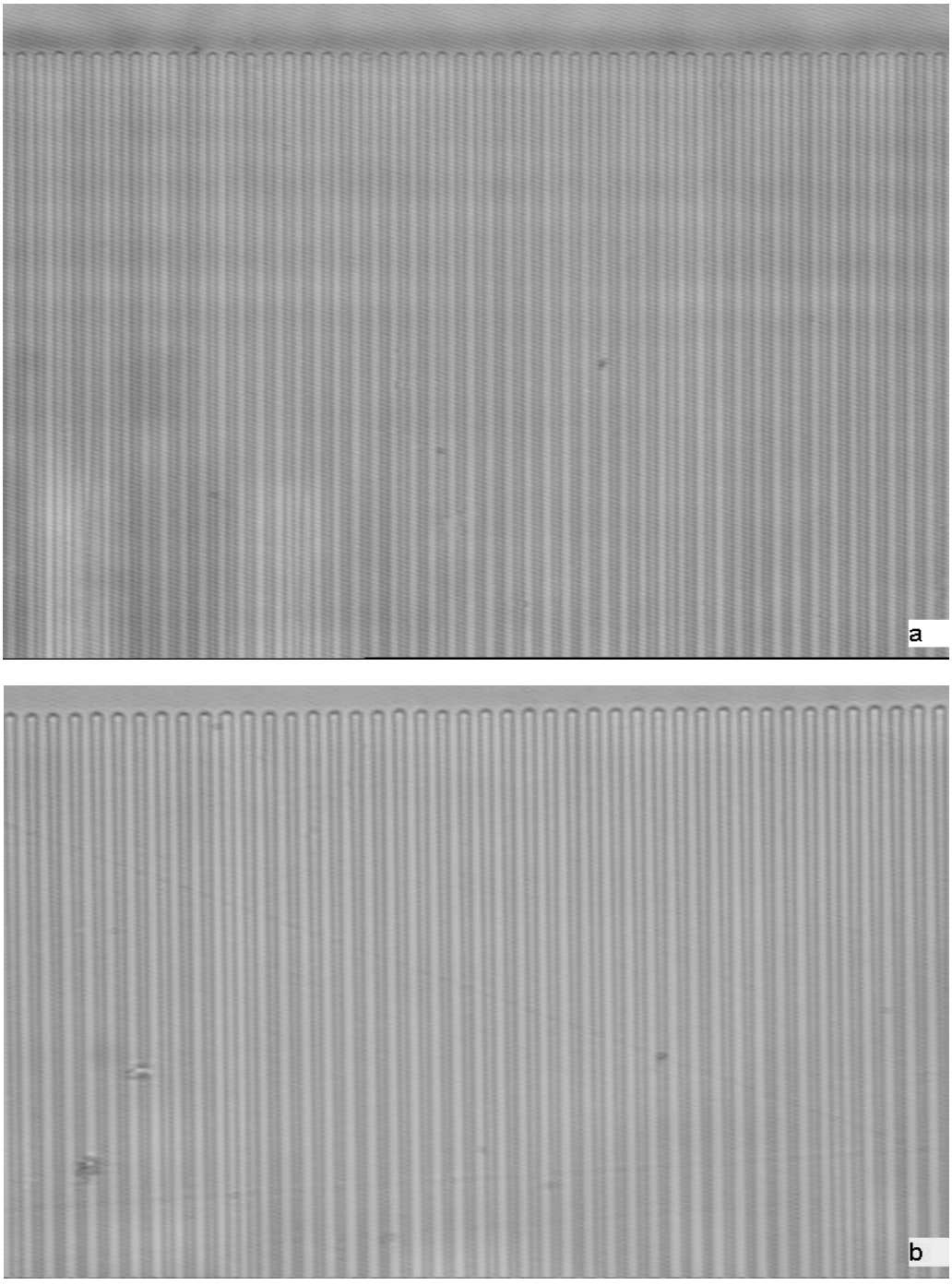


**Figure 4.24.** PPLN sample (code No.476 and No.477) with a 6.5μm period grating poled by using a metal electrode. (a) Al electrode; (b) Ni-Cr (80:20) electrode.

Figures 4.24(a) and 4.24(b) show PPLN with a 6.5μm period grating poled by Al and Ni-Cr electrodes respectively. Table 4.07 gives a comparison of the results of metal electrodes compared to gel electrodes.

**Table 4.07** PPLN quality comparison between two poling electrodes

| No. | Thickness (μm) | Exposure time (s) | Grating Λ (μm) | Electrode | Comments |
|---|---|---|---|---|---|
| 475 | 1.8 | 5.5 | 6.5 | Al | Small areas of over-poling |
| 805 | 1.8 | 8.5 | 30 | Al | Small areas of under-poling |
| 476 | 1.8 | 6 | 6.5 | Al | Some areas of over-poling |
| 807 | 1.8 | 9 | 30 | Al | Some areas of over-poling |
| 477 | 1.8 | 6 | 6.5 | Ni-Cr | Small areas of over-poling |
| 809 | 1.8 | 9 | 30 | Ni-Cr | Same areas of under-poling |
| 1000 | 1.0 | 6 | 6.5 | Ni-Cr & Insulator | Good poling with some grating stripes missing |
| 1001 | 1.0 | 7 | 6.5 | Ni-Cr & Insulator | Good poling with some grating stripes missing |
| 904 | 1.8 | 6 | 6.5 | Gel | Small amount of over-poling |
| 905 | 1.8 | 5.5 | 6.5 | Gel | Good poling |
| 906 | 1.8 | 8.5 | 30 | Gel | Small areas under-poled |
| 907 | 1.8 | 9 | 30 | Gel | Small areas overlapping |

The difference in the insulator covering metal electrode poling process is that the patterned metal grating is produced by a "lift off" technique (described in section 6.4.2 in chapter 6), and is then covered by the insulator. The idea is that the photo-resist (insulator) can suppress the domain wall propagation between the metal strips. A contact window must be opened so that all the metal gratings can contact with the liquid electrode or gel electrode. The details of this process are shown in Figure 4.25. The procedure is described from step A to step G.

A. After spin coating 1.3μm thick photo-resist, the sample was exposed under UV light (intensity of 8.2mW/cm$^2$) for around 6 second.
B. After UV exposure, the sample is placed in chlorobenzene for 4 minutes, then put into developer for around 2 minutes.
C. Evaporating a Ni-Cr (80:20) layer of 1um on the surface of the lithium niobate under conditions of $5\times10^{-6}\,bar$.

D. Soaking the samples in Acetone solution, the metal outside of the opening area is lifted off immediately, leaving the metal grating patterned on the sample.
E. Spin coating of 1.8μm thick photo-resist on the metal patterned surface, then baking the sample at a temperature of 90ºC for around 1 hour.
F. Opening the contact window around the edge of the metal grating so that the electrode can fully contact with each grating strip.
G. Poling the sample.

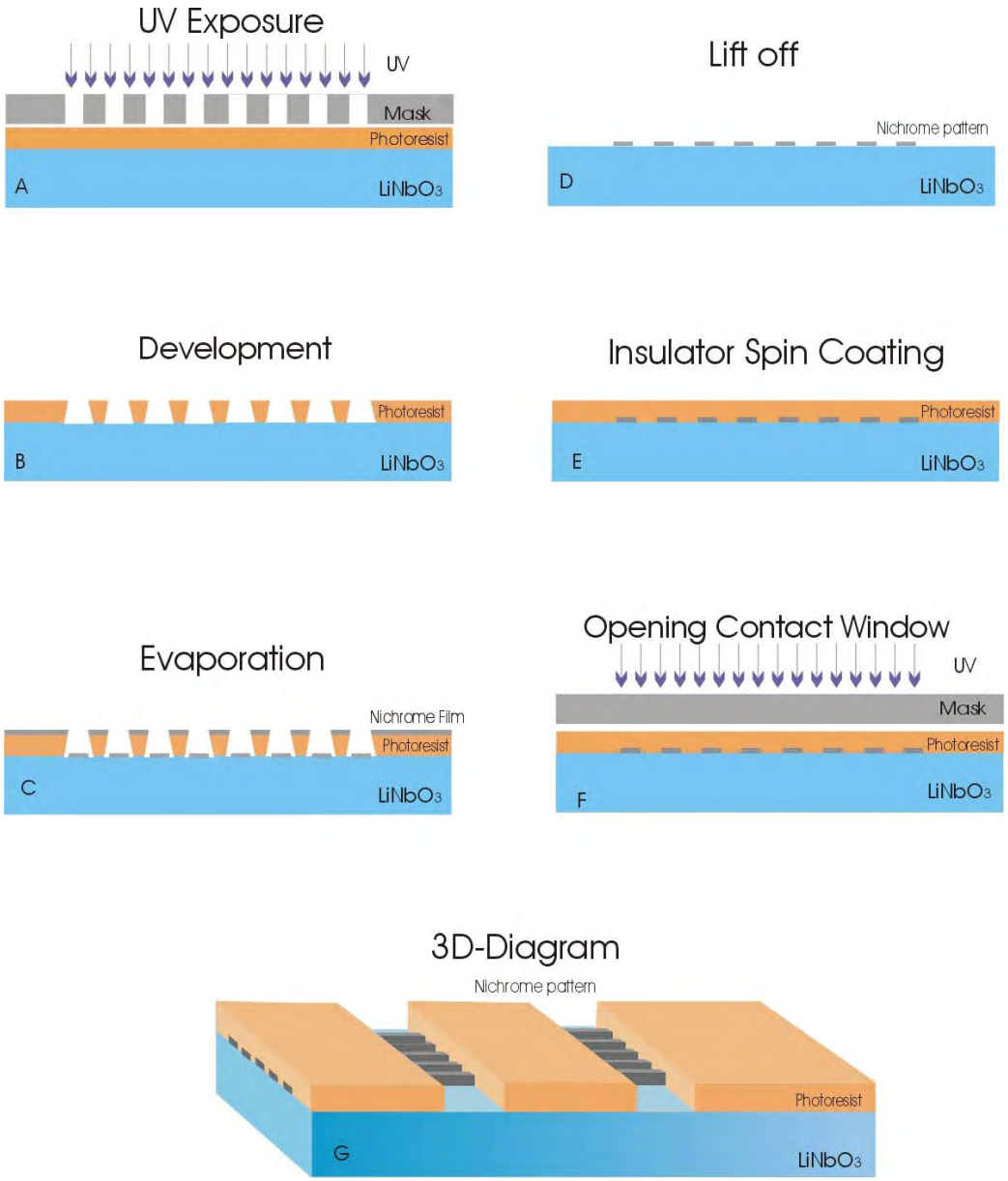


**Figure 4.25.** The insulator covering metal poling process.

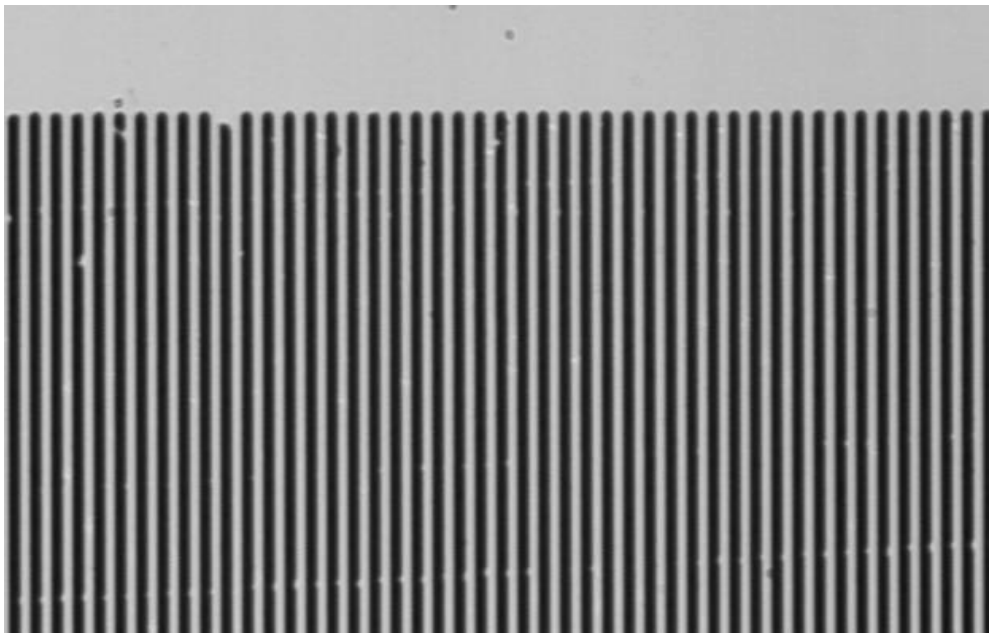

**Figure 4.26.** The metal grating pattern after “lift off” processing.

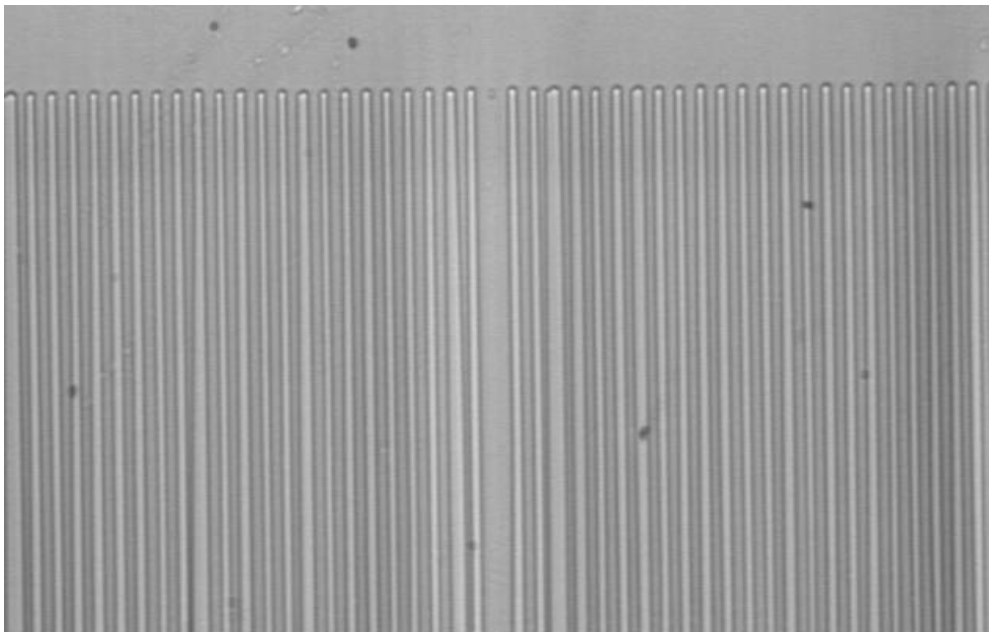

**Figure 4.27.** The poling result of a PPLN sample after wet etching, the sample was patterned with metal electrode using “lift off” technology.

Figure 4.26 shows the metal grating pattern after “lift off” processing. The dark stripes are patterned metal gratings, the rest of area is the uncovered area. Figure 4.27 shows the poling result obtained with this method after wet etching, from the figure we can see that one of domain strips was not switched due to non contact with the electrode.

In contrast to the gel electrode which is patterned on the –*z* face of sample, the metal electrode is patterned on the +*z* face. A suggested reason for this difference is that the density of nucleation spots formed on the +*z* face under the metal electrode is higher than that on the –*z* face of the sample. From the Table 4.07, it was also shown that there is little difference between gel and metal electrodes during the poling processes. However the gel method does show some advantages in the uniformity of the PPLN grating, this is because the quality of the Al electrode is dependent on the evaporation processes, such as the rate of deposition etc. Gel electrodes do not have this problem, and so this may be why the grating uniformity poled by Al electrodes is worse compared with those poled with gel. Another disadvantage of Al electrodes is that it is difficult to completely remove the Al film on the surface of the sample after poling, this Al remnant will affect the poling. However, Al electrodes do offer improved quality over gel electrodes when used in a backswitch poling experiment as discussed in the next section.

### 4.4.7 Backswitch Poling

Backswitch poling is a new poling method currently being investigated in some research institutes and universities [35,36], this involves forward poling a sample giving complete domain inversion and then re-poling it under the opposite electric field with the PPLN grating, see Figure 4.28.

The backswitch poling method have been successfully demonstrated for large periods, some reports regarding the PPLN of small periods (<5μm) poled by this method have been found recently [37]. This method enables higher fidelity and shorter period ($\Lambda \leq 4.5\mu m$) domain of 0.5mm thick, congruent lithium niobate crystal which can not be achieved with conventional poling methods.

According to the known hysteresis loop for lithium niobate, the coercive field required to invert a domain in a sample is $22kV \cdot mm^{-1}$. However it is known that after a domain has been inverted completely, if a sample was to be re-poled shortly after the initial inversion, a much lower coercive field would be required and the domains are inverted much more easily and uniformly. Figure 4.29(b) shows the current curve during the poling process. In the experiments on backswitch poling, the samples are patterned with a periodic grating of photo-resist S1813 on +*z* face (the thickness of

the photo-resist is 1.8μm), then 2μm thick Al film and 1μm thick of Al film was evaporated in on +*z* and –*z* face of the lithium niobate sample respectively. The relevant parameters are listed as following Table 4.08.

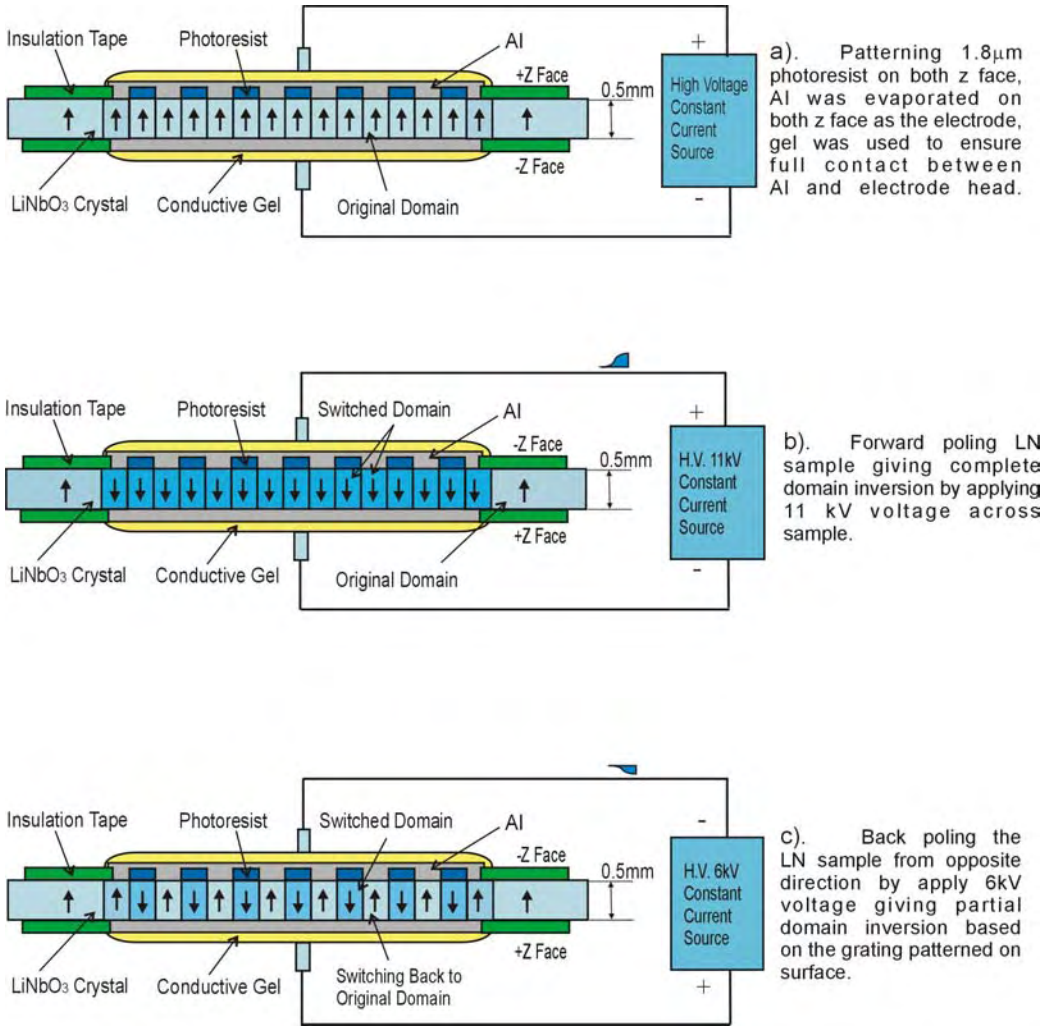


**Figure 4.28.** Backswitch poling by using Al electrode on both sides of *z* face.

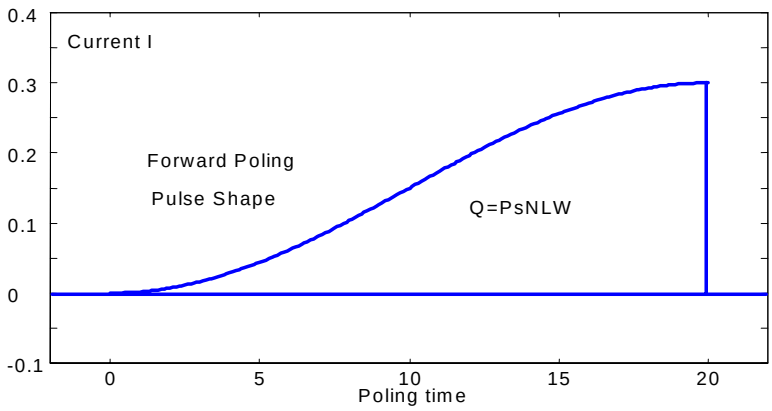


**Figure 4.29(a).** The current waveform of standard forward poling.

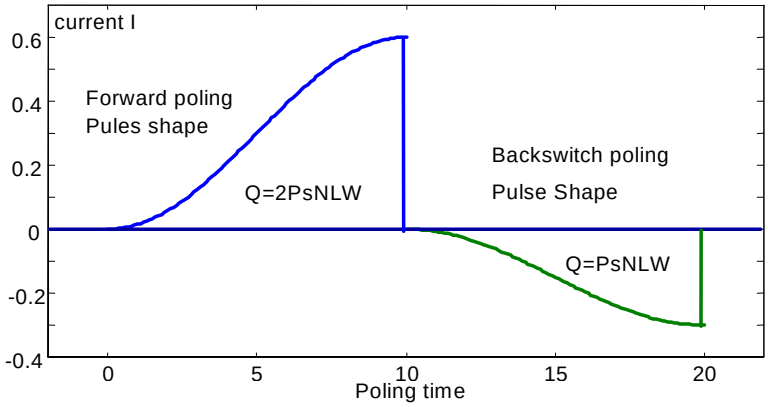


**Figure 4.29(b).** The current waveform of backswitch poling.

**Table 4.08** The relevant parameters of Al evaporation

| Metal | Face | Density | Acoustic impedance | Rate | Thickness |
|---|---|---|---|---|---|
| Al | +z | 2.7 g·cm$^{-3}$ | 8.17 × 10$^{5}$ g·cm$^{-2}$s$^{-1}$ | 2-5nm·s$^{-1}$ | 2μm |
| Al | -z | 2.7 g·cm$^{-3}$ | 8.17 × 10$^{5}$ g·cm$^{-2}$s$^{-1}$ | 2-4nm·s$^{-1}$ | 1μm |

After the preparation of the sample, an external electric field is then applied to the sample by means of standard poling procedures, a little gel is needed to make sure that the electrodes contact with the Al completely on the both sides of sample.

According to Eq.(4.01), the back switch poling involves the following two steps, see Table 4.09. The coercive field for forward and backward direction can be estimated from Figure 4.29 after compensating for the temporal variation in the bias field (the bias voltage is 3kV).

**Table 4.09** The charge and the coercive field of the forward and back switch poling

| Step | Poling processes | Charge required (μC) | Coercive field (kV/mm) |
|---|---|---|---|
| 1 | Forward Switch | $Q = +\int Idt = Ps \cdot 2A = 2Ps \cdot W \cdot L \cdot N$ | 22 |
| 2 | Backward Switch | $Q = -\int Idt = Ps \cdot A = -Ps \cdot W \cdot L \cdot N$ | 12 |

A backswitch poling current waveform, see Figure 4.29(b), is identical to the standard forward switch waveform-raising sine square ( $I = I_{\max} \sin^2(t)$ , where $I_{\max}$ is the maximum current), see Figure 4.29(a), from the start through to the end of forward poling stage, however unlike standard poling, the forward poling stage is sustained until the domains have fully inverted. After completion of the forward poling phase,

the external electric field changes direction, and the backswitching stage starts. This process is stopped when half of the domains are inverted. The whole process is controlled by a computer program coded in VB5.0 with pre-set parameters and pre-determined current pulse shape. The measured oscilloscope traces of current and voltage vs. time during the backswitch poling processes are recorded as Figure 4.30. The poling results for gratings of 30μm and 6.5μm period are shown in Figure 4.31 and Figure 4.32.

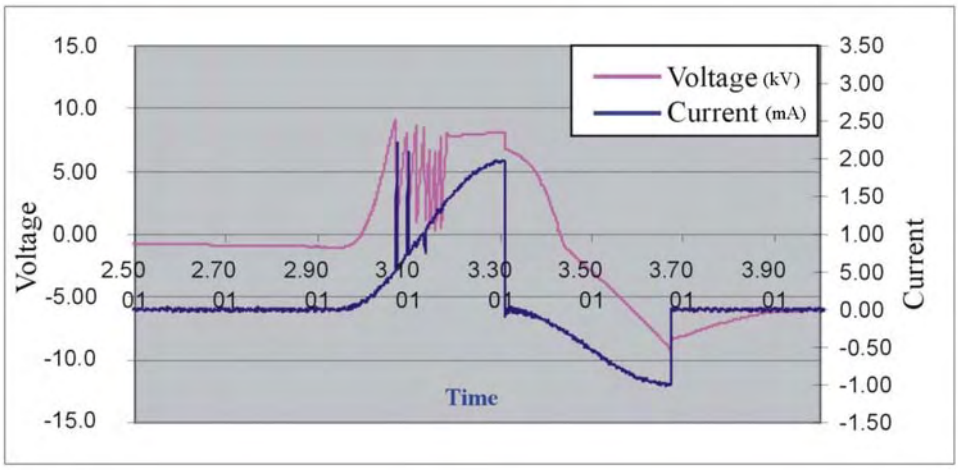


**Figure 4.30.** Oscilloscope curve of a backswitch poling wave from 0.5mm thick $LiNbO_3$. The blue line is the curve of current vs. time, the pink line is the curve of voltage vs. time.

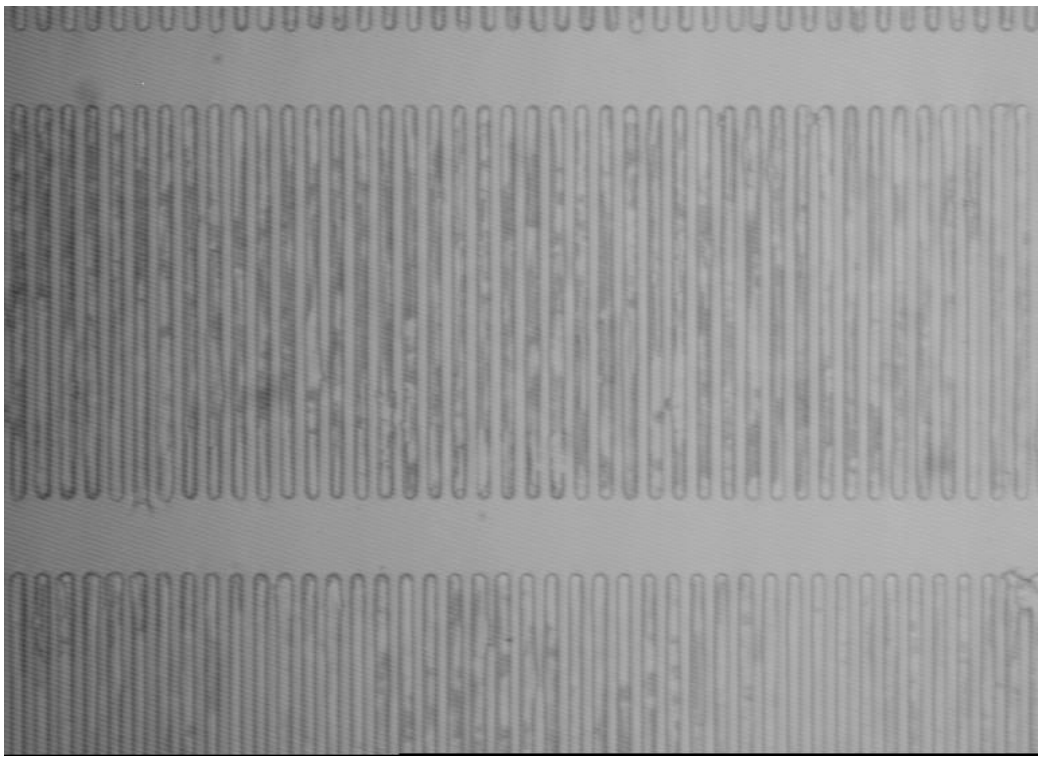

**Figure 4.31.** PPLN sample (code No.701) with a 30μm period grating poled by the backswitch method, the thickness of the photo-resist S1813 was 1.8μm. The Al thickness was 2.0μm on the +*z* face and 1.0μm on the –*z* face. A good quality grating was obtained.

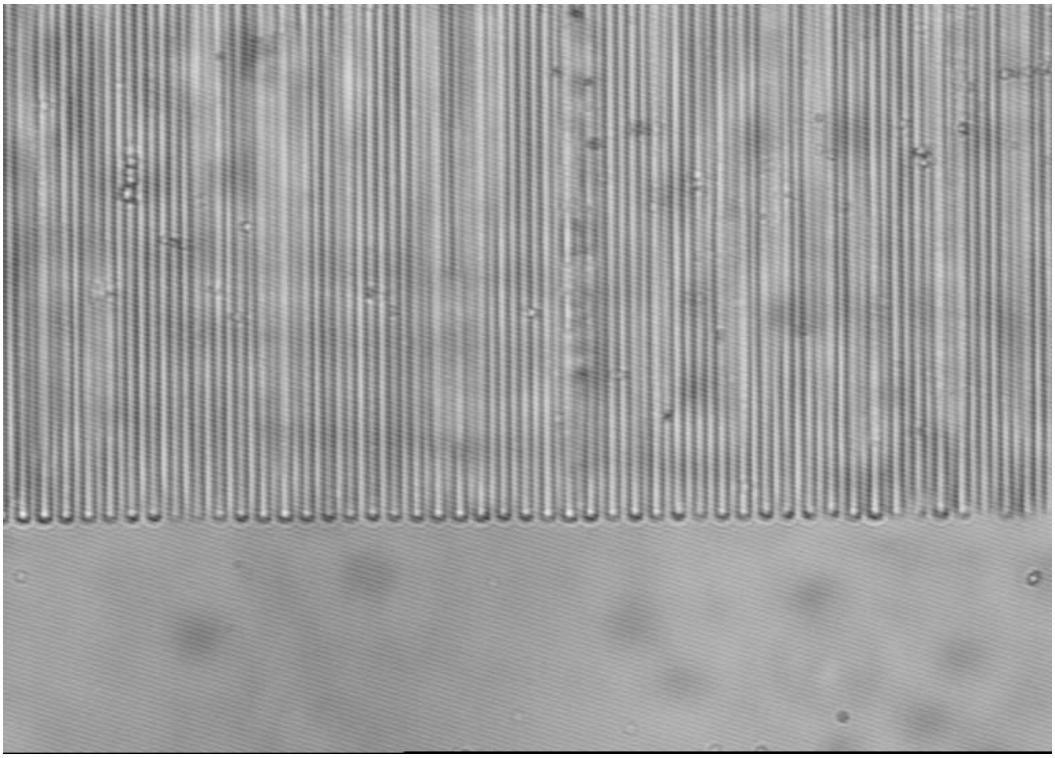

**Figure 4.32.** PPLN sample (code No.700) with a 6.5μm period grating poled by the backswitch method, the thickness of the photo-resist S1813 was 1.8μm. The Al thickness was 2.0μm on the +*z* face and 1.0μm on the –*z* face. The quality of the PPLN with fine periods was also good.

Through viewing the sample under crossed polarizers, it was observed that the grating domains on the -*z* face and the +*z* face were different. On the +*z* face, the inverted domains could be clearly viewed through the crossed polarizers (see Figure 4.33(a), where the grating domains are clear and the edge of the grating is sharp), but on the –*z* face, the pattern of inverted domains is dim and blurred, see Figure 4.33(b).

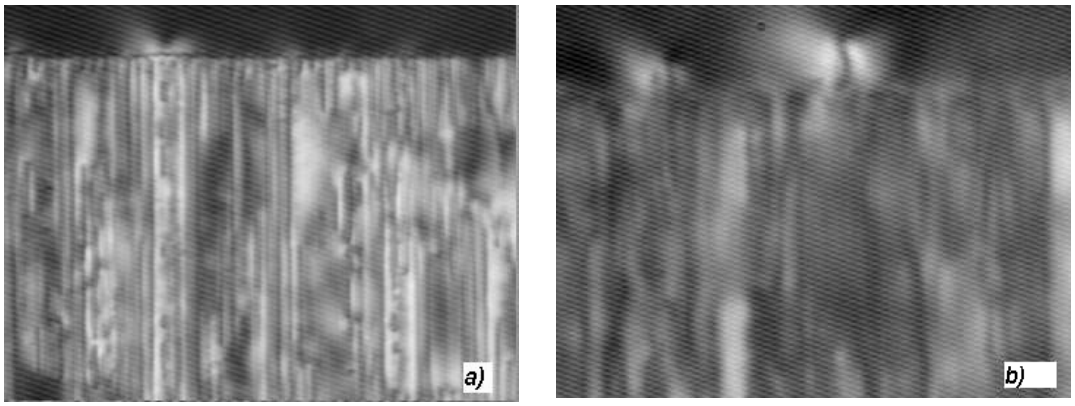


**Figure 4.33.** Views of the sample with 6.5μm period domains in backswitch poled 0.5mm thick $LiNbO_3$ through crossed polarizers. (a) View of the +*z* surface; (b) View of the -*z* surface.

In order to investigate the quality of grating along the *z* axis direction, the samples were cut along the *x*-axis and polished. Figure 4.34 shows that the periodically poled domains observed on the +*z* face of sample were not completely formed throughout the thickness of the crystal. On the +*z* face where the domains begin to form, the uniformity of grating domains is good, see Figure 4.34(a) and 4.34(c), however as the domain tips propagate through the crystal along the *z*-axis toward the –*z* face, the isolated domains began to merge together. When the domain tips nearly reach the –*z* face, they take on a sharp shape (like a needle tip), resulting in bad or random poling at the –*z* face, see Figure 4.34(b) and 4.34(d). The mechanism behind this effect is not well understood, and has not been investigated within the scope of this project.

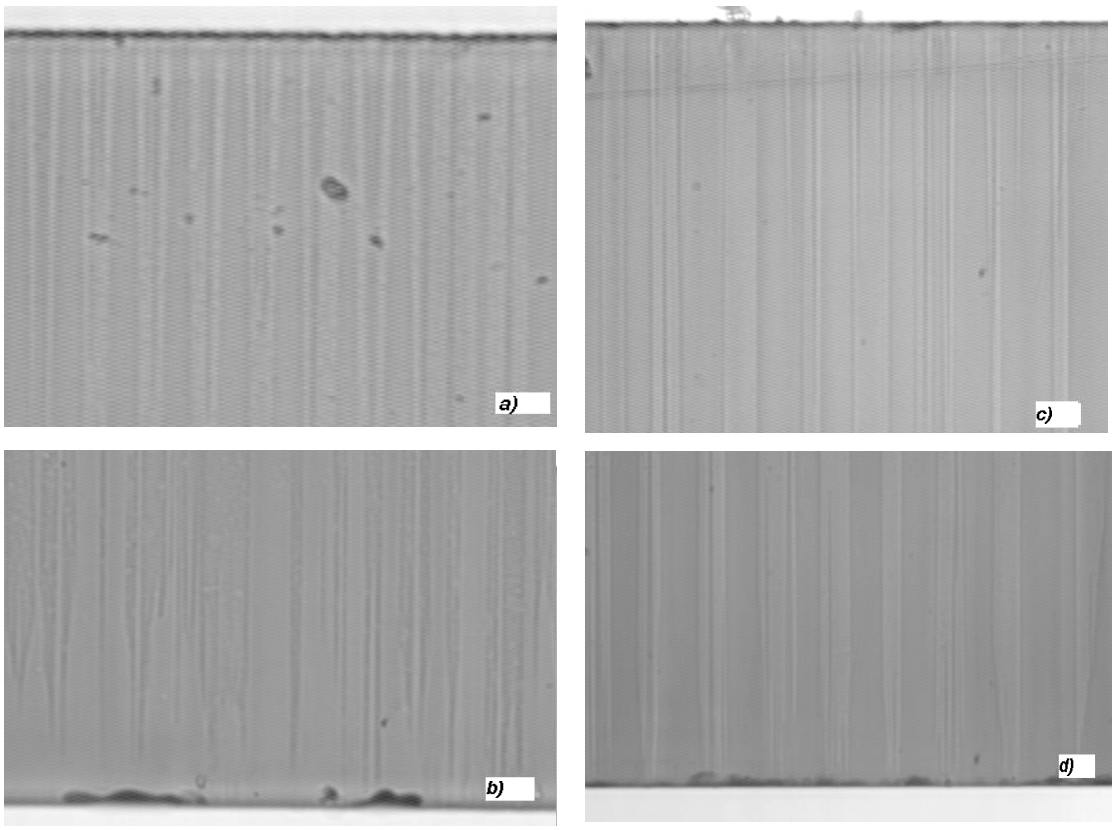


**Figure 4.34.** Domain structures formed by backswitch poling in 0.5mm thick $LiNbO_3$ with a 6.5µm period and a 30µm period grating from the *y* face. (a) The *y* face view of 6.5µm period PPLN (the top is the +*z* face); (b) The *y* face view of the 6.5µm period PPLN (the bottom is the -*z* face); (c) The *y* face view of the 30µm period PPLN, (the top is the +*z* face); (d) The *y* face view of the 30µm period PPLN, (the bottom is the -*z* face).

Backswitch poling in $LiNbO_3$ enables higher fidelity and shorter period domain patterning ( $\Lambda$ <4.5µm) on lithium niobate than that can be achieved with conventional poling [37]. Future work could include the investigation of the poling mechanism and

control of it through variation of the duty cycle of the electrodes and duration of backswitching.

## 4.5 Periodic Poling of Magnesium-oxide-doped Lithium Niobate

According to Bryan *et al.'s* research, the photoconductivity of MgO:$LiNbO_3$ increases a hundred-fold as compared to that of un-doped congruent lithium niobate [38]. Since the photorefractive index change is proportional to the ratio of the photo-galvanic current to photoconductivity [39], MgO:$LiNbO_3$ has a higher photorefractive damage threshold. In addition, it also appears that MgO:$LiNbO_3$ has much lower green-induced infrared absorption (GRIIRA) than does lithium niobate. These features are very important in green and blue light generation by second harmonic generation as photorefractive damage and GRIIRA limit the available second harmonic power. There have been several reports of blue light generation by periodically poled MgO:$LiNbO_3$ (PPMgLN), both in bulk [40,41,42] and waveguide [43,44,45,46] devices. In September 2001, Matsushita Electric Industrial Co., Ltd announced that it had developed a high power, high efficiency SHG blue laser ready for use in next-generation optical disc recording systems, the key element inside is a PPMgLN waveguide.

The low coercive field makes it possible to make thick PPMgLN crystals. According to reports from Kurimura *et al.*, [47] the external electric field for domain inversion is around 4.45 $kV \cdot mm^{-1}$. Periodic poling of 1mm thick MgLN was recently reported by Hirano *et al.* [48] A high average power optical parametric oscillator using PPMgLN and operated at room temperature was demonstrated, in which the material showed high resistance against the photorefractive effect [49]. A comparison of the main differences in properties between pure lithium niobate and Mg doped lithium niobate is listed on Table 4.10. The data is from Casix Inc [50].

**Table 4.10** The comparison of the main properties between pure $LiNbO_3$ and MgO: $LiNbO_3$.

| **Material** | **Congruent $LiNbO_3$** | **MgO:$LiNbO_3$ (5mol%)** |
|---|---|---|
| Coercive Field $E_C$ ($kV \cdot mm^{-1}$) | >20.5 | >4.45 |
| Transparency Window (nm) | 400-5200 | 340-5000 |
| NLO Coefficients $d_{33}$ ($pm \cdot V^{-1}$) | 30.8 | 31 |
| Damage threshold ($MW \cdot cm^{-2}$) | 30 (10ns, 1064nm) | 100 (10ns, 1064nm) |

The 0.5mm thick MgO:$LiNbO_3$ (5mol%) samples were poled at room temperature (20ºC) by our standard electric-field method in order to check that a suitable poling curve can be seen, Figure 4.35 shows the voltage and the current curve:

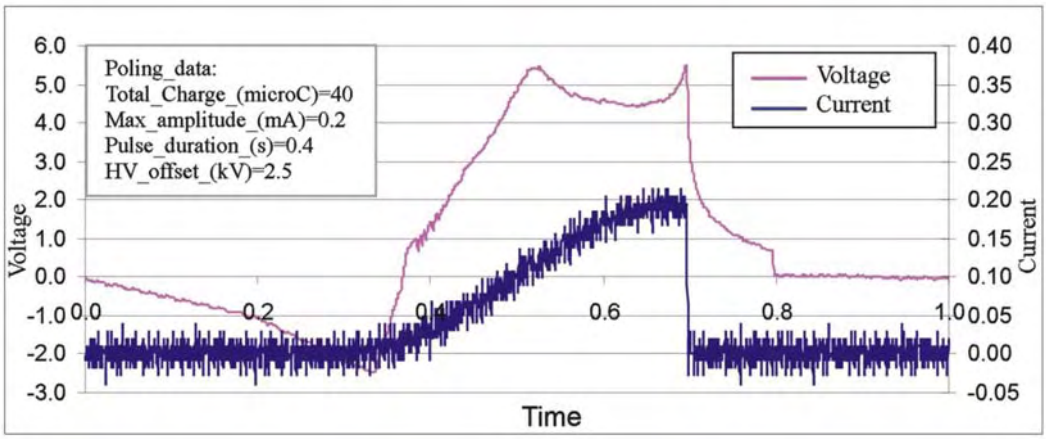


**Figure 4.35.** Oscilloscope traces of poling wave form for 0.5mm thick MgO: $LiNbO_3$. The blue line is the trace of current vs. time, the pink line is the trace of voltage vs. time.

From the above curve, we can find out that the domain starts to switch around 2.2-3.3kV, the result indicates that the coercive field is around 4.5-6.6kV·$mm^{-1}$ for MgO:$LiNbO_3$. Samples with different grating periods and patterns were poled at different temperatures, the parameters of the sample were listed in Table 4.11.

**Table 4.11** The parameters and Mg:LN poling sample:

| Sample code No. | Grating shape | Grating Λ (μm) | Electrode material | Pattern surface | Poling temp. (ºC) | Result & comment |
|---|---|---|---|---|---|---|
| PPMgLN-01 | Normal | 10 | Ni-Cr | +*z* | 25 | Broken-down |
| PPMgLN-02 | Spot | No period | Gel | -*z* | 25 | *Ec*=9kV/mm |
| PPMgLN-03 | Hexagon | 18.3 | Gel | -*z* | 25 | Good |
| PPMgLN-04 | Spot | No period | Gel | -*z* | 25 | *Ec*=12kV/mm |
| PPMgLN-05 | Normal | 18.5-23 | Ni-Cr | +*z* | 25 | Over-poled |
| PPMgLN-06 | Normal | 18.5-23 | Gel | -*z* | 25 | Not good |
| PPMgLN-07 | Normal | 18.5-23 | Al | +*z* | 25 | Not good |
| PPMgLN-08 | Normal | 27-35 | Al | +*z* | -20 | Not poled |
| PPMgLN-09 | Normal | 18.5-23 | Al | +*z* | 25 | poor |
| PPMgLN-10 | Spot | No period | Gel | -*z* | 25 | *Ec*=11kV/mm |
| PPMgLN-11 | Normal | 18.5-23 | Al | +*z* | 25 | Broken-down |
| PPMgLN-12 | Normal | 27-35 | Al | +*z* | -85 | Broken-down |
| PPMgLN-13 | Normal | 10 | Gel | -*z* | 25 | Over-poled |
| PPMgLN-14 | Normal | 6.0 | Gel | -*z* | 25 | Good |

Figure 4.36 shows the poling result of MgO:$LiNbO_3$ samples after wet etching under the microscope. The periodic domain inversion was fairly uniform over the poled area for narrow gratings as well as for 2-D hexagonal cell grating. More detail on the poling of 2-D hexagonally poled grating is discussed in following section.

As is seen from the Figure 4.36, some domain walls were not straight. Possible reasons for the over-poling and non-straight domain walls is that the velocities of domain wall (which is depends on the temperature and applied external electric field) along the *x* and *y* direction are more similar in MgO:$LiNbO_3$ than that in normal $LiNbO_3$ (where the velocity of the domain wall along *y* direction is faster than that along the *x* direction under a high electric field), the detailed relationship between temperature and domain wall velocity is not clear at moment, it needs to be investigated in future work.

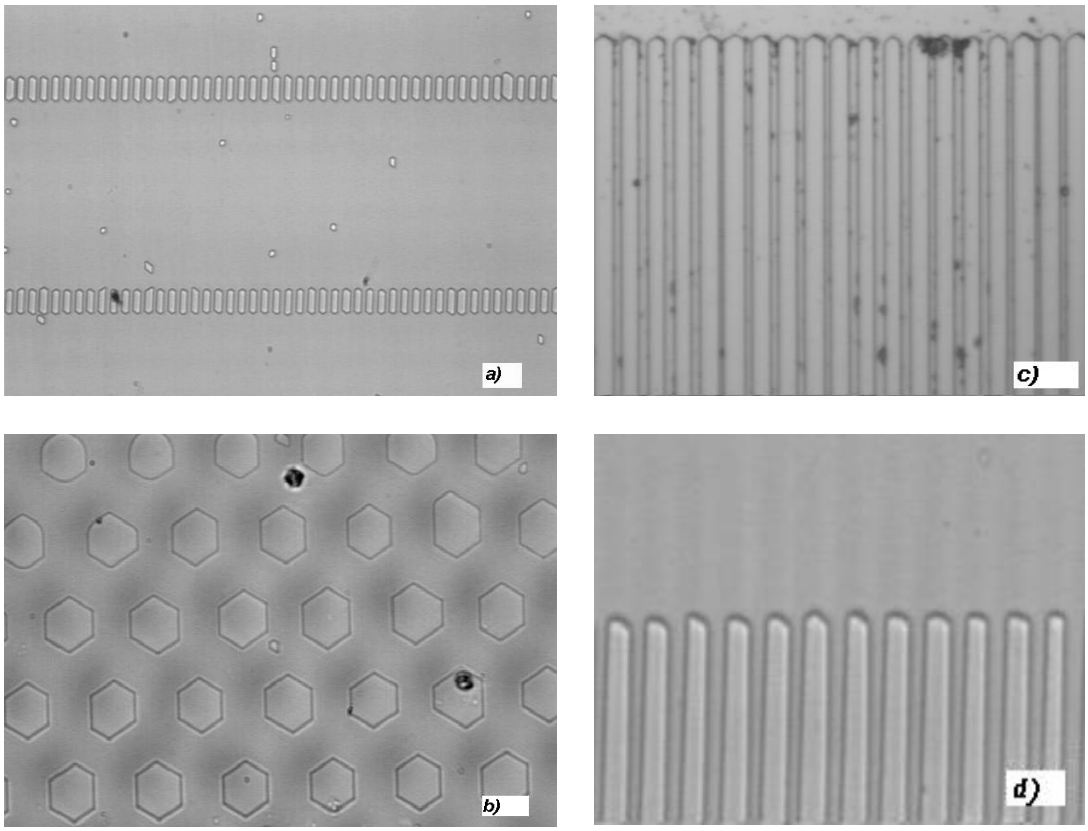


**Figure 4.36.** Domain structures of a PPMgLN poled sample with 0.5mm-thickness. (a) The –*z* face view of a 6.5μm period PPMgLN; (b) The +*z* face view of PPMgLN with 2-D hexagonal cell gratings of 18.3μm period; (c) The –*z* face view of 18.5μm period PPMgLN; (d) The +*z* face view of 10μm period PPMgLN.

## 4.6 Hexagonally Poled Lithium Niobate

The research reported in this section was carried as part of a study into 2-dimensional nonlinear crystals by Dr. Katia Gallo and Dr. Radu Bratfalean in the ORC. Using the same poling fabrication method for PPLN outlined in this chapter but with hexagonal inverted domains, hexagonally poled lithium niobate (HexLN) samples with a spatial period $\Lambda$=18.05μm were fabricated. In this work the HexLN samples were fabricated by the author of this thesis, while the waveguides were fabricated and characterized by Dr. Gallo, Dr. Radu Bratfalean. The use of planar waveguides is attractive for HexLN as the full 2-D nature of HexLN can be exploited.

### 4.6.1 Introduction

Normal nonlinear frequency conversion in PPLN gratings is achieved through quasi-phase-matching by inverting the sign of the nonlinearity periodically in one dimension. In 1998 nonlinear frequency conversion in 2-dimentional nonlinear photonic crystals was suggested and theoretically studied by Berger [51]. Such a crystal has a 2-dimensional periodically switched nonlinear susceptibility. Figure 4.37 shows the reciprocal lattice. The existence of lattice vectors in multiple directions allows for quasi-phase-matching along different paths, as indicated for two cases in Figure 4.37, and for different harmonics simultaneously.

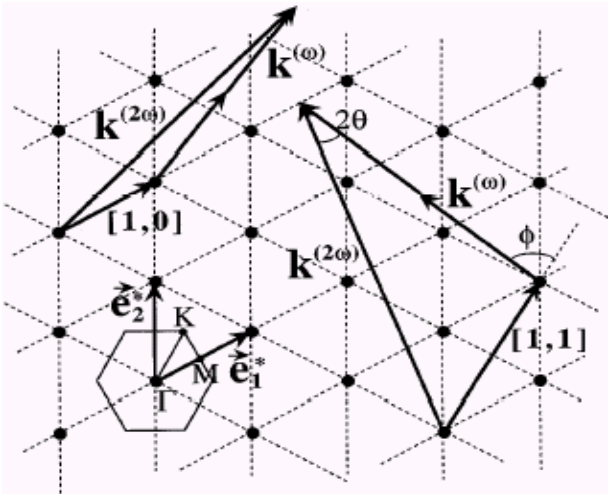


**Figure 4.37.** Reciprocal lattice of HexLN structure showing two different QPM processes [51].

The first example of a 2D nonlinear photonic crystal (NPC) was demonstrated in lithium niobate by N. Broderick *et al.* in the Optoelectronics Research Centre (ORC) [52]. Several experiments carried out in bulk HexLN crystal have shown multiple

harmonic generation (red, green and blue) and SHG with an enhanced tuning range [53,54]. In addition other researchers have demonstrated simultaneous wavelength interchange using a HexLN structure [55].

### 4.6.2 Fabrication of Hexagonally Poled Lithium Niobate

First of all, a thin layer of photo-resist S1813 was deposited onto the -*z* face of a *z*-cut 500μm thick, congruent $LiNbO_3$ crystal, then the hexagonal array with a spatial period $\Lambda$ = 18.05μm was patterned by the processes described in this chapter. The pattern was then transferred to the sample by applying an electric field. Figure 4.38 shows the HexLN sample after wet etching and its calculated reciprocal lattice.

To provide planar confinement and thus higher optical intensities, planar waveguides were produced by Dr. Gallo using proton exchange. After poling, the samples were cleaned and the planar buried waveguide was fabricated on the HexLN sample, via the sequence of proton exchange, annealing and reverse proton exchange [56]. The detailed fabrication procedure is listed in the Appendix B.

After fabrication, the sample was cut and polished on the ±*x* faces of the HexLN waveguide allowing a propagation length of 14mm through the crystal in the *x* axis direction.

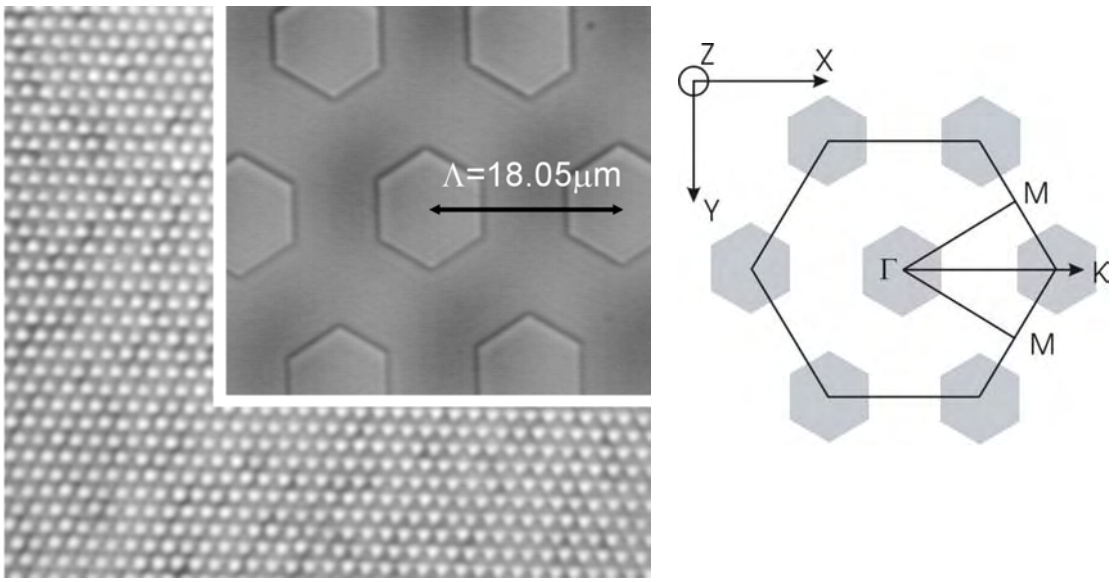


**Figure 4.38.** HexLN crystal (left) and its reciprocal lattice (right), the period of the hexagon cell is 18.05μm and is uniform over the whole sample. The inset figure is an enlarged picture. The propagation of the pump beam was in the ΓK direction.

### 4.6.3 Characterization

The characterization of the HexLN waveguide was carried out by Dr. Katia Gallo, Dr. Radu Bratfalean. Figure 4.39 shows the schematic diagram of the experimental setup they used to characterize the response of the buried HexLN planar waveguides. A pulsed laser source producing 5ns pulses at 1.536μm using an Erbium Doped Fibre Amplifier (EDFA) chain, seeded by an externally modulated laser diode, was used. It had an adjustable repetition rate from 1kHz to 500kHz, and a peak power of up to 20kW. The HexLN waveguide was placed in a computer controlled oven (maintained at a temperature beyond 100ºC) in order to avoid photorefractive effects, the pump laser incidence angle was adjusted by rotating the stage on which the oven was mounted. The pump beam was shaped into an ellipse by using a cylindrical lens (focal length: $f$ = 20cm) before being focused into the planar waveguide through ×10 objective lens.

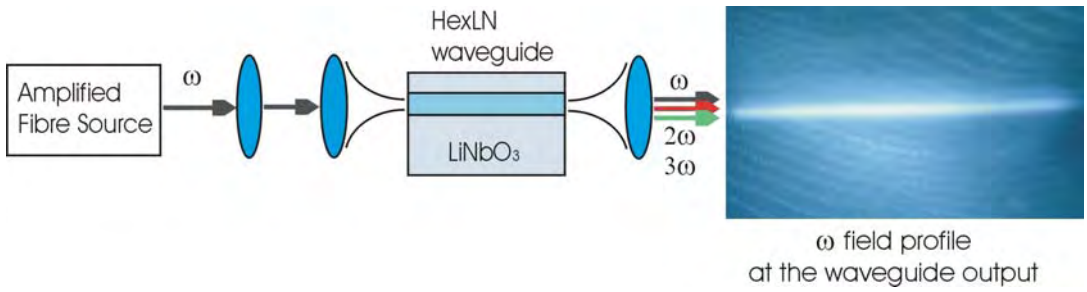


**Fig. 4.39.** Experimental setup used to measure the response of the HexLN waveguide. The source consists of a CW diode laser the output of which is externally modulated and amplified by cascade of several fibre amplifier stages. The inset shows an image of the intensity of the TM0 mode at the pump frequency (ω), taken at the waveguide output.

The fundamental beam was coupled into either the bulk of the HexLN or the planar waveguide by moving the translation stage. When moving from the waveguide to the bulk the angle at which the second harmonic beam was emitted altered and at the same time an increase in the generated red (2ω) and green light (3ω) was apparent.

Figure 4.40(a) shows the internal SHG conversion efficiency $\eta_{SHG}^{internal}$, calculated as the ratio of the average powers of $P_{2\omega}$ at the SHG output to the average power $P_{\omega}$ of fundamental beam at the input of the waveguide, as a function of $P_{\omega}$ for a given pump incidence angle. Figure 4.40(b) shows a typical average SHG power via temperature tuning curve of the HexLN waveguide. The maximum SHG power was recorded at 138$^{o}$C, the "shoulder" at lower temperatures corresponds to the beam getting into the bulk, while the rapid decay of the SHG signal at higher temperatures corresponds to

the beam scattering into the upper cladding (air). The temperature tuning curve is not symmetrical, it was believed that the thermal expansion of the oven contributed to the asymmetry of the tuning curve, as the vertical position of the input beam changes when the temperature is varied.

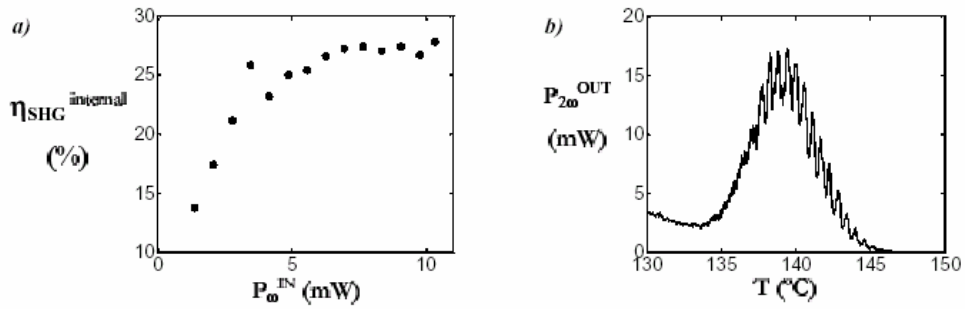


**Figure 4.40.** (a) SHG internal efficiency $\eta_{SHG}^{internal}$ as a function of the average power of $P\omega$ at frequency ω coupled in the waveguide measured for a given pump incidence angle at a 1 kHz pulse repetition rate; (b) Average power of the SHG at the output measured as a function of temperature.

This work shows promise that the SHG response of a planar HexLN waveguide can provide useful information on the properties of both the 2D nonlinear grating and the waveguide, which would allow a further joint optimization of the HexLN and waveguide for maximum efficiency. However these are only preliminary results and considerable score still exists for optimization, the guided-wave configuration appears well suited to fully exploiting the capabilities of HexLN for both telecommunication and fundamental physics.

## 4.7 Periodically Poled Lithium Tantalate

The research reported in this section was carried as part of research done by A. A. Lagatsky *et al*. in the University of St-Andrews. PPLT samples with periods ranging from 7.0μm to 7.619μm were fabricated by the author.

### 4.7.1 Introduction

Lithium tantalite ($LiTaO_3$) is also widely used for quasi-phase-matching (QPM) devices by periodically poling the crystal [57]. Its optical, nonlinear optical and electro-optical properties are similar to those of $LiNbO_3$ crystals but $LiTaO_3$ has a better short wavelength transparency, which extends as short as 280nm ($LiNbO_3$ is transparent from 340nm) [58], it has a higher damage threshold (>500 $MW \cdot cm^{-2}$ for

ns pulsed), also, it has large nonlinear susceptibilities and high resistance against photorefractive damage.

By using the same poling equipment described in this chapter but with a newly designed PPLT mask, PPLT bulk samples with periods ranging from 7.0μm to 10μm were fabricated, the interaction length was around 3.5mm, over 100mW of green light from 300mW of fundamental power was generated. The pulse duration was less than 150fs, and 40% conversion efficiency was obtained.

### 4.7.2 Properties of Lithium Tantalate

The properties of congruent lithium tantalate are similar to those of lithium niobate, see Table 4.12. The domain wall shape and the nucleation density for domains are different in lithium tantalate [59] compared with lithium niobate, thus the fabrication procedure of PPLT is slightly different compared with that of PPLN.

**Table 4.12** The main properties of the lithium tantalate and lithium niobate [60]

| Item | Lithium tantalate | Lithium niobate |
|---|---|---|
| Melting Point | 1650°C | 1253°C |
| Crystal System | Trigonal | Trigonal |
| Point Group | 3m | 3m |
| Lattice parameters (hexagonal), A° | a = 5.154, c = 13.784 | a = 5.148, c = 13.863 |
| Crystal Density, $kg \cdot m^{-3}$ | $7.465 \times 10^3$ | $4.647 \times 10^3$ |
| Curie Temperature ($T_C$),°C | 603.5 ± 5.5 | 1133 ± 3 |
| Congruent Composition, mol% $Li_2O$ | 48.38 | 48.38 |
| Nonlinear Optical Coefficients at 1.06μm, $\times \lvert d_{36}^{KDP} \rvert$ | $d_{22} = 4.4, d_{31} = -2.7, d_{33} = -60$ | $d_{22} = 6.5, d_{31} = -12.3, d_{33} = -86$ |
| $n_o$ at 632.8 nm (TE mode) | 2.1787 | 2.2880 |
| $n_e$ at 632.8 nm (TM mode) | 2.1821 | 2.2030 |
| Optical Transmission (1cm length), nm | 280 -5000 | 340 - 4600 |
| damage threshold (10ns, 1064nm), $MW \cdot cm^{-2}$ | > 500 | >100 |
| Nucleation domain shape | Triangular shape | Hexagonal shape |
| coercive field, $kV \cdot mm^{-1}$ | 21-23 | 20.5-22 |

The Curie temperature of the lithium tantalate is far lower than that of lithium niobate, this is a disadvantage for waveguide fabrication by using thermal indiffusion, for

example, for Ti indiffused waveguides or Zn indiffused waveguides. The optical transmission range of lithium tantalate extends as short as 280nm, this is very attractive property for UV light generation compared with that of lithium niobate, see Figure 4.41 [ 60 ]. Earlier experiments have demonstrated 340nm UV SHG by frequency doubling of a laser diode in a second-order QPM with a duty cycle (mark-space ratio) of 75% [61].

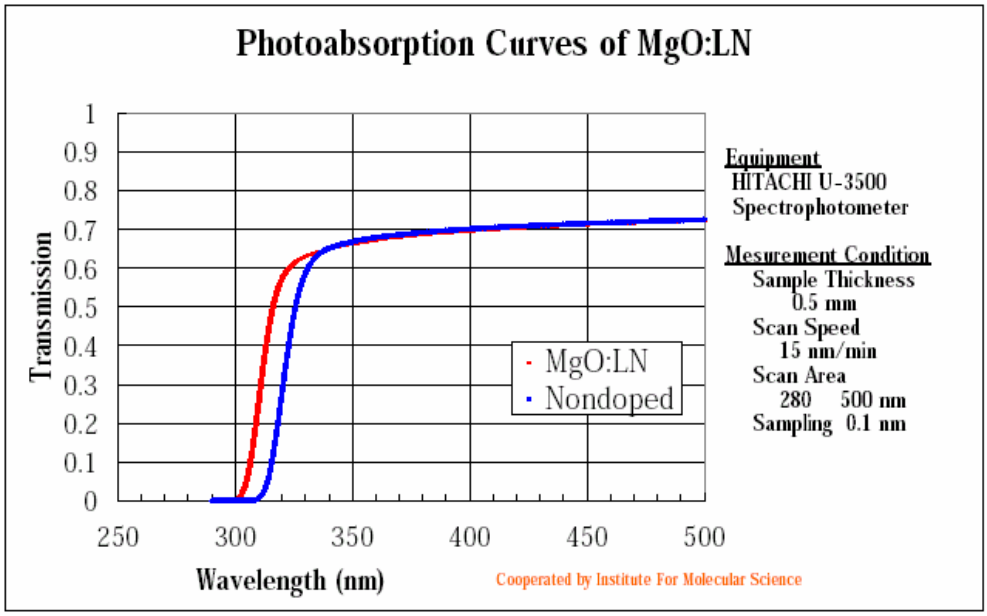


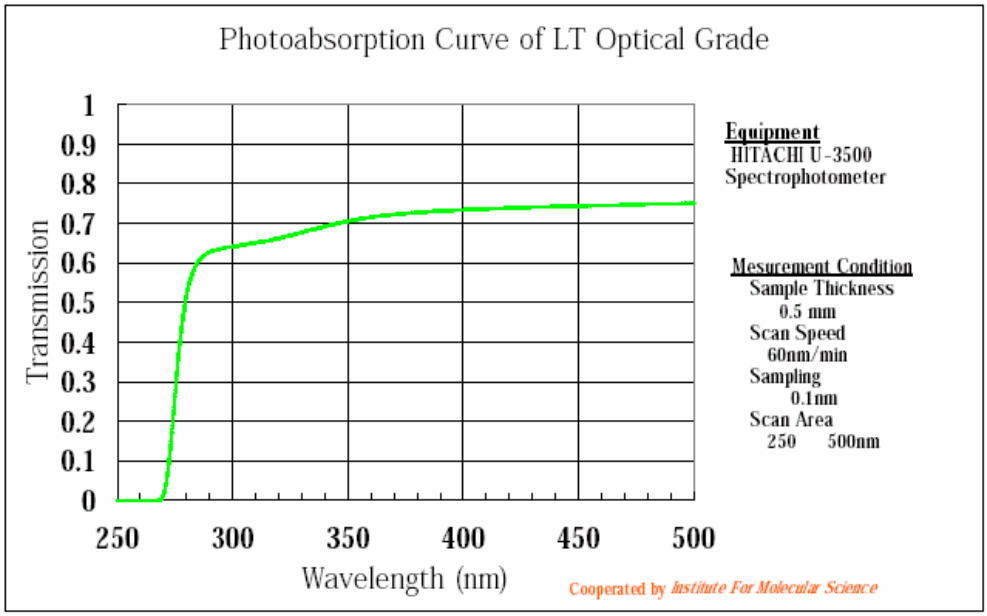


**Figure 4.41.** The transmission range of the lithium niobate (top curve), and of the lithium tantalate (bottom curve) with orientation of *x*-direction [60].

The domains poled in lithium tantalate have a triangular shape, see Figure 4.42 (left-side picture), as opposed to the hexagonal shape of domains in lithium niobate, see

Figure 4.42 (right-side picture). So it is difficult to obtain straight domain walls (at least on one side wall of the switched domains). This is particularly true in the regions deep under the patterned electrodes. However the domain walls of the isolated switched domains seem less likely to touch each other, and thus the domains have much less tendency to merge compare with the hexagonal shape of the domain in lithium niobate.

The direction of the domain grating vector *k* relative to the axis of the crystal has a significant influence on the poled domain wall quality, the triangular domain shape of the test sample poled under high electric field and its crystal axis are shown in left side of Figure 4.42, The domains were revealed by etching in hydrofluoric acid (HF, 48%) for 10 minutes at room temperature.

For *z*-cut lithium tantalate crystals, it was observed that one side of the switched triangular domain wall is straight and parallel to *x* axis, while the other two sides of the triangular domain wall are ±30º relative to the -*y* axis, see the left side of Figure 4.42, therefore the vector *k* of domain grating should be parallel to the *y* axis (in contrast to PPLN where the vector *k* of domain grating should be parallel to the *x* axis, see right side of Figure 4.42), thus this orientation has been used for fabricating crystals used in devices.

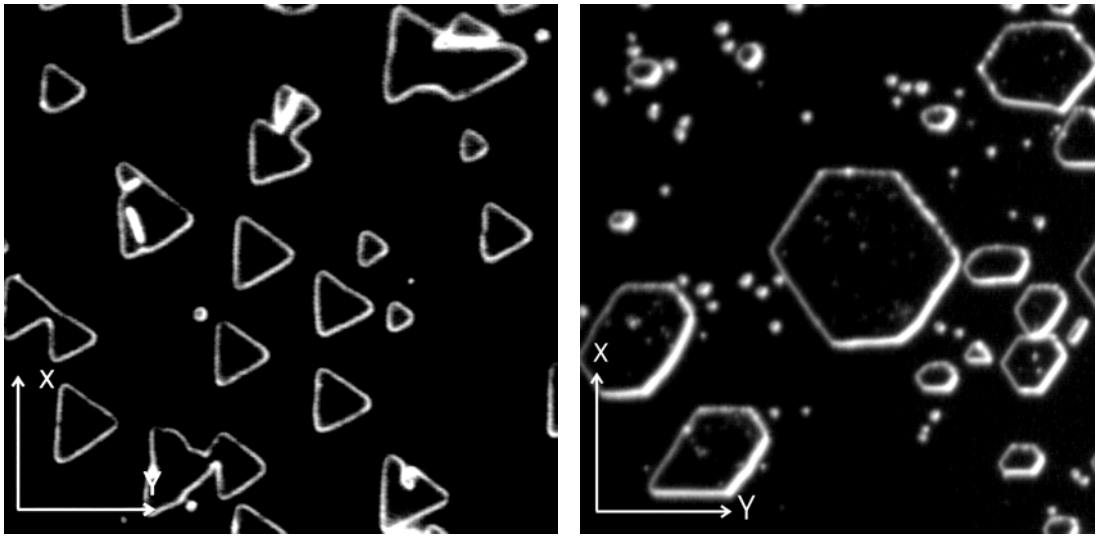


**Figure 4.42.** The switched domain shape of the lithium tantalate (left picture) and of lithium niobate (right picture).

### 4.7.3 Fabrication of Periodically Poled Lithium Tantalate

Initial attempts to pole lithium tantalate by using conductive gel as the electrode on the–*z* face of a patterned substrate were unsuccessful. After poling, only small parts of gratings were observed in the patterned area under the microscope after wet etching, some side walls of the domains were merged together and formed a big switched domain area, the quality of the gratings was poor.

The reason for the poor result is not clear at the moment and is still under further investigation, but it is believed that, in contrast to the poling mechanism of lithium niobate crystals, the nucleation density using the gel or liquid electrodes is far lower than that by using metal electrodes when poling $LiTaO_3$. Previous research also indicated that, by using the same metal electrode, the measured nucleation density was 500/mm$^2$ in congruent lithium tantalate, compared to 1000/mm$^2$ in congruent lithium niobate [62]. So in contrast to PPLN, which can be fabricated with either metal or liquid electrodes, PPLT can be poled by metal electrodes only because of the low domain nucleation density. In addition, the width of the grating has a significant influence on poling quality, the side wall propagation of the switched domain during the poling process can be effectively suppressed by using narrow width gratings. A new grating mask with the following periods listed in Table 4.12 was designed, the mark-space ratio was around 30:70, the width of these gratings is only 200μm.

**Table 4.13** Grating periods for PPLT, the results are from Opt.Lett. 28(3), p.194, 2003 [63].

| No. | Wavelength(nm) | Period Λ (μm) | Crystal temperature ($^o$C) |
|---|---|---|---|
| 1 | 1035 | 7.000 | 150 |
| 2 | 1035 | 7.046 | 100 |
| 3 | 1035 | 7.090 | 50 |
| 4 | 1040 | 7.151 | 100 |
| 5 | 1040 | 7.192 | 50 |
| 6 | 1043 | 7.256 | 50 |
| 7 | 1050 | 7.361 | 100 |
| 8 | 1050 | 7.405 | 50 |
| 9 | 1064 | 7.575 | 100 |
| 10 | 1064 | 7.619 | 50 |

500μm thick lithium tantalate wafers were patterned on +*z* face using a 200nm thick aluminium layer as the electrode, a 22kV·mm$^{-1}$ electric field was applied across the patterned crystal, the total charge needed to switch the domain was calculated based on Eq.(4.01), the spontaneous polarisation of $LiTaO_3$ $P$s = 0.52μC·mm$^{-2}$ was used to calculate the necessary charge.

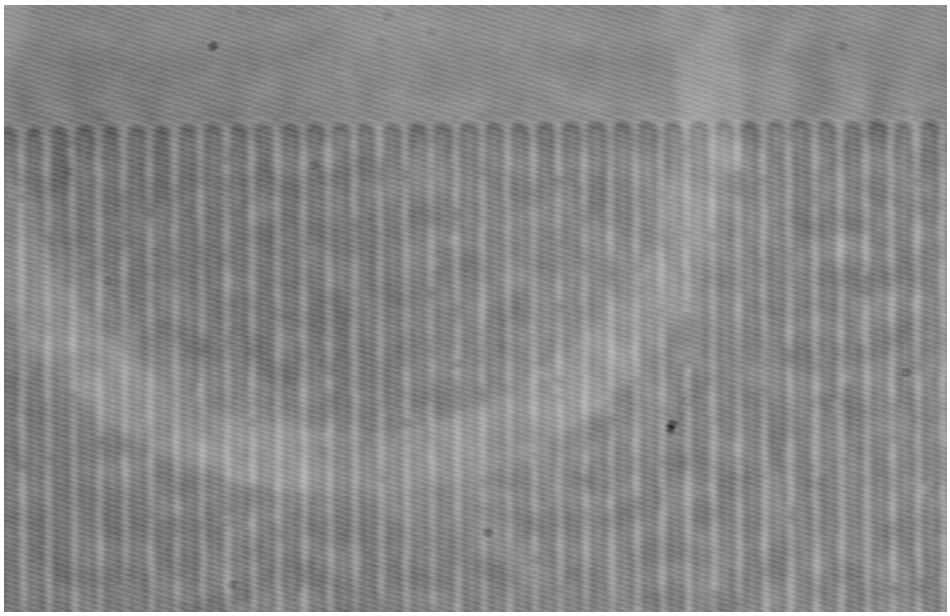

**Figure 4.43.** The revealed domains on the +*z* face with a 7.0μm period grating, the width of the grating is 0.2mm.

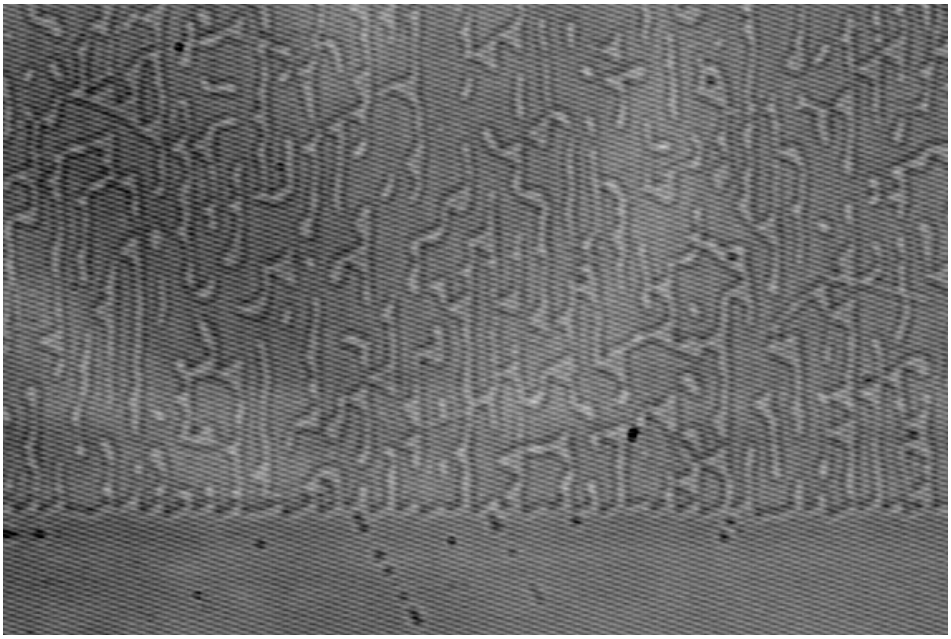

**Figure 4.44.** The revealed domains on the -*z* face with a 7.0μm period grating, the width of the grating is 0.2mm.

The poling results show that the uniformity of the grating was improved and the irregular side growth and formation of non-inverted regions under the grating electrode was largely suppressed, the poling quality was dramatically improved compared with that of our initial attempt. Figure 4.43 shows the revealed domain on the +*z* face with a 7.0μm period and Figure 4.44 shows the revealed domain on the –*z* face.

### 4.7.4 Characterization

The characterization of the PPLT was carried out by A. A. Lagatsky *et al*. The pump source used for characterization was a femtosecond diode-pumped Yb:KYW laser operating at 1048nm (centre wavelength) with pulse duration of 144fs (spectral width of 8nm), repetition rate of 86MHz and average output power of 360mW.

The best results have been obtained by using a 3.5mm-long PPLT crystal. At an incident pump power of around 345mW on the PPLT crystal 105mW of green (524nm) was generated. Taking into account Fresnel losses the conversion efficiency exceeded 40%.

The conversion efficiency and how the green pulse duration depends on the pump beam waist in the PPLT have been investigated. Using different focusing lenses the waist was varied in the range 4.4-21.6μm and the maximum conversion efficiency (~40%) was recorded at focusing spot size of in the range 8-4.4μm. The spectral bandwidth and pulse duration of green pulses was investigated, and spectral broadening with tighter focussing was observed with a pulse duration measured to be 1.2ps at a waist of the pump beam of 14μm.

This work on PPLT demonstrates how careful optimisation of poling techniques, and a thorough investigation of the domain habit of different materials can lead to QPM devices good enough to be used in demanding applications.

This chapter has reviewed and discussed the technology of the applied electrical field poling method. The fabrication procedures for PPLN using an electric field poling technique with liquid gel electrodes is presented, alternative poling techniques, such as backswitch poling, were also demonstrated. Periodically poled magnesium doped

lithium niobate (PPMgLN), periodically poled lithium tantalate (PPLT) and novel hexagonally poled lithium niobate (HexLN) were also presented. The factors affecting poling quality of short period PPLN gratings have been investigated, and the optimum poling conditions for small and large period PPLN and PPLT gratings were obtained. In the following chapters optical waveguide theory and the fabrication of zinc indiffused channel waveguide in periodically poled lithium niobate are discussed.

## References


[1] J. A. Armstrong, N. Bloembergen, J. Ducuing, and P. S. Pershan, "Interactions between Light Waves in a Nonlinear Dielectric", *Phys. Rev*., Vol.**127**, p.1918-1939 (1962)

[2] R. C. Miller, "Optical Harmonic Generation in Single Crystal $BaTiO_3$", *Phys. Rev*., Vol.**134**, p.A1313-A1319 (1964)

[3] J. A. Giordmaine and R. C. Miller, "Tunable Coherent Parametric Oscillation in $LiNbO_3$ at Optical Frequencies", *Phys. Rev. Lett*., Vol.**14**, p.973-976 (1965)

[4] D. Feng, N. B. Ming, J. F. Hong, Y. S. Yang, J. S. Zhu, Z. Yang, and Y. N. Wang, "Enhancement of second-harmonic generation in $LiNbO_3$ crystals with periodic laminar ferroelectric domains", *Appl. Phys. Lett*., Vol.**37**, p.607-609 (1980)

[5] W. S. Wang, Q. Zou and D. Feng, "Study of $LiTaO_3$ crystals grown with a modulated structure: I second harmonic generation in $LiTaO_3$ crystals with periodic laminar ferroelectric domains", *J. Cryst. Growth*, Vol.**79**, p.706-709 (1986)

[6] S. N. Zhu, Y. Y. Zhu, and N. B. Ming, "$LiTaO_3$ crystal periodically poled by applying an external pulsed field", *J. Appl. Phys*., Vol.**77**, p.5481-5483 (1995)

[7] V. Bermúdez, D. Callejo, R. Vilaplana, J. Capmany and E. Diéguez, "Engineering of lithium niobate domain structure through the off-centered Czochralski growth technique", *Journal of Crystal Growth*, Vol.**237–239**, p.677-681 (2002)

[8] S. Miyazawa, "Ferroelectric domain inversion in Ti-diffused $LiNbO_3$ optical waveguide", *J. Appl. Phys*., Vol.**50**, p.4599-4601 (1979)

[9] M. Houe, P. D. Townsend, "An introduction to methods of periodic poling for second harmonic generation", *Appl. Phys*., Vol.**28**, p.1747-1763 (1995)

[10] P. W. Haycock and P. D. Townsend, "A method of poling $LiNbO_3$ and $LiTaO_3$ below Tc", *Appl. Phys. Lett*., Vol.**48**, p.698-700 (1986)

[11] M. Yamada, N. Nada, M. Saitoh and K. Watanabe, "First-order quasi-phase matched $LiNbO_3$ waveguide periodically poled by applying an external field for efficient blue second-harmonic generation", *Appl. Phys. Lett*., Vol.**62**, p.435-437 (1993)

[12] I. Camlibel, "Spontaneous Polarization Measurements in Several Ferroelectric Oxides Using a Pulsed-Field Method", *J. Appl. Phys*., Vol.**40**, p.1690-1693 (1969)

[13] L. E. Myers, G. D. Miller, M. L. Bortz, R. C. Eckardt, M. M. Fejer and R. L. Byer, "Quasi-phase-matching 1.064μm pumped optical parametric oscillator in bulk periodically poled $LiNbO_3$", *IEEE Conference on Nonlinear Optics*, Waikoloa, Hawaii, July 25-29, paper PD8 (1994)

[14] J. Webjörn, V. Pruneri, P. St. J. Russell, J. R. M. Barr, D. C. Hanna, "Quasi-phase-matched blue light generation in bulk lithium niobate, electrically poled via periodic liquid electrodes", *Electron. Lett*., Vol.**30**, p.894-896 (1994)

[15] W. K. Burns, W. McElhanon, L. Goldberg, "Second harmonic generation in field poled, quasi-phase-matched, bulk $LiNbO_3$", *IEEE Photon. Technol. Lett*., Vol.**6**, p.252-254 (1994)

[16] G. D. Miller, R. G. Batchko, W. M. Tulloch, D. R. Weise, M. M. Fejer and R. L. Byer, "42%-efficient single pass cw second-harmonic generation in periodically poled lithium niobate", *Opt. Lett*., Vol.**22**, p.1834-1836 (1997)

[17] L. E. Myers, W. R. Bosenberg, "Periodically poled lithium niobate and quasi-phase-matched optical parametric oscillators", *IEEE J. Quantum Electron.*, Vol.**33**, p.1663-1672 (1997)

[18] V. Pruneri, J. Webjörn, P. St. J. Russell, J. R. M. Barr and D. C. Hanna, "Intracavity second harmonic generation of 0.532μm in bulk periodically poled lithium niobate", *Opt. Commun.*, Vol.**116**, p.159-162 (1995)

[19] E. Fatuzzo and W. J. Merz, "Switching Mechanism in Triglycine Sulfate and Other Ferroelectrics", *Phys. Rev.*, Vol.**116**, p.61-68 (1959)

[20] R. G. Byer, "Parametric Oscillators and Nonlinear Optics", Department of Applied Physics, Stanford University, California, U.S.A, P. G. Harper & B. S. Wherrett, "Nonlinear Optics", Academic Press, (1977)

[21] Ferroelectric Standards Sub-Committee of Ferroelectrics Committee, "IEEE Standard Definitions of Terms Associated with Ferroelectric and Related Materials", *Draft* (2001)

[22] V. Pruneri, "Electric field periodically inverted $LiNbO_3$ for optical frequency conversion", University of Southampton, PhD thesis, (1996)

[23] P. E. Britton, "Fibre laser pumped periodically poled lithium niobate based nonlinear devices", University of Southampton, PhD thesis, (2000)

[24] C. B. E. Gawith, "Novel active waveguide devices in direct-bonded structures", University of Southampton, PhD thesis, (2001)

[25] J. A. Abernethy, "Novel devices in periodically poled lithium niobate", University of Southampton, PhD thesis, (2003)

[26] G. D. Miller, "Periodically poled lithium niobate: Modeling, Fabricating, and Nonlinear-optical performance", Stanford University, PhD thesis, p.18-25 (1998)

[27] W. R. Bosenberg, A. Drobshoff, J. I. Alexander, L. E. Myers and R. L. Byer, "93% pump depletion, 3.5W continuous wave, singly resonant optical parametric oscillator", *Opt. Lett.*, Vol.**21**, p.1336-1338 (1996)

[28] L. E. Myers, "Quasi-phase matched Optical Parametric Oscillators in Bulk Periodically Poled Lithium Niobate", Stanford University, PhD thesis, p.43-44 (1995)

[29] A. L. Alexandrovski and V. V. Volkov, "Formation of domains in lithium niobate in temperature range of 20-200ºC", Moscow State University, Department of Physics, Preprint No.8, (1997)

[30] M. Hayashi, "Kinetics of domain wall motion in ferroelectric switching. General formulation", *J. Phys. Soc. Japn.*, Vol.**33**, p.616-28 (1972)

[31] G. D. Miller, "Periodically poled lithium niobate: Modeling, Fabricating, and Nonlinear-optical performance", Stanford University, PhD thesis, p.18-25 (1998)

[32] E. Fatuzzo and W. J. Merz, "Switching Mechanism in Triglycine Sulfate and Other Ferroelectrics", *Phys. Rev.*, Vol.**116**, p.61-68 (1959)

[33] G. D. Miller, "Periodically poled lithium niobate: Modeling, Fabrication, and Nonlinear-optical performance", Stanford University, PhD thesis, p.38-40 (1998)

[34] M. Reich, F. Korte, C. Gallnich, H. Welling and A. Tünnermann, "Electrode geometries for periodic polling of ferroelectric materials", *Opt. Lett*., Vol.**23**, p.1817-1819 (1998)

[35] R. G. Batchko, V. Y. Shur, M. M. Fejer, and R. L. Byer, "Backswitch poling in lithium niobate for high-fidelity domain patterning and efficient blue light generation", *Appl. Phys. Lett*., Vol.**75**, p.1673-1675 (1999)

[36] R. G. Batchko, M. M. Fejer, R. L. Byer, D. Woll, R. Wallenstein, V. Y. Shur, and L. Erman, "Continuous-wave quasi-phase-matched generation of 60mW at 465nm by single-pass frequency doubling of a laser diode in backswitch-poled lithium niobate", *Opt. Lett*., Vol.**24**, p.1293-1295 (1999)

[37] R. G. Batchko, V. Y. Shur, M. M. Fejer, and R. L. Byer, "Backswitch poling in lithium niobate for high-fidelity domain patterning and efficient blue light generation", *Appl. Phys. Lett*., Vol.**75**, p.1673-1675 (1999)

[38] D. A. Bryan, Robert Gerson, and H. E. Tomaschke, "Increased optical damage resistance in lithium niobate", *Appl. Phys. Lett.*, Vol.**44**, p.847-849 (1984)

[39] Y. Furukawa, K. Kitamura, S. Takekawa, K. Niwa, and H. Hatano, "Stoichiometric $MgLiNbO_3$ as an effective material for nonlinear optics", *Opt. Lett*., Vol.**23**, p.1892-1894 (1998)

[40] A. Harada and Y. Nihei, "Bulk periodically poled MgO-$LiNbO_3$ by corona discharge method", *Appl. Phys. Lett.*, Vol.**69**, p.2629-2631 (1996)

[41] A. Harada, Y. Nihei, Y. Okazaki, and H. Hyuga, "Intra-cavity frequency doubling of a diode-pumped 946nm Nd:YAG laser with bulk periodically poled MgO:$LiNbO_3$", *Opt. Lett*., Vol.**22**, p.805-807 (1997)

[42] K. Mizuuchi, K. Yamamoto, and M. Kato, "Harmonic blue light generation in bulk periodically poled MgO:$LiNbO_3$", *Electron. Lett*., Vol.**32**, p.2091-2093 (1996)

[43] K. Mizuuchi, K. Yamamoto, and M. Kato, "Harmonic blue light generation in X-cut MgO:$LiNbO_3$ waveguide", *Electron. Lett*., Vol.**33**, p.806-808 (1997)

[44] K. Mizuuchi and K. Yamamoto, "Waveguide second-harmonic generation device with broadened flat quasi-phase-matching response by use of a grating structure with located phase shifts", *Opt. Lett.*, Vol.**23**, p.1880-1882 (1998)

[45] T. Sugita, K. Mizuuchi, Y. Kitaoka, and K. Yamamoto, "31% efficient blue second-harmonic generation in a periodically poled MgO$LiNbO_3$ waveguide by frequency doubling of an AlGaAs laser diode", *Opt. Lett*., Vol.**24**, p.1590-1592 (1999)

[46] K. Nakamura, J. Kurz, K. Parameswaran, and M. M. Fejer, "Periodic poling of magnesium-oxide-doped lithium niobate", *J. Appl. Phys*., Vol.**91**, p.4528-4534 (2002)

[47] A. Kuroda and S. Kurimura, Y. Uesu, "Domain inversion in ferroelectric MgO:$LiNbO_3$ by applying electric fields", *Appl. Phys. Lett.*, Vol.**69**, p.1565-1567 (1996)

[48] Y. Hirano, S. Yamamoto, and H. Taniguchi, Technical Digest of Conference on Lasers and Electro-Optics 2001, OSA, San Francisco, p.579-580 (2001)

[49] M. Nakamura, M. Sugihara, M. Katoh, H. Taniguchi, and K. Tadamoto, "Quasi-Phase-Matched Optical Parametric Oscillator Using Periodically Poled MgO-Doped $LiNbO_3$ Crystal", *Jpn. J. Appl. Phys*., Vol.**38**, p.L1234-L1235 (1999)

[50] Data from Casix Inc, website: http://www.casix.com/

[51] V. Berger, "Nonlinear photonic crystal", *Phys. Rev. Lett*., Vol.**81** p.4136-4139 (1998)

[52] N. G. R. Broderick, G. W. Gross, H. L. Offerhaus, D. J. Richardson and D. C. Hanna, "Hexagonally poled lithium niobate: a two-dimensional nonlinear photonic crystal", *Phys. Rev. Lett*., Vol.**84**, p.4345-4348 (2000)

[53] N. G. R. Broderick, T. M. Monro, G. W. Gross, D. J. Richardson, D. C. Hanna and P. G. R. Smith, "Comparison of $2^{nd}$ harmonic generation in 1 and 2D nonlinear periodic crystal", *CLEO/Europe 2000* Nice, CFA1 (2000)

[54] R. Bratfalean, N. G. R. Broderick, D. Richardson, "Observation of simultaneous generation of multiple harmonics in hexagonally poled lithium niobate", *CLEO 2002 Conf.*, Paper CWE3, Long Beach, California, (2002)

[55] A. Chowdhury, C. Staus, B. F. Boland, T. F. Kuech, L. McCaughan, "Experimental demonstration of 1535-1555nm simultaneous optical wavelength interchange with a nonlinear photonic crystal", *Opt. Lett.*, Vol.**26**, p.1353-1355 (2001)

[56] K. R. Parameswaran, R. K. Route, J. R. Kurz, R. V. Roussev, M. M. Fejer, and M. Fujimura, "Highly efficient second-harmonic generation in buried waveguides formed by annealed and reverse proton-exchange in periodically poled lithium niobate", *Opt. Lett.*, Vol.**27**, p.179-181 (2002)

[57] K. Mizuuchi and K. Yamamoto, "Harmonic blue light generation in bulk periodically poled $LiTaO_3$", *Appl. Phys. Lett.*, Vol.**66**, p.2943-2945 (1995)

[58] J. P. Meyn, C. Laue, R. Knappe, R. Wallenstein, M. M. Fejer, "Fabrication of periodically poled lithium tantalate for UV generation with diode lasers", *Appl. Phys.*, B Vol.**73**, p.111-114 (2001)

[59] V. Gopalan, T. E. Mitchell, "In situ video observation of 180° domain switching in $LiTaO_3$ by electro-optic imaging microscopy", *J. Appl. Phys.*, Vol.**85**, p.2304-2311 (1999)

[60] Data from Roditi International Corporation Ltd, website: www.roditi.co.uk/about.html.

[61] K. Mizuuchi and K. Yamamoto, "Generation of 340-nm light by frequency doubling of a laser diode in bulk periodically poled $LiTaO_3$", *Opt. Lett.*, Vol.**21**, p.107-109 (1996)

[62] J. P. Meyn, C. Laue, R. Knappe, R. Wallenstein, M. M. Fejer, "Fabrication of periodically poled lithium tantalate for UV generation with diode lasers", *Appl. Phys.*, B Vol.**73**, p.111-114 (2001)

[63] A. Bruner, D. Eger, M. B. Oron, P. Blau, and M. Katz, "Temperature-dependent Sellmeier equation for the refractive index of stoichiometric lithium tantalate", *Opt. Lett.*, Vol.**28**, p.194-196 (2003)

# Chapter 5

## Introduction to Basic Waveguide Theory

Optical waveguides can maintain a high energy density over a long interaction length, and so can be used to realize SHG devices having substantially higher conversion efficiency than for bulk. Thus PPLN waveguides can provide a fundamental nonlinear platform and can even be used for efficient conversion with diode lasers. The basic theory of waveguides is introduced in this section. The following section is based closely on the treatments by Ghatak and Thyagarajan [1] and Okamoto [2].

### 5.1 Introduction

A waveguide is a dielectric structure where the dielectric constant at the centre of configuration is larger than that at the edges [3]. Using this kind of structure, the optical beam can propagate within the waveguide while maintaining the mode size. This is the basic idea of dielectric waveguide structures [4,5,6].

The waveguides have different forms: planar waveguides, see Figure 5.01, standard optical fibers, channel waveguides, etc.

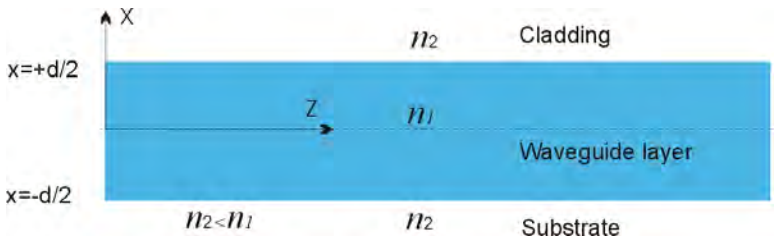


**Figure 5.01.** A symmetric dielectric waveguide structure. The wave is propagating along the +*z* direction.

### 5.2 Maxwell's Equations and Modes in Planar Waveguides

If we assume that light propagates along the *z*-direction of a waveguide structure, the dielectric function, which can be written as $\varepsilon(x,y)$, is uniform along the *z*-direction. We assume a solution of Maxwell's equations of the following forms (for a detailed development of the equations see the referent texts [1,7,8] ).

$$\boldsymbol{E}(x,y,z,t) = \boldsymbol{E}(x,y)e^{-i\beta z+i\omega t} \quad 5.01$$

$$\boldsymbol{H}(x,y,z,t) = \boldsymbol{H}(x,y)e^{-i\beta z+i\omega t} \quad 5.02$$

Where, $\beta$ is the propagation constant (also called the wave-vector).

The terms $\boldsymbol{E}(x,y)$ and $\boldsymbol{H}(x,y)$ are independent of the *z*-coordinate, thus a solution of such a form maintains its shape as the fields propagate along the *z*-direction. Furthermore, each guided mode of the wave is characterized by its frequency $\omega$, and its wave vector $\beta$ along the *z*-direction. The relationship between the frequency and the wave vector along the *z*-direction is shown in Figure 5.02.

A general solution for a waveguide with uniform dielectric medium can be written as:

$$\boldsymbol{E}(x,y,z,t) = \boldsymbol{E}\,e^{-ik_x x-ik_y y}e^{-i\beta z+i\omega t} \quad 5.03$$

$$\boldsymbol{H}(x,y,z,t) = \boldsymbol{H}\,e^{-ik_x x-ik_y y}e^{-i\beta z+i\omega t} \quad 5.04$$

Where: $$k = \omega/c = 2\pi n/\lambda \quad 5.05$$

and $$\varepsilon\mu_0\frac{\omega^2}{c_0^{\,2}} = k_x^2 + k_y^2 + \beta^2 \quad 5.06$$

For a waveguide structure, for example, as shown in Figure 5.01, with $n_1 > n_2$, all allowed modes lie below the solid line defined by $\varepsilon_1\mu_0\omega^2 = \beta^2$ in the $\omega - \beta$ plane. Any point above the solid line is forbidden in the $\omega - \beta$ plane, see Figure 5.02.

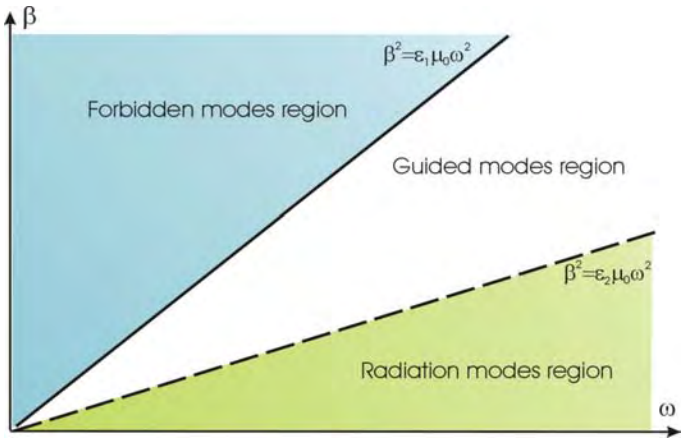


**Figure 5.02.** Forbidden modes, radiation modes and guided modes region in $\omega - \beta$ plane [9].

It is well known that total internal reflection occurs when $\varepsilon_2\mu_0\omega^2 < \beta^2$, which is where the electromagnetic field decays exponentially outside the guiding layer. Thus, the guided modes can only exist in the region above the dashed line defined by

$\varepsilon_2 \mu_0 \omega^2 = \beta^2$ in the $\omega - \beta$ plane. Any point below the dashed line corresponds to a mode that propagates to infinity in the *x*-*y* plane of the surrounding media. Hence any mode below this dashed line is a co-called radiation mode, see Figure 5.02. Thus, the allowed guided mode region exists between two straight lines (the solid line and the dashed line) that go through the origin in the $\omega - \beta$ plane, see Figure 5.02.

As we will see below, at each optical frequency, only a few discrete wave-vector $\beta$ values are consistent with Maxwell's equations, and thus the discrete modes allowed to guide in the waveguide form guided mode bands.

## 5.3 TE and TM Modes of a Symmetric Step Index Planar Waveguide

To help us understand the guided modes in a waveguide it is helpful to consider the simple case of a symmetric step index waveguide. A light wave which consists of electric and magnetic fields can propagate along the *z*-direction of the waveguide in various ways. Transverse-magnetic (TM) modes and transverse-electric (TE) modes are provide two orthogonal mode conditions. In TM modes, the magnetic field vector is normal to the *z*-direction of the light propagation. In TE modes, the electric field vector is normal to the *z*-direction of light wave propagation. From Maxwell's equations [1], we can get:

$$\frac{d^2 E_y}{dx^2} + \left[k_0^2 n^2(x) - \beta^2\right] E_y = 0 \qquad 5.07$$

Where $k_0$ $(= 2\pi n / \lambda_0)$ is the free space wave number and $c$ $(= 1/\sqrt{\varepsilon_0 \mu_0})$ is the speed of light in free space. We now assume the index profile shown in Figure 5.01 as:

$$n(x) = \begin{cases} n_1; & |x| < d/2 \\ n_2; & |x| > d/2 \end{cases} \quad ; \quad n_1 > n_2 \qquad 5.08$$

The standard electromagnetic boundary conditions mean that $E_y$ and $dE_y / dx$ must be continuous at $x = \pm d/2$. Using expression Eq.(5.08) in Eq.(5.07) leads to:

$$\begin{aligned} d^2 E_y / dx^2 + \kappa^2 E_y = 0; \quad & |x| < d/2 \quad && \textit{Waveguide} \\ d^2 E_y / dx^2 - \alpha^2 E_y = 0; \quad & |x| > d/2 \quad && \textit{Cladding} \end{aligned} \qquad 5.09$$

Where: $\kappa^2 = k_0^2 n_1^2 - \beta^2$; $\alpha^2 = \beta^2 - k_0^2 n_2^2$ 5.10

The solution of Eq.(5.09) can be written as:

$$E_y(x) = \begin{cases} A\cos\kappa x + B\sin\kappa x; & |x| < d/2 \\ Ce^{\alpha x} \quad ; & x < -d/2 \\ De^{-\alpha x} \quad ; & x > d/2 \end{cases} \qquad 5.11$$

Where $A, B, C, D$ are constant.

When the refractive index distribution is symmetric, the solutions are either symmetric modes or anti-symmetric modes with respect to the symmetry plane of the waveguide, the *y*-*z* plane. The solutions may be written as:

$$E_y(x) = A\cos\kappa x, \qquad |x| < d/2 \qquad \text{symmetric mode} \qquad 5.12$$

$$E_y(x) = B\sin\kappa x, \qquad |x| < d/2 \qquad \text{anti-symmetric mode} \qquad 5.13$$

$$E_y(x) = Ce^{-\alpha|x|}, \qquad |x| > d/2 \qquad 5.14$$

Matching the continuity conditions of $E_y(x)$ and $dE_y(x)/dx$ at $x = \pm d/2$, we have:

$$\rho\tan\rho = \upsilon \qquad \text{symmetric mode} \qquad 5.15$$

$$-\rho\cot\rho = \upsilon \qquad \text{anti-symmetric mode} \qquad 5.16$$

Where $\rho = \kappa\frac{d}{2}; \upsilon = \alpha\frac{d}{2}$, combining these equations with Eq.(5.10), we have:

$$\upsilon = \sqrt{(V/2)^2 - \rho^2} \qquad 5.17$$

Where $V = k_0 d(n_1^2 - n_2^2)^{1/2}$ is known as the dimensionless waveguide parameter. Therefore the transcendental equations (Eq.5.15 and Eq.5.16) allows determinion of $\kappa$ and $\beta$.

In the $\rho - \upsilon$ plane, the graphical solution of the above equations is shown in Figure 5.03 which shows equation 5.15 (solid curve), equation 5.16 (dashed curve) and their points of intersection with the quadrant of a circle defined by Eq.(5.17). These interactions determine the allowed values of $\rho$ which then yield the value of $\beta$ based on Eq.(5.10). Note that for guided modes the wave-vector can only assume a discrete set of values.

For decreasing $\omega$, $\rho$ moves toward the origin and all the intersections are lost, except for the intersection with the first branch of the tangent function. This corresponds to the fundamental mode, m=0, with no cut-off. All higher modes (m>0) have a “cut off”. They are not guided below a certain critical frequency, the cutoff frequency.

The two circles in Figure 5.03 correspond to $V/2=2$ and $V/2=5$. The number of allowed mode can be from the figure to be:

| $V$ value | Number of symmetric modes | Number of anti-symmetric modes |
|---|---|---|
| 4 | 1 | 1 |
| 10 | 2 | 2 |

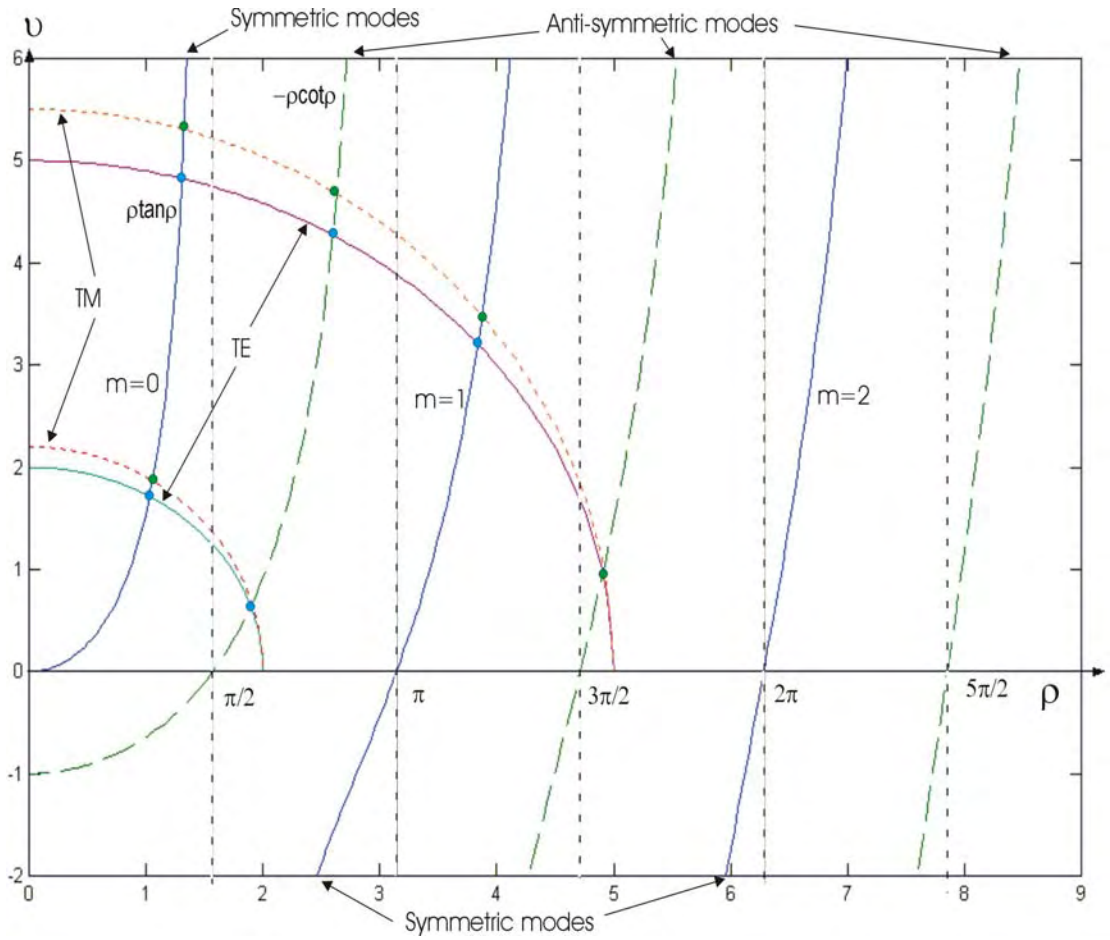


**Figure 5.03.** Graphical solution for Eq.(5.15); Eq.(5.16); Eq.(5.17). The TM modes are shown as dotted lines. $(n_1/n_2)^2$=1.1.

Figure 5.04 and Figure 5.05 shows the vector plot for the fundamental transverse electric (TE) symmetric and anti-symmetric modes in a symmetric waveguide and transverse electric field profiles as a function of *x*. It is often convenient to define the dimensionless propagation constant.

$$b \equiv \frac{\beta^2/k_0^2 - n_2^2}{n_1^2 - n_2^2} = 1 - \frac{\rho^2}{(V/2)^2} = \frac{\upsilon^2}{(V/2)^2} \qquad 5.18$$

Obviously, for a guided mode, we have: $0 < b < 1$

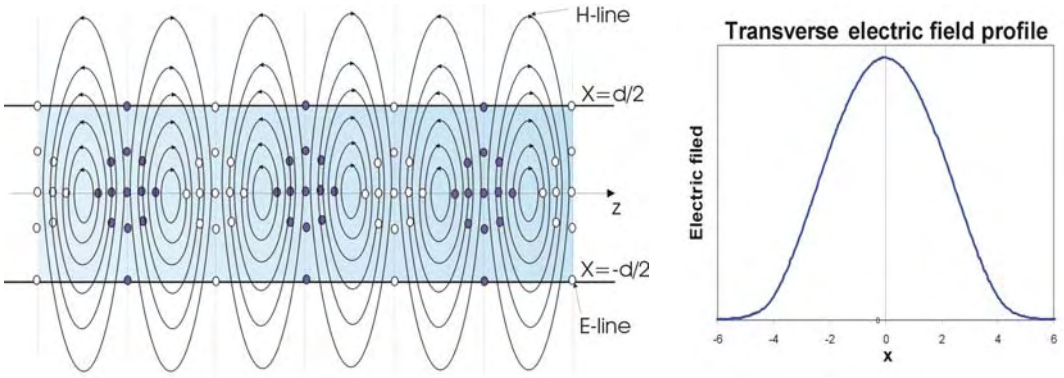


**Figure 5.04.** Vector plot for the fundamental TE mode in a symmetric waveguide (left) and the transverse electric field profile (right) [9].

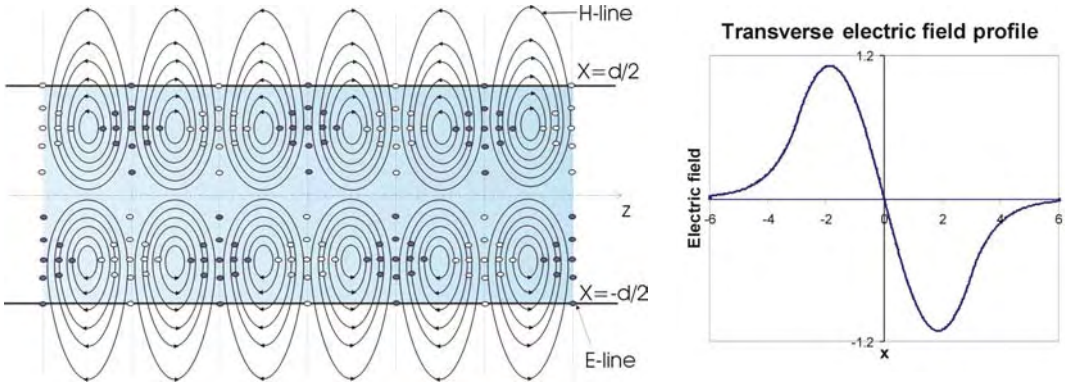


**Figure 5.05.** Vector plot for first anti-symmetric TE mode in a symmetric waveguide (left) and the transverse electric field profile (right) [9].

In the above discussion the TE modes of the waveguide were considered, a similar analysis can also be performed for the TM modes, considering the symmetric modes, the following form [1] is obtained.

$$H_y(x) = A\cos\kappa x\,, \quad |x| < d/2 \qquad 5.19$$

$$H_y(x) = Ce^{-\alpha|x|}\,, \quad |x| > d/2 \qquad 5.20$$

Matching the continuity conditions of $H_y(x)$ and $dH_y(x)/dx$ at $x = \pm d/2$, we have:

$$\rho\tan\rho = (n_1/n_2)^2\upsilon \qquad \text{symmetric mode} \qquad 5.20$$

$$-\rho\cot\rho = (n_1/n_2)^2\upsilon \qquad \text{anti-symmetric mode} \qquad 5.21$$

The graphical solution of Eq.(5.20) and Eq.(5.21) are also included in Figure 5.03, except that the point of intersection lies higher by a factor $(n_1/n_2)^2$. This indicates a lower $\beta$ value for the TM modes than for the corresponding TE modes.

## 5.4 TE and TM Modes of an Asymmetric Index Planar Waveguide

In this section, the TE modes of a guiding layer that is not a symmetric structure are discussed, see Figure 5.06, a similar methodology can be applied to find the TM modes and to describe mode propagation in other waveguide geometries.

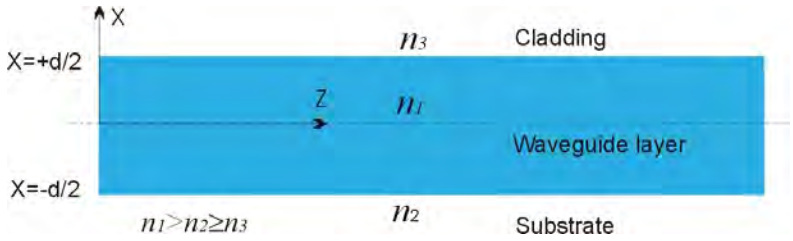


**Figure 5.06.** An asymmetric dielectric waveguide structure. The wave is propagating along the +*z* direction.

In a similar manner to the previous section, equations of the same form as Eq.(5.11) can be obtained:

$$E_y(x) = \begin{cases} Ce^{-\alpha_3 x} & ; \quad x > d/2 & \textit{Cladding} \\ A\cos(\kappa x + \psi); & |x| < d/2 & \textit{Waveguide} \\ De^{+\alpha_2 x} & ; \quad x < -d/2 & \textit{Substrate} \end{cases} \qquad 5.23$$

Where, $\psi$ is the phase constant describing the asymmetry of the waveguide, $\kappa, \alpha_2, \alpha_3$ are defined as:

$$\kappa^2 = k_0^2 n_1^2 - \beta^2 \qquad 5.24$$

$$\alpha_2^2 = \beta^2 - k_0^2 n_2^2 \qquad 5.25$$

$$\alpha_3^2 = \beta^2 - k_0^2 n_3^2 \qquad 5.26$$

And the new determinant equation is:

$$\tan(\kappa d - m\pi) = \frac{(\alpha_2/\kappa) + (\alpha_3/\kappa)}{1 - (\alpha_2\alpha_3/\kappa^2)} \qquad 5.27$$

Previously the normalized frequency *V* and the normalized propagation parameters *b* were introduced as:

$$V = k_0 d (n_1^2 - n_2^2)^{\frac{1}{2}} \qquad 5.28$$

$$b = \frac{\beta^2 - k_0^2 n_2^2}{k_0^2 n_1^2 - k_0^2 n_2^2} = \frac{n_{eff}^{\ 2} - n_2^2}{n_1^2 - n_2^2} \qquad 5.29$$

Where: $n_{eff}$ ($n_{eff} = \beta / k_0$) is known as the effective refractive index, by introducing the asymmetry parameter $a = \dfrac{n_2^2 - n_3^2}{n_1^2 - n_2^2}$, Eq.(5.27) can be written in the form:

$$\tan(V(1-b)^{\frac{1}{2}} - m\pi) = \frac{\sqrt{\dfrac{b}{1-b}} + \sqrt{\dfrac{b+a}{1-b}}}{1 - \sqrt{\dfrac{b(b+a)}{1-b}}} \qquad 5.30$$

$$V\sqrt{1-b} = m\pi + \tan^{-1}\sqrt{\frac{b}{1-b}} + \tan^{-1}\sqrt{\frac{a+b}{1-b}} \qquad 5.31$$

A similar methodology can be applied to the TM modes, Figure 5.07 shows a plot of $V$ versus $b$ with $a$ as a parameter and provides a universal plot for any waveguide;

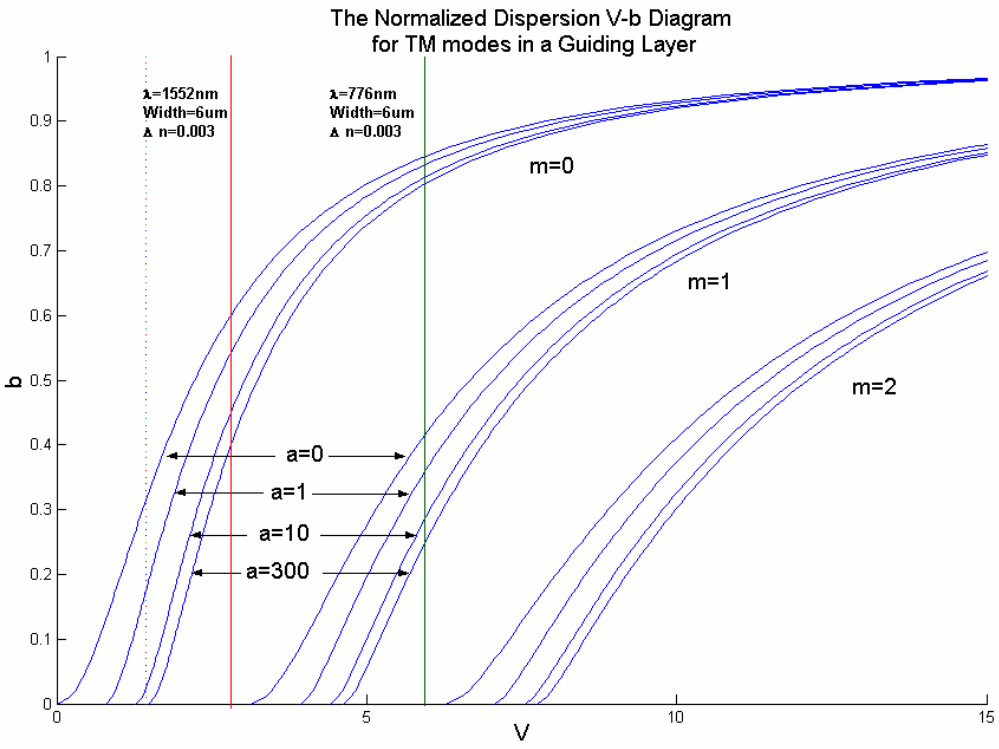


**Figure 5.07.** The normalized dispersion *V-b* diagram for TE modes in a guiding layer.

By substituting the effective refractive index ($n_1 \geq n_{eff} \geq n_2$) into the normalised refractive index parameter, the values of $b$ which lie between zero and one can be obtained based on Eq.(5.29), with higher values demonstrating stronger guidance and $b = 0$ representing the cut off condition for a particular mode [17]. The value of $a$ is used to describe the degree of asymmetry of the waveguide structure. The parameter $a$ ranges from zero for a symmetrical waveguide structure (where $n_2 = n_3$) towards infinity in the limit of very strong asymmetry ($n_2 >> n_3$). Generally $m$ is an integer

starting from 0. When *m* is even, the mode is symmetric, and when *m* is odd, the mode is anti-symmetric (in the symmetric index case). Combining these normalised parameters *b* and *a* provides knowledge of the effective refractive index as a function of frequency which then leads to the normalized frequency *V*. The *V* number provides information about the number of modes and the dispersion characteristics of the planar waveguide structure.

## 5.5 Channel Waveguide Structure and Effective Index Method

Planar or slab dielectric waveguides demonstrate most of the important characteristics of guided optical wave radiation, but the planar or slab structure waveguide is not a very useful geometry for practical applications because of the infinite spatial extent of the wave in one direction. In most practical applications more complicated waveguides structures are used including graded index waveguides and channel waveguides [10,11,12].

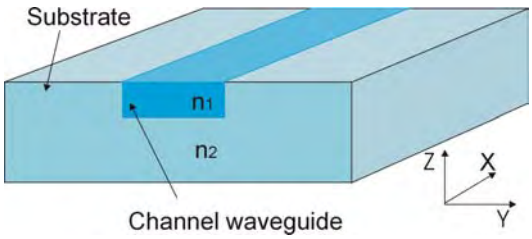


**Figure 5.08.** The channel waveguide structure, refractive index $n_1 > n_2$.

A channel waveguide is a guide which offers confinement in two dimensions as opposed to the one dimensional confinement offered by planar or slab waveguides. Many waveguide fabrication techniques, such as zinc indiffused channel waveguides in lithium niobate, lead to a smoothly varying refractive index in contrast to the step index treated in the analysis in the preceding sections for the planar waveguide. Maxwell's equations cannot be solved for the cladding, core and substrate regions together with the boundaries conditions to obtain the allowed modes without an accurate mathematical model for the refractive index profile of the core. In addition, the development of a field solution for this kind of structure is more complicated than for a step index structure.

There are a variety of ways of modeling channel waveguide structures, including the WKB method [13], finite difference methods [14], the spectral index method [15], the

weighted index method and the effective index method [14]. The effective index method is the simplest of these methods, but still provides reasonably accurate results. The basis of the effective index method for a waveguide such as that shown in Figure 5.08 is that the mode produced within the waveguide can be separated into the product of two functions, one in the *z* direction (vertical direction) which is dependent only on *z* and one in the *y* direction (horizontal direction) which is dependent only on *y*. These can then be solved independently and combined to produce the mode structure. In this way the complicated 2-D channel waveguide structure can be separated into two single structures, one being a step index symmetric planar waveguide in the *y* direction and the other a step index asymmetric planar waveguide in the *z* direction.

If we assume a zinc indiffused channel waveguide can be represented by the simplified structure as shown in Figure 5.08, and the waveguide structure is used to guide 1552nm and 776nm laser beams, the relevant parameters of waveguide are listed in Table 5.01 [16]. Where the refractive index change $\Delta n\,(\approx 3\times 10^{-3})$ is based on the results of NA measurements described in section 7.3 of chapter 7. The refractive index of lithium niobate is based on Eq.(3.02) in chapter 3. The parameters of width and the depth of the channel waveguide are based on the diffusion parameters from chapter 7.

**Table 5.01** The parameters of the waveguide.

| **Material** | $n_1$ | $n_2$ | **Width (μm)** | **Depth (μm)** | **Guided wavelength (nm)** |
|---|---|---|---|---|---|
| $LiNbO_3$ | 2.181 | 2.178 | 6 | 6 | 1552, 776 |

Using the effective index method, in the *z* direction, the modes of the waveguide can be solved using the asymmetric index planar waveguide solution independently of the *y* direction (see section of 5.4), then the modes produced within the waveguide along the *y* direction can be solved based on the symmetric index planar waveguide model independently of the *z* direction (see section 5.3). The normalized frequency *V* along *y* and *z* direction for 1552nm and 776nm wave can be calculated respectively based on Eq.(5.30) and Figure 5.07. The red line in Figure 5.07 represents the *V* value of the 1552nm beam within the waveguide structure (Table 5.01) and the dark green line represents the 776nm solution for second harmonic wave. The results are listed in Table 5.02.

**Table 5.02** The V value for different wavelengths in channel waveguide

| ***V*** | ***V* number at 1552nm** | ***V* number at 776nm** |
|---|---|---|
| *z*-direction (asymmetry) | 2.85 | 6.12 |
| *y*-direction (symmetry) | 2.79 | 5.58 |

Figure 5.03 show that, when $0 < V < \pi$, only one discrete symmetric mode (actually there are two modes, one is TM mode and another is TE mode) [1] is guided in the waveguide, and the waveguide is referred as a single mode waveguide. This can also be seen from the single intersection point of the red line for the 1552nm wavelength in Figure 5.07. It is easy to see that when $\pi < V < 2\pi$, one symmetric and one anti-symmetric mode (actually there are four modes, two are TM mode and another two are TE mode) are guided in the waveguide, the waveguide is referred as a multi-mode waveguide. This can be seen from the two intersection points for the 776nm wavelength (the green line in Figure 5.07).

The terms $\mathrm{TE}_{mn}$ or $\mathrm{TM}_{mn}$ are usually used to indicate the different modes with the first subscript $m$ corresponding to the mode in vertical direction and second subscript $n$ corresponding to the mode in the horizontal direction. All the modes supported at 1552nm and 776nm by the waveguide described by Table 5.01 are listed in Table 5.03.

**Table 5.03** The modes guided by the channel waveguide using the parameter in Table 5.01.

| | | TM0 | TM1 | TE0 | TE1 |
|---|---|---|---|---|---|
| $\lambda = 776$**nm** | TM0 | **TM00** | **TM01** | × | × |
| | TM1 | **TM10** | **TM11** | × | × |
| | TE0 | × | × | **TE00** | **TE01** |
| | TE1 | × | × | **TE10** | **TE11** |
| $\lambda = 1552$**nm** | TM0 | **TM00** | × | × | × |
| | TE0 | × | × | **TE00** | × |

Figure 5.09 shows that the degree of penetration of the transverse electric field into the substrate or cladding regions of the waveguide is wavelength dependent [17]. With a clear difference in the profiles of the TM mode in the waveguides along *y* direction (symmetric structure) and the *z* direction (asymmetric structure) it can also be seen that an asymmetric structure can lead to a poor overlap of the transverse electric field profiles of a propagating mode at different wavelengths [17]. In

frequency mixing processes in which at least two different wavelengths are involved, such as second harmonic generation, or an OPO as discussed in chapter 2 for example, the effective overlap of the mode profile becomes particularly important as the operational efficiency of a waveguide device largely depends on the modal size and overlap of the fundamental and signal beams [18], and the related intensity distribution in the waveguide [19]. As such, when designing SHG device based on channel waveguides, it is often advantageous to apply a single mode waveguide for the fundamental wavelengths, ensuring a good overlap for high intensity interactions.

The single-mode zinc indiffused channel waveguide in the $LiNbO_3$ can be precisely controlled by modifying the zinc indiffusion parameters during the fabrication processes. The fabrication and characterization of zinc indiffused single mode waveguide for 1550nm wavelengths is presented in the following chapters.

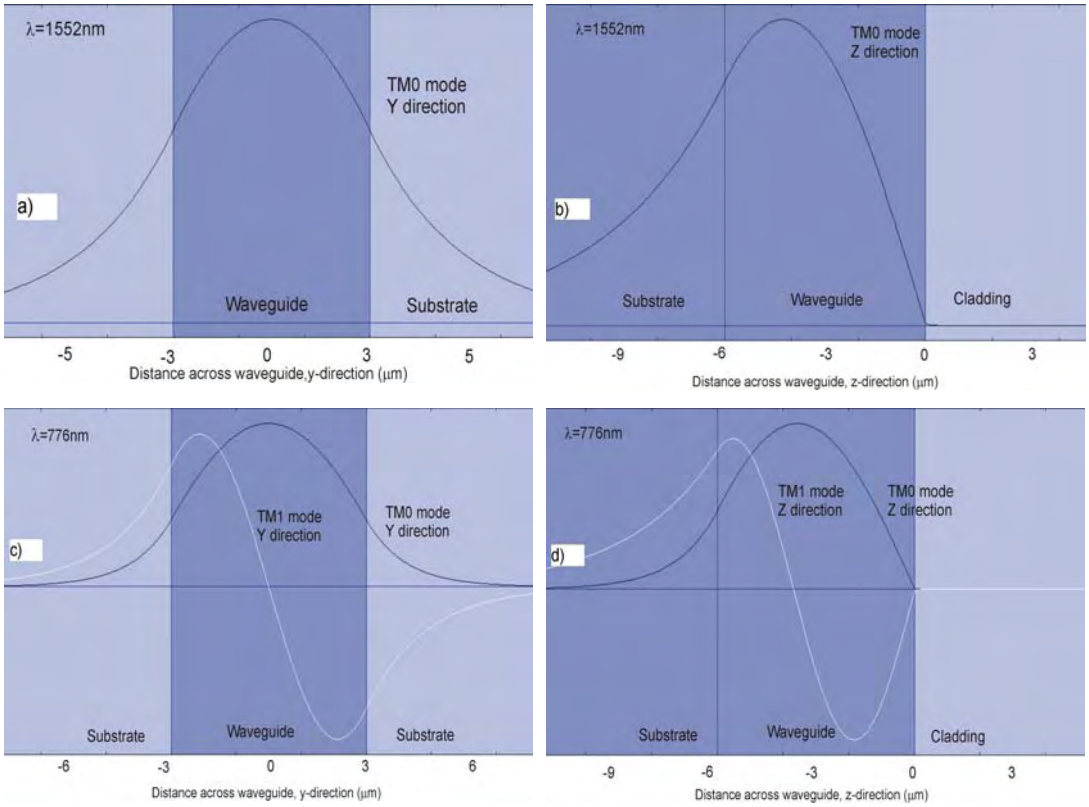


**Figure 5.09.** Transverse electric field profiles for TM modes in the waveguide structure listed in Table 5.01. (a) TM0 mode ($\lambda$=1552nm) along the *y* direction (symmetric structure); (b) TM0 mode ($\lambda$=1552nm) along the *z* direction (asymmetric structure); (c) TM0 and TM1 mode ($\lambda$=776nm) along the *y* direction (symmetric structure); (d) TM0 and TM1 mode ($\lambda$=776nm) along the *z* direction (asymmetric structure). The black and white lines represent the TM0 mode and TM1 mode respectively.

This chapter has introduced basic optical waveguide theory and the effective index method. The single mode conditions for channel waveguides for the different wavelengths were discussed. A modelling for diffused waveguide structures was built and the mode profiles supported by the waveguides were simulated. Fabrication of channel waveguides using the zinc indiffusion in lithium niobate will be discussed in the following chapter

## References


[1] A. Ghatak, K. Thyagarajan, "Introduction to Fiber Optics", Cambridge University Press, (1998)

[2] K. Okamoto, "Fundamentals of Optical Waveguides", Academic Press, (1992)

[3] M. J. Adams, "An introduction to Optical Waveguides", John Wiley, Chichester, (1981)

[4] A. W. Snyder, and J. D. Love, "Optical Waveguide Theory", Chapman and Hall, London, (1983)

[5] R. Magnanini, F. Santosa, "Wave propagation in a 2-D optical waveguide", *Society for Industrial and Applied Mathematics*, Vol.**61**, p.1237-1252 (2000)

[6] D. Marcuse, "Theory of Dielectric Optical Waveguides", Academic Press, New York, (1974)

[7] E. C. Titchmarsh, "Eigen function Expansions", 2nd edition, Oxford at the Clarendon Press, Oxford, (1962)

[8] J. A. Kong, "Electromagnetic Wave Theory", John Wiley, (1986)

[9] H. A. Haus, J. R. Melcher, "Electromagnetic Fields and Energy", Prentice Hall, (1990)

[10] S. Pélissier, F. Pigeon, B. Biasse, M. Zussy, G. Pandraud, and A. Mure-Ravaud, "New technique to produce buried channel waveguides in glass", *Opt. Eng.*, Vol.**37**, p.1111-1114 (1998)

[11] C. B. E. Gawith, D. P. Shepherd, J. A. Abernethy, D. C. Hanna, G. W. Ross, and P. G. R. Smith, "Second-harmonic generation in a direct-bonded periodically poled $LiNbO_3$ buried waveguide", *Opt. Lett.*, Vol.**24**, p.481-483 (1999)

[12] R. E. Collin, "Field Theory of Guided Waves", 2nd edition, IEEE Press, (1991)

[13] D. L. Lee, "Electromagnetic Principles of Integrated Optics", John Wiley, (1986)

[14] G. M. Berry, S. V. Burke, C. J. Smartt, T. M. Benson, P. C. Kendall, "Analysis of multilayered dielectric waveguides: variational treatment", *Electron. Lett.*, Vol.**30**, p.2029-2031 (1994)

[15] P. C. Kendal, M. S. Stern, S. V. Burke, "Planar waveguide analysis by the spectral index method. I: Rib and uniformly buried waveguides", *Opt. Quantum Electron.*, Vol.**25**, p.711-787 (1993)

[16] D. H. Jundt, "Temperature-dependent sellmeier equation for the index of refraction, $n_e$, in congruent lithium niobate", *Opt. Lett.*, Vol.**22**, p.1553-1555 (1997)

[17] N. J. Cronin, "Microwave and optical waveguides", *Institute of Physics Publishing*, (1995)

[18] R. Guenther, "Modern optics", John Wiley and Sons, (1990)

[19] W. P. Risk, "Modelling of longitudinally pumped solid-state lasers exhibiting re-absorption losses", *J. Opt. Soc. Am.*, B Vol.**5**, p.1412-1423 (1988)

[28] K. Noguchi, O. Mitomi and H. Miyazawa, "Millimeter-wave Ti:$LiNbO_3$ optical modulators", *J. Lightwave Tech.*, Vol.**16**, p.615-619 (1998)

[29] M. B. Klein, "Dielectric waveguide phase shifters at 95GHz using the electro-optic effect in $LiNbO_3$", *Ferroelectrics*, Vol.**50**, p.307-312 (1983)

[30] H. J. Coufal, D. Psaltis, and G. T. Sincerbox, "Holographic Data Storage", Springer, New York, (2000)

[31] Y. Yang, I. Nee, D. Psaltis, M. Luennemann, D. Berben, U. Hartwig and K. Buse, "Photorefractive properties of lithium niobate crystals doped with manganese," *J. Opt. Soc. Am.*, B Vol.**20**, p.1491-1502 (2003)

[32] P. Yeh, "Contra-directional two-wave mixing in photorefractive media", *Opt. Commun.*, Vol.**45**, p.323-326 (1983)

[33] R. L. Byer, "Quasi-phase matched nonlinear materials and application to devices", Nonlinear Optics, *Principles, Materials, Phenomena and Devices*, Vol.**7**, p.235-245 (1994)

[34] E. J. Lim, M. M. Fejer, and R. L. Byer, "Second-harmonic generation of green light in periodically poled planar lithium niobate waveguide", *Electron. Lett.*, Vol.**25**, p.174-176 (1989)

[35] G. D. Miller, R. G. Batchko, W. M. Tulloch, D. R. Weise, M. M. Fejer, R. L. Byer, "42%-efficient single-pass CW second-harmonic generation in periodically poled lithium niobate", *Opt. Lett.*, Vol.**22**, p.1834-1836 (1997)

[36] L. E. Myers, G. D. Miller, R. C. Eckardt, M. M. Fejer, and R. L. Byer, "Quasi-phase-matched 1.064-μm-pumped optical parametric oscillator in bulk periodically poled $LiNbO_3$", *Opt. Lett.*, Vol.**20**, p.52-54 (1995)

[37] R. A. Baumgartner and R. L. Byer, "Optical parametric amplification", *IEEE J. Quantum Electron.*, Vol.**15**, p.432-444 (1979)

[38] L. E. Myers, "Quasi-phase matched optical parametric oscillators in bulk periodically poled lithium noibate", Department of Electrical Engineering, Stanford University, PhD thesis, (1995)

[39] M. L. Bortz, D. Serkland, M. M. Fejer, and S. J. B. Yoo, "Near degenerate difference frequency generation at 1.3μm in $LiNbO_3$ waveguides for application as an all-optical channel shifter," *CLEO'94*, CTHD6 (1994)

[40] C. Q. Xu, H. Okayama, and M. Kawahara, "1.5μm band efficient broadband wavelength conversion by difference frequency generation in a periodically domain inverted $LiNbO_3$ channel waveguide", *Appl. Phys. Lett.*, Vol.**63**, p.3559-3561 (1993)

[41] Y. N. Korkishko, V. A. Fedorov, T. M. Morozova, F. Caccavale, F. Gonella, and F. Segato, "Reverse proton exchange for buried waveguides in $LiNbO_3$", *JOSA A.*, Vol.**15**, p.1838-1842 (1998)

[42] J. Amin, V. Pruneri, J. Webjörn, P. St. J. Russell, D.C. Hanna, J. S. Wilkinson, "Blue light generation in a periodically poled Ti: Lithium Niobate channel waveguide", *Opt. Commun.*, Vol.**135**, p.41-44 (1997)

[43] R. C. Twu, C. C. Huang, and W. S. Wang, "Zn Indiffusion Waveguide Polarizer on Y-cut $LiNbO_3$ at 1.32-μm Wavelength", *IEEE Photon. Technol. Lett.*, Vol.**12**, p.161-163 (2000)

[44] A. M. Glass, "Photorefractive Effect", *Opt. Eng.*, Vol.**17**, p.470-479 (1978)

# Chapter 6

## Fabrication of Zinc Indiffused PPLN Channel Waveguides

### 6.1 Introduction

Optical waveguides in lithium niobate have been widely studied for many years, with the main applications including telecommunication systems, nonlinear optics, blue laser sources for next generations of DVD [1,2,3], etc. Several methods are typically used for fabricating waveguides in this material [4,5], the most popular methods being titanium (Ti) diffusion [6,7], proton exchange [8,9,10], and ion implantation [11]. Each one of these established techniques has some limits of applicability.

By combining PPLN and waveguide structures, high optical intensities for the interacting beams can be maintained over considerable distances to improve conversion efficiencies by two to three orders of magnitude as compared to bulk devices. Figure 6.01 shows a schematic drawing of nonlinear frequency mixing in a bulk medium and in a waveguide.

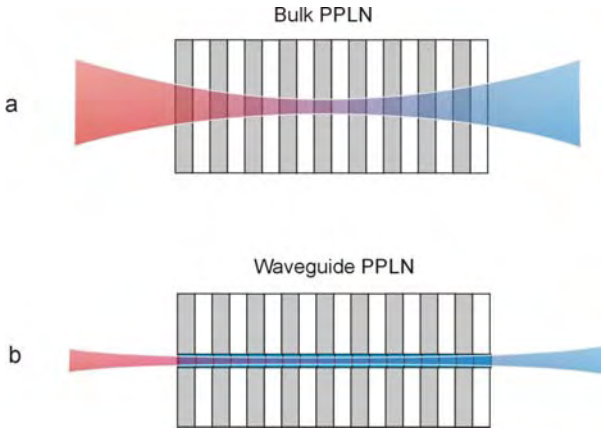


**Figure 6.01.** Schematic drawings of SHG in (a) Diffraction associated with bulk PPLN; (b) Optical confinement provided by waveguide PPLN.

The fabrication of waveguides in PPLN generally involves two steps in a sequence that depends on the choice of waveguide formation technology. For example, proton exchange involves firstly the poling the lithium niobate with a certain period of grating followed by formation of a channel waveguide [12,13], whereas titanium diffusion reverses the order. Annealed-proton-exchanged waveguides are formed at relatively low temperatures (350°C-400°C) [8,9,10,12], so normally the waveguides

are fabricated after the sample has been poled (poling after the waveguide formation results in a poor periodic grating structure) [14]. APE waveguides show increased resistance to photorefractive damage, however only extraordinary guided modes are supported in the waveguide [15]. In addition, proton exchanged layers decrease the nonlinear coefficient in the initial proton exchange layer [14], requiring complex post annealing to recover the nonlinearity, which may even then not be fully recovered [16,17]. An alternative low temperature technique, ion implantation, requires the use of ion accelerators and so is complex and expensive.

The normal temperature for Ti diffusion into $LiNbO_3$ is around 1050°C to 1100°C [6,7,18], and this is the process used to fabricate Ti-diffused $LiNbO_3$ waveguides for conventional optical components (for example, optical modulators, etc). Such devices demonstrate good electro-optic properties, low propagation losses, and support both TE and TM modes [8,9]. However, the process is not compatible with periodically poled materials, because at such high temperatures the periodically switched domain structure is degraded. The alternative sequence process, poling after the formation of waveguides has been used with some success, but the formation of an unwanted thin domain inverted layer during the high temperature process for Ti diffusion may cause problems in the subsequent poling. An additional weakness of this technique is the worsened photorefractive damage in $LiNbO_3$ induced by the incorporation of $Ti^{4+}$ ions, which limits the operation of the Ti:$LiNbO_3$ based devices to the infrared and prevents effective operation in the visible range of the spectrum [7,19]. Several methods for suppressing out-diffusion have been proposed, for example surface polishing off the 50nm out-diffused layer after thermal processing, etc [7,19], but these steps add complexity to the technique. In addition, it is very difficult to pole a uniform periodically poled lithium niobate (PPLN) structure after Ti indiffusion waveguide due to the electrical insulating properties of the lithium out-diffused layer in the waveguide area [7,19].

To overcome such difficulties, lower temperature diffusion (below 1000°C) is desirable, requiring the use of elements with higher diffusion coefficients and lower activation energy. In this case, Zn appears to be a good choice [20,21,22]. Low loss optical waveguides in $LiTaO_3$ and $LiNbO_3$ by Zn diffusion from the vapor phase have been demonstrated previously [20,23,24]. There is also a report on the fabrication of

zinc-diffused waveguides in *y*-cut $LiNbO_3$ for 1.32µm wavelength operation by diffusing metallic Zn for applications in electro-optic (EO) devices [21], and also the fabrication of vapor-phase waveguides in y-cut Czochralski-grown PPLN where the existing periodic domain structure was preserved [24]. The main alternative to vapour phase diffusion is based on the thermal diffusion of a metallic zinc layer which is pre-deposited onto the crystal surface. While this route was successfully applied by Fujimura *et al*. [25] to create zinc waveguides in PPLN, it was determined that low-pressure diffusion was required to prevent unacceptable build-up of residue on the surface during the indiffusion stage and associated optical losses. However, in this research we show that by carefully optimising the thickness of the deposited zinc layer it is possible to achieve high quality waveguides using a simplified thermal indiffusion process, without the additional complexity of low pressure processing.

In this chapter, we present the fabrication of Zn-diffused waveguides on *z*-cut lithium niobate substrates and the fabrication of PPLN waveguides by thermal diffusion of a metallic Zn film. Various fabrication conditions were investigated and optimised to obtain good quality waveguides for different wavelengths through the characterisation of mode profiles, numerical aperture (NA), spot sizes etc., described in chapter 7.

## 6.2 Diffusion of Zinc into Lithium Niobate

The mechanism of zinc indiffusion into the lithium niobate substrate is similar to that of titanium indiffusion which is the most common and most well known method of creating waveguides in lithium niobate [26,27,28].

The previous work done by T. S. Chernaya *et al*. [28] suggested that during the indiffusion processes the Zn atoms diffuse through Li sites if the zinc concentration is below 7.6mol% but change their locations in the lattice and partially occupy the Nb positions if the concentration is in excess of this level. Zinc indiffusion into the Li position was accompanied by a decrease in the concentration of intrinsic Nb-Li defects. This clarifies the structural nature of the “threshold” of Zn concentration (7.6mol%), which manifests itself as singularities in the concentration dependences of various optical properties. The structural origin of the threshold concentration is likely a common feature of all non-photorefractive impurities (Mg, Zn, In, and Sc) in $LiNbO_3$ [28].

While some physical aspects of the mechanism of zinc indiffusion into lithium niobate are still not fully understood, it seems clear that the congruent composition of as-grown lithium niobate crystal is important, as it has a lithium atom concentration ratio (Li/(Li+Nb)) of 48.6% [29,30], which represents a considerable deficiency of lithium ions, and this kind of crystal contains specific structural vacancies (i.e., empty oxygen octahedra) [28,29] and other intrinsic defects (Nb-Li) in its crystal structure [28,29,31,32]. Therefore, various metal atoms, such as Ti, Mg, Zn, In, Fe, Er, Nd and Sc, can be readily introduced into the crystallographic frame by occupying Li sites through thermal indiffusion or doping during the crystal growth processes. This wide ranges of dopants accounts for the versatility of $LiNbO_3$ for many important applications [33].

Nominally pure $LiNbO_3$ devices suffer serious optical damage problems due to the photorefractive effect when exposed to high intensity illumination. This problem can be greatly reduced by doping $LiNbO_3$ single crystals with MgO at a concentration of about 5mol% [34,35]. Moreover, it has been shown that the photorefractive damage in $LiNbO_3$ single crystals can be prevented by doping or indiffusing with ZnO even more efficiently than with MgO [36,37].

One paper [37] reported that photoresistance of zinc indiffused or doped lithium niobate (6mol%) increases two orders of magnitude higher than pure $LiNbO_3$ crystal, the measurement of resistance to optical damage was carried with Ar laser ($\lambda$=488 nm) by means of the direct observation of the facula distortion. Although the reason for the optical damage resistance of zinc doped or indiffused lithium niobate is not clear, Zn doped or indiffused $LiNbO_3$ crystal with 6mol% concentration ZnO has a slightly higher photorefractive resistance that that of magnesium doped Lithium niobate (5mol%). Table 6.01 lists data on the resistance to optical damage of different Zn doped $LiNbO_3$ crystals and MgO doped LiNbO3 [37].

In choosing the process parameters it should be noted that rapid temperature changes have a major effect on $LiNbO_3$. Experimentally, spontaneous poling dots can be found on the surface of 500µm thick $LiNbO_3$ samples when the rate of temperature increase or decrease is larger than $10^oC$ per minute. Therefore during the diffusion process the samples must be raised to and decreased from the diffusion temperature at a rate lower than this in order to avoid spontaneous poling dots.

**Table 6.01** The resistance to optical damage of Zn:LiNbO3 crystals (λ=488 nm) [37].

| No. | ZnO (mol%) | MgO (mol%) | Resistance ($W \cdot cm^{-2}$) |
|---|---|---|---|
| 0 | 0 | 0 | $3.1\times10^{2}$ |
| 1 | 2 | 0 | $6.6\times10^{2}$ |
| 2 | 5 | 0 | $7.1\times10^{2}$ |
| 3 | 6 | 0 | $9.8\times10^{4}$ |
| 4 | 8 | 0 | $9.8\times10^{4}$ |
| 5 | 0 | 5 | $9.7\times10^{4}$ |

The Curie temperature of $LiNbO_3$ is 1210°C. Above this temperature, the properties of $LiNbO_3$ change from a ferroelectric to a paraelectric phase which is nonpolar, and therefore any PPLN domain structure in the sample will be lost. Thus the diffusion temperature must be below the Curie temperature to preserve the polarisation of the switched domain grating, otherwise they will be flipped back into their original polarisation direction.

In addition, when *z*-cut $LiNbO_3$ samples were subjected to high temperatures, of over 1000°C, significant lithium outdiffusion on the positive *z* face occurs [38,39]. When using zinc, $Li_2O$ is lost from the $LiNbO_3$ to form Li-Zn-O compounds on the +*z* crystal surface, which act as a source for zinc indiffusion and as a barrier for lithium outdiffusion, this problem can be avoided by diffusing zinc atoms on the –*z* face of sample. But such outdiffusion will cause particular problems during the indiffusion of zinc waveguides on PPLN, because the PPLN has a periodically switched domain structure, so the outdiffusion layer will be formed periodically, resulting in a periodic change in the zinc concentration, and thus higher losses and a less well confined waveguide. It has also been found that Li-outdiffusion can be effectively reduced through decreasing the diffusion temperature [20]. Therefore a diffusion temperature of lower than 1000°C was adopted to reduce the effect of Li-outdiffusion on the surface of $LiNbO_3$ samples in previous work [20].

## 6.3 Refractive Index Change as a Function of Zn Concentration

The refractive index of Zn:$LiNbO_3$ can be described by following empirical equation 6.01 [40], with a detailed derivation provided by Schlarb and Betzler [41]:

$$n_i^2 = \frac{A_{0,i} + A_{NbLi,i} c_{NbLi} + A_{Zn,i} c_{Zn}}{(\lambda_{0,i} + \mu_{o,i} F)^{-2} - \lambda^{-2}} - A_{IR,i}\lambda^2 + A_{UV} \qquad 6.01$$

Where:

$$c_{NbLi} = \begin{cases} 2(50 - c_{Li})/3 - c_{Zn}/\alpha_{Zn}; & \text{for } c_{Zn} < 2\alpha_{Zn}(50 - c_{Li})/3; \\ 0; & c_{Zn} \geq 2\alpha_{Zn}(50 - c_{Li})/3; \end{cases}$$

$\alpha_{Zn} = 6.5;$

$F = f(T) - f(T_0), \qquad T_0 = 24.5°C;$

$$f(T) = (T + 273)^2 + 4.0238 \times 10^5 \left[ \coth\left( \frac{261.6}{T + 273} \right) - 1 \right];$$

$c_{Li}$ denotes the initial Li content in congruent crystal (measured in mol% $Li_2O$);

The threshold concentration $c_{thr} = 2\alpha_{Zn}(50 - c_{Li}) = 6.5$ mol% for congruent crystals;

$c_{Zn}$ denotes the Zn concentration in crystal (measured in mol% of ZnO);

The wavelength $\lambda$ is given in nm; the temperature $T$ is given in °C;

The subscripts $i$ = e denotes the extraordinary, $i$ = o denotes the ordinary polarization;

The relevant coefficients are listed in following table:

| $n_o$ | $n_e$ |
|---|---|
| $\lambda_{0,o} = 223.219$ | $\lambda_{0,e} = 218.203$ |
| $\mu_{0,o} = 1.1082 \times 10^{-6}$ | $\mu_{0,e} = 6.4047 \times 10^{-6}$ |
| $A_{0,o} = 4.5312 \times 10^{-5}$ | $A_{0,e} = 3.9466 \times 10^{-5}$ |
| $A_{NbLi,o} = -7.2320 \times 10^{-8}$ | $A_{NbLi,e} = 11.8635 \times 10^{-7}$ |
| $A_{Zn,o} = 6.7963 \times 10^{-8}$ | $A_{Zn,e} = 1.9221 \times 10^{-7}$ |
| $A_{IR,o} = 3.6340 \times 1\,0^{-8}$ | $A_{IR,e} = 3.0998 \times 10^{-8}$ |
| $A_{UV} = 2.6613$ | $A_{UV} = 2.6613$ |

Figure 6.02 and Figure 6.03 show how the ordinary index and extraordinary index change as a function of Zn concentration (mol%) for different wavelengths. From these figures it can be seen that the refractive index change increases linearly with the Zn concentration. For a given Zn concentration, the refractive index change increases a little when $\lambda$ shifts to shorter wavelengths, the extraordinary refractive index change is larger than the ordinary refractive index change for a given wavelength. Therefore for a Zn:$LiNbO_3$ waveguide with a known zinc concentration (mol%), we can

calculate the refractive index change when illuminated with a particular wavelength of light. For example, when the Zn concentration of the waveguide is around 2mol%, according to the above figure, the extraordinary refractive index change of a 1550nm incident beam will be around $4.5\times10^{-3}$ which gives a good agreement with the results obtained by W. M. Yong *et al*. [42]

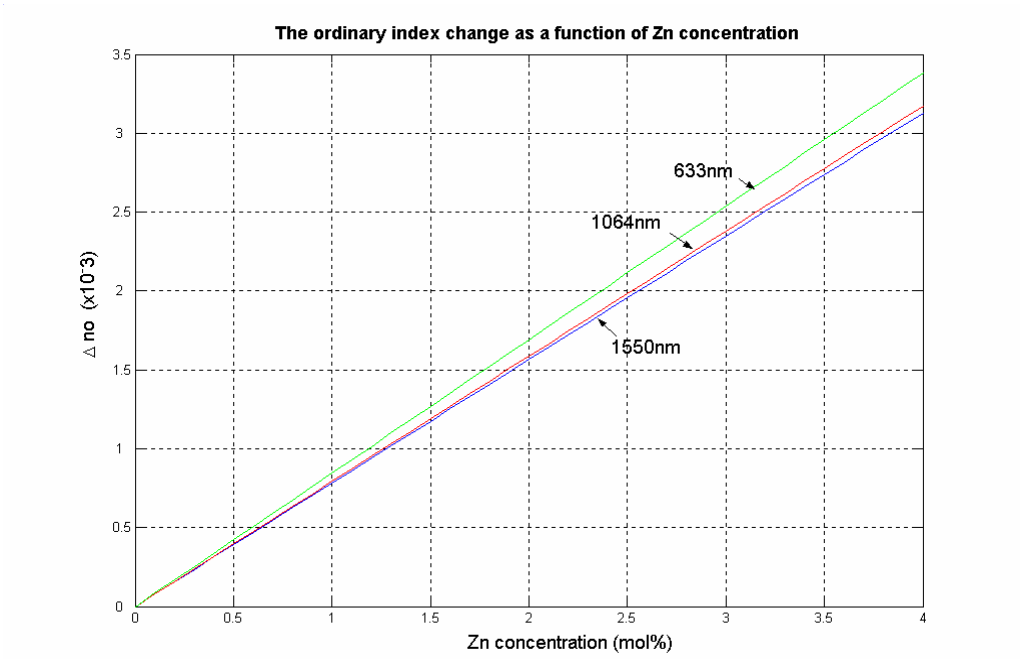


**Figure 6.02.** The ordinary index change as a function of Zn concentration for different wavelengths.

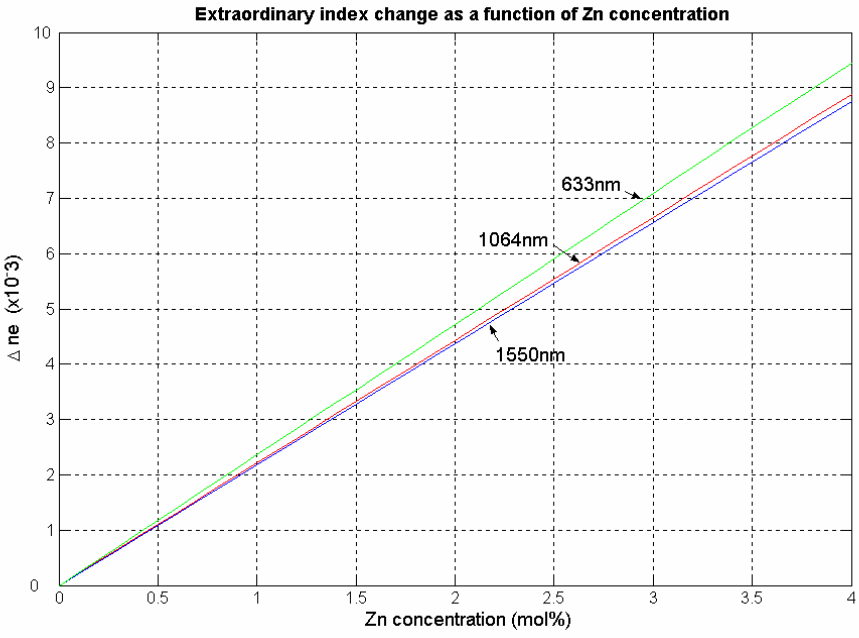


**Figure 6.03.** The extraordinary index change as a function of Zn concentration for different wavelengths.

Using the results of the characterization that will be described in chapter 7, the refractive index change of the zinc indiffused waveguide was found to be around $2.5\times10^{-3}$ at 633nm, and based on Figure 6.02, would imply a zinc concentration in the zinc indiffused waveguide of around 3mol%. This is also consistent with the range of concentrations measured by W. M. Yong *et al*. [42]

## 6.4 Fabrication of Zinc Indiffused Waveguides in Lithium Niobate

The main factors which determine the quality and optical properties of channel waveguides during the fabrication processes are the choice of which crystal face to use for diffusion, the thickness of the deposited zinc film, the diffusion time, the diffusion temperature and the environment. Waveguides in lithium niobate samples under different indiffusion conditions have been made based on the fabrication processes described in this chapter, and the relevant optical properties, such as the NA and mode profiles etc., are reported in chapter 7, feedback from this characterization has been used to optimise the fabrication processes for low-loss, single mode waveguides in the infra-red and visible regions.

For all investigations the zinc indiffused waveguides were defined on the samples by using photolithography and zinc metal evaporation as described in chapter 4. The mask used to define the waveguides has a set of channels with widths ranging from 1µm to 10µm at 100µm spacing.

Initial parameters for zinc film thickness, diffusion temperature and time were taken from previous work carried out in *y*-cut $LiNbO_3$ by Ruey Ching Twu *et al*. [21] A series of *z*-cut, 500µm thick $LiNbO_3$ samples were diffused with zinc film under different fabrication conditions. The waveguides were then visually inspected under a microscope and optically characterised by a laser source, see chapter 7. The following sections describe the main steps required to fabricate the zinc indiffused waveguides on *z*-cut lithium niobate. All fabrication takes place in the ORC in class 1000 clean rooms at class 100 benches.

### 6.4.1 Cleaning and Photolithography

The lithium niobate sample must be thoroughly cleaned to remove surface particulates which could cause contamination or influence the thermal indiffusion process. After cleaning, the samples are spun on the negative *z* face with photo-resist. Initially the standard S1813 photo-resist was used, and according to Table 4.02 in chapter 4, the minimum thickness of photo-resist layer that can be achieved is 1μm. Such a thickness is suitable for patterning the waveguide with widths of over 5μm, but due to the diffraction effects of the UV source, it is very difficult to achieve good patterning of waveguides with widths of 1-5μm which are necessary to make single mode channel waveguides for optical wavelengths lower than 1μm. For such a case photo-resist such as S1805 is suitable, but unfortunately, this kind of photo-resist is not available in the ORC clean room. To allow thinner films, the photo-resist S1813 was diluted by Acetone with different percentage listed in Table 6.02:

**Table 6.02** Thickness via percentage of acetone in dilution**:**

| No. | Photo-resist S1813 (volume %) | Acetone (volume %) | Spin speed (r/min.) | Spin time (min.) | Thickness (μm) |
|---|---|---|---|---|---|
| 1 | 75 | 25 | 6000 | 1.0 | 0.8 |
| 2 | 65 | 35 | 6000 | 1.0 | 0.6 |
| 3 | 50 | 50 | 6000 | 1.0 | 0.5 |

It was found that the diluted photo-resist should be put in a refridgerator (5ºC) for around 24 hours to allow the mixture to become homogeneous. From the results given above for the three thicknesses of photo-resist and from trial exposures it was found that the 0.6μm film is suitable for the fabrication of narrow zinc waveguides.

Zinc indiffused channel waveguide strips spaced 100μm apart and oriented parallel to the *x*-direction, with widths varying from 1μm to 10μm were patterned by photolithography. The patterning process is similar to the steps described in chapter 4. The difference being that during development the samples were soaked in chlorobenzene for 4 minutes and then in developer for 2 minutes (longer than a normal developing). This extra step is common as a “lift off” technique and hardens the surface of the photo-resist in the developer, producing an angled opening wall as shown in Figure 6.04.

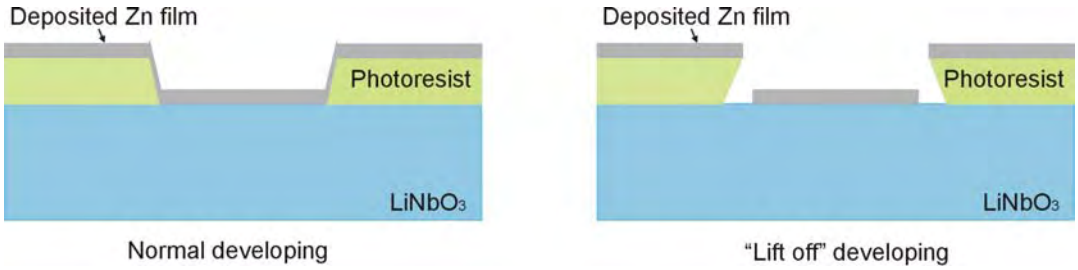


**Figure 6.04**. Schematic drawings of normal developing and "lift of" developing.

Figure 6.05 shows a patterned sample under the microscope, where the photo-resist has been removed, the quality of the patterning is good, and no break points were found in the waveguide area.

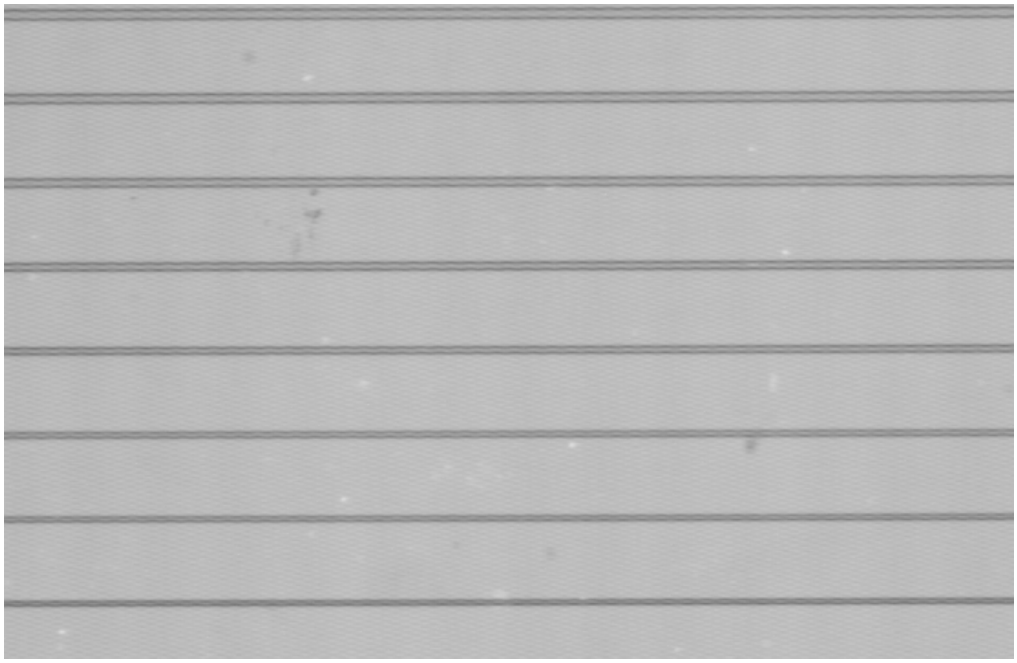

**Figure 6.05.** Patterning of the sample viewed under the microscope, the waveguide strips are spaced by 100μm apart and are oriented parallel to the *x*-direction, with widths varying from 1.5μm to 10μm.

### 6.4.2 Zinc Film Evaporation and Lift-off Technology

After patterning of the samples, metallic zinc was evaporated on the -*z* face of the lithium niobate sample by a standard lift-off technique, see Figure 6.06. Due to the fact that Zn atoms adhere poorly to the surface of $LiNbO_3$ substrates [21], a 5-10nm thickness of nickel (Ni) film is pre-deposited on the surface of the $LiNbO_3$ substrate under conditions of $5\times10^{-6}\,bar$ in order to increase the adhesion, the step (c) in Figure 6.06. Then zinc layers with a thickness ranging from 80nm to 120nm were evaporated on top of the nickel under conditions of $2\times10^{-6}\,bar$, see step (d) in Figure 6.06. After

evaporation of the zinc film, the samples were soaked in acetone solution in an ultrasonic bath for 4-5 minutes to remove the photo-resist and excess zinc film above the photo-resist layer, thus revealing the deposited zinc strips, see step (e) in Figure 6.06. A developed sample viewed under the microscope is shown in Figure 6.07. Finally the samples were indiffused in a tube furnace for different time. The indiffusion time and temperature determined the single mode waveguide conditions for different wavelengths.

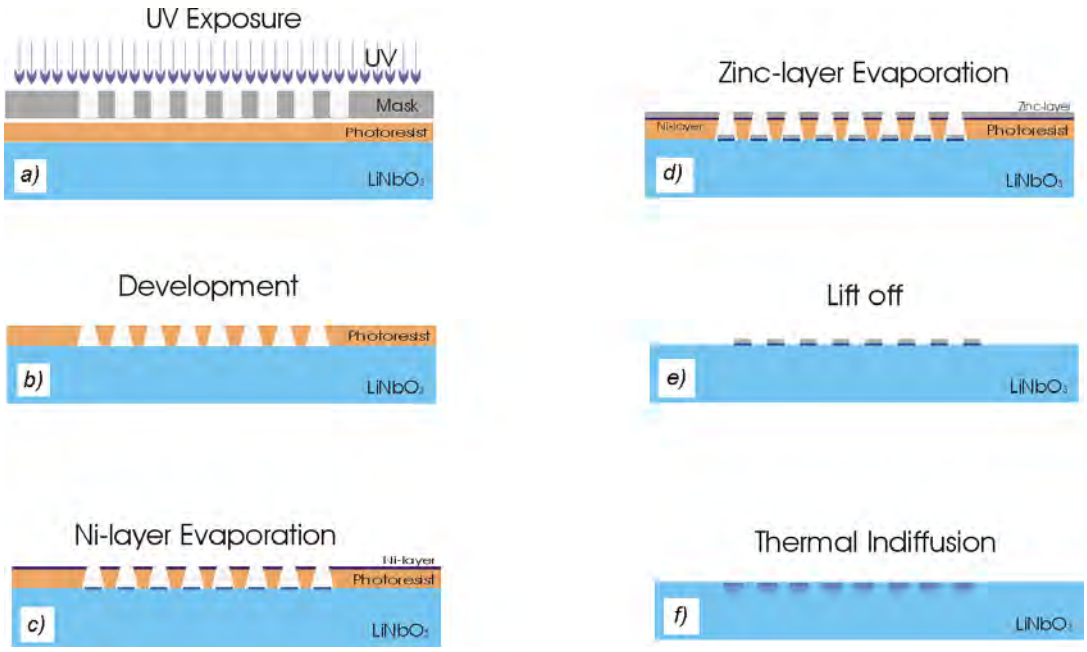


**Figure 6.06.** The step in the "lift off" procedure, (a) UV exposure; (b) Development; (c) Evaporation of a 10nm Ni-layer; (d) Evaporation of the Zn-layer; (e) "Lift off" in Acetone; (f) Thermal indiffusion in the tube furnace.

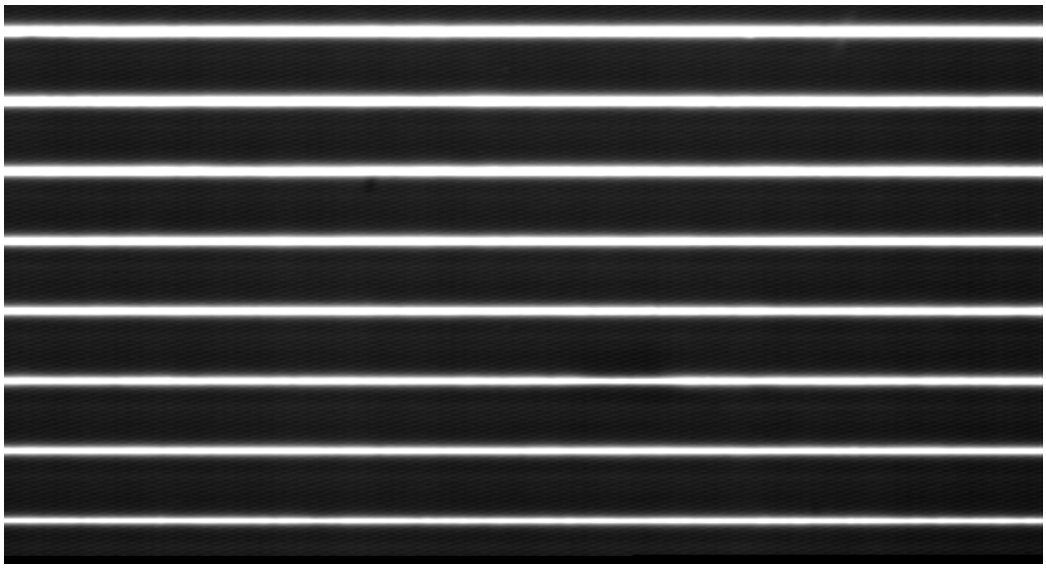

**Figure 6.07.** Zinc strips on the -*z* face of a lithium niobate sample.

### 6.4.3 Thermal Indiffusion

The waveguide patterned samples were placed in a covered platinum crucible, and then the crucible was put in a 70mm diameter tube furnace for thermal indiffusion. The desired indiffusion temperature curve can be programmed into the furnace, and the actual temperature (when the furnace was programmed to be at 900$^{o}$C) was measured using a platinum rhodium thermocouple. The actual temperature around 900$^{o}$C is about 10$^{o}$C below the programmed temperature.

All the indiffusion processing was carried out in dry air. The thermal indiffusion process involves ramping up to the diffusion temperature, maintaining that temperature for a certain time, and then cooling down to room temperature. The indiffusion parameters are listed in Table 6.03.

**Table 6.03** Thermal indiffusion condition

| **Processes** | **Parameter** | **Notes** |
|---|---|---|
| Atmosphere | 100 ml/min | Flow of dry air |
| Start temperature | 20$^{o}$C | Room temperature of the clean room |
| Dwell | 30 minutes | Removing any moisture from the furnace and stabilizing the furnace atmosphere |
| Ramp (up) | 6$^{o}$C/min | To avoid poling dots being formed on the surface of the samples |
| Indiffusion temperature | 900$^{o}$C -930$^{o}$C | Dependent on the thickness of the zinc film and indiffusion time |
| Dwell | 80-240 minutes | Dependent on thickness zinc film and indiffusion temperature |
| Ramp (down) | 6$^{o}$C/min | To avoid poling dots being formed on the surface of the samples |
| To | 20$^{o}$C | Room Temperature of the clean room |

### 6.4.4 Investigation into Diffusion Parameters

Several channel waveguide samples were fabricated using the above procedure, some waveguides samples were patterned on the +*z* face and some samples were patterned on the –*z* face. The next step was to optically test the loss for each sample for various widths of the waveguide by using a He-Ne laser at 633nm. This allowed us to obtain a better comparison of the two sides. No substantial differences in properties were found for channel waveguides indiffused on the +*z* faces and the –*z* faces. But considering that the –*z* face is patterned for poling and that after poling, the mark-space ratio of the PPLN grating on the –*z* face is better than that on the +*z* face, we

decided to diffuse the waveguides on the –*z* face of the samples for all the subsequent work.

Waveguide samples were indiffused under different conditions. Then the samples were optically investigated and characterized by the methods described in section 7.01 of the next chapter. Brief comments and diffusion data are listed in Table 6.04. The maximum thickness investigated was 200nm, at this value obvious remnants remain on the samples. The longest diffusion time investigated was 3 hours, this limit was set for practical convenience and also because longer diffusion time led to reduced surface quality. Similarly 930°C was the maximum temperature used.

**Table 6.04** Thermal indiffusion condition

| No. | Thickness (nm) | Temp. (°C ) | Time (min) | Comment |
|---|---|---|---|---|
| 1 | 80 | 600 | 80 | No waveguide |
| 2 | 80 | 600 | 120 | No waveguide |
| 3 | 80 | 600 | 240 | No waveguide |
| 4 | 80 | 700 | 80 | No waveguide |
| 5 | 80 | 700 | 120 | No waveguide |
| 6 | 80 | 700 | 180 | Very weak guide |
| 7 | 80 | 800 | 80 | No waveguide |
| 8 | 80 | 800 | 120 | Poorly confined waveguide |
| 9 | 120 | 800 | 120 | confined waveguide |
| 10 | 80 | 900 | 80 | Good waveguide, |
| 11 | 80 | 900 | 120 | Good waveguide, high loss |
| 12 | 120 | 900 | 120 | Good waveguide, medium loss |
| 13 | 200 | 900 | 120 | Good waveguide, high loss |
| 14 | 200 | 900 | 180 | Good waveguide, medium loss |
| 15 | 80 | 930 | 80 | Very good waveguide, medium loss |
| 16 | 80 | 930 | 120 | Very good waveguide, low loss |
| 17 | 120 | 930 | 120 | Very good waveguide, low loss |
| 18 | 150 | 930 | 120 | Good waveguide, medium loss |
| 19 | 200 | 930 | 120 | Good waveguide, high loss |
| 20 | 120 | 930 | 180 | Good waveguide, low loss |

### 6.4.5 Surface Roughness Investigation

Remnants were found on the surface of the zinc indiffused channel waveguides under the fabrication conditions listed in Table 6.04. Similar observations were previously reported by W. M. Young *et al*. [20] and Yoon *et al*. [43]. It is believed that during the indiffusion processes, the metallic zinc reacts with the lithium niobate at high temperature in the air and forms compounds which are very stable and thus difficult to remove. This remnant compound is the main cause of surface roughness.

Figure 6.08 shows zinc indiffused waveguides on lithium niobate samples under different indiffusion conditions. The 3D profiles of the remnant strips, see Figure 6.09, were measured by using a Profiler, the height of the average remnants are listed in the Table 6.05.

**Table 6.05** Height of the remnant after different thermal indiffusion condition

| Temp. (°C) | Time (min) | Thickness (nm) | Width (μm) | Roughness (nm) |
|---|---|---|---|---|
| 700 | 180 | 80 | 8 | 75 |
| 800 | 80 | 80 | 8 | 70 |
| 800 | 120 | 80 | 8 | 60 |
| 900 | 80 | 120 | 8 | 73 |
| 900 | 80 | 80 | 8 | 46 |
| 900 | 120 | 80 | 8 | 43 |
| 930 | 80 | 120 | 8 | 54 |
| 930 | 80 | 80 | 8 | 37 |
| 930 | 120 | 80 | 8 | 35 |

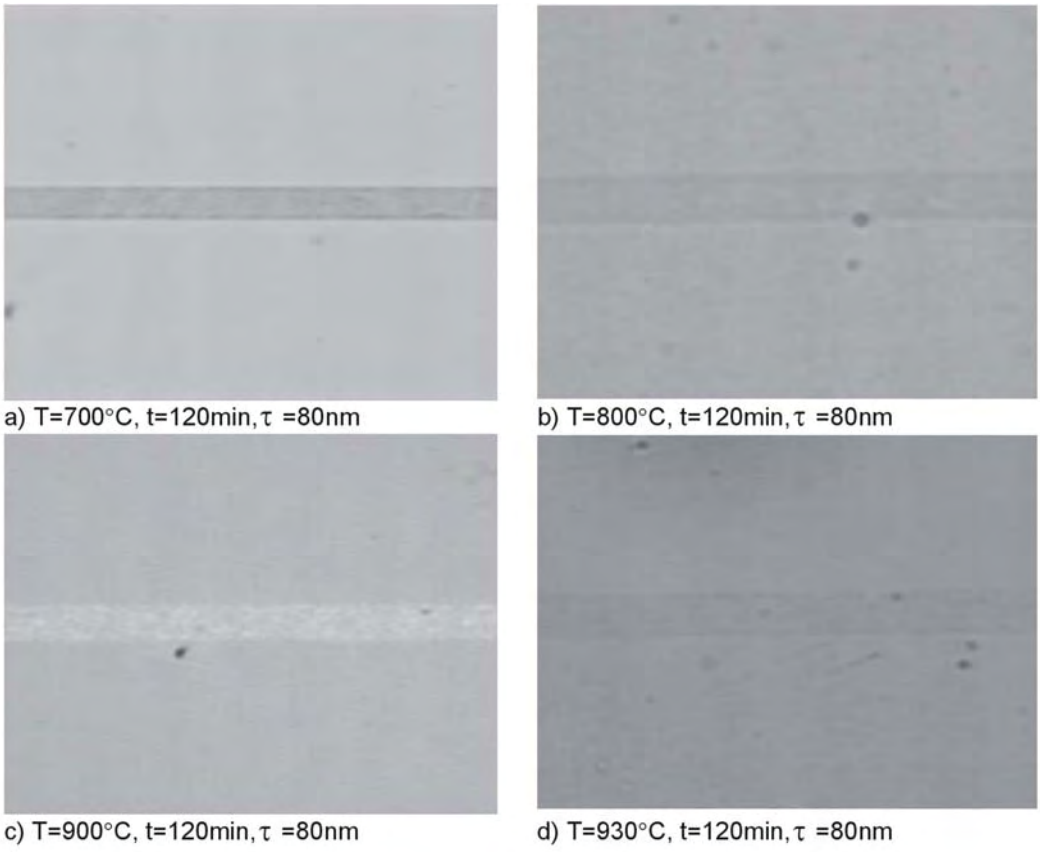


**Figure 6.08.** Microscope pictures of zinc indiffused channel waveguides with different indiffusion temperatures.

It was found that the height of remnant on the surface of the samples varies with different indiffusion conditions. Surface polishing can potentially be used to remove the surface remnant, but this processes needs very accurate equipment and skilful control, also it will increase the chance of introducing new scratches on the surface. So an effort was made to reduce the surface remnant by controlling the indiffusion conditions. Increasing the indiffusion temperature and time or decreasing the zinc film thickness was found effectively to suppress the formation of the remnant on the surface.

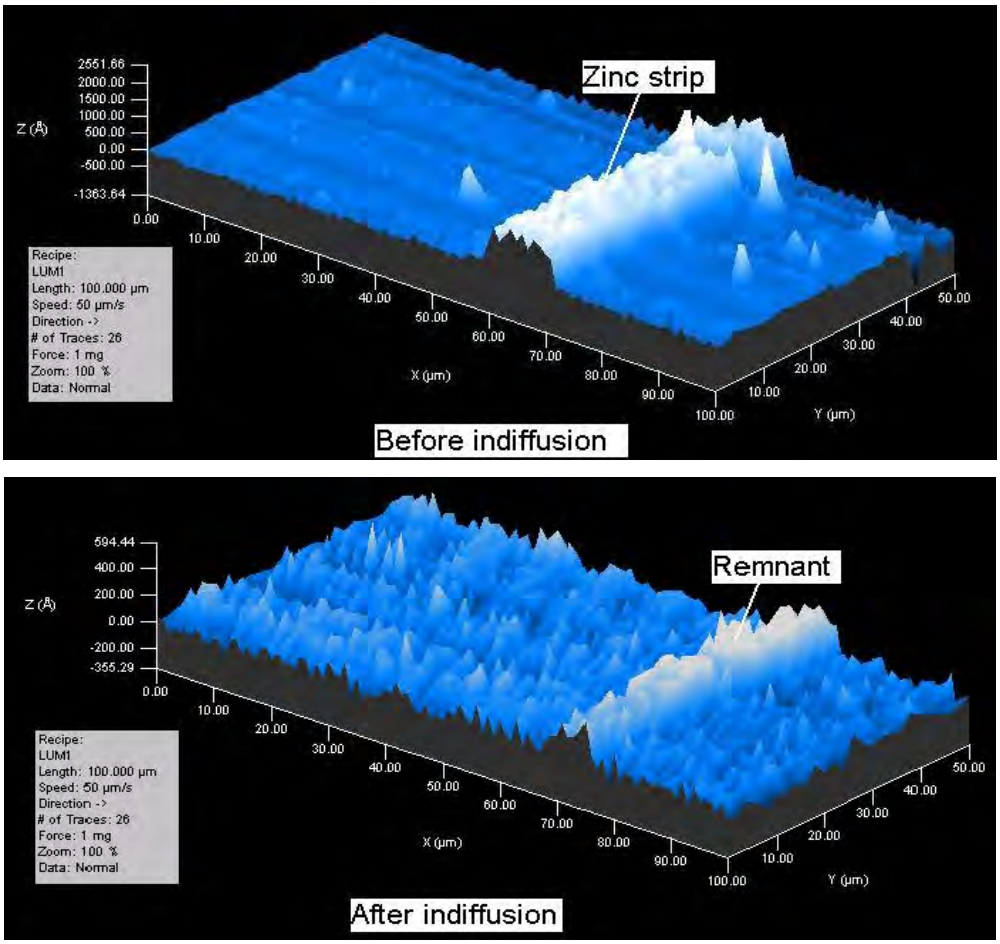


**Figure 6.09.** 3D profile of the zinc strip on surface of $LiNbO_3$ before thermal indiffusion (top figure) and the remnant strips after the thermal indiffusion (bottom figure).

## 6.5 Fabrication of Zinc Indiffused Waveguides in PPLN

In order to create a standardised route towards creating high-quality zinc-diffused waveguides in *z*-cut electric field poled PPLN crystals, two fabrication routes were investigated. The first route involves fabricating the zinc indiffused waveguide before poling the waveguide sample; while the second route is poling the sample first and then indiffusing the zinc waveguide afterwards.

### 6.5.1 Poling after Zinc-diffused Waveguide Fabrication

Initial investigations were carried out based on the assumption that it would be possible to periodically pole the lithium niobate crystals after the zinc indiffusion process (an approach analogous to that used in titanium diffusion).

Four 500μm thick, $LiNbO_3$ samples, 20mm by 35mm, were spin coated by photoresist, patterned by zinc film strips for waveguide formation and indiffused in the tube furnace following the process described in previous sections of this chapter. Then the waveguide samples were patterned for PPLN fabrication of 6-12μm period gratings following the method described in section 4.1.3 of chapter 4. Finally the samples were etched in $HF:HNO_3$ solution (1:2 by volume) at room temperature to reveal the domain structure.

Figure 6.10 show the poling result revealed by wet etching, the period of the PPLN is 10μm and the width of the waveguide is 6μm. From this figure, it can be seen that the zinc indiffused area is under poled while the other area is completely over poled, the grating in the waveguide area is poor, and it appears that the nucleation of the inverted domains is affected by the presence of Zn ions in the waveguide region.

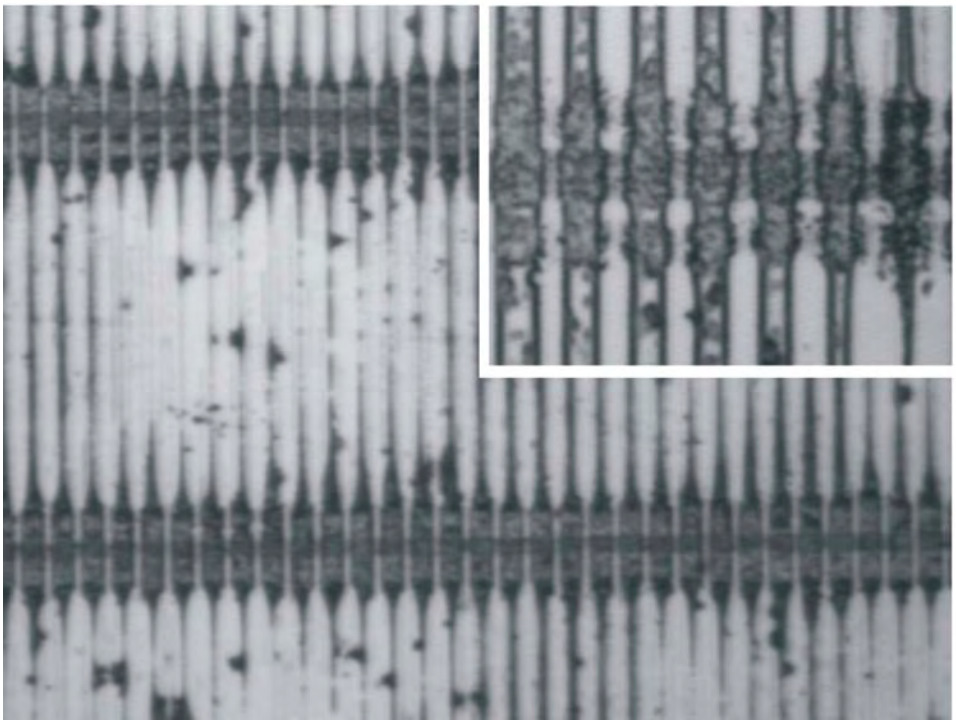

**Figure 6.10.** Poling after thermal diffusion. Periodically poled grating on zinc indiffused waveguide viewed under the microscope after wet etching, the period of the PPLN is 10μm, the width of the waveguide is 6μm. The inset figure is an enlarged picture.

To investigate this, two further $LiNbO_3$ samples were deposited with 80nm of zinc film as shown in Figure 6.11, zinc film was deposited on whole -*z* face of sample 1 and only on half -*z* face of sample 2. Then the two samples were thermally indiffused. The two samples were then patterned with gratings with periods of 10μm, and poled using the method described in chapter 4.

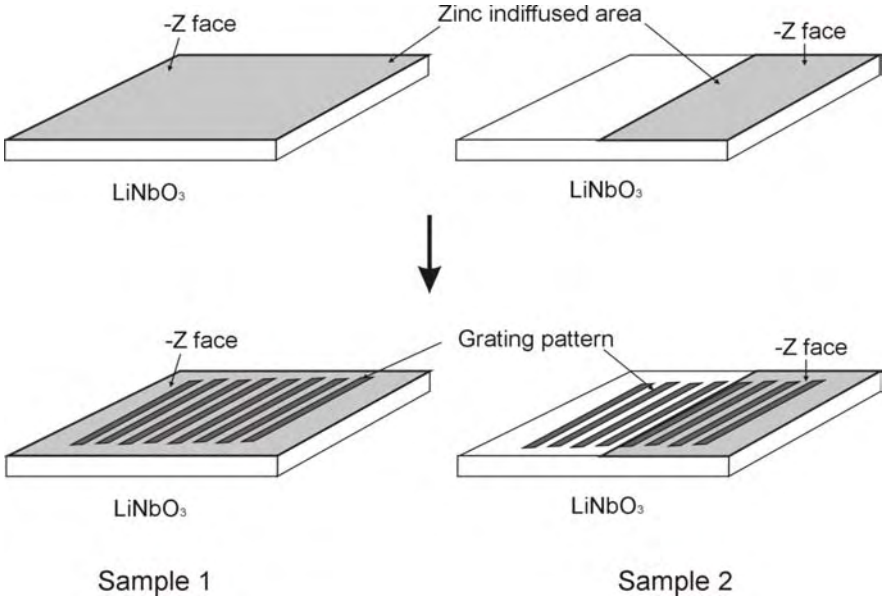


**Figure 6.11.** Schematic drawings of the two $LiNbO_3$ samples that were patterned and poled. Zinc films were deposited and indiffused on whole -*z* face of sample 1, and on half the -*z* face of sample 2.

After poling, it was found that in sample 2, the region without zinc indiffusion poled first (and the grating was totally over poled), followed by the boundary region between the diffused and non-diffused region, then the region that zinc was diffused (the grating itself was almost unpoled). In sample 1, even though the grating was poled (with a slightly higher poling voltage), it appeared that the domains did not follow the grating pattern, and the quality of the PPLN was very poor.

From the above mentioned experiments, it is believed that the poor PPLN structure within the waveguide area is due to the presence of a thin $Li_2O$ out-diffusion induced domain-inverted layer on the +*z* face which is similar to the case of Ti-diffused $LiNbO_3$. This thin layer will block the electric field poling and result in a poor periodic grating. From Figure 6.10, it is clear that nucleation first happens in non-diffused areas, and the poling electric field for the zinc diffused region is a little

higher than for the non-diffused region, so it is difficult to get good uniformity gratings when poling sample with zinc indiffused regions. Thus route one (poling after diffusion) is not a good solution, and route two, fabrication of Zn waveguide on existing PPLN, was investigated. This method involves poling the sample first, and then fabricating the zinc waveguide afterwards. The detailed procedure is described in following section.

### 6.5.2 Poling before Zinc-diffusion Waveguide Fabrication

This route towards fabricating zinc indiffused PPLN waveguides involved poling the samples with PPLN gratings and then afterwards diffusing in the zinc waveguides.

Six 500µm thick, 18mm by 35mm, congruent lithium niobate samples, were first patterned with gratings of 6-12µm period, and then poled using the technique described in section 4.3.3 of chapter 4. After poling, the samples were completely cleaned by acetone solution in order to remove all the photo-resist, and the conductive gel that could cause contamination and influence the thermal diffusion process.

Channel waveguides of widths 2-10µm, with 100µm separation, were then thermally indiffused on the *-z* face of the PPLN samples in the tube furnace following the steps outlined in section 6.4.3. The diffusion parameters were 80 minutes at 900$^{o}$C and 930$^{o}$C respectively. After thermal indiffusion, the residual stresses caused by the formation of PPLN gratings were not clearly visible under a crossed polariser microscope. It is most likely that the stresses in the crystal at the switched domain boundaries were annealed out due to the high temperatures experienced during diffusion. Figure 6.12 shows a picture of the zinc indiffused waveguide on PPLN substrate without etching under the microscope through crossed polarizers.

In order to make sure that the PPLN is still present after these high temperature treatments, three samples with indiffusion temperature from 900$^{o}$C to 930$^{o}$C were etched in a solution of HF:$HNO_3$ (1:2) for approximately 10 minutes to reveal the domain boundaries. Figure 6.13 show the wet etching result of a 6µm wide zinc-diffused waveguide on PPLN with 10µm period gratings under the microscope.

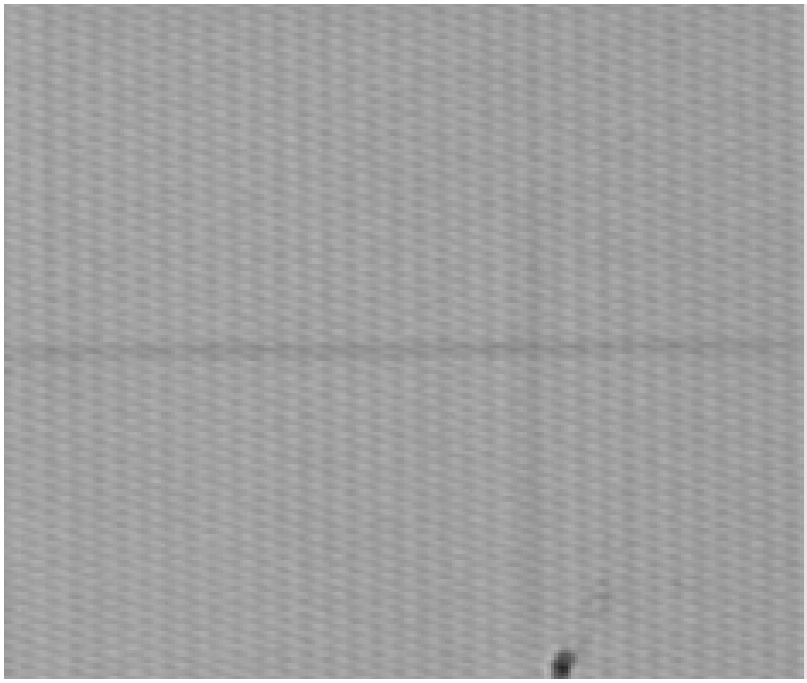

**Figure 6.12.** Poled before thermal diffusion. Zinc indiffused waveguide on PPLN under a crossed polarizer microscope, the period of PPLN is 6.5μm and the waveguide width is around 3.6μm.

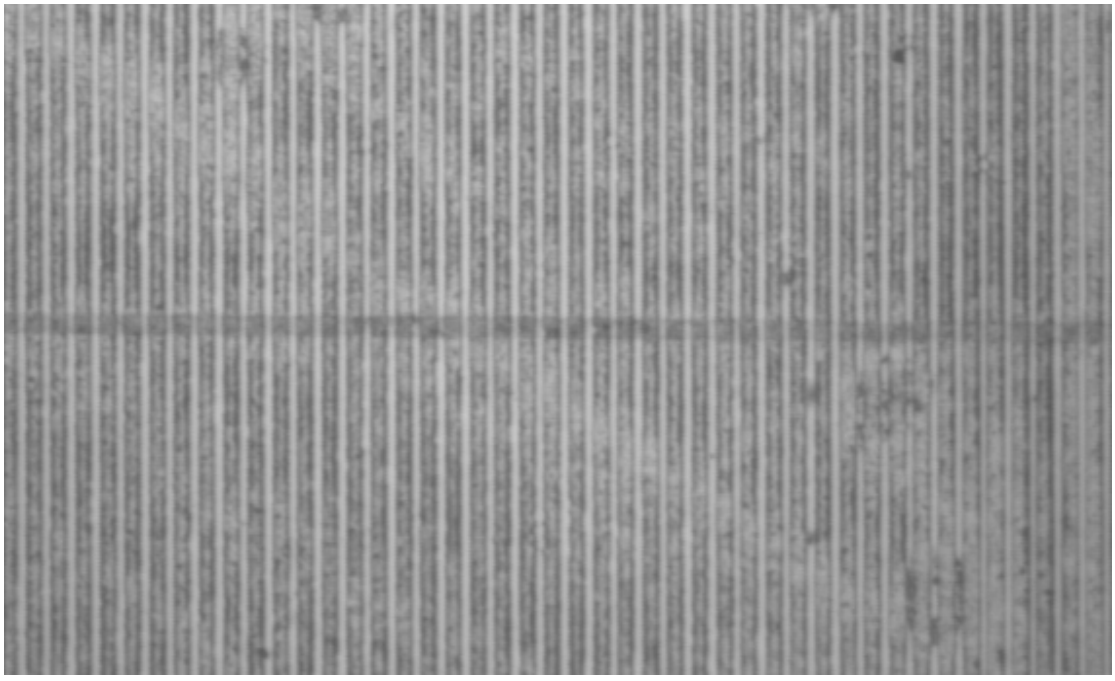

**Figure 6.13.** Poled before thermal diffusion. Zinc indiffused waveguide on PPLN under the microscope after wet etching, The period of PPLN is 10μm and the waveguide is around 6μm. Indiffusion temperature is 930$^{o}$C.

It was found that the diffusion process had not altered the PPLN structure even though the temperature was as high as 930$^{o}$C. The uniformity of the preserved domain

structure of PPLN is not changed over the entire length of the poled sample after the thermal treatment. This result confirms that the periodically inverted domain structure of the PPLN substrate maintains its original form during the diffusion processes.

After waveguide fabrication, the waveguide PPLN samples were cut and the end faces polished to allow optical characterisation. The systematic measurement and characterization of these devices is described in following chapter.

This chapter has reviewed the different fabrication methods of channel waveguides in lithium niobate. Successful fabrication of Zn-diffused waveguides in lithium niobate substrates and formation PPLN waveguides were demonstrated. Various fabrication conditions were investigated, the periodically inverted domain structure and nonlinearity of the PPLN substrate was demonstrated to survive the thermal diffusion processes. The linear and nonlinear optical characterization of the zinc indiffused channel waveguides will be described in chapter 7.

## References

[1] T. Suhara, H. Ishizuki, M. Fujimura and H. Nishihara, "Waveguide Quasi-Phase-Matched Sum-Frequency Generation Device for High-Efficiency Optical Sampling", *IEEE Photon. Technol. Lett*., Vol.**11**, p.1027-1029 (1999)

[2] M. H. Chou, I. Brener, M.M. Fejer, E. E. Chanban and S. B. Christman, "1.5μm-Band Wavelength Conversion Based on Cascaded Second-Order Nonlinearity in $LiNbO_3$ Waveguides", *IEEE Photon. Technol. Lett*., Vol.**11**, p.653-655 (1999)

[3] H. Kanbara, H. Itoh, M. Asobe, K. Noguchi, H. Miyazawa, T. Yanagawa and I. Yokoyama, "All-Optical Switching Based on Cascading of Second-Order Nonlinearities in a Periodically Poled Titanium-Diffused Lithium Niobate Waveguide", *IEEE Photon. Technol. Lett*., Vol.**11**, p.328-330 (1999)

[4] M. Digonnet, M. M. Fejer, and R. L. Byer, "Characterization of proton-exchanged waveguides in MgO:$LiNbO_3$", *Opt. Lett*., Vol.**10**, p.235-237 (1985)

[5] L. Zhang, P. J. Chandler, and P. D. Townsend, "Optical analysis of damage profiles in ion implanted $LiNbO_3$", *Nucl. Instrum. Methods Phys. Res*., B Vol.**59**/**60**, p.1147-1152 (1991)

[6] W. K. Burns, P. H. Klien, E. J. West, L. E. Plew, "Titanium diffusion in Ti:$LiNbO_3$ planar and channel optical waveguides", *J. Appl. Phys*., Vol.**50**, p.6175-6182 (1979)

[7] K. Sugji, M. Fukuma, H. Iwasaki, "A study on Ti diffusion into loin waveguides by electron probe analysis and X-ray diffraction methods", *J. Mater. Sci*., Vol.**13**, p.523-533 (1978)

[8] X. F. Cao, R. V. Ramaswamy, and R. Srivastava, "Characterization of annealed proton exchanged $LiNbO_3$ waveguides for nonlinear frequency conversion", *J. Lightwave Technol*., Vol.**10**, p.1302-1315 (1992)

[9] J. L. Jackel, and J. J. Johnson, "Reverse exchange method for burying proton exchanged waveguides", *Electron. Lett*., Vol.**27**, p.1360-1361 (1991)

[10] Yu. N. Korkishko, V. A. Fedorov, T. M. Morozova, F. Caccavale, F. Gonella, and F. Segato, "Reverse proton exchange for buried waveguides in $LiNbO_3$", *JOSA A.*, Vol.**15**, p.1838-1842 (1998)

[11] S. L. Li, K. M. Wang, F. Chen, X. L. Wang, G. Fu, D. Y. Shen, H. L. Ma, R. Nie "Monomode optical waveguide excited at 1540 nm in $LiNbO_3$ formed by MeV carbon ion implantation at low doses", *Opt. Exp.*, Vol.**12**, p.747-752 (2004)

[12] M. L. Bortz, L. A. Eyres, and M. M. Fejer, "Depth profiling of the $d_{33}$ nonlinear coefficient in annealed proton exchanged $LiNbO_3$ waveguides", *App. Phys. Lett*., Vol.**62**, p.2012-2014 (1993)

[13] J. L. Jackel, J. J. Johnson, "Reverse exchange method for burying proton exchanged waveguides", *Electron. Lett*., Vol.**27**, p.1360-1361 (1991)

[14] L. E. Myers, R. C. Eckardt, M. M. Fejer, R. L. Byer, W. R. Bosenberg, and J. W. Pierce, "Quasi-phase-matched optical parametric oscillators in bulk periodically poled $LiNbO_3$", *J. Opt. Soc. Am*., B Vol.**12**, p.2102-2116 (1995)

[15] A. D. Lallo, A. Cino, C. Conti and G. Assanto, "Second harmonic generation in reverse proton exchanged Lithium Niobate waveguides", *Opt. Exp*., Vol.**8**, p.232-234 (2001)

[16] K. El Hadi, M. Sundheimer, P. Aschieri, P. Baldi, M. P. De Micheli, and D. B. Ostrowsky, "Quasi-phase-matched parametric interactions in proton-exchanged lithium niobate waveguides", *J. Opt. Soc. Am*., Vol.B**14**, p.3197-3203 (1997).

[17] L. Chanvillard, P. Aschieri, P. Baldi, D. B. Ostrowsky, M. De Micheli, L. Huang, and D. J. Bamford, "Soft Proton Exchange on PPLN: a simple waveguide fabrication process for highly efficient non-linear interactions", *Appl. Phys. Lett*., Vol.**76**, p.1089-1091 (2000)

[18] E. Strake, G. P. Bava, I. Montrosset, "Guided modes of Ti:$LiNbO_3$ channel waveguides. A novel quasi-analytical technique in comparison with the scalar finite-element method", *J. Lightwave Technol*., Vol.**6**, p.1126-1135 (1988)

[19] G. Schreiber, H. Suche, Y. L. Lee, W. Grundkötter, V. Quiring, R. Ricken, and W. Sohler, "Efficient Cascaded Difference Frequency Conversion in Periodically Poled Ti:Lithium Niobate Waveguides using Pulsed and CW Pumping", *Appl. Phys*., B Vol.**73**, p.501-504 (2001)

[20] W. M. Young, M. M. Fejer, M. J. F. Digonnet, A. F. Marshall, and R. S. Feigelson, "Fabrication, Characterization and Index Profile Modeling of High-Damage Resistance Zn-Diffused Waveguide in Congruent and MgO:Lithium Niobate", *Lightwave Technol*., Vol.**10**, p.1238-1246 (1992)

[21] R. C. Twu, C. C. Huang, and W. S. Wang, "Zn Indiffusion Waveguide Polarizer on Y-cut $LiNbO_3$ at 1.32μm Wavelength", *IEEE Photon. Technol. Lett*., Vol.**12**, p.161-163 (2000)

[22] T. Suhara, T. Fujieda, M. Fujimura and H. Nishihara, "Fabrication Zn: Lithium Niobate Waveguides by Diffusing ZnO in Low Pressure Atmosphere", *Jpn. J. Appl. Phys*., Vol.**39**, p.L864-L865 (2000)

[23] B. Herreros and G. Lifante, "$LiNbO_3$ Optical Waveguides by Zn diffusion from Vapor Phase", *Appl. Phys. Lett*., Vol.**66**, p.1449-1451 (1995)

[24] R. Nevado, E. Cantelar, G. Lifante and F. Cusso, "Preservation of Periodically Poled Structures in Zn-Diffused Lithium Niobate Waveguides", *Jpn.J.Appl. Phys*., Vol.**39**, p.L488-L489 (2000)

[23] M. Fujimura, H. Ishizuki, T. Suhara and H. Nishihara, "Quasi-phasematched waveguide conversion in Zn-diffused $LiNbO_3$ waveguide," in Proceedings of Conference Lasers and Electro - Optics (CLEO/PR'01), ME1-5, Tech. Digest vol. I, pp. I96-97, Makuhari, July 15-19, (2001).

[26] M. N. Armenise, "Fabrication techniques of lithium niobate waveguides", *IEE. Proc. Part J*, Vol.**135**, p.85-91 (1988)

[27] B. S. Medvedev, V. I. Nalbandyan, A. V. Chinenova, "Ternary System of Niobium, Zinc, and Lithium Oxides", *Inorganic materials*, Vol.**24**, p.830-833 (1988)

[28] T. S. Chernaya, B. A. Maksimov, T. R. Volk, N. M. Rubinina, and V. I. Simonov, "Zn Atoms in Lithium Niobate and Mechanism of Their Insertion into Crystals", *JETP Letters*, Vol.**73**, p.103-106 (2001)

[29] EMIS Data review Series No.5, "Properties of lithium niobate", *INSPEC* London, p.26 (1989)

[30] P. Lerner, C. Legras and J. P. Dumas, *J. Cryst. Growth*, Vol.**3/4**, p.231-235 (1968)

[31] F. P. Safaryan, R. S. Feigelson, A. M. Petrosyan, "An approach to the defect structure analysis of lithium niobate single crystals", *J. Appl. Phys*., Vol.**85**, p.8079-8082 (1999)

[32] D. Xue, K. Betzler, H. Hesse, "Chemical bond analysis of the second order nonlinear optical behavior of Zn-doped lithium niobate", *Opt. Commun*., Vol.**182**, p.167-173 (2000)

[33] L. F. Johnson, A. A. Ballman, "Coherent Emission from Rare Earth Ions in Electro-optic Crystals", *J. Appl. Phys*., Vol.**40**, p.297-302 (1969)

[34] D. A. Bryan, R. Gerson, H. E. Tomaschke, "Increased optical damage resistance in lithium niobate", *Appl. Phys. Lett*., Vol.**44**, p.847-849 (1984)

[35] T. Volk, M. Wohlecke, "Optical Damage Resistance in Lithium Niobate Crystals", *Ferroelectrics Review*, Vol.**1**, p.195-262 (1998)

[36] T. R. Volk, V. J. Pryalkin, N. M. Rubinina, "Optical-damage-resistant $LiNbO_3$:Zn crystal", *Opt. Lett*., Vol.**15**, p.996-998 (1990)

[37] Y. Zhang, Y. H. Xu, M. H. Li, Y. Q. Zhao, "Growth and properties of Zn doped lithium niobate crystal", *Journal of Crystal Growth*, Vol.**233**, p.537-540 (2001)

[38] J. L. Jackel, "Suppression of outdiffusion in titanium diffused $LiNbO_3$: a review", *J. Opt. Commun*., Vol.**3**, p.82-85 (1982)

[39] C. S. Lau, P. K. Wei, C. W. Su, W. S. Wang, "Fabrication of magnesium-oxide induced lithium outdiffusion waveguides", *IEEE Photon. Technol. Lett*., Vol.**4**, p.872-875 (1992)

[40] U. Schlarb, M. Wöhlecke, B. Gather, A. Reichert, K. Betzler, T. Volk, N. Rubinina, "Refractive indices of Zn-doped lithium niobate", *Optical Materials*, Vol.**4**, p.791-795 (1995)

[41] U. Schlarb and K. Betzler, "Influence of the defect structure on the refractive indices of undoped and Mg-doped lithium niobate", *Phys. Rev*., B Vol.**50**, p.751-757 (1994)

[42] W. M. Young, M. M. Fejer, M. J. F. Digonnet, A. F. Marshall, and R. S. Feigelson, "Fabrication, Characterization and Index Profile Modeling of High-Damage Resistance Zn-Diffused Waveguide in Congruent and MgO:Lithium Niobate", *J. Lightwave Technol*., Vol.**10**, p.1238-1246 (1992)

[43] D. W. Yoon and O. Eknoyan, "Characterization of vapour diffused Zn:$LiTaO_3$ optical waveguides", *J. Lightwave Technol*., Vol.**6**, p.877-880 (1988)

# Chapter 7

## Characterization of Zinc Indiffused Waveguides on PPLN

This chapter covers the characterization of the linear and nonlinear optical properties of the zinc indiffused channel waveguides in PPLN. Systematic measurements of the PPLN channel waveguides were made, including mode profiles, numerical aperture (NA), propagation loss, second harmonic generation conversion efficiency and photorefractive effect using a variety of laser sources. Such characterization is vital for optimization and also to allow accurate measurement of nonlinear performance.

### 7.1 Measurement of the Mode Profile versus the Indiffusion Condition

The first measurement made for any waveguide is the mode profile at visible wavelengths. This allows for a rapid measurement of mode size and approximate NA. It also provides a simple visual means of assessing scattering loss, by observation of the waveguide surface.

Characterisation of the zinc indiffused channel waveguides was carried out by using a He-Ne laser ($\lambda$ = 632.8nm) beam which was fibre-butt coupled into the channel waveguides. Before measurements were made the samples were diced into rectangular samples and end polished to provide a high quality launch.

Figure 7.01 show the schematic diagram of the characterization set up. The 10mW power He-Ne laser was coupled into a single-mode optical fibre (core diameter of 6μm) by using a microscope objective 1 ( $f = \times 40$ ), a tuneable attenuator was used to control the power of the input beam. The output beam from the fibre was butt coupled into the zinc indiffused PPLN channel waveguide located on the translation stage 1. The output mode was collected by lens 2 ( $f = \times 10$ ) and was split into two sub-beams using a beam splitting cube, one sub-beam was focused into the CCD camera 2 which was connected to the video monitor. Another sub-beam was focused into CCD camera 1 which was used to detect the mode profile. Bespoke software was used to measure the mode profile, the spot size of the waveguide and the NA, etc. CCD camera 2 is a

conventional video rate CCD, while CCD camera 1 is a slow scan CCD with good linearity and digital output. This combination allows both rapid focussing and high precision measurement. CCD camera 1, CCD camera 2, the beam splitter cube and lens 2 were mounted on a common translation stage in order to fix their relative positions. This makes the alignment easier. Translation stage 2 can be moved along the beam propagation direction so that the near and far field modes profiles and spot sizes can be monitored by CCD camera 2 and recorded by CCD camera 1.

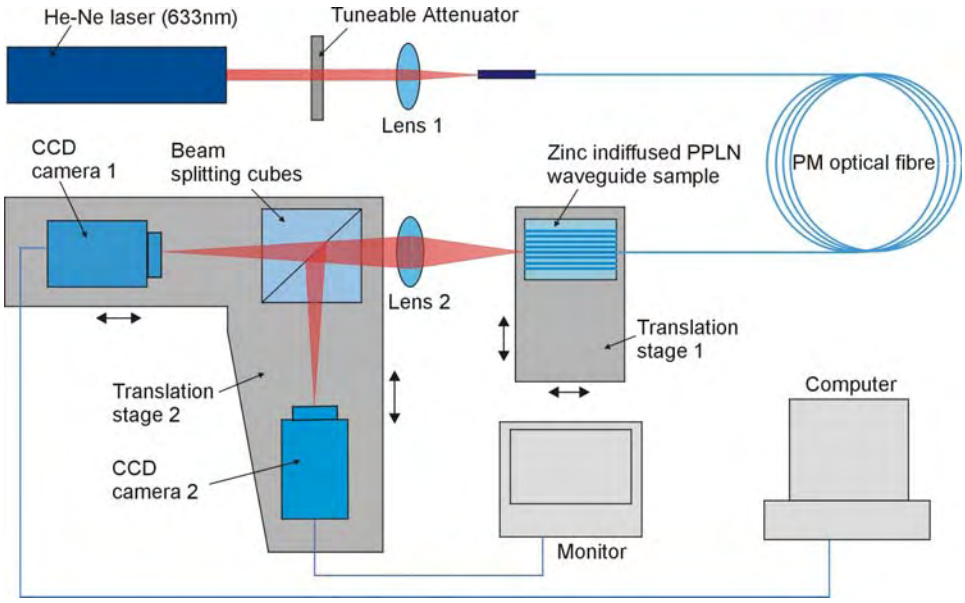


**Figure 7.01.** Schematic diagram of the set up for characterization of mode profile, spot size and numerical aperture (NA).

**Table 7.01** Parameters of thermal indiffusion

| No. | Thickness of Ni film (nm) | Thickness of zinc film (nm) | Diffusion Temp. ( °C ) | Time (min) | Comment |
|---|---|---|---|---|---|
| 1 | 10 | 80 | 600 | 240 | No guide |
| 2 | 10 | 80 | 700 | 180 | Very weak guide |
| 3 | 10 | 80 | 800 | 120 | Weak guide |
| 4 | 10 | 120 | 800 | 120 | Week guide |
| 5 | 10 | 80 | 900 | 80 | Good guide |
| 6 | 10 | 120 | 900 | 120 | Good guide |
| 7 | 10 | 80 | 930 | 80 | Good guide |
| 8 | 10 | 120 | 930 | 120 | Good guide |

The zinc indiffused channel waveguide samples fabricated under the different indiffusion conditions, see Table7.01, were end face polished and characterized. The width of the waveguide (strictly the width of the zinc stripe) ranges from 1um to 10μm with a step of 1μm, the length of the samples are around 10mm, the waveguide

mode profiles were recorded by the video monitor and characterized by the beam profile analyzer software.

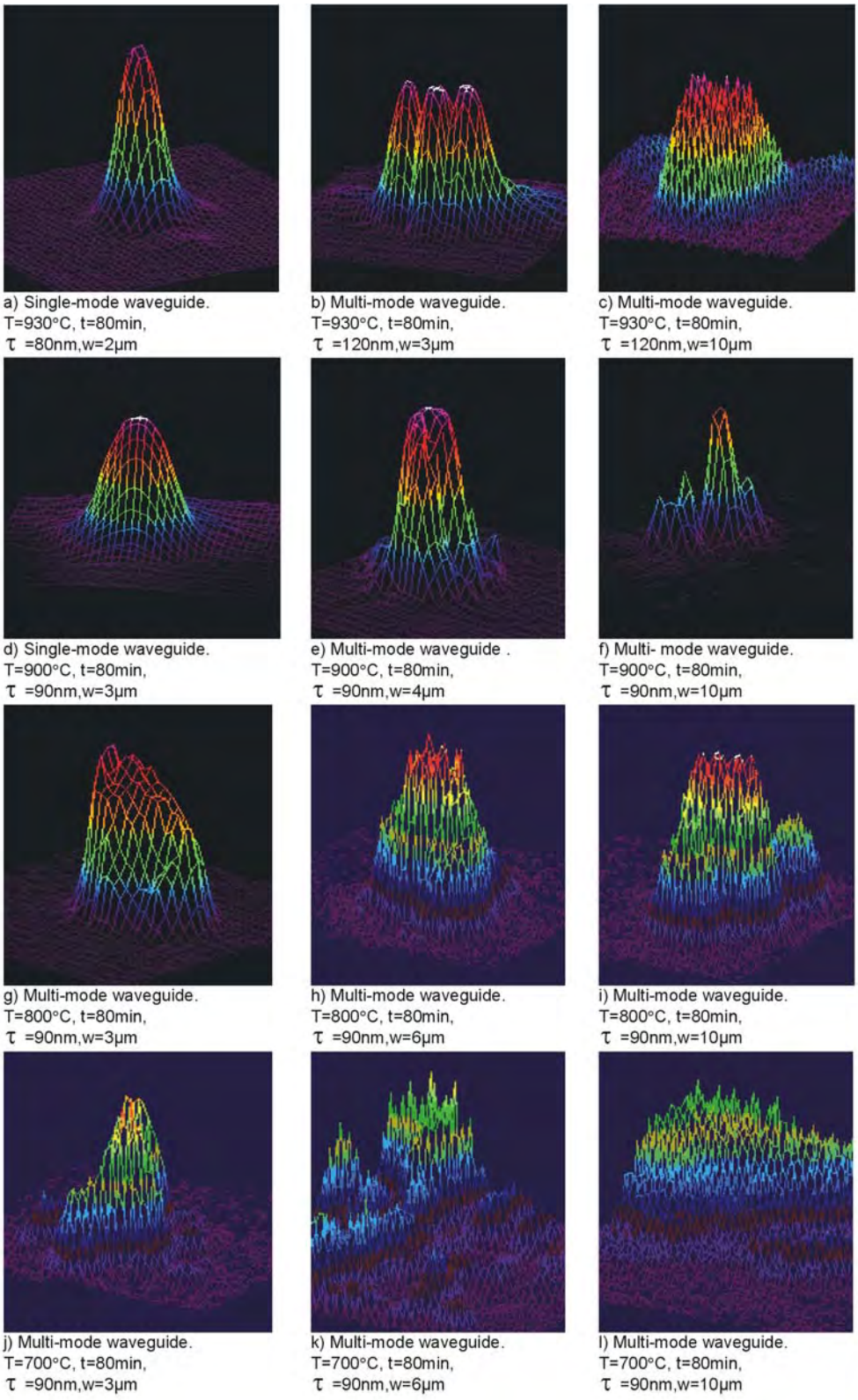


**Figure 7.02.** The mode profiles of the zinc indiffused $LiNbO_3$ waveguide for different thermal indiffusion conditions.

Figure 7.02 show the recorded 3-D mode profiles from zinc indiffused channel waveguides for different indiffusion conditions.

The mode profiles are dependent on the zinc film thickness $\tau$, the diffusion time *t*, diffusion temperature *T*, waveguide width *w* and operation wavelength $\lambda$. From Figure 7.02, the following conclusions can be drawn:

1) Well confined single-mode channel waveguides for a wavelength of 633nm were obtained under the conditions of Figure 7.02(a), (d). When the width of the waveguide increased, the guided beam changed from single-mode to multi-mode, see Figure 7.02(b), (c), (e), (f).
2) Well confined multi-mode channel waveguides were achieved at an indiffusion temperature of 800ºC for a 3µm width waveguide, see figure 7.02(g). As the width of the waveguide increases, weak multi-mode waveguides were obtained, see Figure 7.02(h), (i).
3) Very weak multi-mode waveguides were observed for thermal diffusion at a temperature of 700ºC, under this temperature the zinc is not fully indiffused into the surface of the $LiNbO_3$, see Figure 7.02(j), (k), (l).
4) No channel waveguides were observed at a thermal indiffusion temperature of 600ºC, even though the indiffusion time was extended to 240 minutes. Under this temperature, the zinc film simply cannot be indiffused into the lithium niobate.

## 7.2 Characterization of Polarization Dependence

The polarization dependence was characterized using a polarized 1552.4nm laser source, Figure 7.03 show the schematic diagram of the characterization set up.

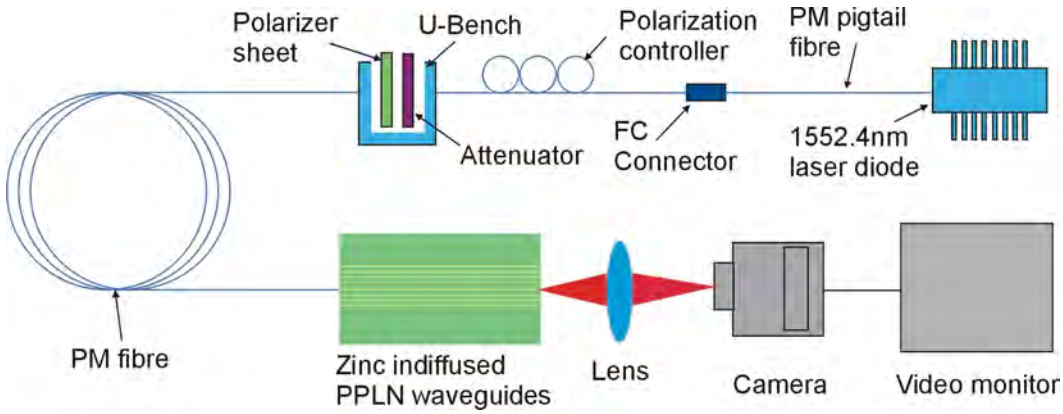


**Figure 7.03.** Schematic diagram of the set up for characterization of polarization dependence.

A 10mW 1552.4nm wavelength semiconductor laser diode with a polarization maintaining pigtailed fibre was connected to a polarization controller using a standard FC connector, an optical U-bench was inserted between the launch fibre and the polarization controller. The polarization direction of the launched beam was modified and controlled by the polarization controller and the polarizing sheet inside the U-bench. An attenuator was used to keep the beam power constant for the TE mode (polarization direction horizontal to the surface of sample) and TM mode (polarization direction normal to the surface of sample). The mode profiles were observed on the monitor, and the output powers were measured by using a power meter.

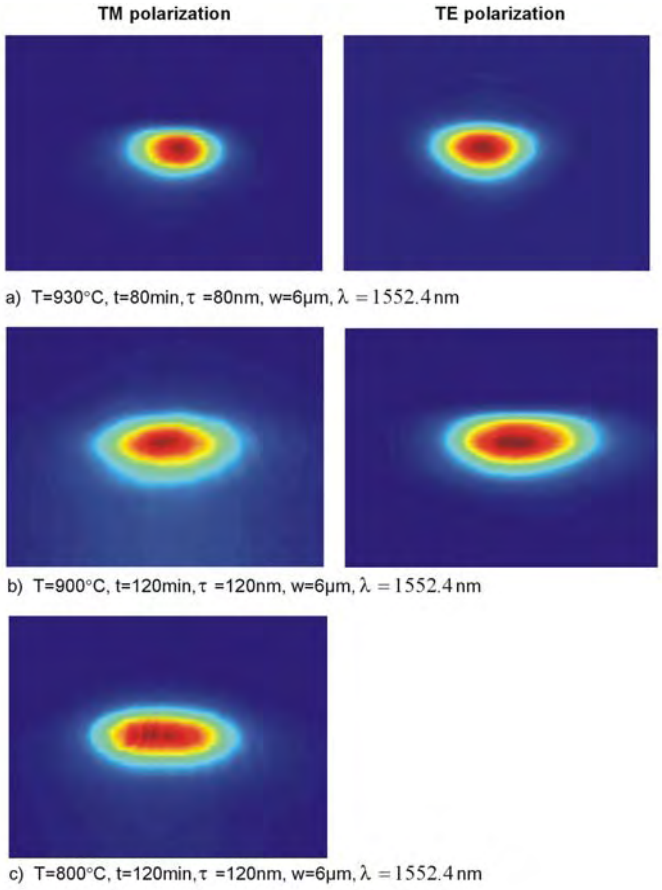


**Figure 7.04.** The mode profile of the TM and TE modes for zinc indiffused waveguides fabricated under different conditions.

As 1550nm is the most important wavelength for telecom applications, an effort was made to optimize for this wavelength for single-mode operation. The polarization measurements also concentrated on this wavelength. Figure 7.04 shows the TM and TE mode profiles for different indiffusion conditions. From Figure 7.04, it is clear that:

1. Both TE and TM mode are guided in the zinc waveguides thermally indiffused at temperatures of 900°C or above. The spot size of the TE mode is slightly larger than that of the TM mode, see Figure 7.04(a), (b).
2. Only the TM mode is confined in the zinc waveguide thermally indiffused at a temperature of 800°C. The TE mode is not guided at all, see Figure 7.04(c).
3. No well confined TM mode is guided in the zinc waveguide indiffused at a temperature of 700°C or lower. Again, the TE mode is not guided at all.

The above experiments show that the zinc indiffused waveguides support both TM and TE mode at 1550nm wavelength when the indiffusion is carried out at, or above, 900°C. Below this temperature, but above 800°C, only the TM mode is confined in the waveguide.

## 7.3 Measurement of the Spot Size and Numerical Aperture

The numerical aperture (NA) of a step index waveguide is defined by following equation [1]:

$$NA = \left(n_1^2 - n_2^2\right)^{1/2} \qquad 7.01$$

Where $n_1, n_2$ represent the refractive index at the core and the substrate of the waveguide respectively. From the above equation, a representation of the refractive index profile in the core can be obtained through the measurement of the numerical aperture (NA).

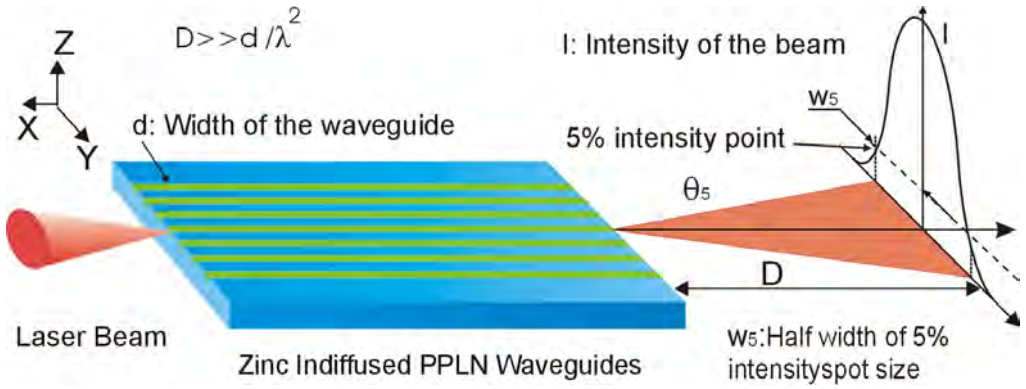


**Figure 7.05.** Far-field technique for the measurement of NA of zinc indiffused PPLN waveguide.

A direct measurement of NA can be obtained by measuring the mode profile at the far field of the waveguide (see Figure 7.05). When $D >> d / \lambda^2$, the NA is given by [1]:

$$NA = \sin\theta_5 = \frac{w_5}{\sqrt{D^2 + w_5^2}} \qquad 7.02$$

Where, $D$ is the distance of the measurement point to exit facet; $d$ is the width of the waveguide; $w_5$ is the half width of 5% intensity spot size at a distance $D$ from the exit facet; $\theta_5$ is the angle between the axis and the 5% intensity point.

The spot size and NA of the waveguide were characterized using the set up shown in Figure 7.01 at 633nm wavelength. The translation stage 2 was moved along the beam propagation direction so that the spot sizes were measured through the near field technique and the NAs were measured using the far field technique, see Table 7.02.

**Table 7.02**. NA and spot size of waveguide versus indiffusion condition, $\lambda$=633nm, Width=2μm

| No. | Time (min) | Thickness (nm) | Diffusion Temp. (°C ) | Width (μm) | Spot size -*y* (μm) | Spot size -*z* (μm) | NA -*y* | NA -*z* |
|---|---|---|---|---|---|---|---|---|
| 1 | 80 | 80 | 930 | 2 | 4.09 | 3.26 | 0.079 | 0.105 |
| 2 | 120 | 80 | 930 | 2 | 4.74 | 3.51 | 0.074 | 0.094 |
| 3 | 150 | 80 | 930 | 2 | 6.34 | 3.71 | 0.064 | 0.082 |
| 4 | 180 | 80 | 930 | 2 | 6.87 | 3.96 | 0.050 | 0.080 |
| 5 | 80 | 80 | 900 | 2 | 4.34 | 3.11 | 0.093 | 0.104 |
| 6 | 120 | 100 | 930 | 2 | 4.43 | 3.23 | 0.080 | 0.109 |
| 7 | 120 | 120 | 930 | 2 | 3.81 | 3.14 | 0.089 | 0.115 |
| 8 | 120 | 150 | 930 | 2 | 3.49 | 3.06 | 0.090 | 0.120 |

Figure 7.06 shows the TM and TE mode profiles for a specific channel waveguide (No.2 in Table 7.02). Here, the width of the deposited zinc was 2.0μm, the waveguide was single moded and supports both TM and TE mode at 633nm wavelength.

The width ( $w_5$ ) of the far-field mode profile of this waveguide was recorded at different distances $D$, the NAs were then calculated using Eq.(7.02) and are listed in Table 7.03. The value for $n_2$ at 633nm is based on Eq.(3.02) and $n_1$ is calculated based on Eq.(7.01).

**Table 7.03** Calculated refractive index change and NA at different distance $D$

| $D$ (μm) | $w_5$-$y$ (μm) | $w_5$-$z$ (μm) | NA -$y$ | NA -$z$ | $n_2$ (633nm) | $n_1$-$y$ (633nm) | $n_1$-$z$ (633nm) | $\Delta n$ -$y$ | $\Delta n$ -$z$ |
|---|---|---|---|---|---|---|---|---|---|
| 0 | 3.5 | 2.5 | | | | | | | |
| 25.4 | 5 | 4 | 0.193 | 0.156 | 2.2027 | 2.2111 | 2.2082 | 0.0084 | 0.0055 |
| 50.8 | 6 | 5.5 | 0.12 | 0.107 | 2.2027 | 2.2059 | 2.2052 | 0.0032 | 0.0025 |
| 76.2 | 7 | 8 | 0.091 | 0.104 | 2.2027 | 2.2045 | 2.2051 | 0.0018 | 0.0024 |
| 101.6 | 9.2 | 10 | 0.09 | 0.097 | 2.2027 | 2.2045 | 2.2048 | 0.0018 | 0.0021 |
| 127 | 11 | 13 | 0.086 | 0.101 | 2.2027 | 2.2043 | 2.2050 | 0.0016 | 0.0023 |
| 254 | 21.4 | 25.6 | 0.084 | 0.1 | 2.2027 | 2.2043 | 2.2049 | 0.0016 | 0.0022 |

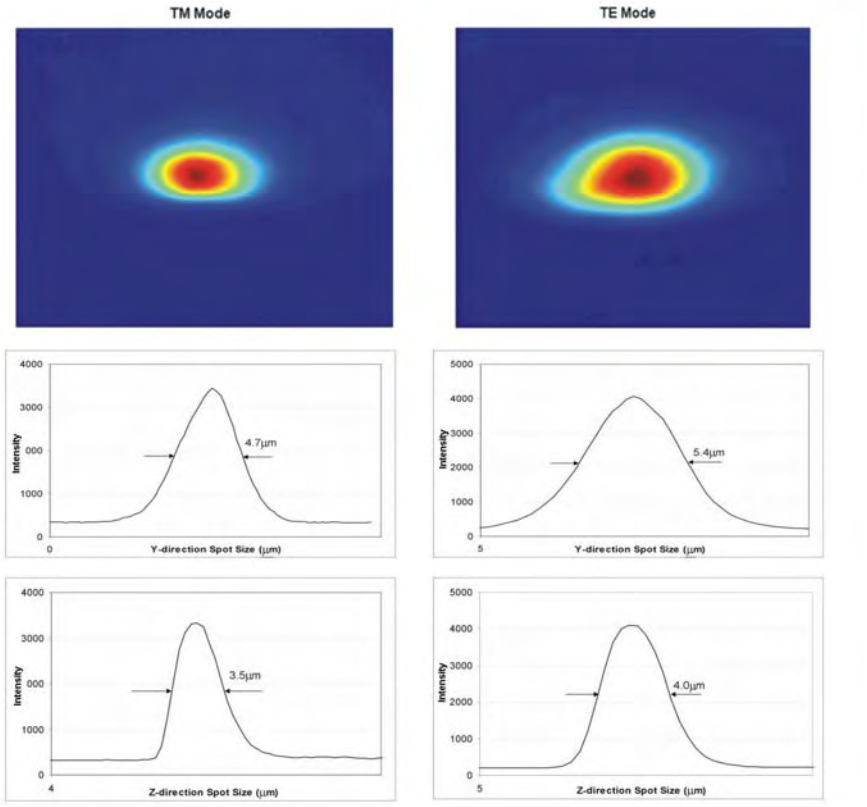


**Figure 7.06.** TM and TE mode profiles of waveguides on sample No 2, the width of the deposited metal strip was 2.0μm, the guide is single mode with a spot size of 4μm in *y* direction and 2.5μm in *z* direction for TM mode and 4.3μm in *y* direction and 3.5μm in *z* direction for TE mode.

Figure 7.07 shows the dependence of the spot size (for sample No.2) on the distance $D$. Obviously larger distances lead to larger spots, and, in turn, give a better estimate of the NA. When the distance $D >> d$ (core size of waveguide), the NA tends to be a constant figure which is 0.08 in *y* direction and 0.11 in *z* direction. This indicates that the refractive index change $\Delta n$ of sample No.2 is around 0.0015 in the *y*-direction and 0.0025 in the *z*-direction, Figure 7.08.

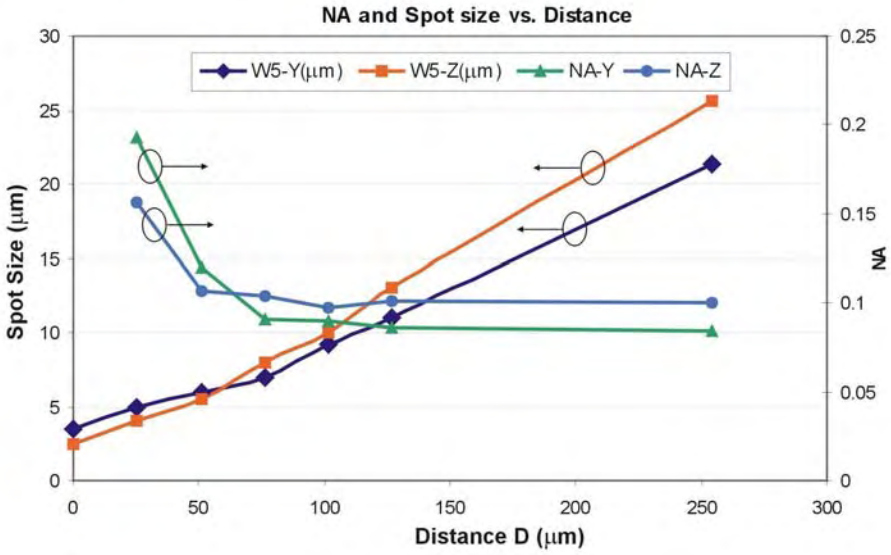


**Figure 7.07.** Dependence of the spot size and the calculated NA on distance between the measurement point of CCD camera to the focusing point of output beam.

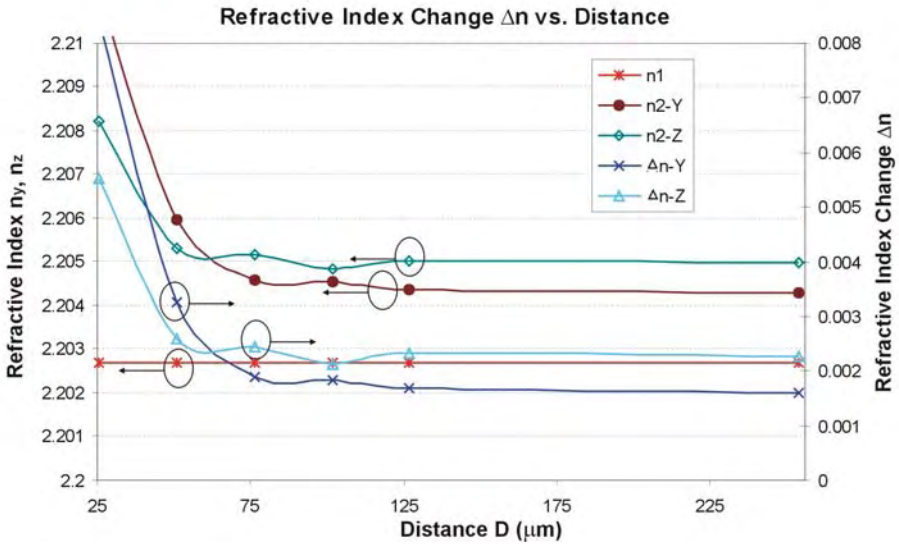


**Figure 7.08.** Dependence of the calculated refractive index and the refractive index change on distance between the measurement points to the focusing point of the output beam.

To provide a cross check for the numerical aperture data, the effective refractive index of the zinc indiffused waveguide was also measured using a prism coupling method. This gave a $n_e$ value of 2.2062 for TM0 mode and 2.2045 for the TM1 mode at 633nm wavelength. This figure is slightly higher than that measured by the NA method, a possible explanation is that prism coupling selects a particular mode (the fundamental mode) whereas the NA measurement looks at the average of all the modes at 633nm. As the fundamental mode has the highest refractive index, it is plausible that the NA measurement should be lower.

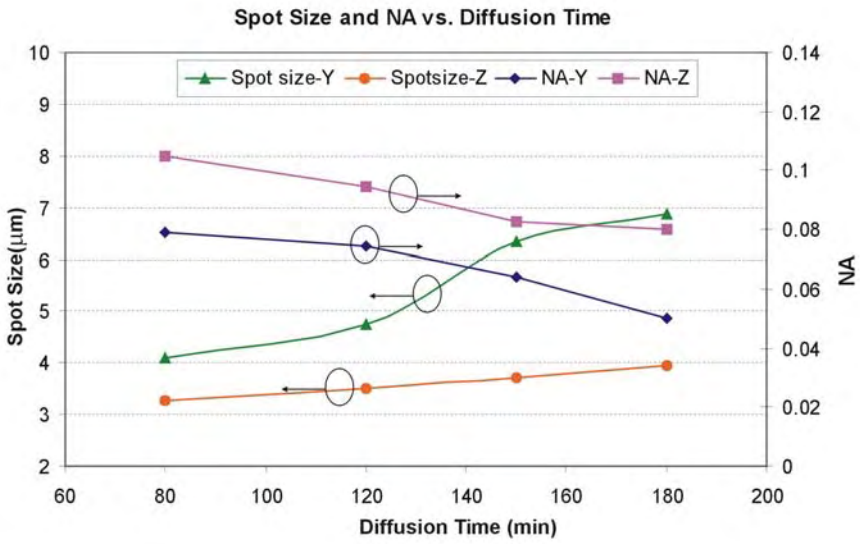


**Figure 7.09.** Dependence of FWHM spot size and NA on diffusion times.

Figure 7.09 shows the dependence of the full width half maximum spot size (FWHM) and the NA on diffusion time, which varied from 80min to 180min. In all cases, the thickness of the Zn films were 80nm and the diffusion temperature was 930°C. Longer diffusion times give larger spot sizes and a smaller NA. It is observed that the spot size change in the *z* direction with longer diffusion times is smaller than it is in the *y* direction, the reason for this is not clear and would require further study.

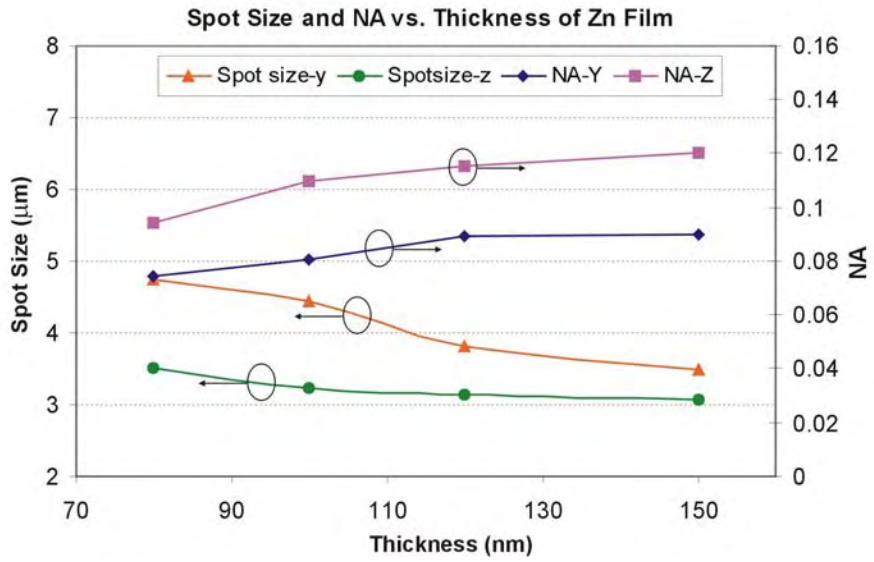


**Figure 7.10.** Dependence of FWHM spot size and NA on thickness of the Zn film.

The dependence of the FWHM spot size and the NA on the thickness of the Zn film (which varied from 80nm to 150nm) was also characterized, see Figure 7.10. The samples were indiffused at a temperature of 930°C for 120min. The dependence of

the width of single mode channel waveguides for different wavelengths as a function of diffusion time at a fixed diffusion temperature of 930°C is shown in Figure 7.11, with a Zn film that was 120nm thick.

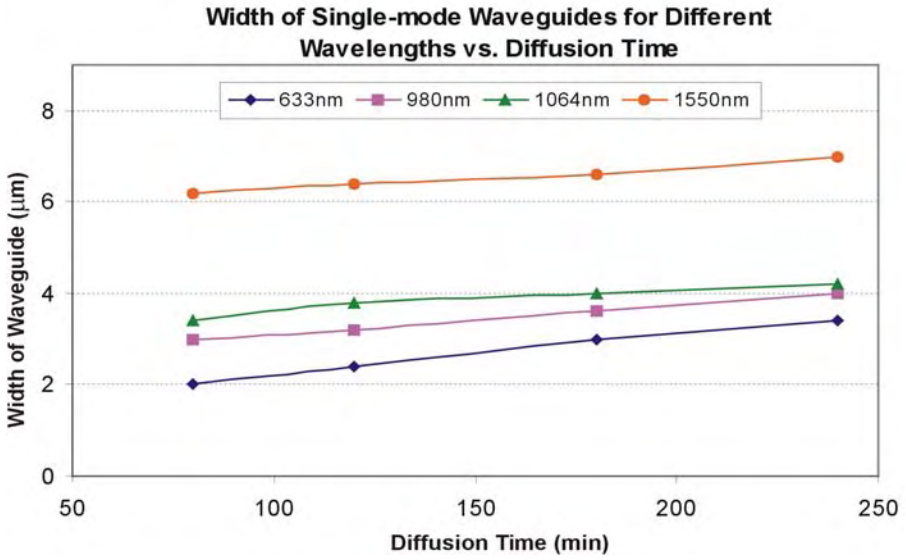


**Figure 7.11.** Dependence of the width of the single mode waveguide for different wavelengths on the diffusion times.

From Figure 7.10, it is clear that when a thicker Zn film is deposited, a smaller mode spot size is obtained with better confinement in the waveguide. This in turn leads to a higher optical intensity confined within the waveguide core. However, a thicker Zn film results in a rougher surface due to the Zn remnant (which is probably caused by Zn–$LiNbO_3$ reaction in the air), so resulting in a higher propagation loss due to the scattering of light on the waveguide surface. When the Zn film is over 150nm, the remnant on surface is much rougher than that occurring with 120nm of zinc.

From Figure 7.09 to Figure 7.11, it is clear that fabrication of channel waveguides for different wavelengths requires different diffusion conditions, samples with a thicker Zn film diffused for a shorter time are better for the fabrication of single mode channel waveguides with strong confinement and small spot size, but thinner Zn films and longer diffusion times are better for single-mode channel waveguides with smaller NAs and larger spot sizes. The trade-off of diffusion conditions for fabrication of single mode channel waveguides for wavelengths of 980nm, 1064nm and 1550nm are listed in Table 7.04.

**Table7.04** Trade off diffusion conditions of Waveguide fabrication for different wavelengths.

| Wavelength (nm) | Thickness of zinc layer (nm) | Diffusion time (min) | Diffusion Temp. (C°) | Deposited zinc strip width (μm) |
|---|---|---|---|---|
| 633 | 80 | 80 | 930 | 2.0 |
| 980 | 80 | 80 | 930 | 3.2 |
| 1064 | 80 | 120 | 930 | 3.6 |
| 1550 | 120 | 120 | 930 | 6.4 |

## 7.4 Measurement of the Propagation Loss

The cut back method was used to measure the propagation loss. Normally, the total insertion loss of a waveguide ($L_T$) includes the coupling loss $Lc$, the propagation loss $L_P$ and the reflection loss $L_R$ at both end-faces of waveguide. This can be presented as Eq.(7.03) [2].

$$L_T = L_C + L_P + L_R \qquad 7.03$$

First we measure the total loss of the waveguide $L_{T1}$ of a sample with length $S_1$, then we cut and polish the sample along a line parallel with end face, and then re-measure the total loss $L_{T2}$ with length $S_2$, the length of section being cut is $S_3$, see Figure 7.12, based on Eq.(7.03), we can get the propagation loss:

$$L_{T1} = L_{C1} + L_{P1} + L_{R1}; \quad L_{T2} = L_{C2} + L_{P2} + L_{R2};$$

Due to: $L_{C1} \approx L_{C2}; \quad L_{R1} \approx L_{R2}$

(assuming the quality of the polish is similar)

We Have: $L_{T1} - L_{T2} = L_{P1} - L_{P2} = L_{P3}$ 7.04

Propagation loss: $\alpha = L_{P3} / S_3$ 7.05

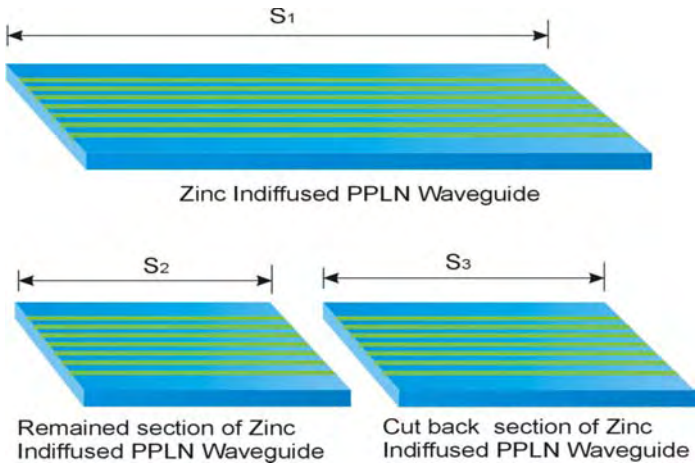


**Figure 7.12.** The cut back techniques for measurement of propagation loss of zinc indiffused PPLN waveguide.

Obviously, the more sections the sample is cut into, the more accurate the propagation loss will be. The calculated results are listed in Table 7.05.

The reason for the high propagation loss of waveguides on sample No.1, 4, 5, 6 is that after the thermal indiffusion, metal remnants were left on the surface of the sample, and it is difficult to remove these remnants. The remnant can be reduced by increasing the indiffusion temperature and decreasing the thickness of the zinc film.

**Table 7.05** The propagation loss of zinc indiffused waveguide.

| No. | Time (min) | Thickness (nm) | Diffusion Temp. (°C ) | Width (μm) | Wavelength (nm) | Loss $L_P$ (dB/cm) | Length (mm) |
|---|---|---|---|---|---|---|---|
| 1 | 80 | 80 | 900 | 6.4 | 1552.4 | 1.2 | 20 |
| 2 | 80 | 120 | 930 | 6.4 | 1552.4 | 0.9 | 20 |
| 3 | 120 | 120 | 930 | 6.4 | 1552.4 | 0.85 | 20 |
| 4 | 120 | 150 | 930 | 6.4 | 1552.4 | 1.22 | 20 |
| 5 | 120 | 180 | 930 | 6.4 | 1552.4 | 1.3 | 20 |
| 6 | 120 | 200 | 930 | 6.4 | 1552.4 | 1.35 | 20 |

**Table 7.06** Comparison of the propagation losses between the different methods

| Method | $\lambda$ (nm) | Loss (dB/cm) | Ref. |
|---|---|---|---|
| Metallic Zinc indiffused waveguide | 1550 | 0.85~1 | |
| Vapor phase zinc indiffused waveguide | 1550 | 1 | [3] |
| Ti-indiffused waveguide | 1550 | 0.15 | [4] |
| Annealed proton exchange waveguide | 1550 | 0.35~0.4 | [5] |
| Soft proton exchange waveguide | 1550 | 0.3 | [6] |

Table 7.06 shows the comparison of the propagation loss of the zinc indiffused waveguide with Ti-indiffused and proton exchange waveguides. The propagation loss of our zinc indiffused waveguides at 1550nm wavelength is higher than that of Ti-diffused and proton exchange waveguides in lithium niobate, and so zinc indiffused waveguides are not suitable for integrated OPO devices which require very low losses, but maybe acceptable as “low loss” waveguides for SHG devices.

## 7.5 SHG Conversion Efficiency

In the preceding sections results on waveguide mode size, NA and loss have shown how compromises must be made to achieve low losses and reasonable modal confinement. In this section these optimised waveguides are characterized for nonlinear conversion efficiency.

A DFB single-mode laser diode with a polarization maintaining pigtailed fibre (central wavelength of 1552.4nm) was used to study how effectively periodic poling would be preserved inside the Zn waveguide after thermal diffusion, which is a necessity for quasi-phase-matched second harmonic generation (SHG).

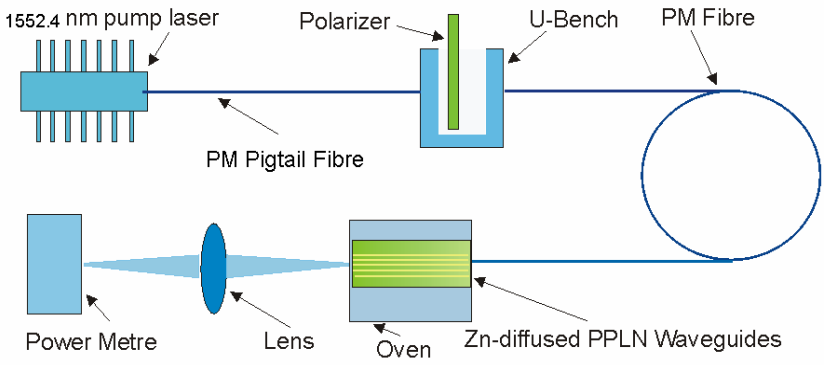


**Figure 7.13.** Schematic diagram of the set up for characterization of SHG for the 1552.4nm wavelength.

A schematic diagram of the set up is shown in Figure 7.13. The incident beam was TM polarized in order to take advantage of the nonlinear susceptibility coefficient $d_{33}$. Fibre was used to couple the incident beam into the channel waveguide in the PPLN samples which were put in a temperature tuneable oven. The mode profile of the SHG (776.2nm) from the waveguide was recorded using a CCD camera and the output power of the SHG was measured as a function of temperature. NA and refractive index change $\Delta n$ of the PPLN waveguides samples listed in Table 7.07 have been measured and calculated based on the methods described in section 7.3 of this chapter. The periods of PPLN varied from 18.05μm to 18.70μm with a step of 0.05μm and the width of the waveguide ranged from 5.6μm to 6.6μm with a step of 0.2μm. All samples were cut and end polished.

**Table 7.07** Fabrication parameters of PPLN waveguide samples

| No. | Time (min) | Thickness (nm) | Diffusion Temp.(°C ) | Width of waveguide(μm) | Grating Λ (μm) | Length (mm) | NA-z | $\Delta n$ |
|---|---|---|---|---|---|---|---|---|
| 1 | 120 | 120 | 930 | 5.6-6.6 | 18.05-18.6 | 10 | 0.115 | 0.003 |
| 2 | 120 | 120 | 930 | 5.6-6.6 | 18.5-18.7 | 10 | 0.112 | 0.003 |
| 3 | 80 | 120 | 930 | 5.6-6.6 | 18.5-18.7 | 10 | 0.082 | 0.002 |

The waveguides in above mentioned samples are single-mode waveguides for the fundamental beam ($\lambda$ = 1552.4nm) and multi-mode waveguides for the SHG beam ($\lambda$ = 776.2nm), the number of modes and the mode profiles can be simulated based on the effective index method described in chapter 5.

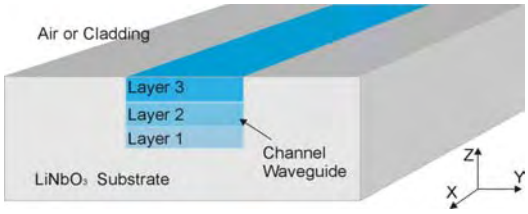


**Figure 7.14.** Three-layer channel waveguide structure model.

In order to simplify the simulation, a three-layer channel waveguide structure model, see Figure 7.14, has been built based on the parameters listed in Table 7.08, this waveguide model was used only to predict the number of the SHG modes and the mode profiles supported in the waveguide, the theoretical value of the SHG conversion efficiency was calculated based on the Hermite-Gaussian fitting [10] which gives a more accurate result. The transverse electric field profiles of the fundamental mode and the different SHG modes along the *y*-direction and the *z*-direction supported by the waveguides are shown in Figure 7.15 and Figure 7.16 respectively. The 2-D intensity distribution of the electric field for the modelling of the fundamental mode and the different SHG modes are shown at the right side of the Figure 7.19. The index values used in this model were determined "by hand" to give a qualitative fit to the measured data.

**Table 7.08** The modelling parameters:

| | **Index *n*** | **Thickness (μm)** |
|---|---|---|
| Cover | 1 | / |
| Layer3 | 2.184 | 2 |
| Layer2 | 2.181 | 3 |
| Layer1 | 2.180 | 2 |
| Substrate | 2.178 | / |
| Wavelength | 1552.4nm | 776.2nm |
| Total Depth of 3-layer | 7μm | |
| Width | 6.6μm | |

Figure 7.17 and Figure 7.18 show the different SHG powers and mode profiles based on tuning the temperature for different periods of PPLN waveguide. SHG quasi-phase matching (QPM) curves as a function of temperature were recorded for the TM00 mode at the fundamental wavelength to the different phase-matching modes at the SHG wavelength.

TM00, TM01 and TM02 of the SHG modes were recorded for sample No.1, TM10, TM11 and TM02 of the SHG modes were obtained for sample No.2. The quasi-phase matching temperature for the TM00, TM01, TM10 modes for SHG for sample No.1

were 14.8°C, 32°C and 58°C respectively, the QPM temperature for the TM02, TM10, TM11 modes for SHG for sample No.2 were 173°C, 183°C, 197 °C respectively.

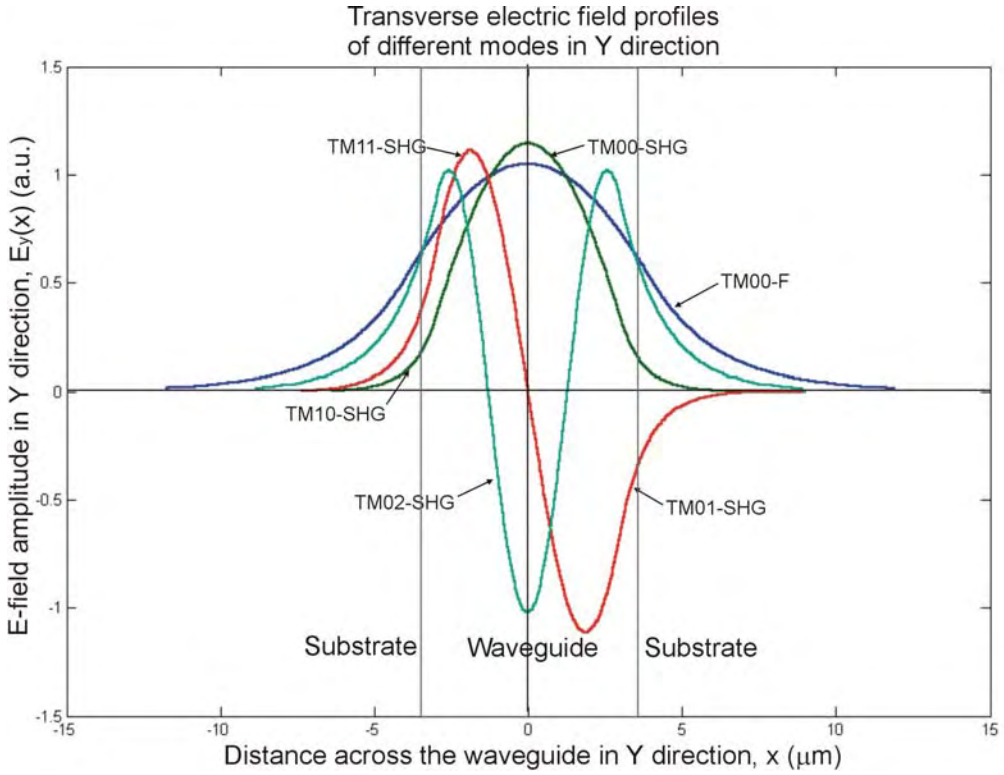


**Figure 7.15.** The transverse electric field profiles of fundamental mode and different SHG modes along *y*-direction.

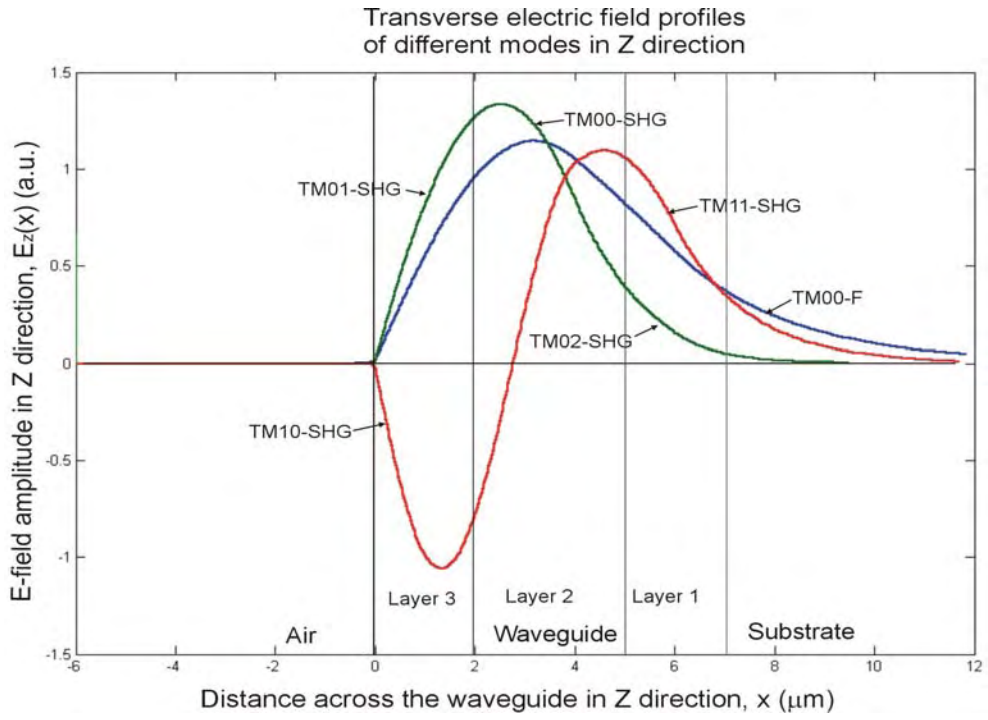


**Figure 7.16.** The transverse electric field profiles of fundamental mode and different SHG modes along *z*-direction.

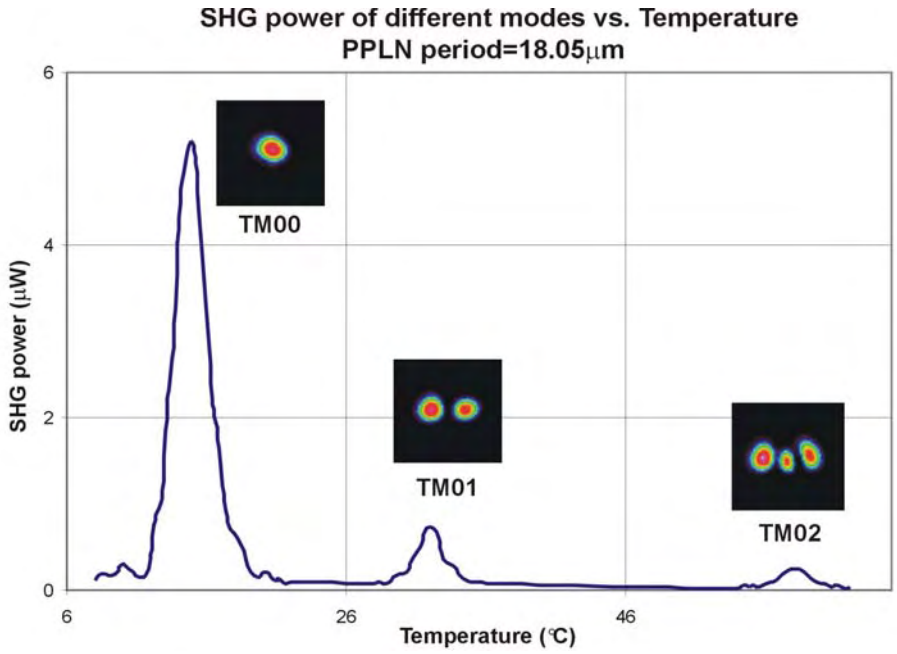


**Figure 7.17.** SHG power of different modes based on the QPM temperature for sample No.1, see Table 7.07. The inset pictures are the measured mode profiles of the different SHG modes.

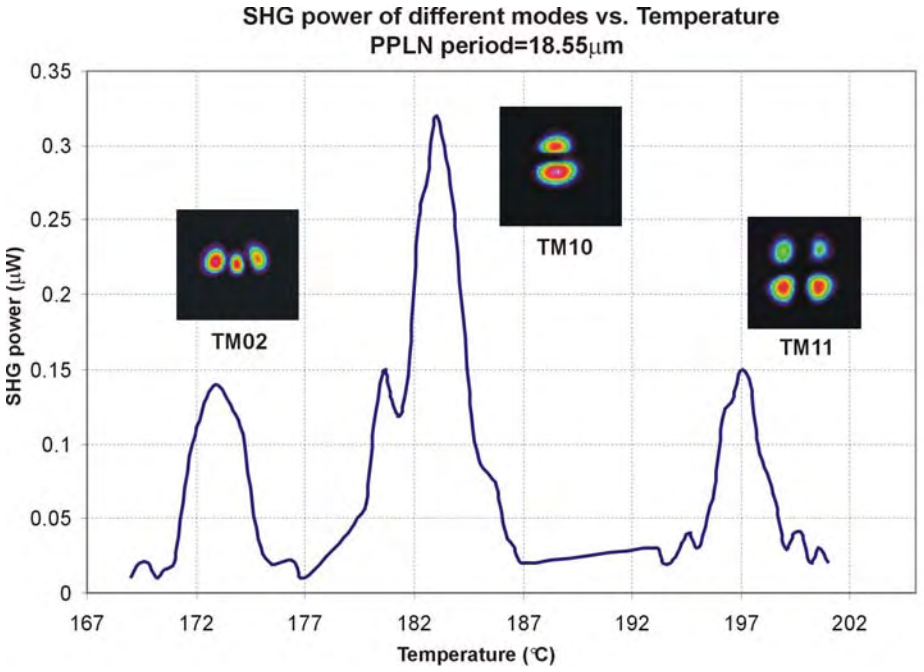


**Figure 7.18.** SHG power of different modes based on the QPM temperature for sample No.2, see Table 7.07. The inset pictures are the measured mode profiles of the different SHG modes.

The maximum SHG output power was recorded for the fundamental TM00 mode to SHG TM00 mode at 14.8°C in sample No.1, the SHG output power of the TM01 or TM02 mode is far lower than that of SHG TM00 mode. Indeed, it is has to be the case because of the symmetric refractive index profile along the horizontal direction, the

interaction overlap between the fundamental TM00 mode and SHG TM00 mode is bigger than that between the fundamental mode and other modes, see Figure 7.15. In fact in a horizontally symmetric waveguide there should be no overlap between the TM00 mode of the fundamental and the TM01 mode of the second harmonic. The fact that this mode was excited indicates that the channel waveguides are not uniform structures due to the thickness variation of the zinc film along the width and the length of the waveguides, thus resulting in an asymmetry in either the refractive index change or the nonlinear coefficient in the waveguides.

No SHG of the TM00 mode was found in sample No.2 and No.3, this is because the QPM temperature for SHG of the TM00 mode converted from 1552.4nm is out of the temperature tuning range of the oven used in this experiment.

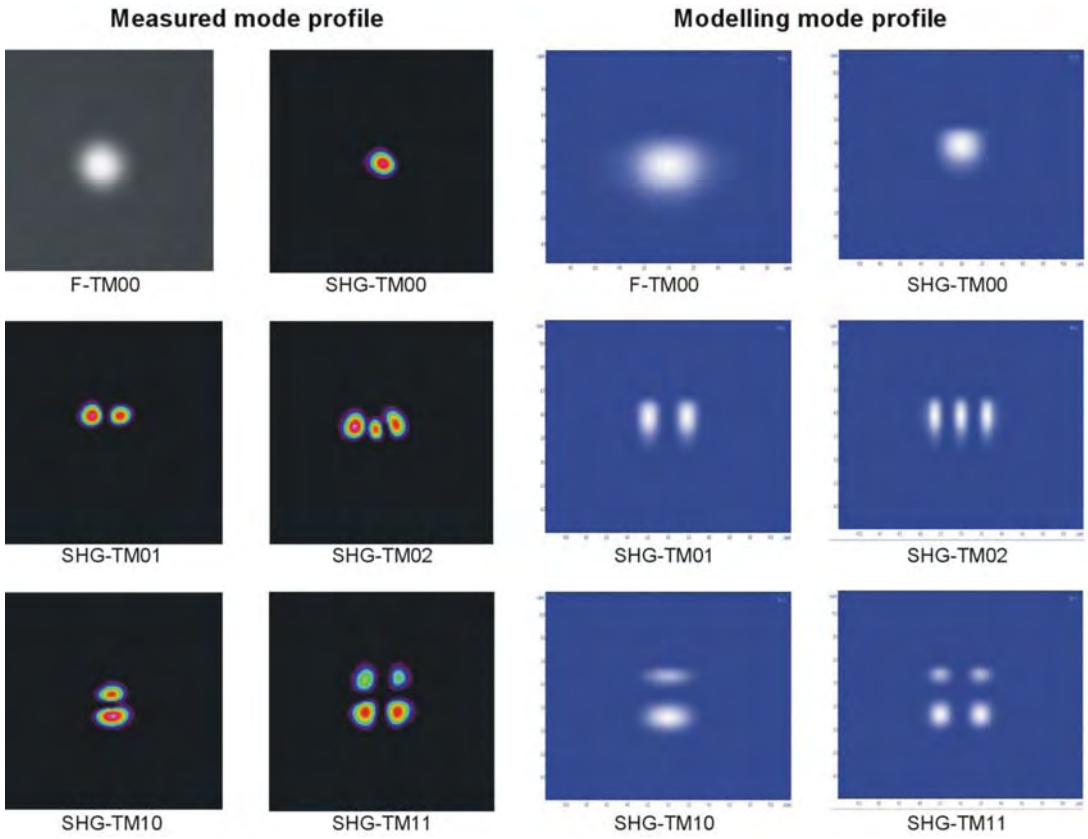


**Figure.7.19.** Different SHG modes converted from the fundamental mode at 1552.4nm wavelength through Zn-PPLN waveguide samples at different QPM temperatures. The mode profiles on the left side were recorded through experiments, the mode profiles on the right side were obtained through simulation based on the modelled waveguide structure.

The left hand side of Figure 7.19 shows all the recorded SHG modes profiles converted from the fundamental beam of sample No.1 and No.2 which are in good agreement with the mode profiles of the simulations based on the waveguide structure model, see Figure 7.14.

It can also be seen from sample No.2 that, for the same input power, the conversion efficiency from the TM00 of the fundamental beam to the TM10 mode of the SHG was higher than that of the TM02 or TM11 modes of the SHG beam. We believe that this is because the overlap area between the fundamental TM00 mode and the TM10 mode of the SHG is larger than that between the fundamental and the TM02 mode or the TM11 mode of the SHG due to the asymmetric profile of the refractive index along the vertical direction, see Figure 7.16.

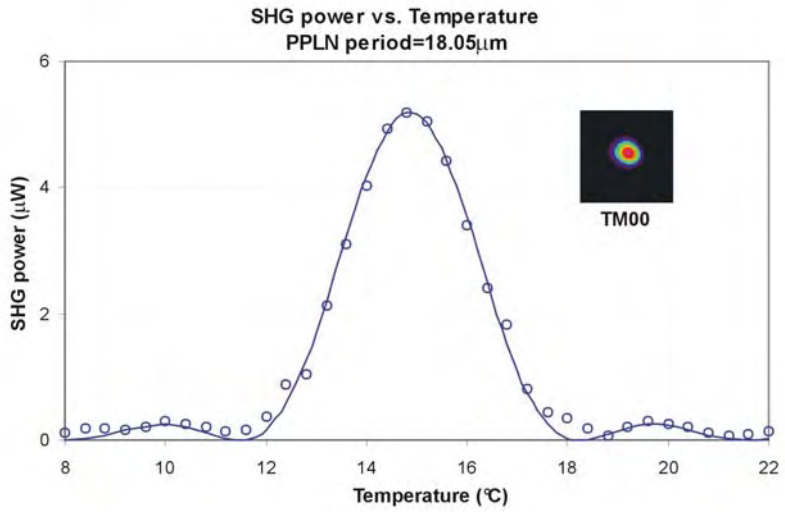


**Figure 7.20.** SHG power vs. QPM temperature for PPLN waveguide ( $\Lambda$ = 18.05μm), the solid line corresponds to a sinc-square function. The inset picture is the mode profile at 776.2nm (TM00 mode).

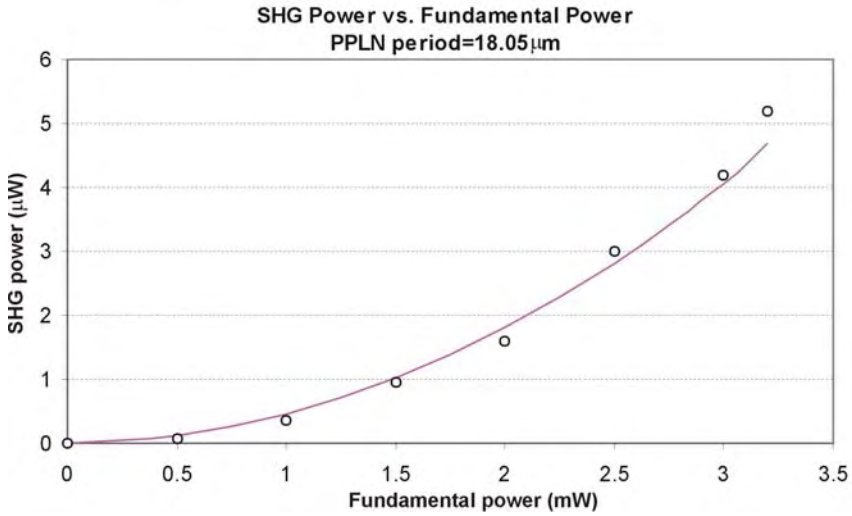


**Figure 7.21.** Second harmonic power as a function of the pump power, the solid line is the best quadratic fit to the measured data points.

A maximum output external SHG power of 5.2μW was recorded for an internal pump power of 3.2mW of the fundamental beam at 14.8°C, allowing for 14% reflection loss

at the two end faces, a conversion efficiency of 59%$W^{-1}\cdot cm^{-2}$ was achieved, see Figure 7.20. The output SHG power as a function of the input pump power was also measured, see Figure 7.21. In comparison to prior techniques, this conversion efficiency is lower than the 150%$W^{-1}\cdot cm^{-2}$ achieved in Reverse Proton Exchange (RPE) waveguides [7] and 130%$W^{-1}\cdot cm^{-2}$ achieved in Soft Proton Exchange (SPE) waveguides (not in SHG) [6], similar to the 65%$W^{-1}\cdot cm^{-2}$ achieved in APE PPLN waveguides [8] and much higher than the 9.4%$W^{-1}\cdot cm^{-2}$ achieved in titanium-indiffused waveguides [9].

The experimental normalized conversion efficiency was also compared to the theoretical value. The normalized SHG conversion efficiency $\eta_{nor}$, defined by $P_{2\omega} = \eta_{nor} L^2 P_\omega^2$, is given by [10] :

$$\eta_{nor} = \frac{8\pi^2 d_{eff}^2}{m^2 n^3 c \varepsilon_0 \lambda_\omega^2} |\upsilon|^2 \qquad 7.06$$

$$\upsilon = \int_{-\infty}^{+\infty}\int_{-\infty}^{+\infty} d(z,y)\left[E_\omega(z,y)\right]^2 E_{2\omega}(z,y)\,dzdy \qquad 7.07$$

where $d_{eff}$ is the effective nonlinear coefficient ($d_{eff} = 2d_{33}/\pi$), $n$ is the effective index of the transverse mode at the fundamental frequency, $m$ is the order of the QPM, $\upsilon$ is the overlap integral of the interacting waveguide modes, $\lambda_\omega$ is the fundamental wavelength, $c$ is the vacuum speed of light, $\varepsilon_0$ is the permittivity of free space. $E(x,y)$ represents the normalized spatial profiles of the transverse waveguide modes at the two wavelengths defined by $\iint E(z,y)^2 dzdy = 1$, $d(z,y)$ is the nonlinear coefficient in the zinc indiffused waveguide normalized to the nonlinear coefficient in the bulk lithium niobate (and thus ranging from 0 to 1).

To calculate the overlap integral in our device, based on our measured mode profiles, a Hermite-Gaussian fit as proposed by Campbell [11] was applied to the measured fundamental and second harmonic field distributions to represent normalised spatial mode profiles at each wavelength. From our experimental data the offset in peak power intensity between the fundamental and SHG fields was measured to be 1μm vertically (z-direction) and 0μm horizontally, such that the second harmonic was generated slightly offset to the fundamental mode. Subsequent analysis of the normalised modal overlap (between the Hermite-Gaussian fitted fundamental mode

and the SHG mode) yields a predicted maximum SHG conversion efficiency of $177\%W^{-1}cm^{-2}$ (see the Matlab code in Appendix A), about 3 times larger than the measured efficiency. This difference is attributed to the asymmetric nature of our real-life mode profiles with their larger offset between overlapping field intensities, and also the potential for local zinc-induced changes in the nonlinear coefficient.

Based on the same mode profile fitting model and the equation used by Franco [12], the coupling efficiency from single mode fibre to the zinc indiffused channel waveguide was calculated. Subsequent simulation and analysis of the normalised modal overlap between the Gaussian fitted mode from single mode fibre (the mode field diameter for 1550nm wavelength is 10.4μm) and Hermite-Gaussian fitted fundamental mode of the zinc indiffused channel waveguide yields a predicted maximum coupling efficiency of 64.4% which is similar with our measured coupling efficiency of 52% (see the Matlab code in Appendix A). The coupling efficiency between the fibre and the channel waveguide can be improved through modifying the mode field diameter (MFD) of the fibre, see Figure 7.22.

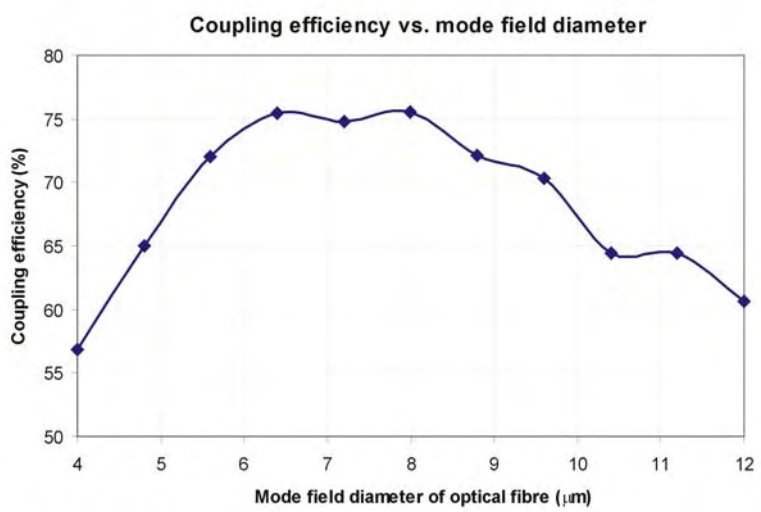


**Figure 7.22**. The coupling efficiency between optical fibre and zinc-diffused channel waveguide dependence on the mode field diameter (MFD) of the launched optical fibre. The wavelength is 1550nm

In addition, the photorefractive effect induced by visible radiation was characterized using an argon laser at 514.5nm. 100μW laser power was coupled into the waveguide using × 20 optic lens at 140°C. The photorefractive effect will cause the output power to drop and fluctuate, after 1 hour of launch, the ratio of the average output power (within 1 minute) to the input power ($P_{out} / P_{in}$) and the ratio of the output power

fluctuation (within 1 minute) to the input power ( $\Delta P_{out} / P_{in}$ ) were measured to be 93% and 5% respectively for PPLN waveguide, 75% and 12% respectively for bulk PPLN sample. This indicates that the influence of the photorefractive effect is indeed reduced by the presence of zinc in the PPLN substrate.

## 7.6 The Quasi-Phase-Matching Curve versus Wavelength

In order to get more information regarding the nonlinear properties of zinc indiffused PPLN waveguides, the quasi-phase-matching (QPM) curve versus the wavelength, was characterized. A tunable laser source with wavelengths range from 1540nm to 1565nm was connected to erbium doped fiber amplifier (EDFA) through a standard G652 single mode fiber, and then coupled into the zinc PPLN waveguide sample which was located inside the oven, a lens was used to focus the output beam from the channel waveguide into the detector. The polarization direction of the launched beam could be modified and controlled by the polarization controller. The SHG power was measured using a power meter. Figure 7.23 show the schematic diagram of the characterization set up.

The period of the PPLN was 18.05nm and the diffusion condition is the same as for sample No.1. Before characterizing the quasi-phase-matching curve versus the wavelength, the fundamental powers of the different wavelengths at point B and point C, see Figure 7.23, have been measured in order to make sure that the incident power at different wavelengths is stable. Figure 7.24 shows that the power variation of different wavelengths at points B and C are less than 3%, the insertion loss of the polarization controller is around 1dB.

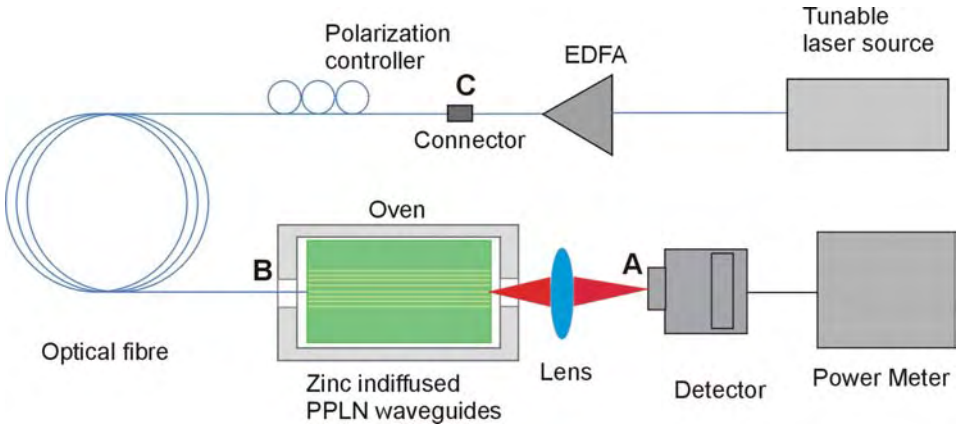


**Figure 7.23.** The schematic diagram of the characterization set up for measurement of QPM curve versus the wavelength.

In order to take advantage of the maximum nonlinear coefficient $d_{33}$, the polarization of the fundamental beam was rotated to be in the TM direction by using a polarization controller. The power ratios of the TM component to the total power of incident beam at different wavelengths were measured by using the 1550nm polarizer sheet inserted at point A. Figure 7.24 shows that the power ratio of the TM component to the fundamental beam after the polarization controller is over 99.5% for different wavelength ranging from 1550nm to 1560nm. This is important for relative SHG characterization based on different wavelengths.

The output power of the SHG beam from the channel waveguide was measured for different wavelengths at room temperature, the quasi-phase-matching wavelength for this sample was recorded as 1552.03nm at a temperature of 21.4°C. A maximum output power of 10.5μW was generated from the 7.5dBm power of fundamental beam.

Figure 7.25 shows that the bandwidth of FWHM (Full Width of Half Maximum) is around 0.7nm which is little broader than calculated acceptance bandwidth of a 10mm long waveguide (0.35nm). This is because that the waveguide is not homogeneous along the whole interaction length (this effect is modeled and shown in Figure 8.12) and the temperature is not uniform along the length of the waveguide, either another reason is that the periodically switched domain ratio is not a perfect 50:50 or some domains were merged together during the poling and thermal indiffusion processes resulting in a slightly shorter effective interaction length for the waveguide compared to the physical length of the device.

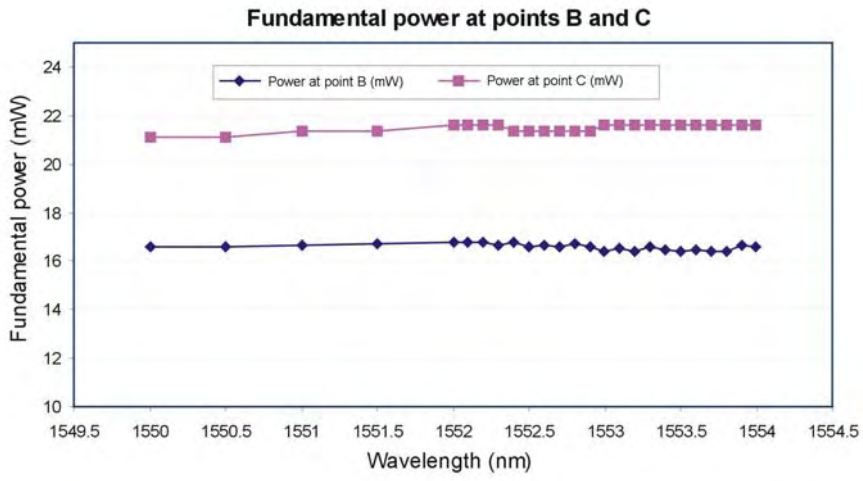


**Figure 7.24.** Showing that the power variation at different wavelengths at point B and C are less than 3%.

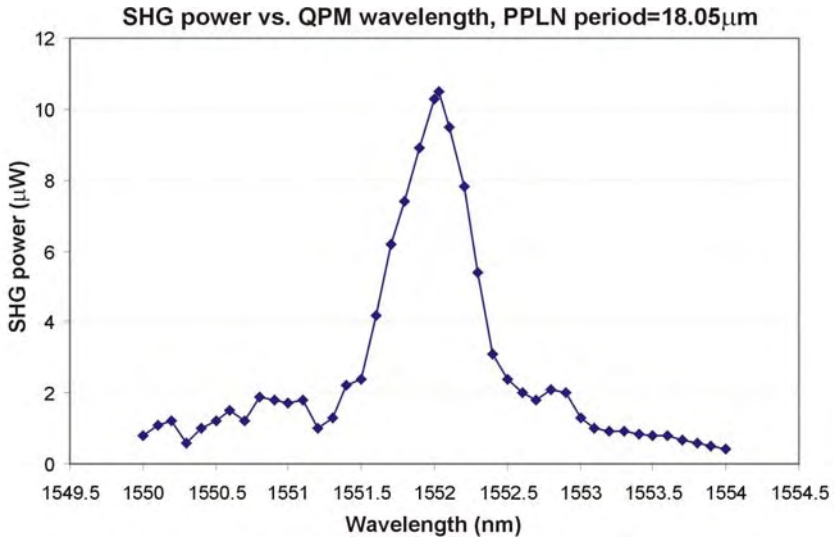


**Figure 7.25.** The SHG power dependence on the fundamental wavelength. The bandwidth (FWHM) is 0.7nm.

The variation of the maximum SHG power at different wavelengths was also studied, Figure 7.26 shows that the QPM wavelength shifts to the infrared side when the temperature is increased, the maximum of the SHG power converted for different fundamental wavelengths varied from 10.5μW at a temperature of 21.4°C to 9.7μW at a temperature of 150.3°C, the reason for the SHG power drops when the pump wavelength shifts to the infrared side is that the SHG conversion efficiency is proportional to frequency square of the incident beam ($\eta \propto \omega^2$), the variation of the SHG power is around 8% for the measured temperature range of 128.9°C. The variation of the pump power over this range is less than 1.5%, see Figure 7.24.

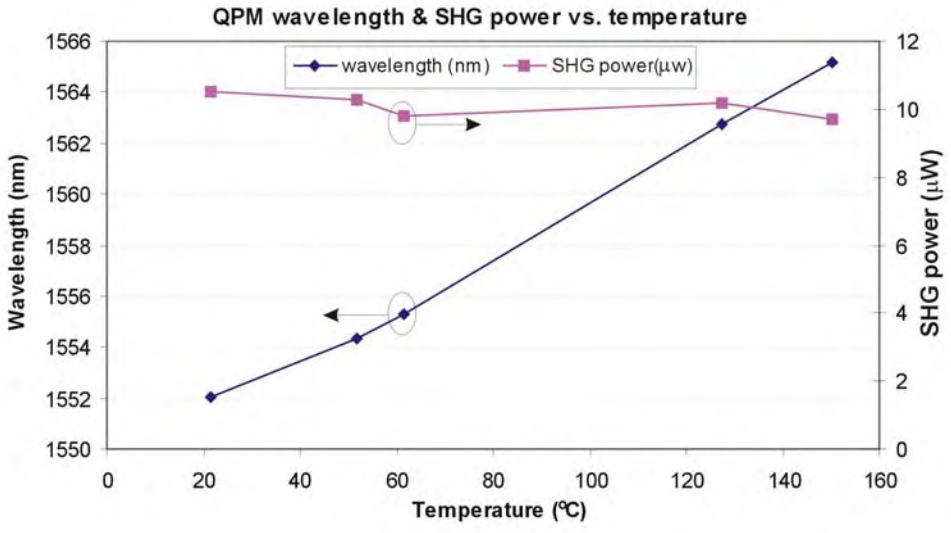


**Figure 7.26.** The QPM wavelength shifts to the infrared side when the temperature increased, the variation of the SHG power is around 8% for different wavelength.

## 7.7 SHG Conversion Efficiency under the High Power Condition

An optical parametric oscillator (OPO) was used to study the SHG conversion efficiency of the PPLN waveguides under high peak power conditions, the relevant parameters of the incident beam from the OPO are listed in Table 7.09.

**Table 7.09** The parameter of the incident beam from the OPO.

| | |
|---|---|
| Central wavelength (nm) | 1556.0 |
| Bandwidth of the beam (nm) | 1.2 |
| Pulse duration (ps) | 5 |
| Pulse frequency (MHz) | 120 |
| Average power (mW) | 250 |
| Peak power of pulse (W) | 417 |

Figure 7.27 shows the schematic diagram of the set up. The incident pulse beam from the optical parametric oscillator (OPO) reflected by mirror 1 and mirror 2 was coupled into the single mode fibre (for the 1550nm wavelength), then launched into the PPLN waveguide located inside of the oven. The polarization direction of the launched beam was controlled by the polarization controller which was inserted between the lens and the launch fiber. The fundamental beam was TM polarized in order to take advantage of the nonlinear coefficient $d_{33}$. The mode profile and the power of the SHG beam were measured as a function of temperature.

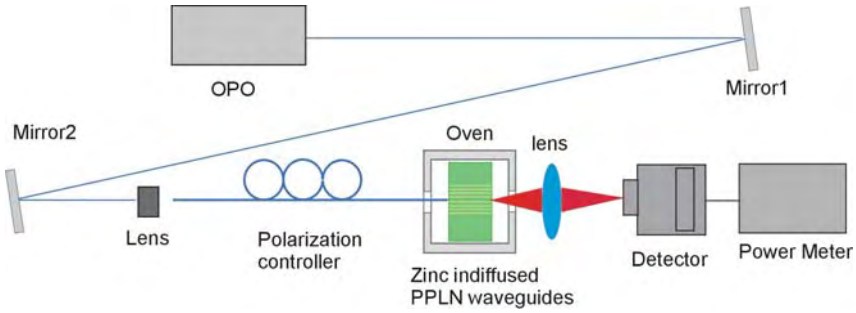


**Figure 7.27.** Schematic diagram of the set-up for measuring SHG conversion efficiency under high power conditions.

With 90mW average power in the fundamental beam from the OPO, 23.25mW average output power was coupled into the 3.5mm length zinc-indiffused PPLN channel waveguide ( $\Lambda = 18.05\mu m$), representing 25.8% coupling efficiency.

Figure 7.28 shows the maximum external average SHG output power (TM00 mode) of 16.2mW which was recorded for an internal average pump power of 23.3mW at 43.0°C, allowing for the 14% reflection loss on the two end faces, a conversion

efficiency of 17%$W^{-1}\cdot cm^{-2}$ was achieved. The average power conversion efficiency was 81%. The TM01 and TM02 modes of the SHG beam converted from TM00 mode of fundamental beam were also observed at different temperatures, see Table 7.10. This SHG conversion efficiency using the high power OPO is lower than that using the low power DFB laser diode. The main reason for this is that the bandwidth of the DFB laser (around 3 $\times 10^{-5}$nm) is far narrower than the acceptance bandwidth of the 10mm length PPLN waveguide (0.35nm), so almost 100% of the incident beam power contributes to the process of the SHG conversion. But for the OPO, the bandwidth of the output beam (1.2nm) is larger than the acceptance bandwidth of the 3.5mm PPLN waveguide (0.7nm), thus only part of the fundamental beam power plays a role in the process of SHG conversion. Despite the lower efficiency the higher peak power yields a much greater overall conversion efficiency of 81% vs. the 0.19% obtained for the DFB laser.

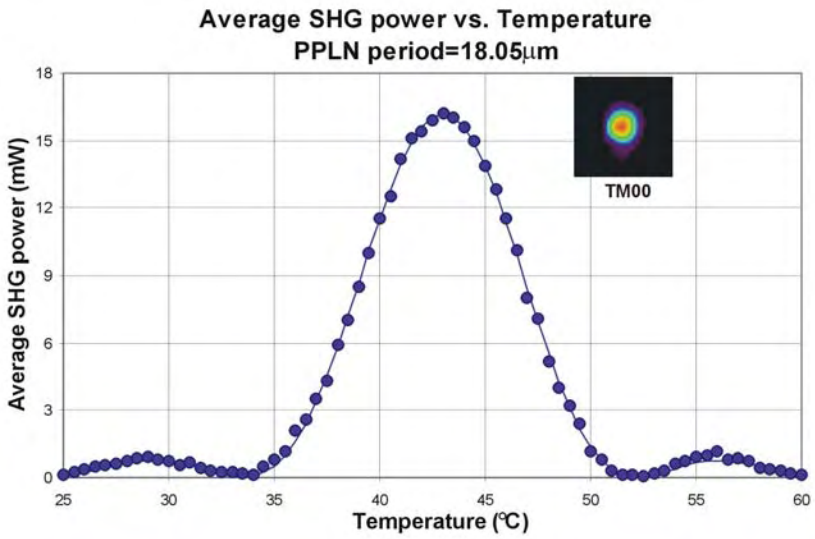


**Figure 7.28.** SHG power vs. QPM temperature for PPLN waveguide ( $\Lambda$ = 18.05μm) under the high power condition, the solid line corresponds to a sinc-square function fitted to the measured data points. The inset picture is the mode profile at 776.2nm (TM00 mode).

**Table 7.10** The QPM temperature and maximum average power of different SHG modes

| SHG mode | QPM temperature (°C) | Maximum average power (mW) |
|---|---|---|
| TM00 | 43 | 16.2 |
| TM01 | 62 | 2.3 |
| TM02 | 90 | 0.78 |

This chapter has covered the characterization of the linear optical properties of the PPLN channel waveguide, such as the mode profile, the NA, the propagation loss and the polarization dependence, and then the nonlinear process of quasi-phase-matched

SHG in the PPLN waveguide devices. The SHG conversion efficiency for a 1552.4nm wavelength was measured, individual modes of the second harmonic were observed by tuning the temperature, a peak conversion efficiency of 59%$W^{-1}cm^{-2}$ was achieved at room temperature. Using a short pulse source and an appropriately short waveguide, second harmonic generation conversion efficiency of 81% was obtained. The use of PPLN waveguides for visible light generation will be discussed in chapter 8.

## References


[1] A. Ghatak, K. Thyagarajan, "Introduction to Fiber Optics", *Cambridge University Press*, (1998)

[2] J. Wilson, J. Hawkes, "Optoelectronics, an introduction", *Prentice Hall*, 3th Edition, (1998)

[3] T. Suhara, T. Fujieda, M. Fujimura and H. Nishihara, "Fabrication Zn: Lithium Niobate Waveguides by Diffusing ZnO in Low Pressure Atmosphere", *Jpn. J. Appl. Phys*., Vol.**39,** p.L864-L865 (2000)

[4] G. Schreiber, H. Suche, Y.L.Lee, W. Grundköter, V. Quiring, R. Ricken, and W. Sohler, "Efficient Cascaded Difference Frequency Conversion in Periodically Poled Ti: Lithium Niobate Waveguides using Pulsed and CW Pumping", *Appl. Phys*., Vol.**B73**, p.501-504 (2001)

[5] K. R. Parameswaran, M. Fujimura, M. H. Chou, and M. M. Fejer, "Low-Power All-Optical Gate Based on Sum Frequency Mixing in APE Waveguides in PPLN", *IEEE Photon. Technol. Lett*., Vol.**12**, p.654-656 (2000)

[6] L. Chanvillard, P. Aschieri, P. Baldi, D. B. Ostrowsky, M. De Micheli, L. Huang, and D. J. Bamford, "Soft Proton Exchange on PPLN: a simple waveguide fabrication process for highly efficient non-linear interactions", *Appl. Phys. Lett*., Vol.**76**, p.1089-1091 (2000)

[7] K. R. Parameswaran, R. K. Route, J. R. Kurz, R. V. Roussev, M. M. Fejer, M. Fujimura, "Highly efficient second-harmonic generation in buried waveguides formed by annealed and reverse proton exchange in periodically poled lithium niobate", *Opt. Letts*., Vol.**27**, p.179-181 (2002)

[8] M. H. Chou, I. Brener, M. M. Fejer, E. E. Chanban and S. B. Christman, "1.5-μm-Band Wavelength Conversion Based on Cascaded Second-Order Nonlinearity in $LiNbO_3$ Waveguides", *IEEE Photon. Technol. Lett*., Vol.**11**, p.653-655 (1999)

[9] G. Schreiber, H. Suche, Y. L.Lee, W. Grundkötter, V. Quiring, R. Ricken, and W. Sohler, "Efficient Cascaded Difference Frequency Conversion in Periodically Poled Ti: Lithium Niobate Waveguides using Pulsed and CW Pumping", *Appl. Phys.*, B Vol.**73**, p.501-504 (2001)

[10] E. J. Lim, H. M. Hert, M. L. Bortz , and M. M. Fejer, "Infrared Radiation Generated by Quasi-phase-matched Difference-Frequency Mixing in a Periodically Poled Lithium Niobate Waveguide", *Appl. Phys. Lett*., Vol.**59**, p.2207-2209 (1991)

[11] J. C. Campbell, "Coupling of fibers to Ti-diffused $LiNbO_3$ waveguides by butt-joining", *Appl. Opt.* Vol.**12**, p.2037-2039 (1979)

[12] M. A. R. Franco, L. C. de Vasconcellos, and J. M. Machado, "Coupling Efficiency Between Optical Fiber and Ti:$LiNbO_3$ Channel Waveguide", *Telecomunicações*, Vol.**07**, p.54-59 (2004)

# Chapter 8

## Visible Second Harmonic Generation in Zinc Indiffused PPLN Channel Waveguides

### 8.1 Introduction

Nonlinear optical processes and quasi-phase-matching (QPM) permit the extension of conventional laser sources to shorter wavelength spectral regions, such as the green, blue and ultraviolet.

Recently, compact and reliable coherent green, blue and ultraviolet light sources are becoming increasingly interesting for various applications in fields such as optical data storage and biomedicine. Quasi-phase-matched second harmonic generation (SHG) is one of the most attractive methods for achieving such coherent light sources, because it has the significant advantage of being able to phase match an arbitrary wavelength and thus allows access to higher nonlinear coefficients using an appropriate period of the domain inversion.[1,2,3,4].

Air-cooled argon-ion lasers at 488nm are widely used in the biomedical area, as a blue laser source, they are used for applications such as DNA analysis and cell analysis using fluorescent microscopy, etc. The concept of frequency-doubling a semiconductor laser using QPM to create 488nm would be an attractive replacement for these existing argon-ion lasers due to its potentially smaller footprint and compact assembly (no external power conditioning, control boxes, or cooling fans would be required), power stability and better electrical efficiency.

Visible light generation using QPM has been reported for bulk and waveguide type devices in $LiNbO_3$ [4], $LiTaO_3$ [5], and $KTiOPO_4$ (KTP) [6,7]. Continuous wave (CW) multiwatt powers of green light have been efficiently generated via intracavity frequency doubling of a Nd:YAG laser [8,9] using nonlinear crystals. For example, Nighan *et al*. [10] reported more than 6W of green light generated with 30% efficiency in a diffraction limited output beam. Efficient SHG to the green, blue and ultraviolet has also been performed by using MgO doped lithium niobate. For

example, S. Sonoda *et al*.[11] reported the generation of 2.2mW of CW 475nm radiation with 60%$W^{-1}\cdot cm^{-2}$ conversion efficiency and K. Mizuuchi *et al*.[12] have achieved a conversion efficiency of 340%$W^{-1}$ in CW operation showing 22.4mW of SHG at 340nm wavelength. However, visible light generation in these devices have suffered some limitations, such as complicated fabrication processes, difficulty in fabricating uniform nonlinear gratings, and lower resistance to photorefractive damage.

Zinc indiffused PPLN channel waveguides are one of the most attractive technologies for blue light generation because of their large nonlinear coefficient [13], high resistance to photorefractive damage [14] and low cost of fabrication.

This chapter describes work on zinc indiffused PPLN channel waveguides as a nonlinear material for SHG to the green and blue. The basic fabrication processes for PPLN and zinc indiffused channel waveguides on lithium niobate crystal have been described in chapter 4 and chapter 6 respectively. This chapter focuses on the characterization of the SHG of visible light.

Visible generation provides a far more stringent test of the zinc diffused PPLN process than 1550nm wavelength doubling, particular scattering losses will be higher, periods need to be finer and smaller waveguides are needed for single mode operation.

## 8.2 Green Light Generation in Zinc Indiffused PPLN Channel Waveguides

500μm thick *z*-cut congruent lithium niobate crystals were patterned by standard photolithography with a grating period of 6.5μm and poled based on the fabrication processes for PPLN described in chapter 4. Then channel waveguides were indiffused in the PPLN samples according to the fabrication procedure demonstrated in chapter 6.

A 1064nm Nd:YAG laser was used to study the uniformity of the periodically switched domain structure outside and inside the Zn waveguide after the thermal diffusion and assess the efficiency of green light generation through the bulk PPLN and in the Zn indiffused channel PPLN waveguides. The incident beam was TM polarized in order to take advantage of the optimal non-linear susceptibility tensor

coefficient $d_{33}$. First of all, the bulk PPLN grating outside the channel waveguide area was assessed through characterization of the SHG conversion efficiency of the bulk, and then characterization of the PPLN inside the channel waveguide was carried out.

A ×10 microscope objective was used to focus the incident beam into the bulk PPLN and channel waveguide. An end polished PPLN waveguide sample (grating period of 6.5μm, 3.6μm width waveguide) was put inside a temperature tuneable oven, the output power of the SHG (532nm) from the bulk PPLN and the zinc indiffused waveguide were measured using a power meter, a band pass filter (50% transmittance at 532nm, 0% transmittance at 1064nm) was used to block the 1064nm fundamental beam. The sample was heated to around 200°C, then cooled down to room temperature at a rate of 1.0°C/min. A maximum output SHG power of 1.8mW was recorded for 330mW fundamental power at 1064nm at a temperature of 188.2°C, which corresponds to a conversion efficiency of $1.84\%W^{-1}\cdot cm^{-1}$ for the bulk PPLN sample. The quasi-phase-matching (QPM) curve versus the tuning temperature is shown in Figure 8.01 and the curve of SHG power versus the fundamental power is shown in Figure 8.02.

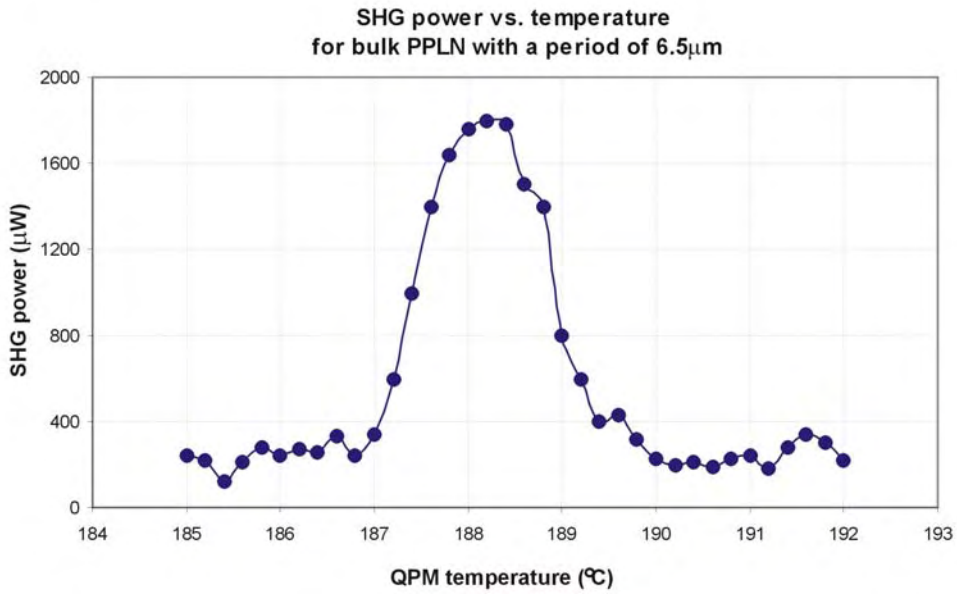


**Figure 8.01.** The quasi-phase-matching (QPM) curve vs. temperature for bulk PPLN with a period of 6.5μm. The wavelength of the fundamental beam is 1064nm.

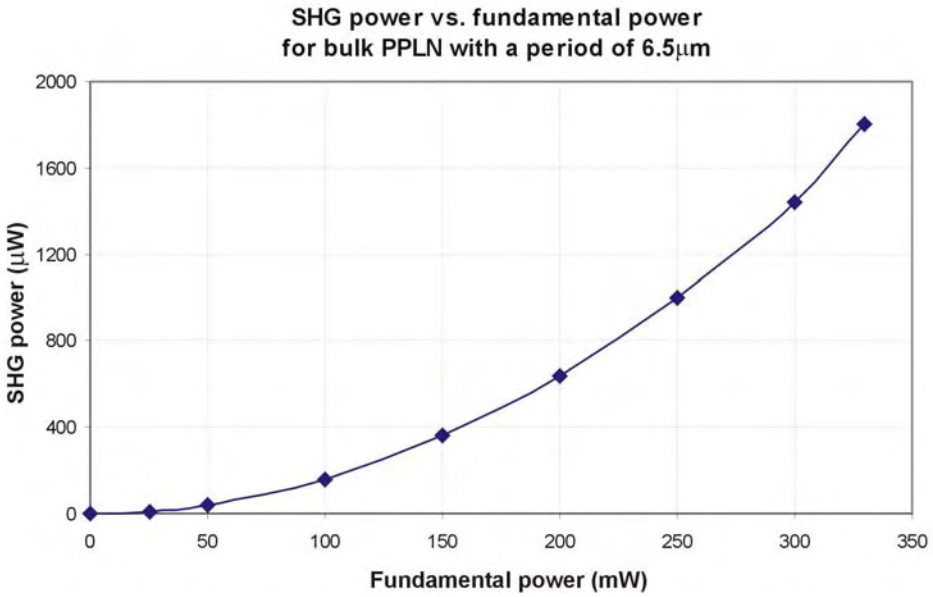


**Figure 8.02.** The curve of SHG power vs. incident fundamental power for the bulk PPLN with period of 6.5μm. The wavelength of the fundamental beam is 1064nm.

Using the microscope objective, around 10% of the fundamental power was coupled into the channel waveguide. The quasi-phase-matching (QPM) curve versus temperature for the channel waveguide PPLN shown in Figure 8.03 indicates that the QPM temperature for the TM00 mode at the SHG wavelength (532nm) converted from the TM00 mode of the fundamental beam is around 145.1°C. A maximum output external SHG power of 150μW was obtained from 30mW of internal pump power in the fundamental beam, which corresponds to a conversion efficiency of 16.7%$W^{-1}\cdot cm^{-2}$ for a waveguide length of 10mm.

Several factors are believed to have reduced the SHG conversion efficiency of the PPLN channel waveguide compared to the 1550nm waveguides. First of all, the uniformity of the grating through the whole channel waveguide may not be the same, the mark-space ratio of the PPLN domain grating inside the waveguide was slightly different from the optimum mark-space ratio of 50:50 outside of the waveguide. Secondly it was shown, from the visual assessment of etched parts of the samples, that there were some random fluctuations in the position of the domain walls. Because of these imperfections the conversion efficiency was more than one order of magnitude lower that the calculated value for a perfect grating. However the shape of the phase-matching curve as well as its acceptance temperature range of 0.6°C (temperature bandwidth of the half maximum SHG power) was close to those expected for a

perfect grating, indicating that the whole physical length of the waveguide was contributing to the conversion process and that the random fluctuations in the domain wall positions was independently distributed.

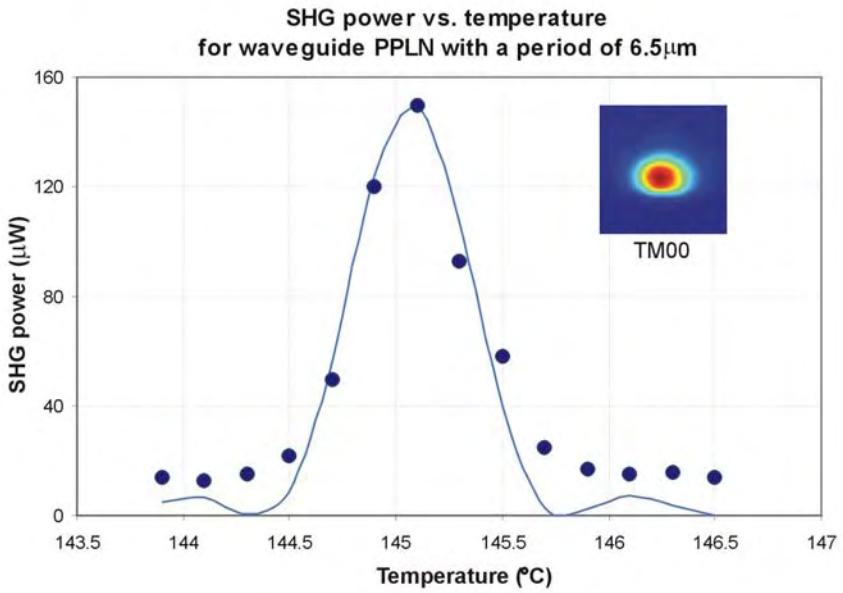


**Figure 8.03.** Dependence of the SHG output power vs. temperature. The spots represent experimental data, while the continuous line represents the theoretical response of the device. The inset picture is the mode profile at 532nm (single mode).

In addition, a photorefractive effect induced by the green light is another possible reason for the low SHG conversion efficiency. It occurs when the bound charge inside the waveguide is rearranged from the illuminated to the dark regions in response to a spatially modulated light pattern of the incident beam, this creates a static space charge field, and therefore yields, by the electro-optic effect, a pattern in the refractive index which acts as phase grating, which in turn will degrade the quality of the waveguide, and results in a poor overlap of the interacting beams inside the waveguide. The physical mechanism for the photorefractive effect in lithium niobate has been described in chapter 3.

The photorefractive effect was characterized by using an argon laser, an incident beam at 514.5nm was coupled into the waveguide by the objective lens, the output power was measured based at different temperatures and different input powers. Before presenting the characterization, the following symbols are defined and listed in Table 8.01.

**Table 8.01** Definition of the symbols used in the characterization of photorefractive effect

| Item | Definition |
|---|---|
| $P_0$ | The output power from the waveguide at the starting measurement time. |
| $P_t^{max}$ | The maximum output power from the waveguide during a period of 10seconds at the measurement time t. |
| $P_t^{min}$ | The minimum output power from the waveguide during a period of 10seconds at the measurement time t. |
| $P_t$ | The average output power from the waveguide at the measurement time t, $P_t = (P_t^{max} + P_t^{min})/2$. |
| $P_t / P_0$ | The output power change ratio at measurement time t. |
| $\Delta P_t$ | The output power variation during 10 seconds measurement time t, $\Delta P_t = P_t^{max} - P_t^{min}$. |
| $\Delta P_t / P_t$ | The output power variation expressed as a ratio at the measurement time t, |
| $\Delta P/P$ | The average output power variation ratio over all sample times, $\Delta P/P=\{\sum_{t=0}^{n}(\Delta P_t/P_t)\}/n$. |

Figure 8.04 shows the average output power variation ratio ($\Delta P/P$) and its dependence on temperature at different powers. The dependences of the output power change ratio ($P_t / P_0$) at different output powers on time at different temperatures were also measured, see Figure 8.05 and Figure 8.06. Finally the photorefractive effect in a bulk PPLN sample was investigated to provide a comparison with that in the waveguide PPLN.

Figure 8.07 shows the dependence of the average power variation ratio ($\Delta P/P$) for different output powers ranging from 100μW to 1500μW at a temperature of 20 ºC and 140ºC for waveguide and bulk PPLN respectively.

From Figure 8.04 to Figure 8.07, the following conclusions were drawn.

1. The photorefractive effort can be reduced through the zinc indiffusion inside the waveguide not only at high temperature (140ºC), but also at room temperature (20ºC).
2. The photorefractive effort induced by the high power incident beam is much stronger than that induced by the low power beam.

3. Increasing the temperature can effectively reduce the photorefractive effort in both bulk and waveguide PPLN sample.

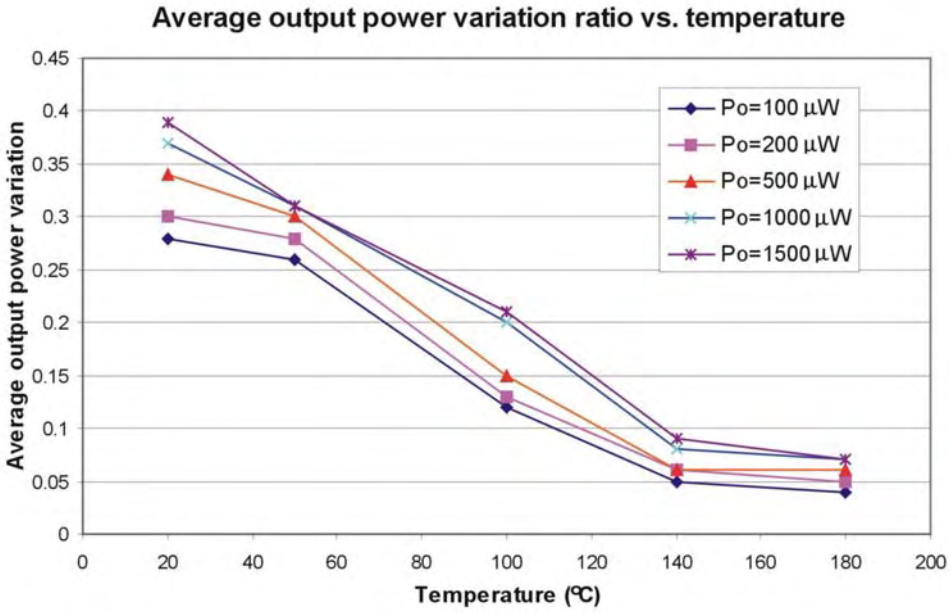


**Figure 8.04.** The output power variation ratio (ΔP/P) dependence on the different temperatures under the different powers for the Zn indiffused waveguide.

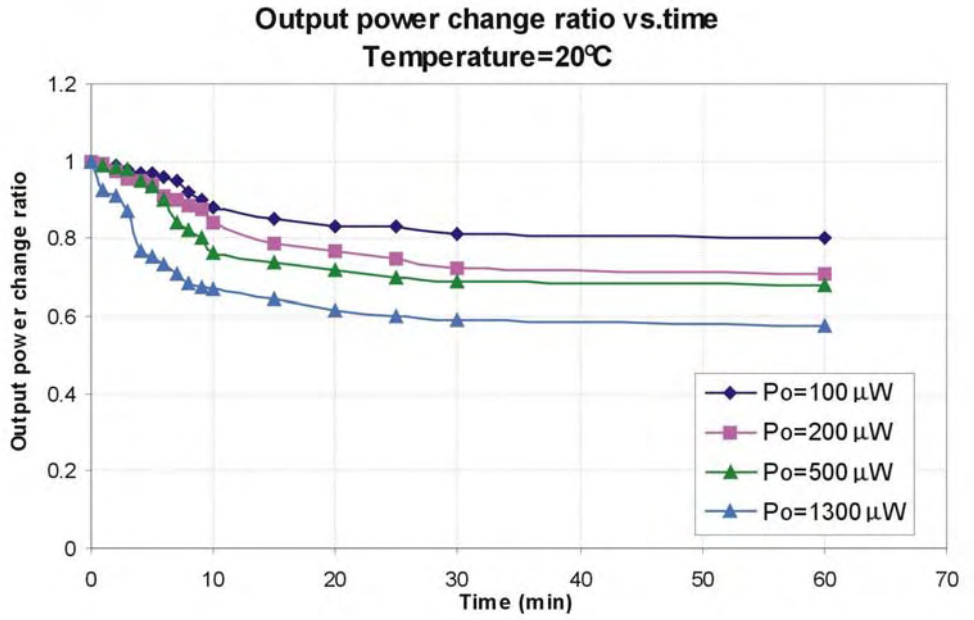


**Figure 8.05.** The output power change ratio ($P_t / P_0$) at different output powers showing the dependence on time at a temperature of 20ºC for the Zn indiffused waveguide.

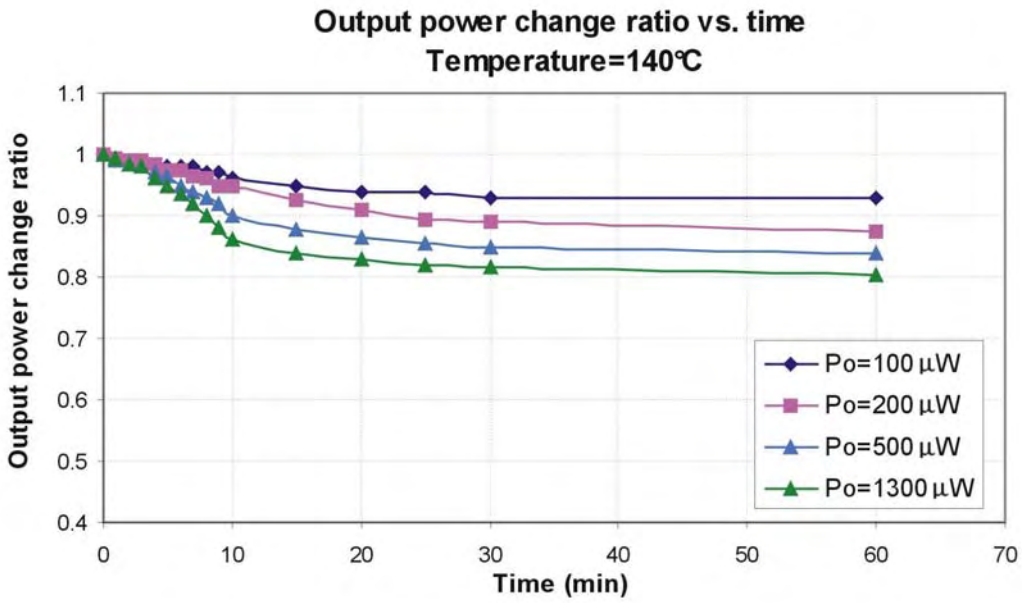


**Figure 8.06.** The output power change ratio ($P_t / P_0$) at different output powers showing the dependence on time at a temperature of 140ºC for the Zn indiffused waveguide.

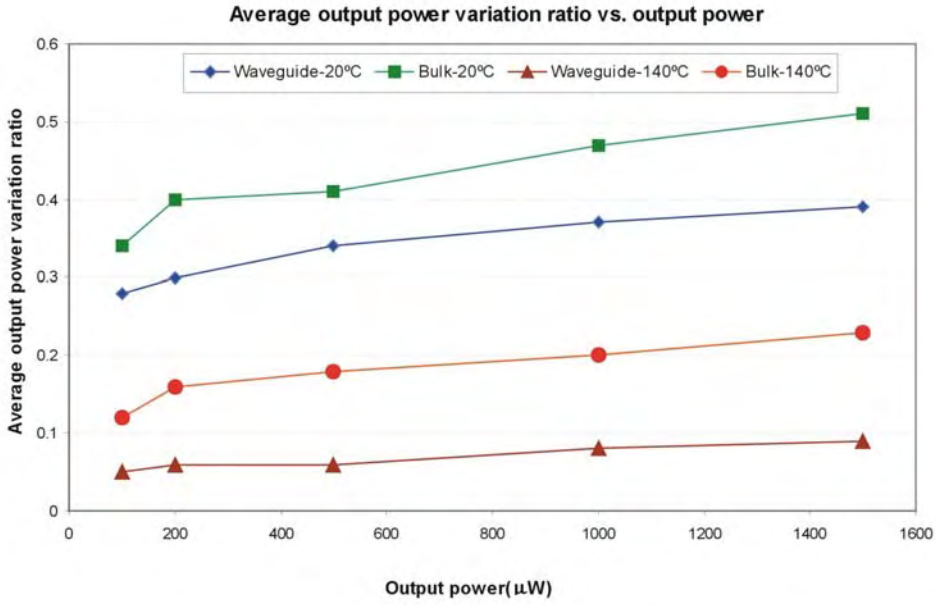


**Figure.8.07.** The dependence of the average output power variation ratio (ΔP/P) for different output powers $P_0$ ranging from 100µW to 1500µW at a temperature of 20 ºC and 140ºC for zinc indiffused waveguides and bulk PPLN respectively.

## 8.3 Blue Light Generation in Zinc Indiffused PPLN Channel Waveguides

Having investigated green generation we now move on to blue generation. 500µm wide gratings with a period of 8.8µm were patterned on –*z* face of the sample. This

period was chosen as suitable for third order QPM frequency doubling to the blue from an infrared wavelength of approximately 835nm. Poling was carried out by using the method described in chapter 4. The channel waveguide was then fabricated, parallel to the *x*-axis, on the PPLN sample by diffusing Zn strips, 80nm thick and ranging in width from 1.8µm to 2.4µm in 0.2µm steps at 930ºC over a period of 80 minutes, this width of the waveguide was chosen in order to get single mode waveguides for the fundamental beam at a wavelength of 835nm. The sample was then cut and polished, yielding 12mm long channel waveguides on the PPLN sample.

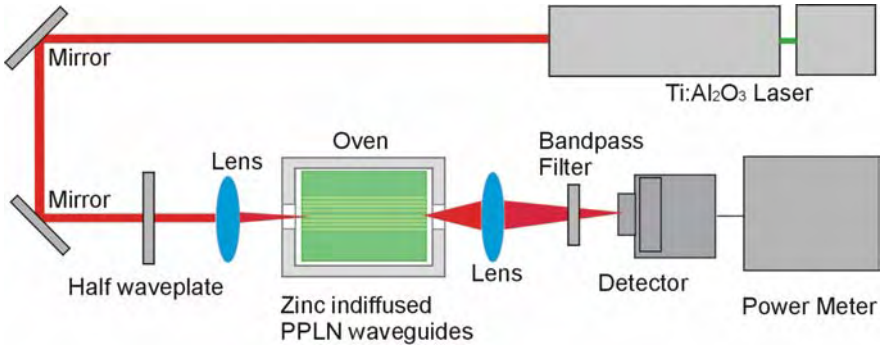


**Figure 8.08.** Schematic diagram of the set up for blue light generation by using a tuneable titanium sapphire (Ti:$Al_2O_3$) laser.

A tuneable titanium sapphire (Ti:$Al_2O_3$) laser was used for the characterization of the SHG from the channel waveguides. A schematic diagram of the set up was shown in Figure 8.08. The incident beam from the Ti:$Al_2O_3$ laser was coupled into the PPLN waveguide sample located inside the oven, the output beam from the channel waveguide was focused on to the detector by using a microscope objective. The polarization direction of the launched beam could be modified and controlled by the 836nm half wave plate which was inserted between the lens and the mirror. The fundamental beam was TM polarized in order to take advantage of the optimal non-linear susceptibility tensor coefficient $d_{33}$, an optical band-pass filter (95% transmission at 417.5nm, 0% transmission at the 835nm) was used to block the fundamental beam from the output side of waveguide, the mode profile of the SHG light from Zn-diffused PPLN waveguide was recorded using the CCD camera and the power of the SHG was measured by using a power meter at different temperatures.

Figure 8.09 shows the third order SHG output from the waveguide as a function of temperature. The width of the waveguide was around 2.0µm and the fundamental beam in this case was polarized along the *z*-direction, i.e. TM polarized, producing an

interaction with the $d_{33}$ coefficient. As shown in the figure, phase matched conversion was achieved from the TM00 mode at the fundamental beam to the TM00 mode at the SHG beam. The maximum power obtained in the blue was 8.63μW for a coupled power of 12.1mW, allowing for the 14% reflection loss at each end face of the sample, the conversion efficiency of third order SHG was 3.52%$W^{-1}$·$cm^{-2}$. According to the Eq.(7.06), we have $\eta \propto \frac{1}{\lambda^2 m^2}$, where *m* is the order of the QPM and $\lambda$ is the fundamental wavelength. Thus the conversion efficiency of third order SHG for the 835nm is equivalent to 19.5%$W^{-1}$·$cm^{-2}$ if scaled to 1064nm wavelength and first order QPM. See Table 8.02.

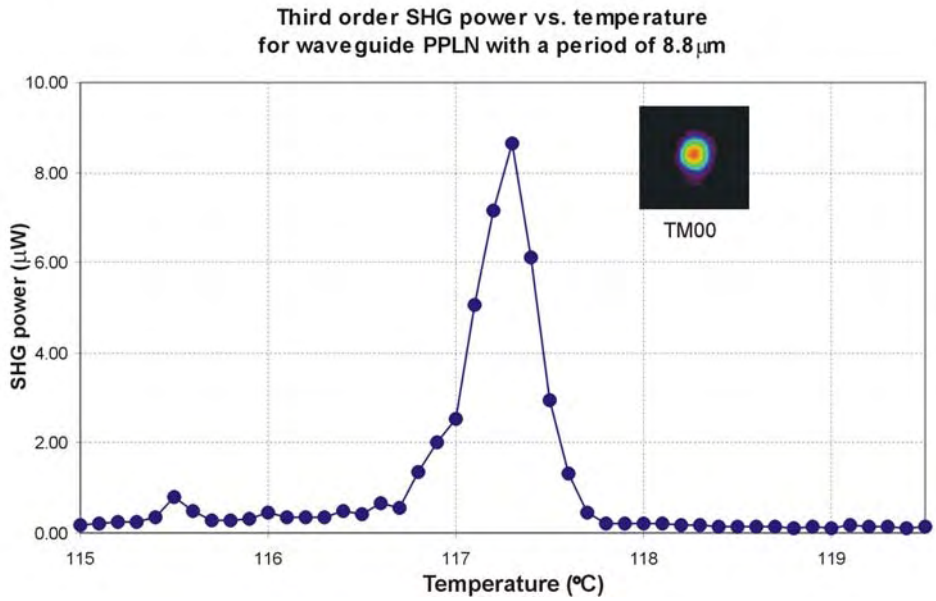


**Figure 8.09.** Dependence of the third order SHG output power vs. temperature. The inset picture is the mode profile at 417.5nm (single mode).

**Table 8.02** $\eta$ scaled to 1064nm wavelength and first order QPM equivalent

| **Wavelength** | **1552.4nm** | **1064nm** | **835nm (3rd order)** |
|---|---|---|---|
| Measured $\eta$ | 59%$W^{-1}$·$cm^{-2}$ | 16.7%$W^{-1}$·$cm^{-2}$ | 3.52%$W^{-1}$·$cm^{-2}$ |
| $\eta$ scaled to 1064nm and first order QPM equivalent | 125.6%$W^{-1}$·$cm^{-2}$ | 16.7%$W^{-1}$·$cm^{-2}$ | 19.5%$W^{-1}$·$cm^{-2}$ |

From Table 8.02, it can be seen that the scaled conversion efficiency of the third order SHG in this demonstration device is similar to that achieved for first order second harmonic green generation but is more than 6 times smaller than that expected from the scaled SHG conversion efficiency of the device for 1550nm. In addition, the

bandwidth of the QPM temperature curve (0.4°C) is considerably wider than that calculated based on theory (0.25°C).

It is believed that variations in the effective index profile along the length of the waveguide due to variations in the width of zinc stripe during the lift off patterning process, have a more detrimental effect on the phase matching in the small core channel waveguide than in the larger guides used at 1550nm. Moreover the uniformity of the PPLN grating with larger periods along the whole length of waveguide is better than that with the small periods.

The variations in the width of zinc strips along the waveguide during the lift off patterning process and its influence on the SHG conversion efficiency was further investigated based on the following method. First of all, the widths of the zinc film strips after the lift off process were measured at the different point (from point A to point H) along the length of the waveguide by using the Alpha Step, the length of the sample is 10mm, the width of the waveguides are 2.0μm and 7.0μm, see Figure 8.10. The waveguide width variation is listed in Table 8.03, the standard deviation was calculated based on Eq.(8.01):

$$S = \sqrt{(\sum_{1}^{N}(X_N - \bar{x})^2)/(N-1)} \qquad 8.01$$

Where : $\bar{x} = (\sum X_N)/N$ .

Then based on the measured data the effective index change inside the waveguide was calculated, finally the QPM curve as a function of temperature was derived based on the effective index change and the calculated shift in the QPM curve.

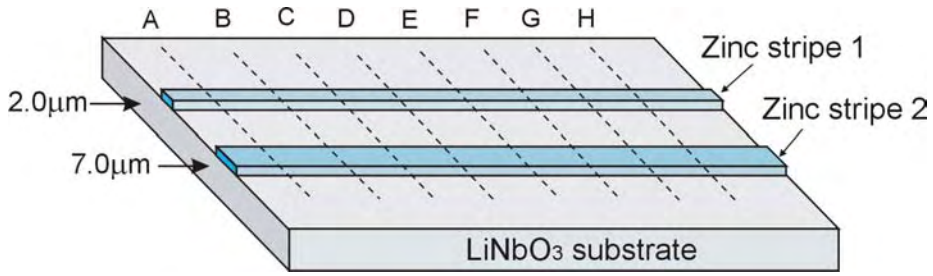


**Figure 8.10.** The widths of the zinc stripes after the "lift off" process were measured at different points (from point A to point H) along the length of the waveguide by using the Alpha Step.

**Table 8.03** The width variation of the zinc stripe along the waveguide.

| Measured point | Width of stripe 1 (nm) | Width of stripe 2 (nm) |
|---|---|---|
| A | 1880 | 6900 |
| B | 1920 | 6930 |
| C | 1900 | 7020 |
| D | 2020 | 7080 |
| E | 2070 | 7050 |
| F | 2120 | 7140 |
| G | 2060 | 7080 |
| H | 2080 | 7120 |
| Standard deviation | 95nm | 98nm |

In order to simplify the analysis, a vastly simplified model was used based on a step index fibre. It was assumed that the zinc indiffused channel waveguide has a same structure as normal single mode optical fiber used to guide a 1550nm or 835nm laser beam, the refractive index profile in the core ($n_1$) and the cladding ($n_2$) has a step profile, other parameters are listed in Table 8.04.

**Table 8.04** The parameters of the waveguide for 1550nm and 835nm wavelength.

| Diameter of core (μm) | $n_1$ | $n_2$ | Variation of core (nm) | $\lambda$ (nm) |
|---|---|---|---|---|
| 2.0 | 2.1797 | 2.1767 | +/-100 | 835 |
| 7.0 | 2.1459 | 2.1429 | +/-100 | 1550 |

Based on the above mentioned waveguide model and data listed in the Table 8.03, modeled QPM curves have been simulated using Matlab. Figure 8.11 and Figure 8.12 show the results of simulation of a single mode waveguide for both the 835nm wavelength and 1550nm wavelength respectively. A comparison of the relevant calculated data for the two waveguides is listed in Table 8.05.

**Table 8.05** Comparison of the QPM curve shifting due to the waveguide width variation.

| Wavelength(nm) | 835 | | 1550 | |
|---|---|---|---|---|
| Width of waveguide(μm) | 2 | | 7 | |
| QPM temperature (ºC) | 117.3 | | 140.5 | |
| Bandwidth of QPM temperature (ºC) | 0.3 | | 1.7 | |
| Variation of width (nm) | 100 | 200 | 100 | 200 |
| Variation to width ratio (%) | 5 | 10 | 1.7 | 3.4 |
| QPM Temperature shift (ºC) | 0.4 | 0.8 | 0.2 | 0.4 |
| Shift of QPM bandwidth ratio (%) | 133.3 | 266.6 | 12 | 24 |

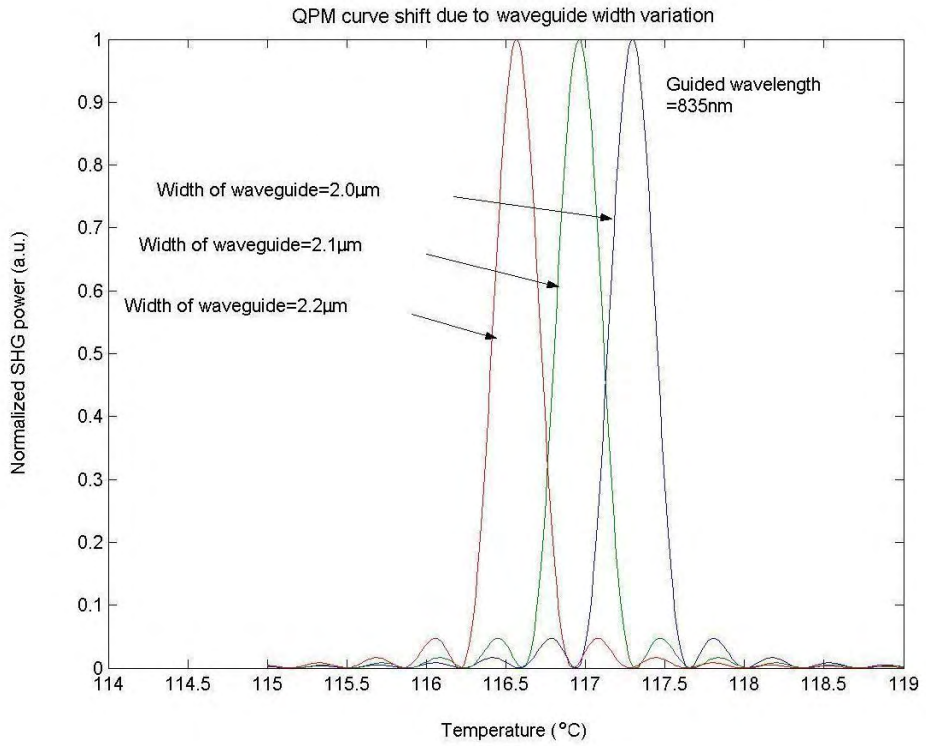


**Figure 8.11.** The QPM temperature curve shift due to waveguide width variation, the width of the waveguide is 2.0µm, and the wavelength is 835nm.

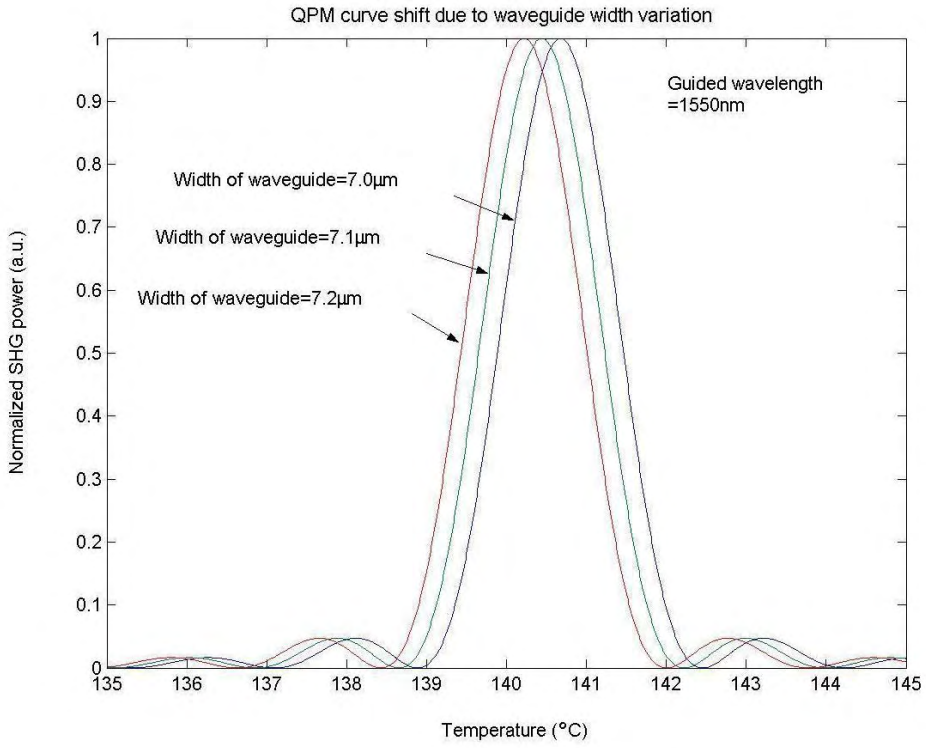


**Figure 8.12.** The QPM temperature curve shift due to waveguide width variation, the width of the waveguide is 7.0µm, the wavelength is 1550nm.

From Figure 8.11, Figure 8.12 and Table 8.05, it is clear that for the same width variation of the waveguide, the temperature shift of the QPM curve is smaller in single mode waveguides for the 1550nm wavelength than that in the single mode waveguides for the 835nm wavelength, thus the width variation has a more detrimental effect on the efficiency in the small core waveguide than in the larger core one, resulting in a lower SHG conversion efficiency for the shorter wavelength. The simple modelling results give a good explanation of the experimental data.

This chapter has described visible light generation by using the PPLN waveguide devices fabricated based on procedures described in chapter 6. Green light (532nm) was obtained by frequency doubling incident beams from a Nd:YAG laser through a PPLN waveguide device and a conversion efficiency of 16.7%$W^{-1}\cdot cm^{-2}$ for first order SHG was achieved. The photorefractive effect induced by the green light was investigated. Blue light (417.5nm) SHG was achieved through third order QPM by frequency doubling a tuneable titanium sapphire (Ti:$Al_2O_3$) laser and a conversion efficiency of 3.52%$W^{-1}\cdot cm^{-2}$ for third order SHG was achieved.

## References

[1] R. G. Batchko, D. R. Weise, T. Plettner, G. D. Miller, M. M. Fejer and R. L. Byer, "Continuous-wave 532-nm-pumped singly resonant optical parametric oscillator based on periodically poled lithium niobate", *Opt. Lett.*, Vol.**23**, p.168-170 (1998)

[2] S. Wang, V. Pasiskevicius, J. Hellström and F. Laurell, H. Karlsson, "First-order type II quasi-phase-matched UV generation in periodically poled KTP", *Opt. Lett.*, Vol.**24**, p.978-980 (1999)

[3] J. Amin , V. Pruneri, J. Webjörn, P. St. J. Russell, D. C. Hanna, J. S. Wilkinson, "Blue light generation in a periodically poled Ti: Lithium Niobate channel waveguide", *Opt. Commun.*, Vol.**135**, p.41-44 (1997)

[4] K. Kintaka, M. Fujimura, T. Suhara and H. Nishihara, "Third harmonic generation of Nd:YAG laser light in periodically poled $LiNbO_3$ waveguide", *Electron. Lett.*, Vol.**33**, p.1459-1461 (1997)

[5] K. Mizuuchi, K. Yamamoto, M. Kato, "Harmonic blue light generation in X-cut MgO:$LiNbO_3$ waveguide", *Electron. Lett.*, Vol.**33**, p.806-808 (1997)

[6] M. Pierrou, F. Laurell, H. Karlsson, T. Kellner, C. Czeranowsky, G. Huber, "Generation of 740mW of blue light by intracavity frequency doubling with a first-order quasi-phase-matched $KTiOPO_4$ crystal", *Opt. Lett.*, Vol.**24**, p.205-207 (1999)

[7] S. Wang, V. Pasiskevicius, J. Hellström, F. Laurell, H. Karlsson, "First-order type II quasi-phase-matched UV generation in periodically poled KTP", *Opt. Lett.*, Vol.**24**, p.978-980 (1999)

[8] W. A. Clarkson, K. I. Martin, and D. C. Hanna, "High power single frequency operation and efficient intracavity frequency doubling of a Nd:YAG ring laser pumpted by a diode bar", *The Twelfth UK National Quantum Electronics Conference*, Southampton, UK, p.2-4 (1995)

[9] C. Yelland and W. Sibbett, "Stable 4W CW green laser pumped by fibre coupled diode laser array", *The Twelfth UK National Quantum Electronics Conference*, Southampton, UK, p.2-4 (1995)

[10] W. L. Nighan, and J. Cole, ">6W of stable, 532nm,TEM00 output at 30% efficiency from an intracavity doubled, diode pumped multi-axial mode Nd:$YVO_4$ laser", *Advanced Solid State Laser*, San Francisco, USA, post-deadline paper PD4 (1996)

[11] S. Sonoda, I. Tsuruma, and M. Hatori, "Second harmonic generation in electric poled x-cut MgO-doped $LiNbO_3$ waveguides", *Appl. Phys. Lett*., Vol.**70**, p.3078-3080 (1997)

[12] K. Mizuuchi, T. Sugita, and K. Yamamoto, "Efficient 340-nm light generation by a ridge-type waveguide in a first-order periodically poled MgO:$LiNbO_3$", *Opt. Lett*., Vol.**28**, p.1344-1346 (2003)

[13] W. M. Young, M. M. Fejer, M. J. F. Digonnet, A. F. Marshall, and R. S. Feigelson, "Fabrication, Characterization and Index Profile Modeling of High-Damage Resistance Zn-Diffused Waveguide in Congruent and MgO: Lithium Niobate", *J. Lightwave Technol*., Vol.**10**, p1238-1242 (1992)

[14] T. R. Volk, V. J. Pryalkin, N. M. Rubinina, "Optical-damage-resistant $LiNbO_3$:Zn crystal", *Opt. Lett*., Vol.**15**, p.997-999 (1990)

# Chapter 9

# Conclusions and Future Work

## 9.1 Conclusions

In this research, the fabrication of periodically poled lithium niobate (PPLN) and MgO-doped lithium niobate (PPMgLN) with grating periods ranging from 30μm to 5.0μm has been demonstrated. Different poling methods have been tried and compared, the work also shows that the grating quality of PPLN is determined by several factors, in particular, supplier variation, grating pattern design, thickness of the photo-resist, and the UV exposure time have all been investigated and analysed in detail.

It is widely believed that poling processes are governed by two mechanisms, nucleation of new domains and domain wall spreading under applied field [1,2,3]. The surface quality of the sample thus directly influences poling quality. Two factors were considered in this research, conductivity and surface defects, generally low conductivity is good for poling, because the low conductivity can reduce charge motion beneath the patterned electrodes [4], and surface defects are undesirable for forming new domains in term of uniformity. It was found that by carefully baking the sample after spin-coating the photo-resist can effectively reduce the spontaneous poling dots on the surface of sample, and, therefore, improve the poling quality.

The photo-resist thickness is more critical for fine period gratings than for longer period ones, increasing the thickness of the photo-resist was found to greatly improve the quality of poling. Good quality PPLN samples with fine period gratings were obtained by using 1.8μm thick photo-resist S1813.

The grating pattern design on the mask is crucial for high poling quality of PPLN, a new mask was designed for different period gratings. During the scope of this project, it was found that for large period gratings, better poling quality was achieved by using multiple small openings within each domain of the grating, allowing an increased

density of edges and corners in the photo-resist. For fine period gratings, narrow width gratings or a set of narrow sub-sections in the grating structure result in better poling quality. In addition, the mark-space ratio of the mask is important for poling quality, for large periods of PPLN, a suitable mark-space ratio is 40:60. For small periods of PPLN, a 30:70 mark-space ratio is suggested.

There is little difference in outcome between gel and metal electrodes used for the poling processes, but the gel method does show some advantages in lower electrode remnant on the surface of the PPLN grating after poling. However, Al electrodes are much better than gel electrodes in the backswitch poling method [5].

HexLN samples with a spatial period of 18.05μm and PPLT bulk samples with periods ranging from 7.0μm to 10μm were successfully fabricated. A planar buried waveguide was fabricated by Dr. Gallo in a HexLN sample using proton exchange. Second harmonic generation (red light) and third harmonic generation (green light) for 1536nm wavelength were observed. A PPLT sample was characterized by A. A. Lagatsky *et al*., where 40% conversion efficiency was obtained.

A novel process for forming zinc indiffused channel waveguides in PPLN was demonstrated. Both TE and TM modes are well confined, and guided in the zinc waveguides thermally indiffused at temperatures of 900°C or above. The SHG conversion efficiency for a 1552.4nm wavelength was measured, individual modes of the second harmonic were observed by tuning the temperature, a peak conversion efficiency of $59\%W^{-1}\cdot cm^{-2}$ was achieved at the room temperature. Using a short pulse source and an appropriately short waveguide, an SHG conversion efficiency of 81% was achieved.

Visible light generation by using the PPLN waveguide devices was investigated. Green light (532nm) was obtained by frequency doubling incident beams from a Nd:YAG laser and a conversion efficiency of $16.7\%W^{-1}\cdot cm^{-2}$ for first order SHG was achieved. Blue light (417.5nm) SHG was achieved through third order QPM by frequency doubling a tuneable titanium sapphire ($Ti:Al_2O_3$) laser and a conversion efficiency of $3.52\%W^{-1}\cdot cm^{-2}$ for third order SHG was achieved.

## 9.2 The Future Work

Despite the accomplishments of this research, a great deal remains to be done to realize the full potential of electric field periodic poling techniques and zinc indiffused PPLN waveguide devices. Further investigations are needed to optimize the waveguide fabrication conditions for different wavelengths. Efforts to achieve shorter domain periods while maintaining duty cycle uniformity over large areas must continue. With even finer periods to allow first order operation in the blue and better power handling capability, greater conversion efficiency for visible lasers can be realized. The following topics provide important areas for future work.

### 9.2.1 Segmented Tapered Waveguides

The input coupling efficiency of the waveguides in experiments described in the previous chapters is around 20-35% which is lower than ideal. The main reason is that the NA and mode size of a launched fibre (or the input beam through the objective lens) cannot match with that of the zinc indiffused channel waveguide due to the different refractive index and core size of the waveguide. The mode size of the single mode zinc indiffused waveguide can be modified to match better that of the fibre through decreasing the $\Delta n$ (refractive index difference) between the core and substrate, but a small $\Delta n$ also results in a waveguide that is more sensitive to the deviation of core size, hence decreasing the SHG efficiency.

Axial tapering of a dielectric waveguide structure is an effective method in transforming the mode properties of the input beam. In a tapered waveguide the mode size can be transformed in different portions of the waveguide. This increases the input and output coupling efficiency [6,7]. Tapered waveguide structure also allow effective coupling between single-mode to multi-mode waveguides, which is important in nonlinear guided-wave mixers, for example SHG device as described above.

The axial tapering of a dielectric waveguide can be effectively achieved by using a segmented taper structure which consists of segments that repeat with a period $\Lambda$.Each segment with the length of $l$ would be zinc indiffused producing an index-change $\Delta n$ and is separated by an un-diffused region [8], Figure 9.01(a) shows a schematic plot

of a periodically segmented waveguide. Based on theoretical and experimental investigations in previous literature [9,10,11,12], the equivalent refractive index in the segmented waveguide is taken to be: $n_{eq} = \Delta n \Gamma$, where the duty cycle $\Gamma = l / \Lambda$.

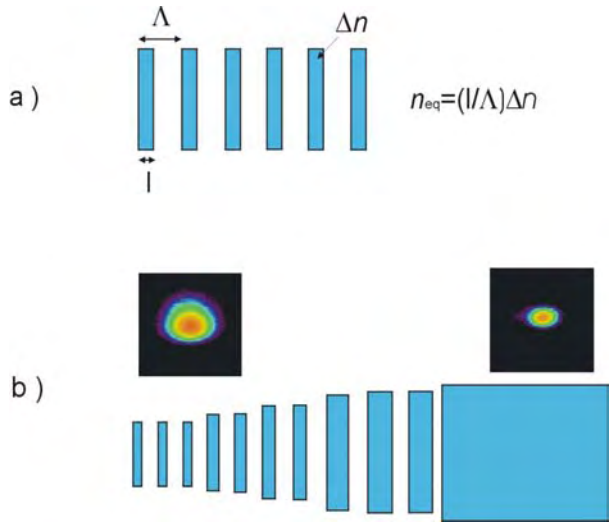


**Figure 9.01.** Segmented taper waveguide structure. (a) Schematic picture of a periodically segmented waveguide; (b) Tapered waveguide using segmented structure. Duty cycle and the width of segments can be modified simultaneously to optimize the mode size transformation.

The effective refractive index of the waveguide can be controlled and modified by changing the physical width and duty cycle of the segmented structure, resulting in mode size transformation in different portions of the waveguide, as illustrated in figure 9.01(b).

### 9.2.2 Further Improvement of Device Efficiency

Although high conversion efficiency has been demonstrated for a 1550nm wavelength in this research, there is still a need to increase the conversion efficiency especially for visible light generation. Fine period PPLN gratings are crucial for first order QPM blue light generation, improving the uniformity of the PPLN grating for fine periods and the quality of the waveguide could effectively increase the conversion efficiency. Thus the existing poling techniques need to be improved in order to get fine periods of PPLN with high quality.

Recently, several poling methods have been reported to pole fine period PPLN, such as using the corona technique and the atomic force microscopy (AFM) poling method [13,14]. PPLN sample with periods lower than 1μm have been obtained, results show

# Appendix A

## Matlab Code

### Matlab code for SHG conversion efficiency

```
%To estimate the overlap integral in our device, the Gaussian fitting was
%used to represent the normalized spatial profiles of the transverse
%waveguide modes at the two wavelength along the y direction.the Hermit-
Gaussian fitting was
%used to represent the normalized spatial profiles of the transverse
%waveguide modes at the two wavelength along the x direction. the hermit
guanssian fitting
%can be expressed as following:
%f(x)=C1xexp(-x.^2/(d).^2);  x</=d
%f(x)=C2exp(-(x-d)/b);       x>d


%Gaussina fit for SHG  mode in y direction=exp(-(y-0).^2./(2.*1.8.^2))
%Hermite-Gaussina fit for SHG  mode in x direction.
d=2.6; b=1.15; c1=1; c2=0.95;
x=0:0.1:2.6;
y=2.6:0.1:20;
f1=c1.*x.*exp(-x.^2./(d.^2));
f2=c2.*exp(-(y-d)./b);
plot(x,f1,y,f2)

hold on
%Gaussian fit for fundamentalmode in y direction=exp(-(y-0).^2./(2.*2.8.^2))
%Hermit-Gaussian fit for fundamentalmode in x direction
dd=3.6; bb=1.4; cc1=1; cc2=1.33;

x=0:0.1:3.6;
y=3.6:0.1:20;
ff1=cc1.*x.*exp(-x.^2./(dd.^2));
ff2=cc2.*exp(-(y-dd)./bb);

plot(x,ff1./1.2,y,ff2./1.2)

%F1 is the normalized spatial profiles of the transverse waveguide modes at
%fundamental wavelength, when x</=3; F2 is when x>3;
%V1 and V2 are the integral of the spatial profiles of the fundamental mode
%when x>/=3 and >3 respectively.
%_____________________________________________________________________

c1=1; c2=0.75;g7=2;g9=1.3;g6=4; g8=0.9;
cc1=1; cc2=1.81; gg6=6.5;gg7=2.5;gg8=1.25; gg9=3.4;

F1=inline('(1.*x.*exp(-(x-3.4).^2./(2.5.^2)).*exp(-(y-0).^2./(2.*2.6.^2))).^1')
V1=dblquad(F1,0,6.5,-10,10)

F2=inline('(1.81.*exp(-(x-6.5)./1.25).*exp(-(y-0).^2./(2.*2.6.^2))).^1')
V2=dblquad(F2,6.5,10,-10,10)


%S1 is the normalized spatial profiles of the transverse waveguide modes at
%SHG wavelength, when x</=2.5; F2 is when x>2.5;
%V11 and V22 are the integral of the spatial profiles of the fundamental mode
%when x>/=2.5 and >2.5 respectively.

S1=inline('(1.*x.*exp(-(x-1.3).^2./(2.^2)).*exp(-(y-0).^2./(2.*1.8.^2))).^1')
S2=inline('(0.75.*exp(-(x-4)./0.9).*exp(-(y-0).^2./(2.*1.8.^2))).^1')
```

```
V11=dblquad(S1,0,4,-10,10)
V22=dblquad(S2,4,10,-10,10)

%ef is the normalized constant of the spatial mode profile for fundamental
%wavelength
%es is the normalized constant of the spatial mode profile for SHG
%wavelength
ef=1./sqrt(V1+V2)
es=1./sqrt(V11+V22)


%F is the normalized overlap of spatial mode profiles between the
%fundamental mode and the SHG mode
%0.16 is the value of the ef(normalized constant for fundamental)
%0.262 is the value of es (normalized constant for SHG)

Fa=inline('(0.1.^2.*1.*x.*exp(-(x-3.4).^2./(2.5.^2)).*exp(-(y-
0).^2./(2.*2.6.^2))).^1.*0.2.*sqrt(1.*x.*exp(-(x-1.3).^2./(2.^2)).*exp(-(y-
0).^2./(2.*1.8.^2)))')

Fb=inline('(0.1.^2.*1.81.*exp(-(x-6.5)./1.25).*exp(-(y-
0).^2./(2.*2.6.^2))).^1.*0.2.*sqrt(0.75.*exp(-(x-4)./0.9).*exp(-(y-
0).^2./(2.*1.8.^2)))')

%V is the overlap integral of the interacting modes

Va=dblquad(Fa,0,3.4,-10,10)
Vb=dblquad(Fb,3.4,10,-10,10)

V=Va+Vb


a=17e-12; %Effective nonlinear coefficient
b=V;
c=2.175;    %The extraordinary refractive index of lithium niobate at 1550nm
d=8.8542e-12; %Permittivity of free space
f=3e8;   %The vaccum speed of light
g=1.55e-6; %Fundamental wavelength
%w is the normallized SHG conversion efficiency

w=(((a.^2)./(c.^3)).*((8.*pi.^2)./(f.*d.*g.^2))).*b.^2.*1e8
```

## Matlab code for coupling efficiency from fibre to channel waveguide.

```
%To estimate the overlap integral in our device, the Gaussian fitting was
%used to represent the normalized spatial profiles of the transverse
%waveguide modes at 1550nm for fiber and mode in waveguide along the y
direction.the Hermit-Gaussian fitting was
%used to represent the normalized spatial profiles of the transverse
%waveguide modes at the two wavelength along the x direction. the hermit
guanssian fitting
%can be expressed as following:
%f(x)=C1xexp(-(x-gg9).^2/(gg7).^2);  x</=gg6
%f(x)=C2exp(-(x-gg6)/gg8);       x>gg6

%Gaussina fit for mode in fiber for 1550nm, the mode field diameter for
%single mode fiber G652 at 1550nm is 10.4um. so the deviation of the
%Gaussian is 2.6um.
s=2.6;m=4.2;
x=-10:0.1:20;
y=exp(-(x-m).^2./(2.*s.^2));
plot(x,y.*3.8)

hold on
%Gaussian fit for fundamentalmode in y direction=exp(-(y-0).^2./(2.*2.8.^2))
%Hermit-Gaussian fit for fundamentalmode in x direction
```

```
cc1=1; cc2=1.45; gg6=6.5;gg7=2.5;gg8=1.25; gg9=3.4

x=0:0.1:6.5;
y=6.5:0.1:20;
ff1=cc1.*x.*exp(-(x-gg9).^2./(gg7.^2));
ff2=cc2.*exp(-(y-gg6)./gg8);

plot(x,ff1,y,ff2)
%_____________________________________________________________________

s=2.6;m=4.2;
cc1=1; cc2=1.45; gg6=6.5;gg7=2.5;gg8=1.25; gg9=3.4;

%F1 is the normalized spatial profiles of the transverse waveguide modes at
%fundamental wavelength, when x</=6.5; F2 is when x>6.5;
%V1 and V2 are the integral of the spatial profiles of the fundamental mode
%when x>/=3 and >3 respectively.

F1=inline('(1.*x.*exp(-(x-3.4).^2./(2.5.^2)).*exp(-(y-0).^2./(2.*2.6.^2))).^1')
V1=dblquad(F1,0,6.5,-10,10)

F2=inline('(1.45.*exp(-(x-6.5)./1.25).*exp(-(y-0).^2./(2.*2.6.^2))).^1')
V2=dblquad(F2,6.5,15,-10,10)

%S1 is the normalized spatial profiles of the transverse  modes at
%fundamental wavelength inside the fibre,

S1=inline('exp(-(x-4.2).^2./(2.*2.6.^2)).*exp(-(y-0).^2./(2.*2.6.^2))')
V11=dblquad(S1,-5,15,-10,10)

%ef is the normalized constant of the spatial mode profile for fundamental
%wavelength
%es is the normalized constant of the spatial mode profile for 1550nm
%wavelength inside fibre

ef=1./sqrt(V1+V2)
es=1./sqrt(V11)

%F is the normalized overlap of spatial mode profiles between the
%fiber and waveguide
%0.1 is the value of the ef(normalized constant for fundamentalmode in
%waveguide
%0.15 is the value of es (normalized constant for mode in fibre

Fa=inline('0.1.*sqrt(1.*x.*exp(-(x-3.4).^2./(2.5.^2)).*exp(-(y-
0).^2./(2.*2.6.^2))).*0.15.*sqrt(exp(-(x-4.2).^2./(2.*2.6.^2)).*exp(-(y-
0).^2./(2.*2.6.^2)))')

Fb=inline('0.1.*sqrt(1.45.*exp(-(x-6.5)./1.25).*exp(-(y-
0).^2./(2.*2.6.^2))).*0.15.*0.15.*sqrt(exp(-(x-4.2).^2./(2.*2.6.^2)).*exp(-(y-
0).^2./(2.*2.6.^2)))')

%V is the overlap integral of the interacting modes

Va=dblquad(Fa,0,6.4,-10,10)
Vb=dblquad(Fb,6.4,15,-10,10)

V=(Va+Vb).^2
```

promise that ferroelectric domains can be tailored in sub-micrometer and even nanometer scale in bulk ferroelectrics, leading to the development of nano-structured nonlinear photonic devices.

## References


[1] M. Hayashi, "Kinetics of domain wall motion in ferroelectric switching. I. General formulation," *Journal of the Physical Society of Japan*, Vol.**33**, p.616-628 (1972)

[2] L. E. Myers, "Quasi-phasematched Optical Parametric Oscillators in Bulk Periodically Poled Lithium Niobate", Stanford University, PhD thesis, p.43-44 (1995)

[3] G. D. Miller, "Periodically poled lithium niobate: Modeling, Fabricating, and Nonlinear-optical performance", Stanford University, PhD thesis, p.18-25 (1998)

[4] E. Fatuzzo and W. J. Merz, "Switching Mechanism in Triglycine Sulfate and Other Ferroelectrics", *Phys. Rev.*, Vol.**116**, p.61-68 (1959)

[5] R. G. Batchko, V. Y. Shur, M. M. Fejer and R. L. Byer, "Backswitch poling in lithium niobate for high-fidelity domain patterning and efficient blue light generation", *Appl. Phys. Lett.*, Vol.**75**, p.1673-1675 (1999)

[6] T. U. Haq, K. Webb, N. C. Gallagher, "Synthesis of waveguide mode control devices based on aperiodic gratings", *J. Opt. Soc. Am.*, A Vol.**13**, p.1501-1505 (1996)

[7] A. Shahar, W. J. Tomlinson, A. Y. Yan, M. Seto and R. J. Deri, "Dynamic etch mask technique for fabricating tapered semiconductor optical waveguides and other structures", *Appl. Phys. Lett.*, Vol.**56**, p.1098-1100 (1990)

[8] M. H. Chou, M. A. Arbore, and M. M. Fejer, "Adiabatically tapered periodic segmentation of channel waveguides for mode-size transformation and fundamental mode excitation", *Opt. Lett.*, Vol.**21**, p.794-796 (1996)

[9] Z. Weissman and A. Hardy, "2-D mode tapering via tapered channel waveguide segmentation", *Electron. Lett.*, Vol.**28**, p.1514-1516 (1992)

[10] L. Li and J. J. Burke, "Linear propagation characteristics of periodically segmented waveguides", *Opt. Lett.*, Vol.**17**, p.1195-1197 (1992)

[11] K. Thyagarajan, C. W. Chein, R. V. Ramaswany, H. S. Kim, and H. C. Cheng, "Proton-exchanged periodically segmented waveguides in $LiNbO_3$", *Opt. Lett.*, Vol.**19**, p.880-882 (1994)

[12] D. Nir, S. Ruschin, A. Hardy and D. Brooks, "Proton-exchanged periodically segmented channel waveguides in lithium niobate", *Electron. Lett.*, Vol.**31**, p.186-188 (1995)

[13] A. Harada and Y. Nihei, "Bulk periodically poled Mgo-$LiNbO_3$ by corona discharge method", *Appl, Phys. Lett.*, Vol.**69**, p.2629-2631 (1996)

[14] G. Rosenman, P. Urenski, A. Agronin, and Y. Rosenwaks, "Submicron ferroelectric domain structures tailored by high-voltage scanning probe microscopy", *Appl. Phys. Lett.*, Vol.**82**, p.103-105 (2003)

# Appendix B

## Publications, International Conference Papers and Patents

### Journal Papers

1. L. Ming, C. B. E. Gawith, K. Gallo, M. V. O'Connor, G. D. Emmerson, P. G. R. Smith, "High conversion efficiency single-pass second harmonic generation in a zinc-diffused periodically poled lithium niobate waveguide" *Optics Express*, Vol.**13**, pp.4862-4868 (2005)

2. L. Ming, C. B. E. Gawith, and P. G. R. Smith, "Green light generation using zinc-indiffused channel waveguides in periodically poled lithium niobate", *Optics communications, (submitted).*

3. M. A. Watson, M. V. O'Connor, P. S. Lloyd, D. P. Shepherd, D. C. Hanna, C. B. E. Gawith, L. Ming, P. G. R. Smith, O. Balachninaite, "Extended operation of synchronously pumped optical parametric oscillators to longer idler wavelengths", *Optics Letters* Vol.**27**(23) pp.2106-2108 (2002)

4. K. Gallo, R. T. Bratfalean, A. C. Peacock, N. G. R. Broderick, C. B. E. Gawith, L. Ming, P. G. R. Smith, D. J. Richardson, "Second harmonic generation in hexagonally poled lithium niobate slab waveguides", *Electronics Letters* Vol.**39**(1) pp.75-76 (2003)

5. A. A. Lagatsky, E. U. Rafailov, A. R. Sarmani, C. T. A. Brown, W. Sibbett, L. Ming and P. G. R. Smith, "Efficient femtosecond green-light source with a diode-pumped mode-locked $Yb^{3+}$:$KY(WO_4)_2$ laser", *Optics Letters*, Vol.**30**, pp.1144-1146 (2005)

### International Conference Papers

6. L. Ming, C. B. E. Gawith, P. G. R. Smith, "New approach to fabricating channel waveguides in z-cut PPLN using zinc-diffusion", *CLEO/IQEC 2004* San Francisco 16-21 May 2004 CWA33

7. Peter G. R. Smith, Lu Ming, Martin O'Connor, Corin B. E. Gawith, "Zinc diffused lithium niobate waveguides for high conversion efficiency second harmonic generation", *International Workshop: « LiNbO3: from material to device, from device to system »*, Supélec, Campus de Metz, May 23-25 2005

8. K. Gallo, R. T. Bratfalean, A. C. Peacock, N. G. R. Broderick, C. B. E. Gawith, L. Ming, P. G. R. Smith, D. J. Richardson, "Quadratic interactions in an hexagonally poled lithium niobate buried waveguide", *Nonlinear Guided Waves and Their Applications* Stresa, Italy 1-6 Sep 2002 NLWC5

9. A. A. Lagatsky, E. U. Rafailov, A. R. Sarmani, C. T. A. Brown, W. Sibbett, L. Ming and P. G. R. Smith, "Efficient frequency doubling of femtosecond pulses in a periodically-poled $LiTaO_3$ crystal at room temperature", *European Conference on Lasers and Electro-Optics 2005(E-CLEO), Munich, Germany (accepted for presentation)*

10. A. A. Lagatsky, E. U. Rafailov, A. R. Sarmani, C. T. A. Brown, W. Sibbett, L. Ming and P. G. R. Smith, "Efficient femtosecond green generation in a periodically poled $LiTaO_3$ crystal using a diode-pumped Yb:KYW laser", *Advanced Solid State Photonics 2005 (ASSP), Vienna, Austria (accepted for presentation)*

## Patents

11. "Fabrication of Zinc-diffused Waveguide in Periodically Poled Lithium Niobate", New International Patent Application PCT/GB2004/004806. World Intellectual Property Organization, International Publication Number: WO 2005/052682 A1, International Publication Data: 9 June 2005,

12. "Fabrication of Zinc-diffused Waveguide in Periodically Poled Lithium Niobate", Corresponding to British Patent Application No.0327267.1 and No.0405177.7